

NASA CR-76036

Final Report
Volume III - Appendix
September 1966

SGC 920FR-1

STUDY OF CONCEPTUAL DEEP SPACE MONITOR COMMUNICATIONS SYSTEMS USING A SINGLE EARTH SATELLITE

GPO PRICE \$ _____

CFSTI PRICE(S) \$ _____

Hard copy (HC) 3.00

Microfiche (MF) 165

Prepared for

653 July 65

MISSION ANALYSIS DIVISION
OFFICE OF ADVANCED RESEARCH AND TECHNOLOGY
NATIONAL AERONAUTICS AND SPACE ADMINISTRATION
Moffett Field, California

FACILITY FORM 602

N67-18654
(ACCESSION NUMBER)

316
(PAGES)

CR-76036
(NASA CR OR TMX OR AD NUMBER)

(THRU) _____

(CODE) _____

07
(CATEGORY)



STUDY OF CONCEPTUAL DEEP SPACE MONITOR
COMMUNICATIONS SYSTEMS USING A
SINGLE EARTH SATELLITE

Final Report

Volume III - Appendix

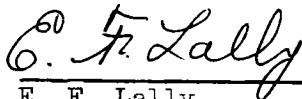
SGC 920FR-1

September, 1966

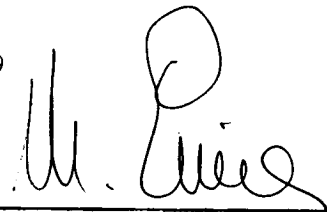
Prepared for

MISSION ANALYSIS DIVISION
OFFICE OF ADVANCED RESEARCH AND TECHNOLOGY
NATIONAL AERONAUTICS AND SPACE ADMINISTRATION
Moffett Field, California

Contract NAS 2-3179



E. F. Lally
Program Manager
Advanced Technology Center



M. Eimer
Vice President, Engineering

Prepared by

SPACE-GENERAL CORPORATION
9200 East Flair Drive
El Monte, California


U. S. Government

CONTENTS

	<u>Page</u>
SECTION 1.0 - INTRODUCTION	1
SECTION 2.0 - OUTLINE	2
SECTION 3.0 - MISSION ANALYSIS	5
3.1 Launch Vehicle Capabilities	5
3.2 Launch Site Selection	13
3.3 Orbit Selection Analysis	17
3.3.1 Line of Sight to Spacecraft	17
3.3.2 Environment Considerations	60
3.3.3 Earth Atmosphere R.F. Occultation	77
SECTION 4.0 - SATELLITE DISCIPLINE PARAMETRIC REQUIREMENTS AND DESIGN INTERFACE CONSIDERATIONS	107
4.1 Communications	107
4.1.1 Satellite Receiver	107
4.1.2 Satellite Transmitter	115
4.1.3 Antenna Electrical Design Requirements	124
4.1.4 Antenna Mechanical Design Requirements	157
4.2 Power	201
4.2.1 Nuclear Power Systems	202
4.2.2 Non-Nuclear Power Systems	214
4.2.3 Summary	221
4.3 Attitude Control	252
4.3.1 Mission Characteristics	252
4.3.2 Physical Characteristics	253
4.3.3 Disturbance Torques	259
4.3.4 Stellar Sensors	271
4.3.5 Attitude Control System	273
4.3.6 Resume	275
4.4 Environment Control	291
4.4.1 Solar Panel Thermal Control	291
4.4.2 RTG Power Units	293
4.4.3 Maser Amplifier Cooling	295
4.4.4 Transmitter Wave Guide Thermal Considerations	297
4.4.6 Other Environment Effects	298

ILLUSTRATIONS

	<u>Page</u>
3.1-1 Payload Capability Versus Orbit Inclination at 185 Kilometers Altitude, Launch from Cape Kennedy	7
3.1-2 Saturn IB/Centaur Shroud	8
3.1-3 Voyager Saturn IB/Centaur Shroud	9
3.1-4 Saturn IB Shroud	10
3.1-5 Titan III-C Shroud	11
3.1-6 Titan III-C Shroud	12
3.2-1 Payload vs Orbital Altitude for ETR Launch at 140° Azimuth and Dog Leg I_n to Polar Orbit	15
3.2-2 Payload vs Circular Orbital Altitude for WTR Launch into Polar Orbit	16
3.3.1.2-1 Satellite Spacecraft Line-of-Sight Geometry	37
3.3.1.2-2 Spacecraft Occultation Zones	38
3.3.1.2-3 Spacecraft Occultation Zones	38
3.3.1.2-4 Spacecraft Occultation Zones	38
3.3.1.2-5 Spacecraft Occultation Zones	38
3.3.1.2-6 Mercury Mission - Precession Rate vs Altitude	39
3.3.1.2-7 Mars Mission - Precession Rate vs Altitude	40
3.3.1.2-8 Jupiter Mission - Precession Rate vs Altitude	41
3.3.1.2-9 DSMCS Orbit Orientation	42
3.3.1.3-1 Mercury Flyby Trajectory	47
3.3.1.3-2 Mercury Flyby Orbit Altitude Envelope	48
3.3.1.3-3 Mercury Flyby Orbit Altitude Envelope	49
3.3.1.3-4 Mars Lander of 1981 Round Trip	50
3.3.1.3-5 Mars Round Trip Line-of-Sight Envelope	51
3.3.1.3-6 Optimum Launch Dates for Jupiter Flyby of 1978	52
3.3.1.3-7 Satellite-Spacecraft-Jupiter Relationships Jupiter Flyby - 1973 - Fast Transit Trajectory 680 Days	53
3.3.1.3-8 Satellite-Spacecraft-Jupiter Relationships Jupiter Flyby - 1978 - Fast Transit Trajectory 680 Days	54
3.3.1.3-9 Satellite-Spacecraft-Jupiter Relationships Jupiter Flyby - 1978 - Slow Transit Trajectory 1060 Days	55

ILLUSTRATIONS (Continued)

	<u>Page</u>
3.3.1.3-10 Jupiter Flyby Orbit Altitude Envelope	56
3.3.1.3-11 Jupiter Flyby Orbit Altitude Envelope	57
3.3.1.3-12 Jupiter Flyby Orbit Altitude Envelope	58
3.3.1.3-13 Venus Flyby Trajectory (1980)	59
3.3.2.1-1 Trapped Electron Radiation - 1975, 1985, Polar Orbit . . .	71
3.3.2.1-2 Trapped Electron Radiation 1978 - Polar Orbit	72
3.3.2.1-3 Trapped Proton Radiation 1975 - 1985 Polar Orbit	73
3.3.2.1-4 Charged Particle Ranges	74
3.3.2.1-5 Trapped Radiation Dose Rates - Shielded 1975, 1985 Polar Orbit	75
3.3.2.4-1 Orbital Decay Rates, 1975 - 1985 - Circular Orbits	76
3.3.3-1 Path Length - Altitude Relationship	95
3.3.3-2 Altitude vs Path Length	96
3.3.3-3 Altitude vs Path Length	97
3.3.3-4 Earth's Atmosphere Water Vapor Attenuation	98
3.3.3-5 Water Vapor Effects Upon Tangency Point	99
3.3.3-6 Attenuation vs Frequency	100
3.3.3-7 Attenuation vs Frequency	101
3.3.3-8 Attenuation vs Frequency	102
3.3.3-9 Altitude vs Electron Density	103
3.3.3-10 Signal Tangent Altitude - Kilometers	104
3.3.3-11 Wave Passing Through Atmosphere	105
3.3.3-12 Frequency vs Refraction Angle	106
4.1.1-1 Amplifier Temperature vs Frequency	114
4.1.2-1 Output Power Efficiency vs Frequency	122
4.1.2-2 Conversion Efficiency vs Frequency	123
4.1.3-1 Reflector Distortion Due to Thermal Loads	135
4.1.3-2 Relative Power vs Sight Angle	136
4.1.3-3 Relative Side Lobe vs Reflector Error	137
4.1.3-4 Reflector Distortion Gain Loss vs Reflector Error	138
4.1.3-5 Standard Deviation vs Reflector Errors	139

ILLUSTRATIONS (Continued)

		<u>Page</u>
4.1.3-6	Precision Diameter/ d rms Surface Deviation	140
4.1.3-7	Antenna Gain Limits	141
4.1.3-8	Feed Movement vs F/D	142
4.1.3-9	Gain/Feed Movement Relationships	143
4.1.3.3-1	Reflector Distortion Due to Manufacturing and Erection Errors	150
4.1.3.3-2	Reflector Distortion Due to Thermal Loads	151
4.1.3.3-3	Diameter/Frequency/Feed Motion Relationship	152
4.1.3.3-4	Diameter/Frequency/Feed Motion Relationship	153
4.1.3.3-5	Antenna Weight vs Diameter	154
4.1.3.3-6	Solid Antenna Gain vs Mass	155
4.1.3.3-7	Petal Antenna Gain vs Mass	156
4.1.4.2-1	Comparison of D/σ Versus Diameter for Different Types of Antenna Configurations	173
4.1.4-1	Paraboloid of Revolution Approximation	174
4.1.4-2	Loading Cases	175
4.1.4-3	Vertical Displacement vs Number of Conical Shell Elements	176
4.1.4-4	Horizontal Displacement vs Number of Conical Shell Elements	177
4.1.4-5	Inertial Axisymmetric Loading of 0.1 g	178
4.1.4-6	Inertial Asymmetric Loading of 0.1 g	179
4.1.4-7	Axisymmetric Thermal Loading	180
4.1.4.1-1	Achievable RMS's	181
4.1.4.1.2-1b	Asymmetric Thermal Condition	182
4.1.4.1.2-2	The Temperature Distribution Along a Meridian for the Axisymmetric Thermal Condition	183
4.1.4.1.2-3	Antenna Angle Definitions	184
4.1.4.1.3a-1	The Temperature Distribution in the Solid Parabolic Antenna for the Asymmetric Thermal Condition	185
4.1.4.1.3b-1	Diagram showing that the Thermal Energy Impinging on the Side of the Antenna Away from the Sun is a Func- tion of the Ratio of the Wire Size to Grid Hole Width	186

ILLUSTRATIONS (Continued)

	<u>Page</u>
4.1.4.1.3b-2 Temperature Distribution in the Grid Type Parabolic Antenna for Asymmetric Thermal Condition (Degrees Fahrenheit)	187
4.1.4.1.3b-3 RMS Cross Plot at 2.3 GHz	188
4.1.4.1.3b-4 RMS Cross Plot at 100 GHz	189
4.1.4.1.3b-5 RMS Cross Plot at 30 GHz	190
4.1.4.1.3b-6 RMS Cross Plot at 100 GHz	191
4.1.4.2.1-1 Relationship between Manufacturing Tolerance and Antenna Diameter (Solid Rigid Antenna)	192
4.1.4.2.1-2 Comparison of D/σ vs Diameter for Different Types of Parabolic Antennas	193
4.1.4.2.2-1 Typical Multiple Paraboloidal Antenna Array	194
4.1.4.2.4-1 Present and Anticipated Manufacturing and Erection Tolerances for Mesh Type Antennas	195
4.1.4.2.5a-1 Diagrams Showing Relationships Between Segments of Erectable Feed or Secondary Reflector Support	196
4.1.4.2.5a-2 Comparison of the Ratio of the Tip Deflection d_{total} to the Extended Length (S) of an Erectable Feed or Secondary Reflector Structure with the Number of Erectable Segments Used for Various Ratios of Extended Length (S) to Compressed Length (C)	197
4.1.4.2.5a-3 Erection and Calibration Tolerances for Erectable Feed vs Antenna Diameter	198
4.1.4.2.5b-1 Normal Deflection of Secondary Reflector (or Feed) vs Diameter Caused by Thermal Gradient	199
4.1.4.3-1 Antenna Weight vs Diameter	200
4.2-3 Power System Types vs Mission Requirements	224
4.2.1.1-1 Cost Availability of Isotopic Power Fuels	225
4.2.1.1-2 Radioisotope Snaps and Associated Snap Work	226
4.2.1.1-2 Radioisotope Snaps and Associated Snap Work (Continued)	227
4.2.1.1-2 Radioisotope Snaps and Associated Snap Work (Continued)	228
4.2.2.1.1-1 Primary Space Batteries	232
4.2.2.1.1-2 Sealed Secondary Space Batteries	233
4.2.2.1.2-1 Chemical Dynamic Systems	234
4.2.2.2.2-1 Solar Dynamic Systems	235

ILLUSTRATIONS (Continued)

	<u>Page</u>
4.2.1.1-1 RTG Fuel Configuration	237
4.2.1.1-2 RTG Configuration	237
4.2.1.4-1 SNAP-8 Power System	238
4.2.1.5-1 Thermoelectric Performance vs Temperature	239
4.2.1.5-2 Advanced Reactor Thermoelectric System Weight vs Power Level	240
4.2.1.5-3 Shield Weight vs Separation Distance	241
4.2.1.5.4 Optimum Reactor-Payload Separation Distance vs Power Level	242
4.2.1.5.5 Reactor Thermoelectric System Schematics	243
4.2.1.5-6 Reactor Thermoelectric Power System (2kWe)	244
4.2.2.2.3-1 Temperature of Solar Panels	245
4.2.2.2.3-2 Temperature Effect on Silicon Solar Cells	246
4.2.2.2.3-3 Solar Cell Degradation vs Proton Flux	247
4.2.2.2.3-4 Solar Cell Endurance	248
4.2.2.2.3-5 Effect of Shielding on Solar Cell Endurance	249
4.2.2.2.3-6 Effect of Shielding on Solar Cell Endurance	250
4.2.2.2.3-7 Effect of Shielding on Solar Cell Endurance	251
4.3-6 Torque and Momentum Requirements of Gravity Gradient Origin	284
4.3-1 NB Geometric Configuration	285
4.3-2 SB Geometric Configuration	286
4.3-3 Relationship Between Orbit-Plane Axes and Inertial Axes .	287
4.3-4 Relationship Between Body Axes and Inertial Axes	288
4.3-5 Functional Block Diagram of Fluid Flywheel Attitude Control System	289
4.3-6 GN ₂ ACS System Schematic	290
4.4.3-1 State-of-the-Art of Closed-Cycle Cryogenic Coolers	301
4.4.3-1 State-of-the-Art of Closed-Cycle Cryogenic Coolers (Continued)	302
4.4.3-1 State-of-the-Art of Closed-Cycle Cryogenic Coolers (Continued)	303

ILLUSTRATIONS (Continued)

		<u>Page</u>
4.4.3-1	State-of-the-Art of Closed-Cycle Cryogenic Coolers	304
4.4.2-1	Suggested Mounting for 3 RTG System	305
4.4.3-1	Specific Power vs Temperature for Closed-Cycle Cryogenic Coolers	306
4.4.3-2	Specific Power vs Specific Weight for Closed-Cycle Cryogenic Coolers	307
4.4.3-2	Minimum Area Required to Radiate 1 kW	308
4.4.4-1	An Estimate of Minimum Heat Flow from Wave Guide to Maser Cavity	309

Eight monthly reports were published during the study. They consisted of work notes prepared during each month and were in rough draft form. This Appendix summarizes the technological survey material presented in the monthly reports. The large volume of material presented in the monthly reports precludes complete coverage in the final report, therefore a condensation of the material appears here. The outline in Monthly Report 8 will provide topic and material location information for all the monthly reports. The following outlines the condensed technological survey material presented in this Appendix volume.

2.0	OUTLINE	Volume III - APPENDIX
1.0		Introduction
2.0		Outline
3.0		Mission Analysis
3.1		Launch Vehicle Capabilities
3.2		Launch Site Selection
3.3		Orbit Selection Analysis
3.3.1		Line of Sight to Spacecraft
3.3.1.1		Objective
3.3.1.2		Summary
3.3.1.3		Selected Orbits
3.3.2		Environment Considerations
3.3.2.1		Radiation Belts
3.3.2.1.1		Allowable Radiation Doses
3.3.2.2		Solar Plasma
3.3.2.3		Micrometeoroid Flux
3.3.2.4		Atmospheric Drag
3.3.3		Earth Atmosphere RF Occultation
4.0		Satellite Discipline Parametric Requirements and Design Interface Considerations
4.1		Communications
4.1.1		Satellite Receiver
4.1.2		Satellite Transmitter
4.1.3		Antenna Electrical Design Requirements
4.1.3.1		Antenna Types

- 4.1.3.2 Mechanical to Electrical Relationships
- 4.1.3.3 Practical Antenna Characteristics
- 4.1.4 Antenna Mechanical Design Requirements
 - 4.1.4.1 Structural Design Analysis
 - 4.1.4.1.1 Thermodynamic Analysis
 - 4.1.4.1.2 Axisymmetric Thermal Conditions
 - 4.1.4.1.3 Asymmetric Thermal Conditions
 - 4.1.4.1.3a Solid Antennas
 - 4.1.4.1.3b Grid Antennas
 - 4.1.4.2 Manufacturing and Deployment Surface Characteristics
 - 4.1.4.2.1 Rigid Single Piece Antennas
 - 4.1.4.2.2 Multiple Paraboloid Arrays
 - 4.1.4.2.3 Erectable Petal Paraboloid Antennas
 - 4.1.4.2.4 Inflatables and Mesh Type Structures
 - 4.1.4.2.5 Feed Position
 - 4.1.4.2.5a Erection Tolerances
 - 4.1.4.2.5b Operation Tolerances
 - 4.1.4.3 Antenna Weights Summary
- 4.2 Power
 - 4.2.1 Nuclear Systems
 - 4.2.1.1 Radioisotope Thermoelectric Generators
 - 4.2.1.2 SNAP-1
 - 4.2.1.3 SNAP-2
 - 4.2.1.4 SNAP-8
 - 4.2.1.5 SNAP-10A
 - 4.2.1.6 SNAP-50
 - 4.2.2 Non-Nuclear Power Systems
 - 4.2.2.1 Chemical Systems
 - 4.2.2.1.1 Batteries
 - 4.2.2.1.2 Chemical-Dynamic Systems
 - 4.2.2.1.3 Fuel Cells
 - 4.2.2.2 Solar Powered Systems
 - 4.2.2.2.1 Solar Collectors
 - 4.2.2.2.2 Solar Dynamic Systems
 - 4.2.2.2.3 Photovoltaic Systems

- 4.2.3 Summary
- 4.3 Attitude Control
 - 4.3.1 Mission Characteristics
 - 4.3.2 Physical Characteristics
 - 4.3.3 Disturbance Torques
 - 4.3.4 Stellar Sensors
 - 4.3.5 Attitude Control System
 - 4.3.6 Resume
- 4.4 Environment Control
 - 4.4.1 Solar Panel Thermal Control
 - 4.4.2 RTG Power Units
 - 4.4.3 Maser Amplifier Cooling
 - 4.4.4 Transmitter Wave Guide Thermal Considerations
 - 4.4.5 Transmitter Cooling
 - 4.4.6 Other Environment Effects

The launch vehicles considered for the D.S.M.C.S. mission are the Saturn IB/Centaur, Saturn IB and Titan III C. Payloads that these vehicles can place in earth orbit were determined as a function of circular orbital altitude and inclination for launches from Eastern and Western test ranges. This information was obtained by means of a trajectory computer program which optimizes the direct burn flight profile to place the maximum payload into a 185 kilometer circular orbit. The payloads at higher orbital altitudes were obtained by first computing the characteristic velocity requirement to transfer from the 185 kilometer orbit to the higher circular orbit altitude on a Hohmann ellipse using the equation:

$$\Delta V = \sqrt{\frac{\mu}{R+h_1}} \left[\left(1 - \frac{R+h_1}{R+h_2}\right) \sqrt{\frac{2}{1 + \frac{R+h_1}{R+h_2}}} + \sqrt{\frac{R+h_1}{R+h_2} - 1} \right] \quad (1)$$

where

ΔV = characteristic velocity meters/second

μ = earth gravity constant $3.98604 \times 10^5 \text{ km}^3/\text{sec}^2$

R = earth radius, 6378.39 km

h_1 = lower circular orbit altitude 185 kilometers

h_2 = upper circular orbit altitude, kilometers

The payload weight was then computed from the characteristic velocity equation:

$$W_p = W_o \exp \left(- \left(\frac{\Delta V}{g_o I_{sp}} \right) \right) - W_s \quad (2)$$

where

W_o = total weight injected into a 185 kilometer orbit
(kilograms)

W_s = stage weight inerts (kilograms)

I_{sp} = specific impulse (sec)

g_o = gravity acceleration (9.81 meters/sec²)

Figure 3.1-1 presents payload capabilities for the three launch vehicles as a function of orbit inclination for the 185 kilometer circular parking orbit. DSMCS parking orbit payloads are available from the figure at 90° inclination. The Saturn V launch vehicle provides payload capabilities in excess of DSMCS requirements and therefore was not considered in this study. Shroud configurations for the launch vehicles of interest are shown in Figures 3.1-2 through 3.1-6. (Reference 3.1-1.)

Reference 3.1-1, SNAP-8 Unmanned Applications Study SGC 778FR-1, Summary Volume.

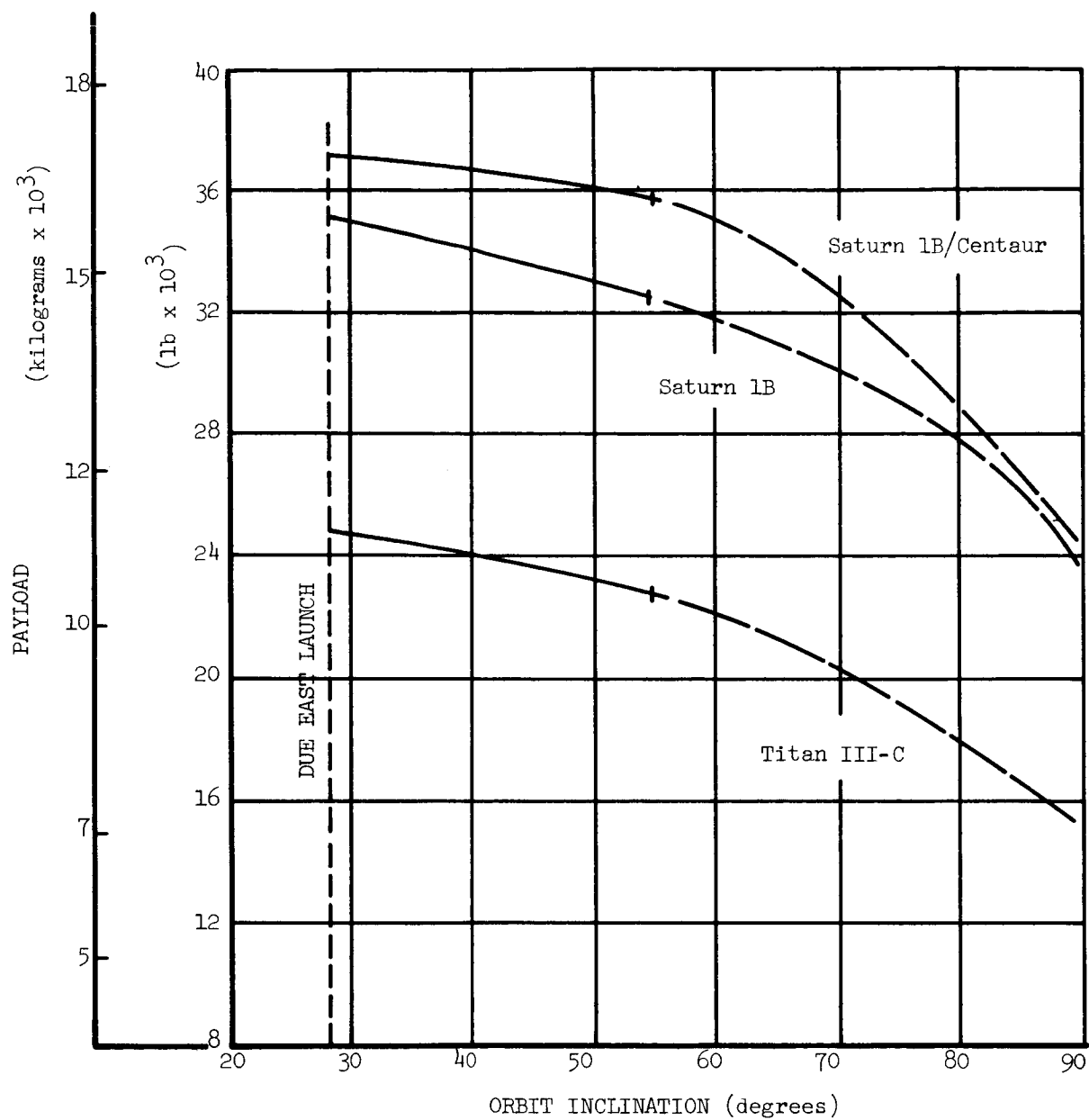


Figure 3.1-1. Payload Capability Versus Orbit Inclination
at 185 Kilometers Altitude, Launch from
Cape Kennedy

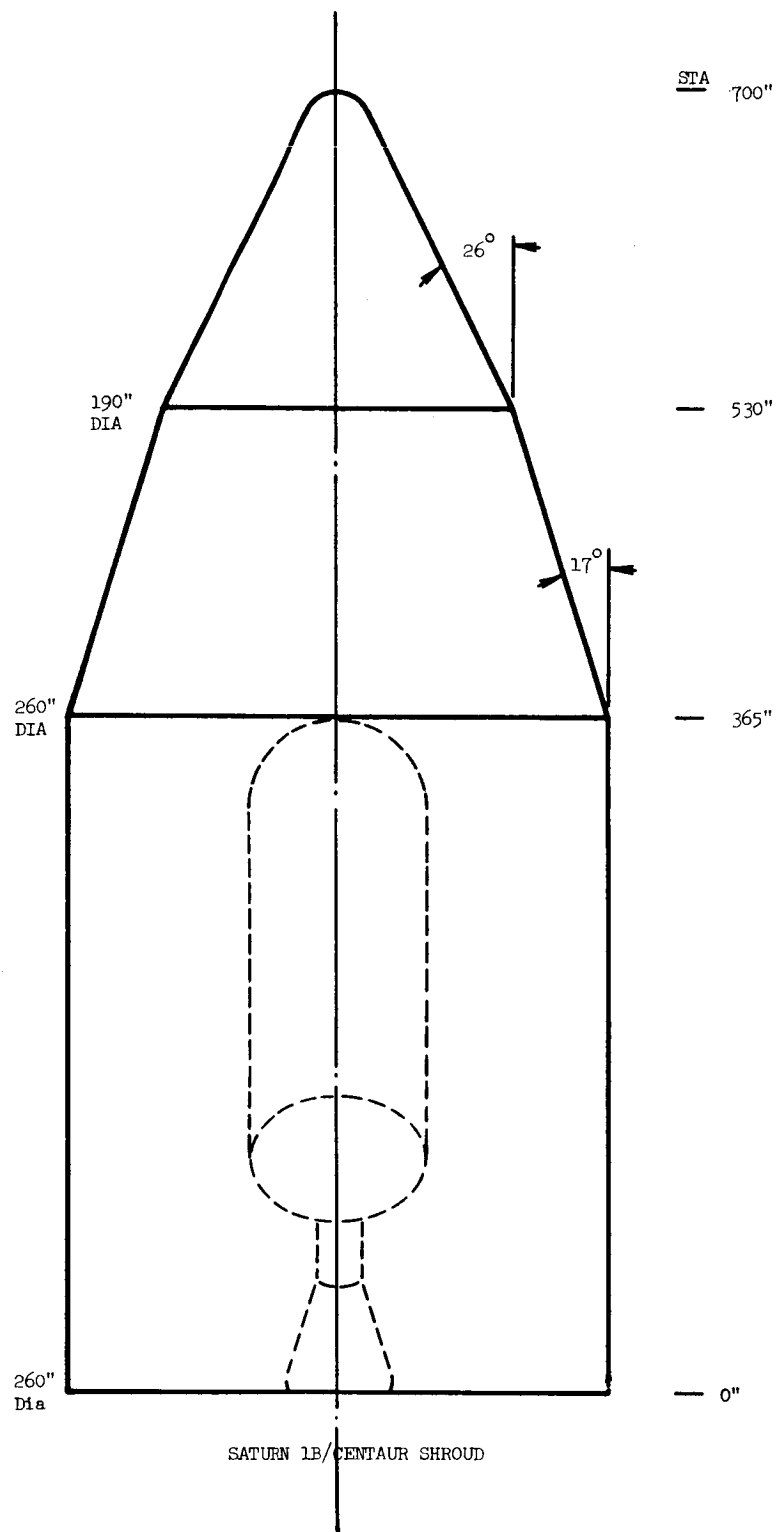


Figure 3.1-2. Saturn IB/Centaur Shroud*

* Reference 3.1-1

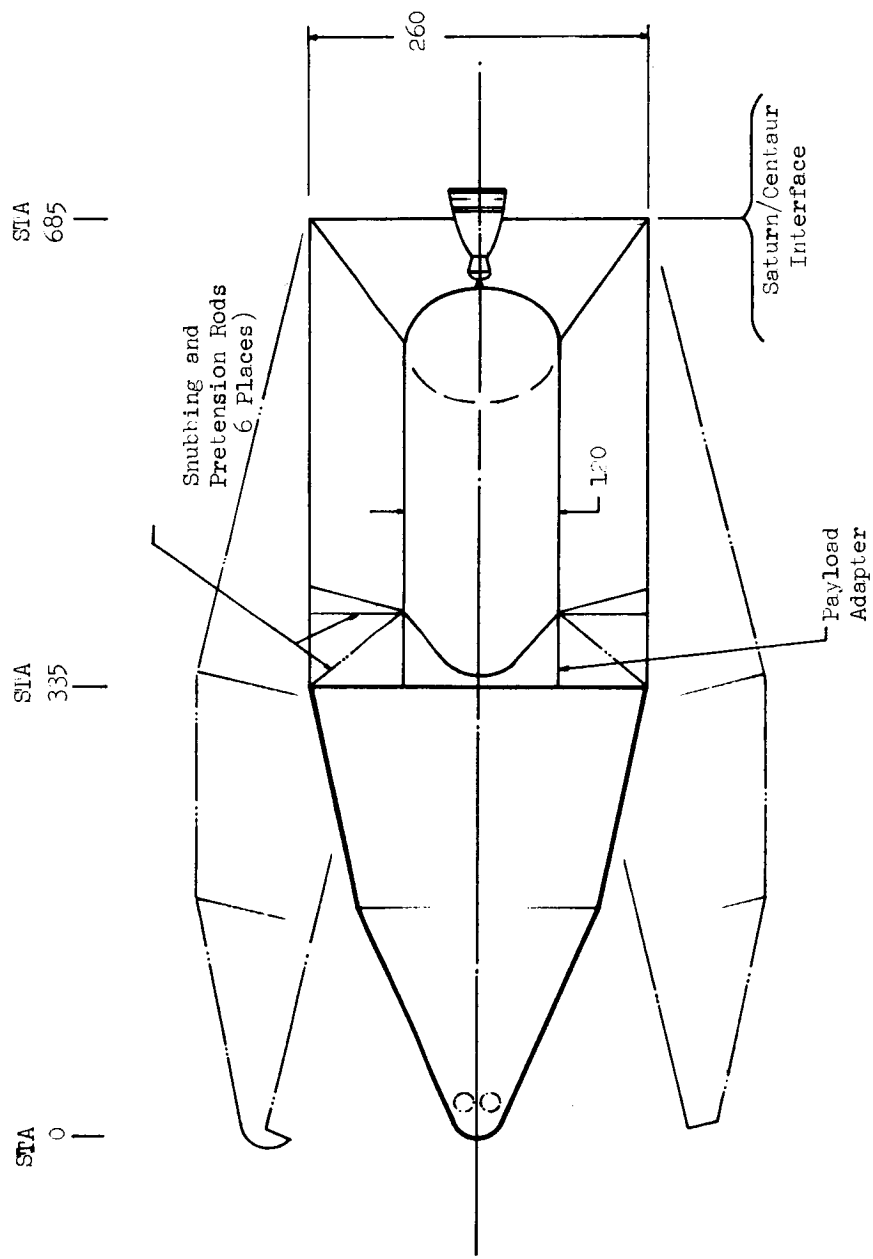


Figure 3.1-3. Voyager Saturn IB/Centaur Shroud*

* Reference 3.1-1

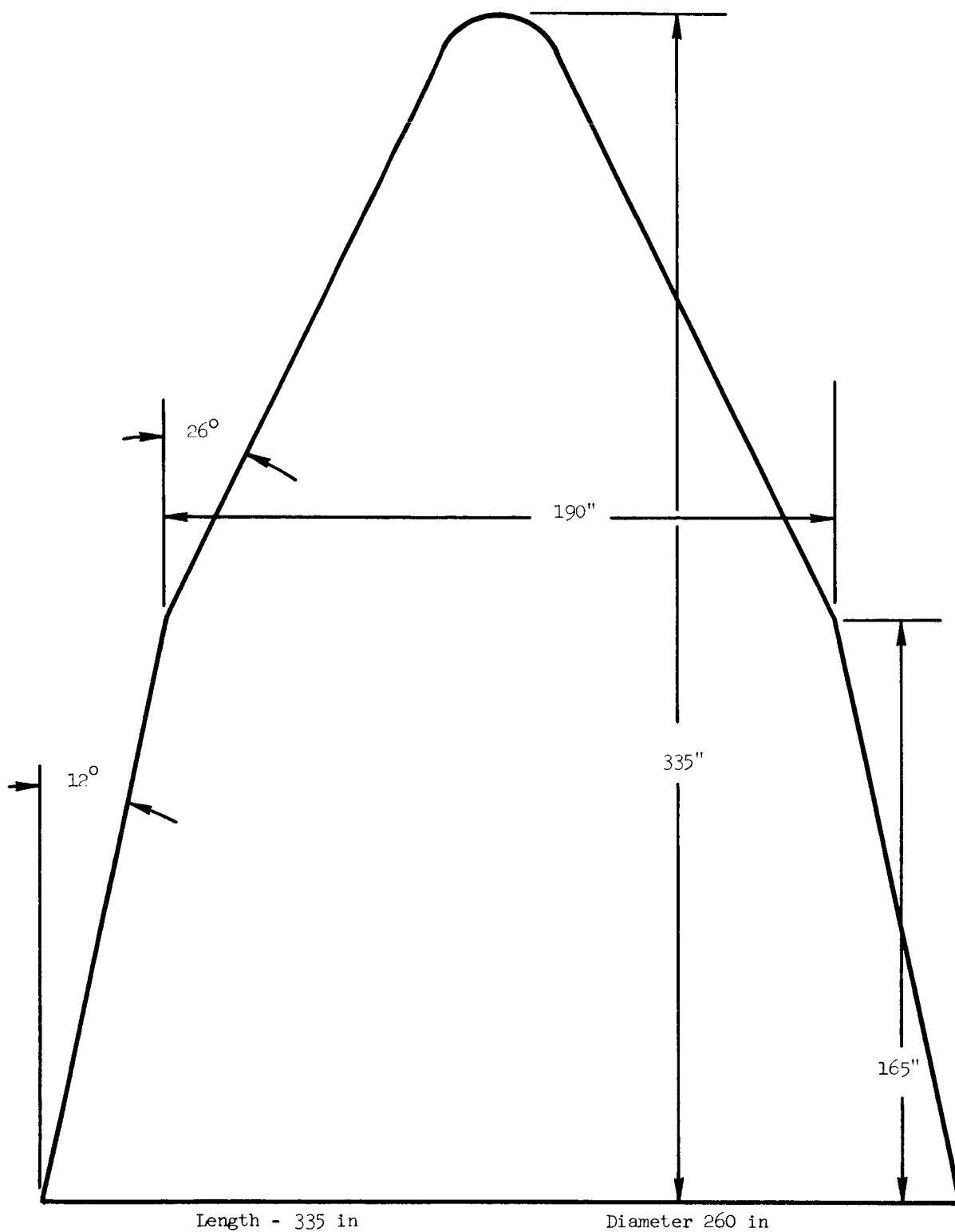


Figure 3.1-4. Saturn IB Shroud*

* Reference 3.1-1

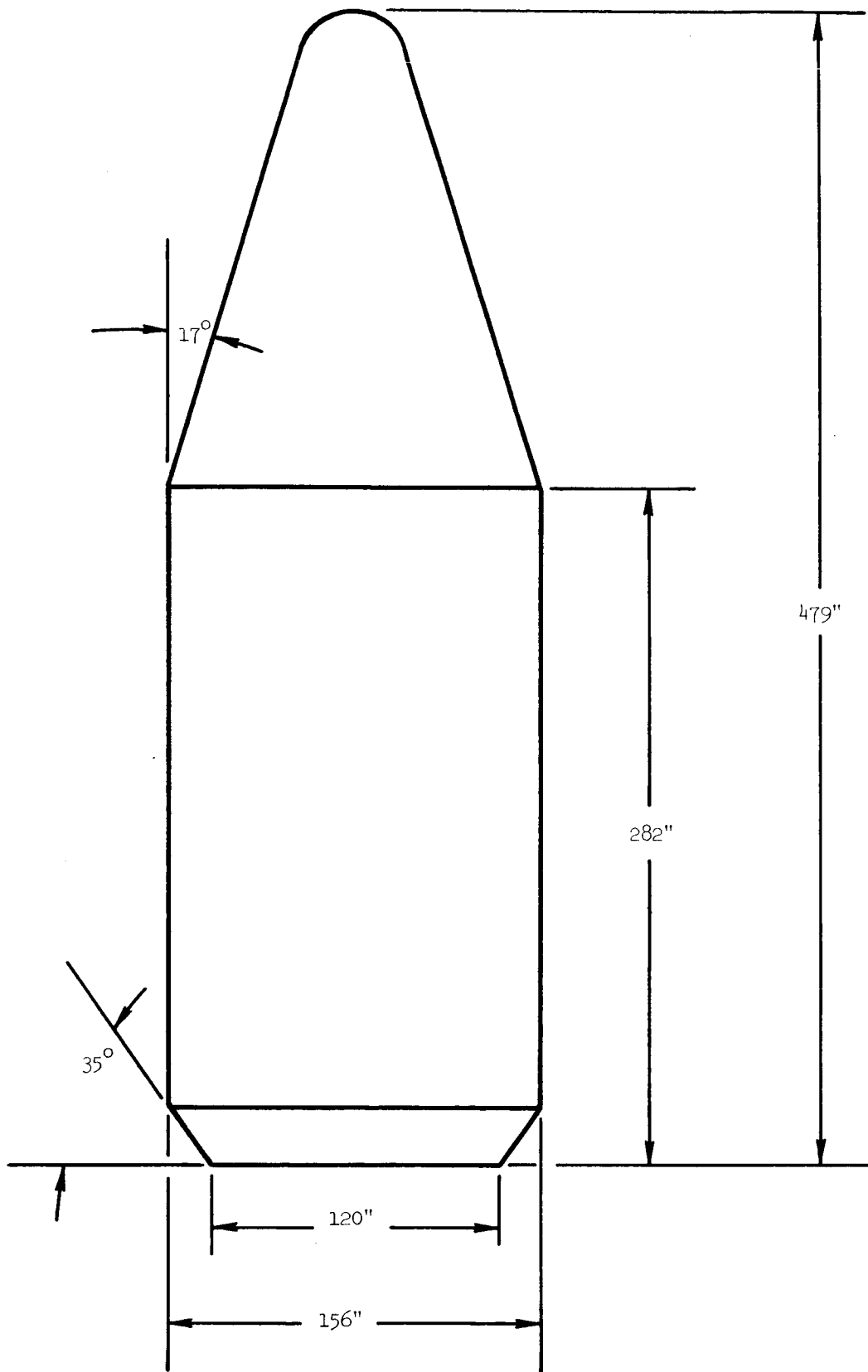


Figure 3.1-5. Titan III-C Shroud*

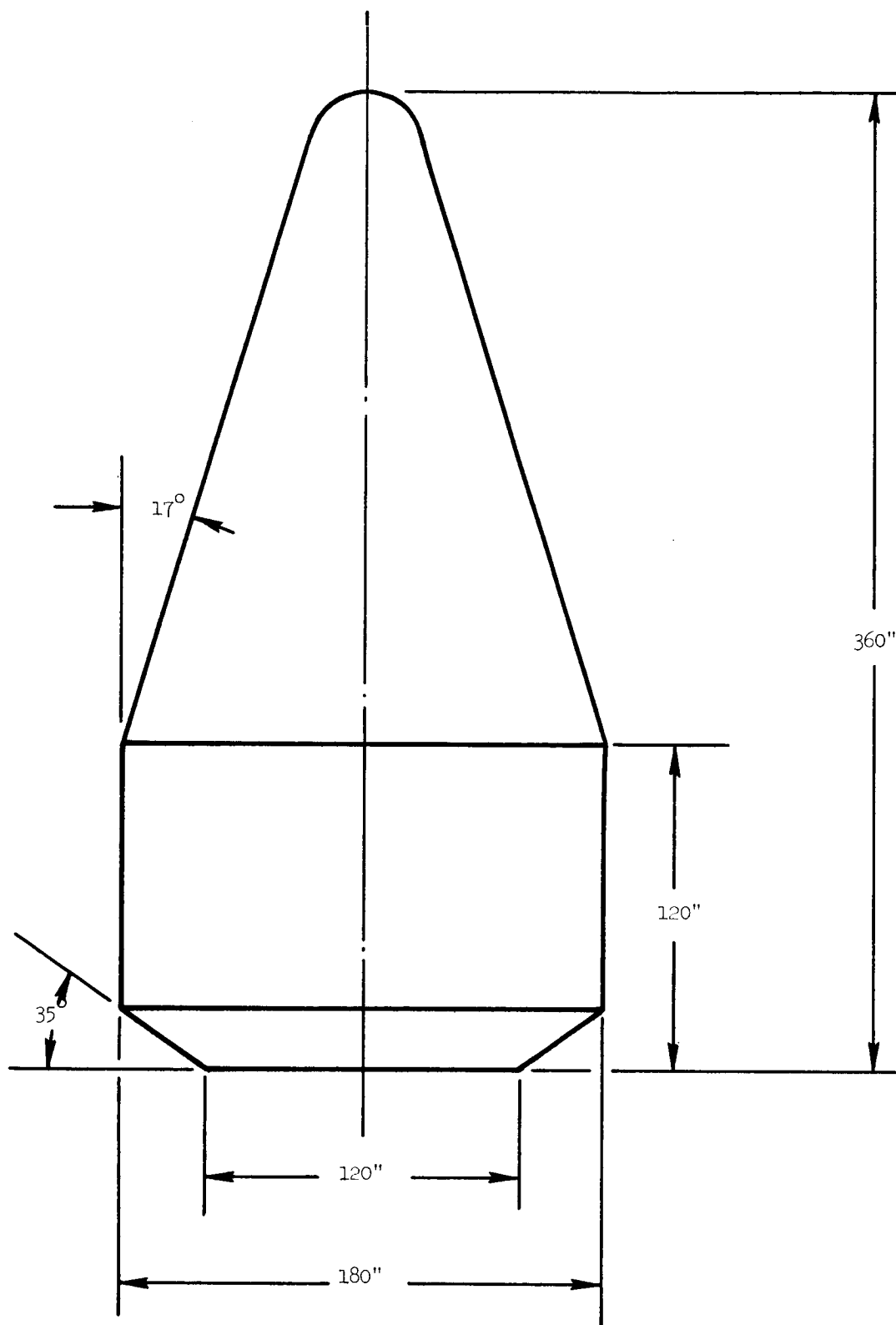


Figure 3.1-6. Titan III-C Shroud*

Figures 3.2-1 and 3.2-2 plot payload capabilities as a function of orbital altitudes for the Saturn IB/Centaur, Saturn IB and Titan IIIC for launches into polar orbit from the Eastern (ETR) and Western (WTR) Test Ranges respectively. Table 3.2-1 presents the payloads required for the various missions. Selected orbit altitudes discussed in Section 3.3.1, Line of Sight to Spacecraft, were used to derive the available payload weights of Table 3.2-1.

The Saturn IB is the preferred launch vehicle for DSMCS applications. A sacrifice in payload compared to the Saturn IB/Centaur is accepted for the increased packaging volume made available by the 6.1 meter (20 ft) diameter Saturn IB shroud. The standard Saturn IB/Centaur shroud provides only 3.05 meters (10 ft) diameter for payload. The Voyager 6.1 meter (20 ft) diameter Saturn IB/Centaur shroud, Figure 3.1-3, could be used but a payload sacrifice is imposed because of the large shroud which is attached to the S-IVB stage and surrounds the Centaur stage as well as the payload.

Table 3.2-1
AVAILABLE DSMCS PAYLOADS FOR SELECTED ORBITS (KILOGRAMS)

Site/Launch Vehicle Mission	ETR			WTR		
	Saturn 1B/ Centaur	Saturn 1B	Titan III C	Saturn 1B/ Centaur	Saturn 1B	Titan III C
Mercury Flyby	10,000	8,820	6,550	11,100	8,600	7,250
Manned Mars	9,600	8,400	6,250	12,100	9,750	7,900
Jupiter Flybys (3 Missions)	9,600-9,950	8,400-8,950	6,250-6,700	12,100-12,700	9,750-10,600	7,900-8400

lbs x 10³
kilograms

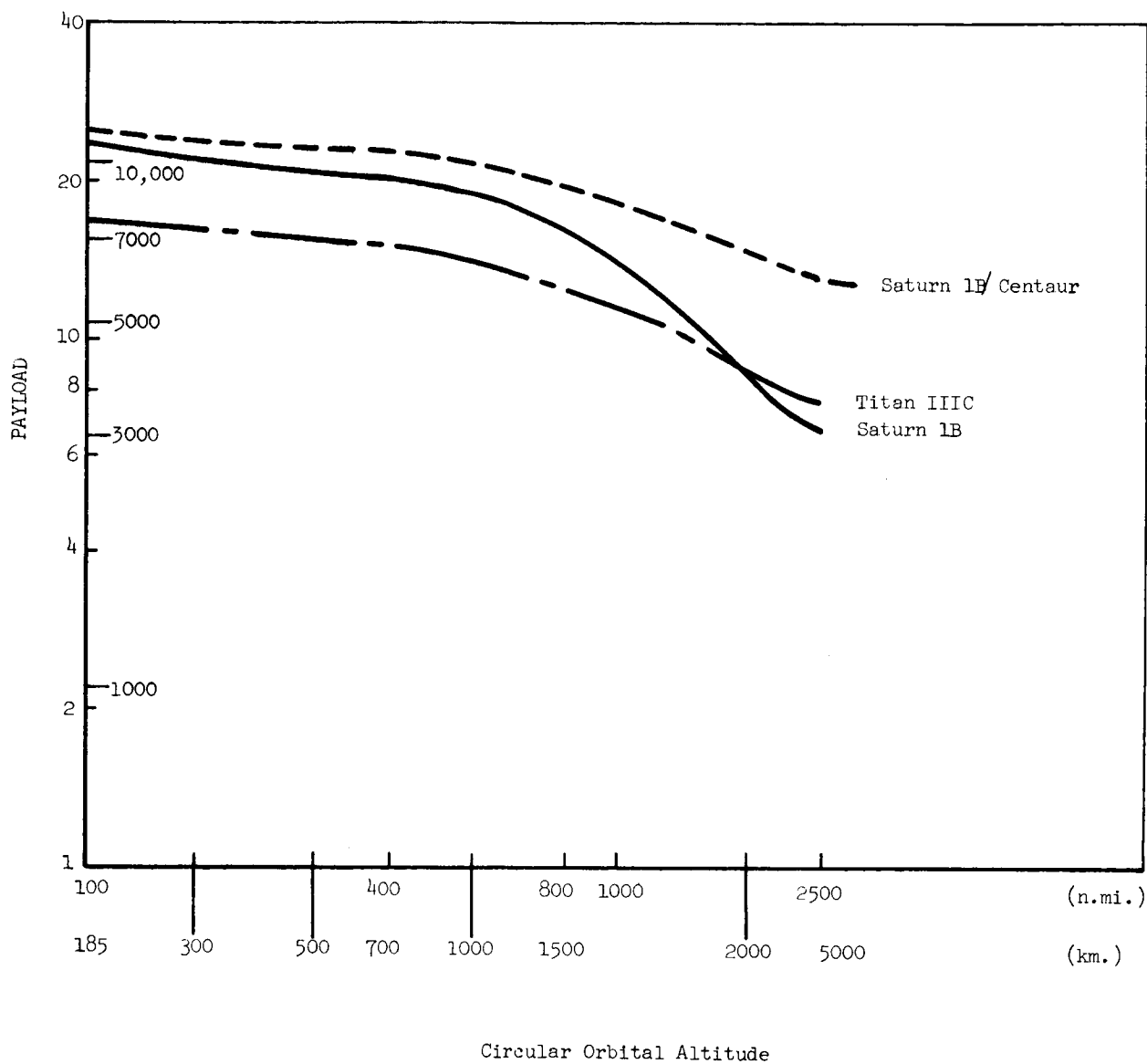


Figure 3.2-1. Payload vs Orbital Altitude for ETR Launch at 140° Azimuth and Dog Leg I_n to Polar Orbit

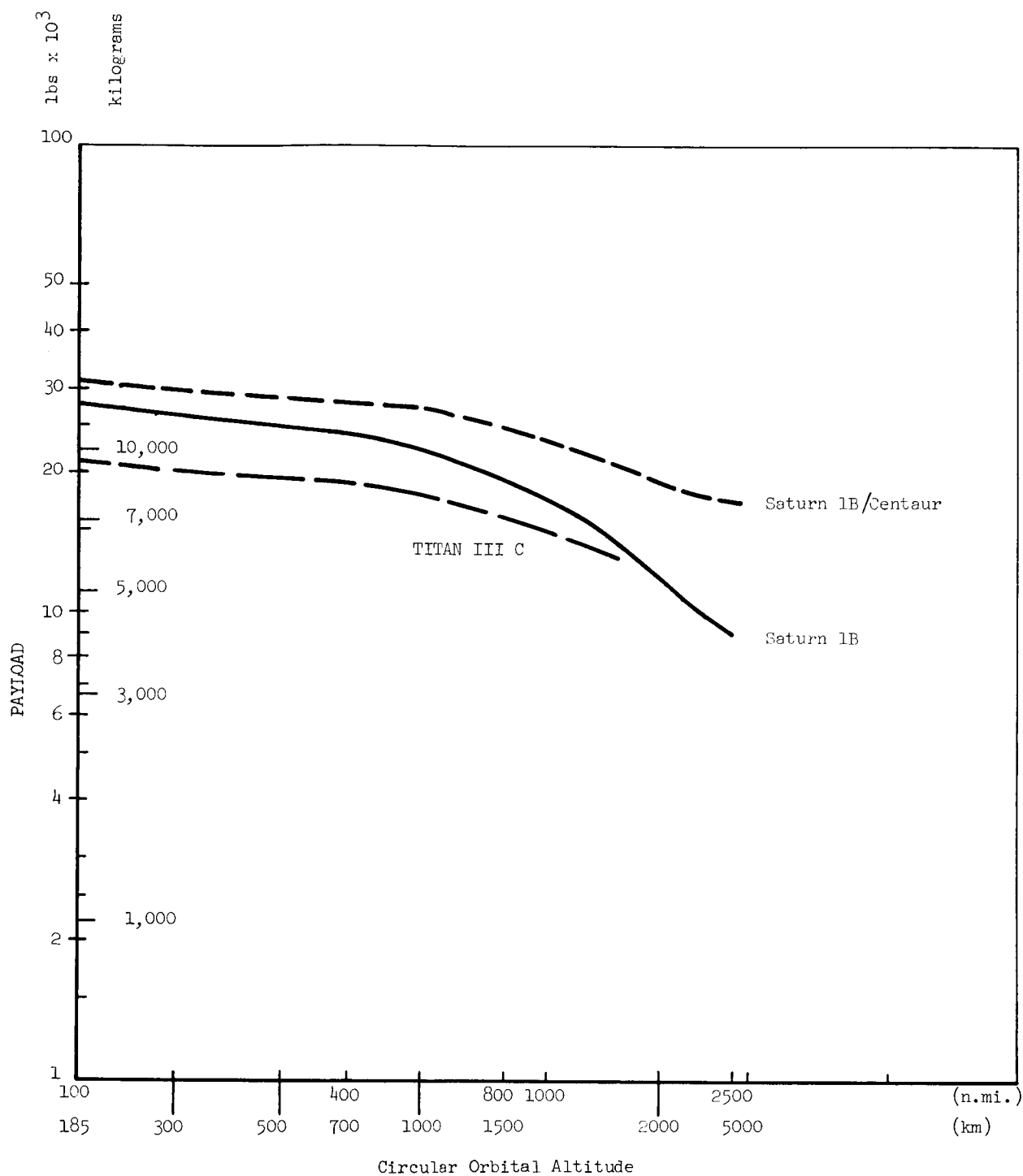


Figure 3.2-2. Payload vs Circular Orbital Altitude for WTR Launch Into Polar Orbit

3.3 ORBIT SELECTION ANALYSIS

3.3.1 LINE OF SIGHT TO SPACECRAFT

3.3.1.1 OBJECTIVE

Selected DSMCS orbits corresponding to a variety of spacecraft trajectories were calculated. This was accomplished through the use of a three dimensional, two-body interplanetary trajectory computer program. The program developed specifically for this task, features an iterative routine which can be employed to solve for DSMCS orbits that provide continuous line of sight for a given mission.

3.3.1.2 SUMMARY

The general problem of the DSMCS/Spacecraft line of sight reduces to finding the appropriate orbital precession rate to provide continuous line of sight during given spacecraft missions. The satellite-spacecraft geometry is shown in Figure 3.3.1.2-1.

Figure 3.3.1.2-2 illustrates the DSMCS in a typical orbit with orbit altitude h of approximately $1/2$ earth radius with the orbit plane normal to the spacecraft/earth radial vector. The angle α represents the visibility band. Thus, if the radial vector is kept within α , DSMCS/spacecraft line of sight will be maintained. Note that in Figure 3.3.1.2-3 when the orbit altitude h is increased, the visibility band α also increases. In Figure 3.3.1.2-4 the DSMCS orbit plane is positioned approximately parallel to the earth/spacecraft radial vector. It is interesting to note here that some occultation will occur even with exceedingly large orbit altitudes. The DSMCS orbit altitude becomes somewhat less important with proper orientation of the orbit plane as shown in Figure 3.3.1.2-5. As has been shown in Section 3.3.3 the Earth radius has been extended 40 km to accommodate atmospheric attenuation influences.

It is apparent that suitable results for the general satellite/spacecraft line-of-sight problem can be achieved through the proper orientation of the satellite orbit plane and a selection of the minimum orbit altitude. The most favorable line-of-sight results are obtained when the earth/spacecraft radial vector is normal to the satellite orbit plane. However, in the case of an inertially fixed satellite orbit plane, the retention of this angle is not

always possible. In fact, the radial vector can move outside of the visibility band due to the relative movements of the earth/spacecraft.

If the heliocentric spacecraft trajectory is known, an angle can be determined through which the satellite orbit plane must be periodically rotated in order to maintain line of sight. With the angle of rotation and time of plane change known, a method to produce the desired plane change is required. Nodal precession from an orbit precessing the desired amount and in the proper direction would provide a passive solution, passive from the standpoint of not requiring satellite onboard maneuvers. Within certain limits the satellite inclination and orbit altitude can be varied to yield a wide range of nodal precession rates in the direction of or against the orbital motion of the satellite. However, to be consistent with the requirements of minimum orbit altitude for maximum payload, the satellite inclination is restricted to a few degrees from polar. As the complement angle (90-inclination) of the inclination increases, a corresponding increase in orbit altitude is required to eliminate the occultation occurring from the satellite moving more frequently behind the earth.

The preceding analysis is applied to the following spacecraft/DSMCS missions.

- 1) Mercury Flyby - Fast transit
- 2) Manned Mars Orbit and Return - 30 day stay
- 3) Jupiter Flyby - 1973 opportunity - Fast transit
- 4) Jupiter Flyby - 1978 opportunity - Fast transit
- 5) Jupiter Flyby - 1978 opportunity - Slow transit

The spacecraft heliocentric trajectory parameters for these missions along with a Venus mission that could not be satisfied are presented in Tables 3.3.1.2-1 through 3.3.1.2-6. Table 3.3.1.2-7 summarizes DSMCS orbits required for the corresponding missions. Figures 3.3.1.2-6, -7 and -8 present precession rates versus altitudes for inclinations from polar orbit to ± 5 degrees. Each curve represents the interest area of altitudes surrounding the altitudes noted in Table 3.3.1.2-7 that provide continuous line of sight for the three types of missions. Table 3.3.1.2-8 is a general presentation of inclination from polar orbit and precession rate for altitudes to 1800 kilometers.

The computer program used to determine line of sight values describes the motion of a spacecraft in its heliocentric orbit, the motion of an earth orbiting satellite, and computes the line of sight properties between the two. The program was written in the Fortran IV programming language for the IBM 7000 series computers.

METHOD OF APPROACH

In order to develop a computer program for the general line of sight problem, it was necessary to compute the relative motion of three bodies, namely: earth motion in heliocentric coordinates, satellite motion in earth orbit, and spacecraft motion in heliocentric coordinates.

The following is an outline of the computational procedure:

- A. Given heliocentric ecliptic orbital parameters: semi-major axis (a), orbit inclination (i), argument of perigee (ω), longitude of the ascending node (Ω), eccentricity (e), radial distance from Sun center (r), right ascension (α), and declination (β), compute the orbital motion of the earth and the spacecraft.
- B. Given initial geocentric equatorial orbit parameters a , i , ω , r , and e . Compute the orbital motion of the earth orbiting satellite in geocentric equatorial coordinates. Orbital perturbation arising from nodal precession is considered.
- C. Transform satellite motion from geocentric equatorial motion to geocentric ecliptic coordinates, and to heliocentric coordinates.
- D. Transform spacecraft motion from heliocentric ecliptic to geocentric ecliptic.
- E. Compute component of unit vector from earth center to satellite in geocentric ecliptic coordinates.
- F. Compute component of line of sight vector from satellite to spacecraft in geocentric ecliptic coordinates.
- G. Compute look angle (Ψ) between line of sight vector and the satellite position vector.

H. Compute the instantaneous minimum circular satellite altitude which will result in a continuous unbroken line of sight between spacecraft and satellite.

The computational procedure presented in steps A through H is a "real time" solution, that is, the real time motions of the three aforementioned bodies are considered. At each computational interval, the satellite's orbit is divided into 36 equal increments of ten degrees each at which time the look angles and minimum satellite orbit altitudes are computed. The 36 look angles are evaluated to determine the minimum circular satellite orbit which will yield the required continuous line of sight at that instantaneous real time position. This procedure is repeated for every computational increment throughout the duration of the spacecraft's flight, and the value for the minimum satellite circular orbit at each step is stored. The stored values of the minimum satellite circular orbit altitude are then compared to yield the smallest value for the satellite's orbit altitude that will result in the continuous line of sight for the duration of the spacecraft mission.

MATHEMATICAL FORMULATION

The method employed to describe the relative orbital motions of the earth, spacecraft, and satellite is the several conventional Keplerian equations and will not be presented here. The one exception to the ordinary Keplerian solution for orbital motion is the method for computing the eccentric anomaly for values of eccentricity greater than 0.7. A Newton-Raphson method of iterating the known value of the mean anomaly to achieve the eccentric anomaly was developed.

Referring to computational step B under Method of Approach, the equations are as follows:

The position vector of the satellite in terms of the orbital parameters.

1. inclination (i)
2. longitude of the ascending node (Ω) measured from the vernal equinox
3. eccentricity (e)

4. semi-major axis (a)
5. argument of perigee (ω)
6. true anomaly (θ)

in earth centered equatorial coordinates is given by:

$$\bar{r} = x' \bar{i} + y' \bar{j} + z' \bar{k} \quad (1)$$

where

$$x' = \frac{a(1-e^2)}{1+e \cos \theta} \left[\cos \theta (\cos \omega \cos \Omega - \cos i \sin \Omega \sin \omega) - \sin \theta (\sin \omega \cos \Omega + \cos i \sin \Omega \cos \omega) \right] \quad (2)$$

$$y' = \frac{a(1-e^2)}{1+e \cos \theta} \left[\cos \theta (\cos \omega \sin \Omega + \cos i \cos \Omega \sin \omega) + \sin \theta (-\sin \Omega \sin \omega + \cos \Omega \cos \omega \cos i) \right] \quad (3)$$

$$z' = \frac{a(1-e^2)}{1+e \cos \theta} \left[\cos \Omega \sin \omega \sin i + \sin \theta \sin i \cos \omega \right] \quad (4)$$

The transformation from equatorial coordinates (x', y', z') to ecliptic coordinates (x, y, z) of equation 3 is accomplished by

$$\begin{bmatrix} x \\ y \\ z \end{bmatrix} = \begin{bmatrix} 1 & 0 & 0 \\ 0 & \cos \epsilon & -\sin \epsilon \\ 0 & \sin \epsilon & \cos \epsilon \end{bmatrix} \begin{bmatrix} x' \\ y' \\ z' \end{bmatrix}$$

where ϵ is the angle between equatorial and ecliptic planes ($\epsilon \approx 23.44^\circ$) and the x' and x axis both point to the vernal equinox.

The position vector to the satellite in ecliptic coordinates is expressed by:

$$\bar{r} = x \bar{i} + y \bar{j} + z \bar{k}$$

A unit vector in this direction can be defined as

$$u = \frac{r_e x \bar{i}}{|\bar{r}|} + \frac{r_e y \bar{j}}{|\bar{r}|} + \frac{r_e z \bar{k}}{|\bar{r}|}$$

and

$$\bar{u} = u_1 \bar{i} + u_2 \bar{j} + u_3 \bar{k}$$

where

$$u_1 = \frac{r_e x}{|\bar{r}|}, u_2 = \frac{r_e y}{|\bar{r}|}, u_3 = \frac{r_e z}{|\bar{r}|}$$

r_e = earth radius

$$|\bar{r}| = \left\{ x^2 + y^2 + z^2 \right\}^{1/2}$$

The unit length of the vector \bar{u} is one earth radius.

$$|\bar{u}| = r_e$$

The position vector from earth center to spacecraft in ecliptic coordinates is determined in the same manner as is the position vector of the satellite in equation (4). (5)

The components xx , yy , and zz , of the spacecraft in term of latitude (β) and longitude (λ) are determined by: (6)

$$xx = |\bar{r}| \cos \beta \cos \lambda$$

$$yy = |\bar{r}| \cos \beta \sin \lambda$$

$$zz = |\bar{r}| \sin \beta$$

The line of sight vector from the satellite to the spacecraft can now be determined by

$$\bar{r}_v = \bar{r}_{SC} - \bar{r}_{SA}$$

where \bar{r}_v = radial vector from the satellite radius vector (\bar{r}_{SA}) to the spacecraft radius vector (\bar{r}_{SC}). (In subsequent analysis, the subscripts e, SA and SC, will pertain to the earth, satellite, and the spacecraft respectively.)

and

$$\bar{r}_v = (x_{SA} - x_{SC}) \bar{i} + (y_{SA} - y_{SC}) \bar{j} + (z_{SA} - z_{SC}) \bar{k}$$

The corresponding unit vector is simply:

$$\bar{u}_{SA} = u_1 \bar{i} + u_2 \bar{j} + u_3 \bar{k}$$

where

$$u_{1SA} = r_e \frac{(x_{SA} - x_{SC})}{|\bar{r}|}$$

$$u_{2SA} = r_e \frac{(y_{SA} - y_{SC})}{|\bar{r}|}$$

$$u_{3SA} = r_e \frac{(z_{SA} - z_{SC})}{|\bar{r}|}$$

and

$$|\bar{r}| = \left[(x_{SA} - x_{SC})^2 + (y_{SA} - y_{SC})^2 + (z_{SA} - z_{SC})^2 \right]^{1/2}$$

The look angle Ψ is now defined as

$$\Psi = \cos^{-1} \left[\bar{u} \cdot \bar{u}_{SA} \right]$$

g. A final computation is required to compute the satellite circular orbit (H_{SA}). (7)

H_{SA} can be found as a function of the look angle Ψ by the following expression:

$$H_{SA} = \frac{r_e + H_{ion}}{\cos \Psi} - r_e$$

where

r_e = earth radius

H_{ion} = input altitude of disturbing ionosphere

Ψ = total look angle

Computer program inputs are listed in Sections A and B of Table 3.3.1.2-9, the outputs are listed in Section C and is the printout key for the printed results. Figure 3.3.1.2-9 presents the orbit orientation and related parameters of the DSMCS orbit analysis.

TABLE 3.3.1.2-1
PLANETARY TRAJECTORY PARAMETERS

<u>MISSION</u>	<u>MERCURY FLYBY</u>
Earth Departure Date	JED-2445963.75, UCD - 20 Sept. 1984
Planet Arrival Date	JED-2446078.75, UCD - 13 Jan. 1985
Transit Time	115 Days
Eccentricity	.4253256
Angular travel (β)	221° 27' 52.62"
True anomaly	-177° 32' 25.74"
Semi-major axis	10.5438304 x 10 ⁷ km
Longitude of Earth at departure	357° 20' 44.42"
Δ Velocity Requirement from 286 KM Parking Orbit	5,308 mps

TABLE 3.3.1.2-2
PLANETARY TRAJECTORY PARAMETERS

<u>MISSION</u>	<u>MARS</u>
Earth Departure Date	JED-2444954.75, UCD - 16 Dec. 1981
Planet Arrival Date	JED-2445164.75, UCD - 14 July 1982
Transit Time	210 days
Eccentricity	.22620032
Angular travel (β)	156° 48' 39.57"
True anomaly	-0° 31' 10.69"
Semi-major axis	1.9021347 x 10 ⁸ km
Longitude of Earth at departure	84° 6' 20.71"
Δ Velocity Requirement from 286 KM Parking Orbit	3,579 mps

TABLE 3.3.1.2-3
PLANETARY TRAJECTORY PARAMETERS

<u>MISSION</u>	<u>JUPITER FLYBY</u>
Earth Departure Date	JED-2441783.75, UCD - 11 Apr. 1973
Planet Arrival Date	JED-2442463.75, UCD - 20 Feb. 1975
Transit Time	680 days
Eccentricity	.68980767
Angular Travel (β)	156° 41' 48.78"
True anomaly	6° 12' 14.83"
Semi-major axis	4.8211339 x 10 ⁸ km
Longitude of Earth at departure	201° 10' 25.73"
Δ Velocity Requirement from 286 KM Parking Orbit	6,526 mps

TABLE 3.3.1.2-4

PLANETARY TRAJECTORY PARAMETERS

<u>MISSION</u>	<u>JUPITER FLYBY</u>
Earth Departure Date	JED-2443786.75, UCD - 5 Oct. 1978
Planet Arrival Date	JED-2444466.75, UCD - 15 Aug. 1980
Transit Time	680 days
Eccentricity	.73890522
Angular travel (β)	156° 41' 38.61"
True anomaly	0° 12' 10.03"
Semi-major axis	5.7283067 x 10 ⁸ km
Longitude of Earth at departure	11° 34' 20.27"
Δ Velocity Requirement from 286 KM Parking Orbit	6,846 mps

TABLE 3.3.1.2-5

PLANETARY TRAJECTORY PARAMETERS

<u>MISSION</u>	<u>JUPITER FLYBY</u>
Earth Departure Date	JED-2443776.75, UCD - 25 Sept. 1978
Planet Arrival Date	JED-2444836.75, UCD - 20 Aug. 1981
Transit Time	1060 days
Eccentricity	.69305284
Angular travel (β)	194° 38' 3.06"
True anomaly	-14° 57' 51.6"
Semi-major axis	4.8187107 x 10 ⁸ km
Longitude of Earth at departure	1° 44' 42.61"
Δ Velocity Requirement from 286 KM Parking Orbit	7,011 mps

TABLE 3.3.1.2-6
PLANETARY TRAJECTORY PARAMETERS

<u>MISSION</u>	<u>VENUS FLYBY</u>
Earth Departure Date	JED-2444324.75, UCD - 26 Mar. 1980
Planet Arrival Date	JED-2444444.75, UCD - 24 July 1980
Transit Time	120 days
Eccentricity	.17193166
Angular travel (β)	140° 5' 36.26"
True anomaly	-178° 26' 16.57"
Semi-major axis	12.7345429 x 10 ⁷ km
Longitude of Earth at departure	185° 39' 26.93"
Δ Velocity Requirement from 286 KM Parking Orbit	3,783 mps

TABLE 3.3.1.2-7

SELECTED DSMCS ORBITS

Mission	Circular Orbit Altitude (km)	Inclination (degrees)	Precession Rate (deg/day)	Mission Transit Time (days)
Mercury Flyby	842	90.5	0.057	115
Manned Mars Orbit and Return	1116	93.4	0.34	450
Jupiter Flyby 1973 Fast Transit	933	91.1	0.12	680
Jupiter Flyby 1978 Fast Transit	817	91.3	0.15	680
Jupiter Flyby 1978 Slow Transit	1117	90.9	0.09	1060

TABLE 3.3.1.2-8
NEAR POLAR ORBIT PRECESSION RATES VS ALTITUDE

Altitude (Kilometers)	Inclination from Polar Orbit (Deg.)	Precession Rate (Deg/day)	Altitude (Kilometers)	Inclination from Polar Orbit (Deg.)	Precession Rate (Deg/day)
100	0.5	.08334	400	0.5	.07112
	1.0	0.1666		1.0	0.1422
	1.5	0.2500		1.5	0.2133
	2.0	0.3333		2.0	0.2844
	2.5	0.4165		2.5	0.3554
	3.0	0.4998		3.0	0.4265
	3.5	0.5830		3.5	0.4975
	4.0	0.6662		4.0	0.5685
	4.5	0.7493		4.5	0.6394
	5.0	0.8324		5.0	0.7103
200	0.5	.07898	500	0.5	.06756
	1.0	0.1579		1.0	0.1351
	1.5	0.2369		1.5	0.2026
	2.0	0.3158		2.0	0.2702
	2.5	0.3948		2.5	0.3377
	3.0	0.4737		3.0	0.4051
	3.5	0.5525		3.5	0.4726
	4.0	0.6314		4.0	0.5400
	4.5	0.7101		4.5	0.6074
	5.0	0.7888		5.0	0.6747
300	0.5	.07492	600	0.5	.06423
	1.0	0.1498		1.0	0.1284
	1.5	0.2247		1.5	0.1926
	2.0	0.2996		2.0	0.2568
	2.5	0.3744		2.5	0.3210
	3.0	0.4493		3.0	0.3852
	3.5	0.5241		3.5	0.4493
	4.0	0.5989		4.0	0.5134
	4.5	0.6737		4.5	0.5774
	5.0	0.7482		5.0	0.6414

TABLE 3.3.1.2-8

NEAR POLAR ORBIT PRECESSION RATES VS ALTITUDE - Continued

Altitude (Kilometers)	Inclination from Polar Orbit (Deg.)	Precession Rate (Deg/day)	Altitude (Kilometers)	Inclination from Polar Orbit (Deg.)	Precession Rate (Deg/day)
700	0.5	.06110	1000	0.5	.05283
	1.0	0.1222		1.0	0.1056
	1.5	0.1833		1.5	0.1584
	2.0	0.2443		2.0	0.2113
	2.5	0.3054		2.5	0.2641
	3.0	0.3664		3.0	0.3168
	3.5	0.4274		3.5	0.3696
	4.0	0.4884		4.0	0.4223
	4.5	0.5494		4.5	0.4750
	5.0	0.6103		5.0	0.5276
800	0.5	.05817	1100	0.5	.05040
	1.0	0.1163		1.0	0.1008
	1.5	0.1745		1.5	0.1511
	2.0	0.2326		2.0	0.2015
	2.5	0.2907		2.5	0.2519
	3.0	0.3489		3.0	0.3022
	3.5	0.4069		3.5	0.3525
	4.0	0.4650		4.0	0.4028
	4.5	0.5230		4.5	0.4531
	5.0	0.5810		5.0	0.5033
900	0.5	.05542	1200	0.5	.04811
	1.0	0.1108		1.0	.09621
	1.5	0.1662		1.5	0.1443
	2.0	0.2216		2.0	0.1924
	2.5	0.2770		2.5	0.2404
	3.0	0.3323		3.0	0.2885
	3.5	0.3877		3.5	0.3365
	4.0	0.4430		4.0	0.3845
	4.5	0.4983		4.5	0.4325
	5.0	0.5535		5.0	0.4804

TABLE 3.3.1.2-8

NEAR POLAR ORBIT PRECESSION RATES VS ALTITUDE - Continued

Altitude (Kilometers)	Inclination from Polar Orbit (Deg.)	Precession Rate (Deg/day)	Altitude (Kilometers)	Inclination from Polar Orbit (Deg.)	Precession Rate (Deg/day)
1300	0.5	.04595	1600	0.5	.04017
	1.0	.09189		1.0	.08035
	1.5	0.1378		1.5	0.1205
	2.0	0.1837		2.0	0.1606
	2.5	0.2296		2.5	0.2008
	3.0	0.2755		3.0	0.2409
	3.5	0.3214		3.5	0.2810
	4.0	0.3673		4.0	0.3211
	4.5	0.4131		4.5	0.3612
	5.0	0.4589		5.0	0.4012
1400	0.5	.04391	1700	0.5	.03846
	1.0	.08782		1.0	.07692
	1.5	0.1317		1.5	0.1153
	2.0	0.1756		2.0	0.1538
	2.5	0.2195		2.5	0.1922
	3.0	0.2633		3.0	0.2306
	3.5	0.3072		3.5	0.2690
	4.0	0.3510		4.0	0.3074
	4.5	0.3948		4.5	0.3458
	5.0	0.4385		5.0	0.3841
1500	0.5	.04199	1800	0.5	.03683
	1.0	.08398		1.0	.07367
	1.5	0.1259		1.5	0.1105
	2.0	0.1679		2.0	0.1473
	2.5	0.2098		2.5	0.1841
	3.0	0.2518		3.0	0.2209
	3.5	0.2937		3.5	0.2577
	4.0	0.3356		4.0	0.2944
	4.5	0.3775		4.5	0.3312
	5.0	0.4193		5.0	0.3679

Table 3.3.1.2-9

INPUTS - SECTION A

SYMBOL	DESCRIPTION	UNITS
ASCR	Semi-major axis of the spacecraft heliocentric orbit	A.U.
ECCSC2	Eccentricity of the spacecraft heliocentric orbit	--
GLOED	Initial longitude of the earth measured from the vernal equinox - positive counterclockwise	DEG
GLSC2	Inclination of the spacecraft orbit - measured positive upward from the ecliptic plane	DEG
THSC2	Initial true anomaly of the spacecraft. Measured positively counterclockwise from perihelion	DEG
HP - HA	Where HP = HA DSMCS circular orbit altitude	km
OMDSIF	Initial DSMCS longitude of the ascending node measured positively counterclockwise from the vernal equinox in the equatorial plane	DEG
GIDSIF	Inclination of the DSMCS orbit measured with respect to the earth's equatorial plane	DEG
DELT	Print interval - Results will be printed every DELT steps	DAYS
TDAYS	Total computation time. Computations will terminate at TDAYS	DAYS
HION	Altitude of disturbing ionosphere	km
TDISC	Time for discontinuity. A discontinuity may consist of either a planet stay time or new spacecraft trajectory, or both. If TDISC = 0, Section B inputs are not required	DAYS
ICNT	FLAG; If ICNT = 1, the .36 values of h min. and look angle are printed out each time point	--
TT	Title card - Identification label; may use up to 72 alpha-numeric characters.	--

Table 3.3.1.2-9 (Continued)

INPUTS - SECTION B

SYMBOL	DESCRIPTION	UNITS
TSTAY	Target stay time	DAYS
ASC2	Semi-major axis of the inbound spacecraft trajectory	A.U.
ECCSC2	Eccentricity of the inbound spacecraft trajectory	--
GISC2	Inclination of the inbound spacecraft trajectory	DEG
THSC02	True anomaly of the inbound spacecraft trajectory	DEG
ITARG	FLAG to determine the target planet; necessary only when TSTAY \neq 0	--
ITARG	{ <ul style="list-style-type: none"> = 1, Target is the planet Mercury = 2, Target is the planet Venus = 3, Target is the planet Earth = 4, Target is the planet Mars = 5, Target is the planet Jupiter 	

Note: The subscript "2" refers to heliocentric coordinates

Table 3.3.1.2-9 (Continued)

OUTPUT - SECTION C

SYMBOL	DESCRIPTION	UNITS
TIME	Instantaneous time from launch	DAYS
HMIN	Minimum DSMCS orbit altitude necessary to avoid occultation computed at the most unfavorable position of the orbit	km .
PSI	Total look angle; measured from the DSMCS/spacecraft radial vector to the DSMCS orbit plane	DEG
HMIN(N)	Minimum DSMCS orbit altitude necessary to avoid occultation computed at the DSMCS's real time position	km .
PSI (N)	Total look angle computed at the DSMCS's real time position	DEG
THETS(N)	True anomaly of the DSMCS when HMIN(N) and THET(N) are computed	DEG
OMEGA	Longitude of the ascending node of the DSMCS orbit plane; measured from the vernal equinox	DEG
XE	Component of the earth distance in the ecliptic plane; positive in the direction of the vernal equinox	km .
YE	Component of the earth distance in the ecliptic plane; positive direction determined by the right-hand rule; orthogonal to X.	km .
XP	Component of the spacecraft distance; positive direction as in XE	km .
YP	Component of the spacecraft distance; positive direction as in YE	km .
ZP	Component of the spacecraft distance; normal to the XP, YP plane	km .

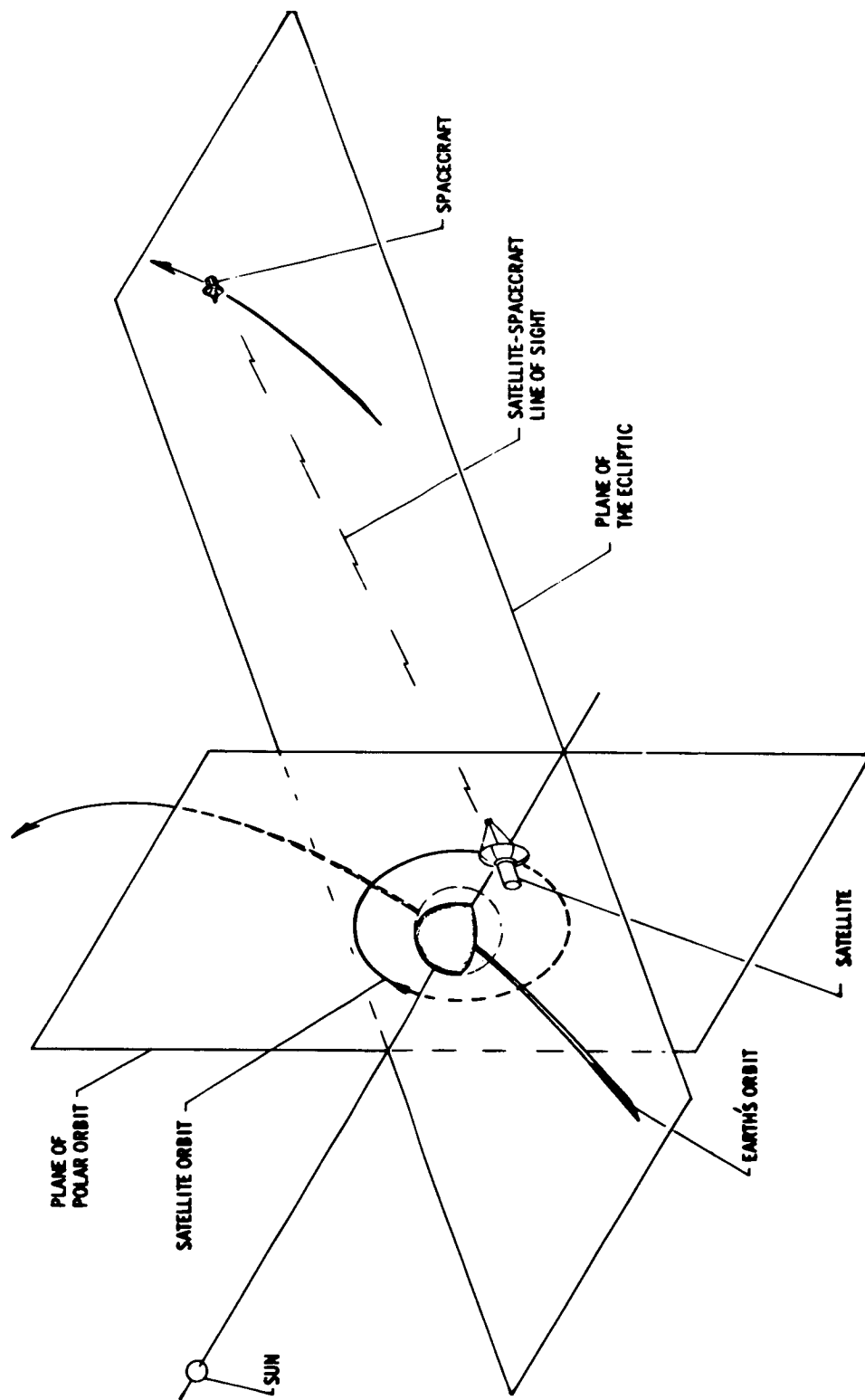


Figure 3.3.1.2-1. Satellite-Spacecraft Line-of-Sight Geometry

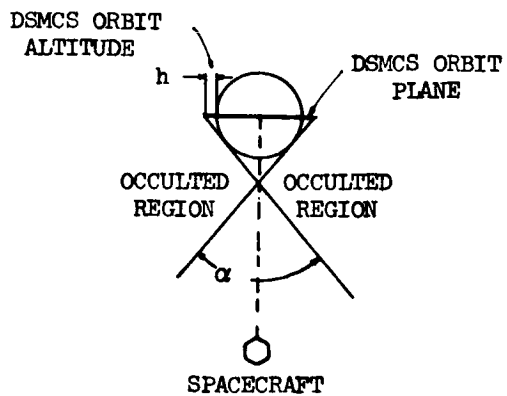


Figure 3.3.1.2-2.
Spacecraft Occultation Zones

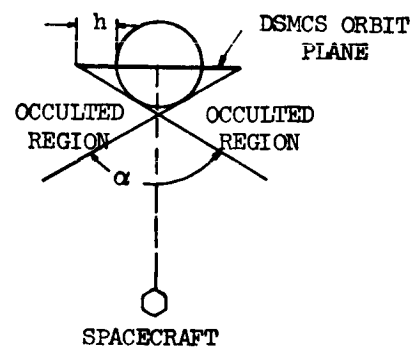


Figure 3.3.1.2-3.
Spacecraft Occultation Zones

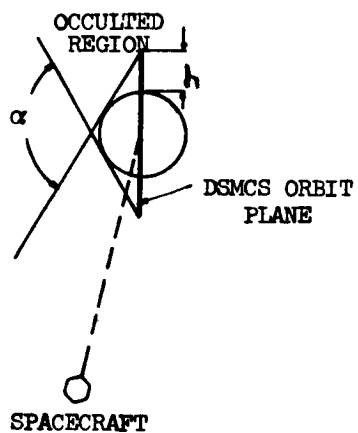


Figure 3.3.1.2-4.
Spacecraft Occultation Zones

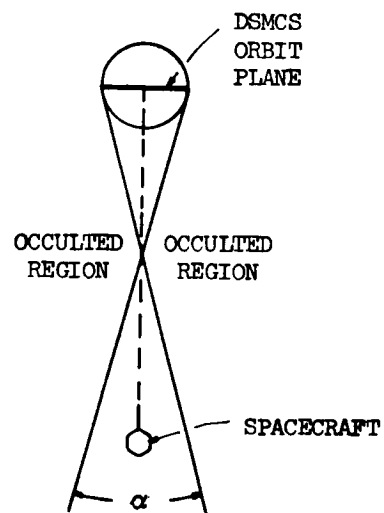


Figure 3.3.1.2-5.
Spacecraft Occultation Zones

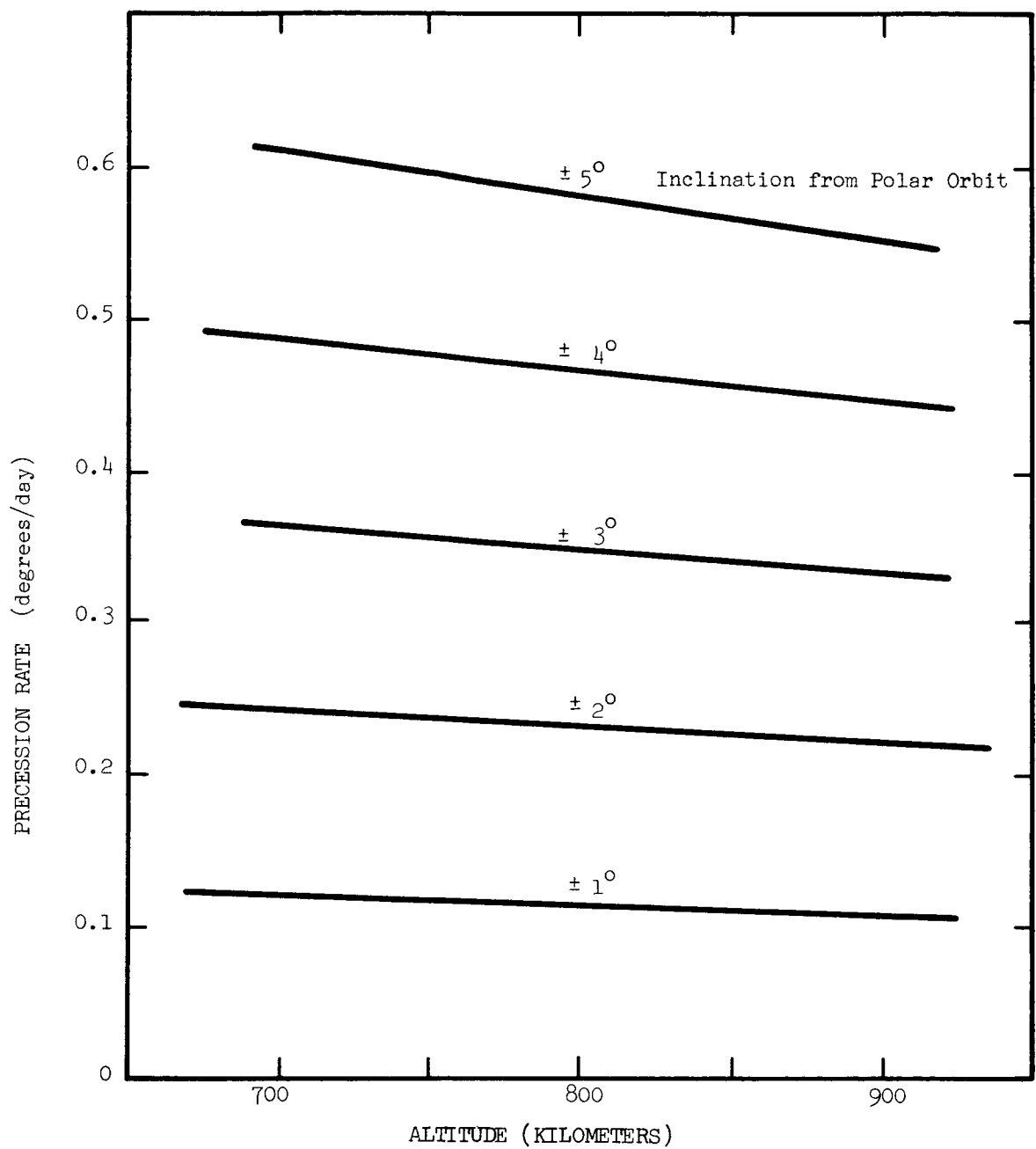


Figure 3.3.1.2-6. Mercury Mission - Precession Rate vs Altitude

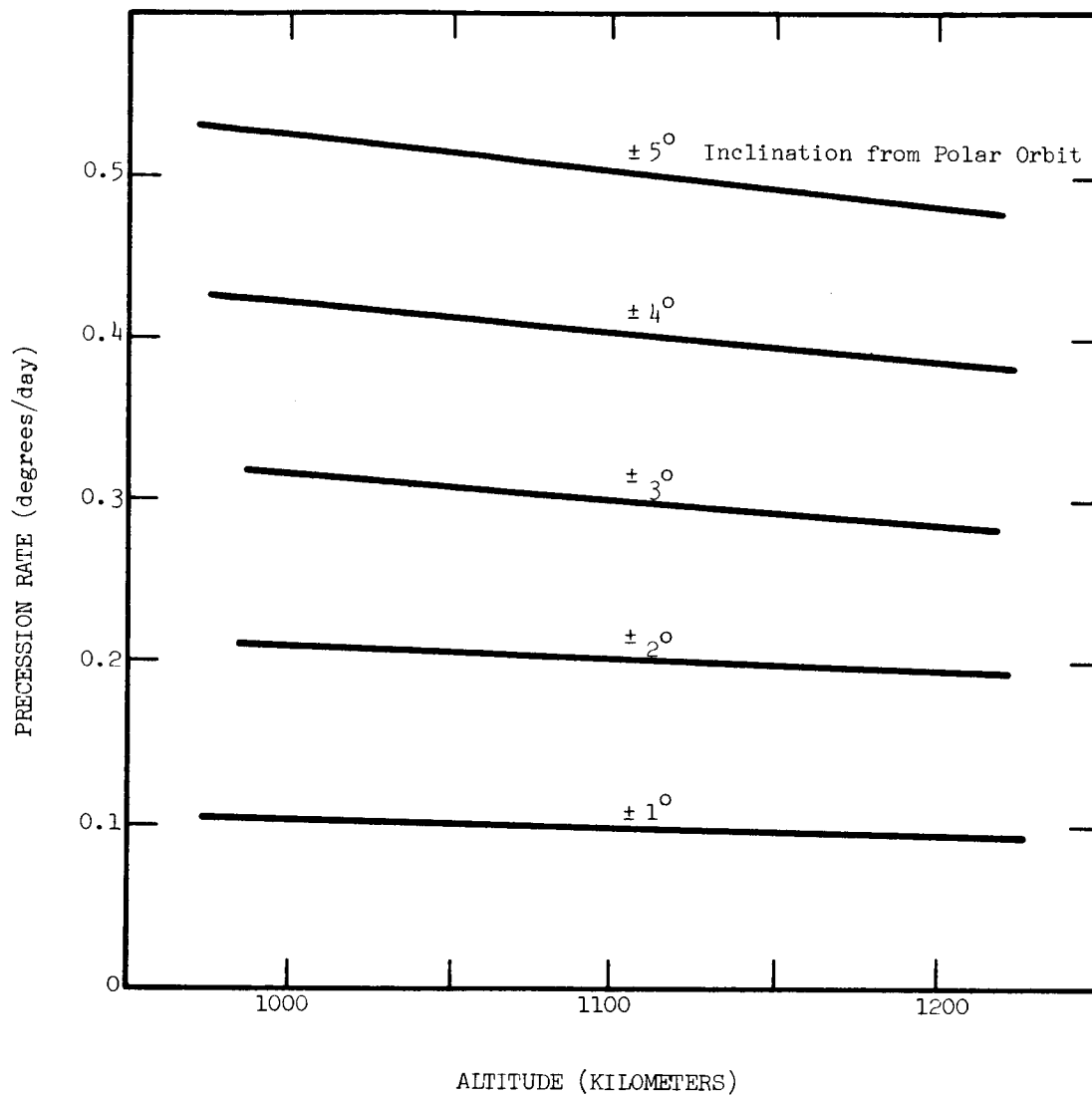


Figure 3.3.1.2-7. Mars Mission - Precession Rate vs Altitude

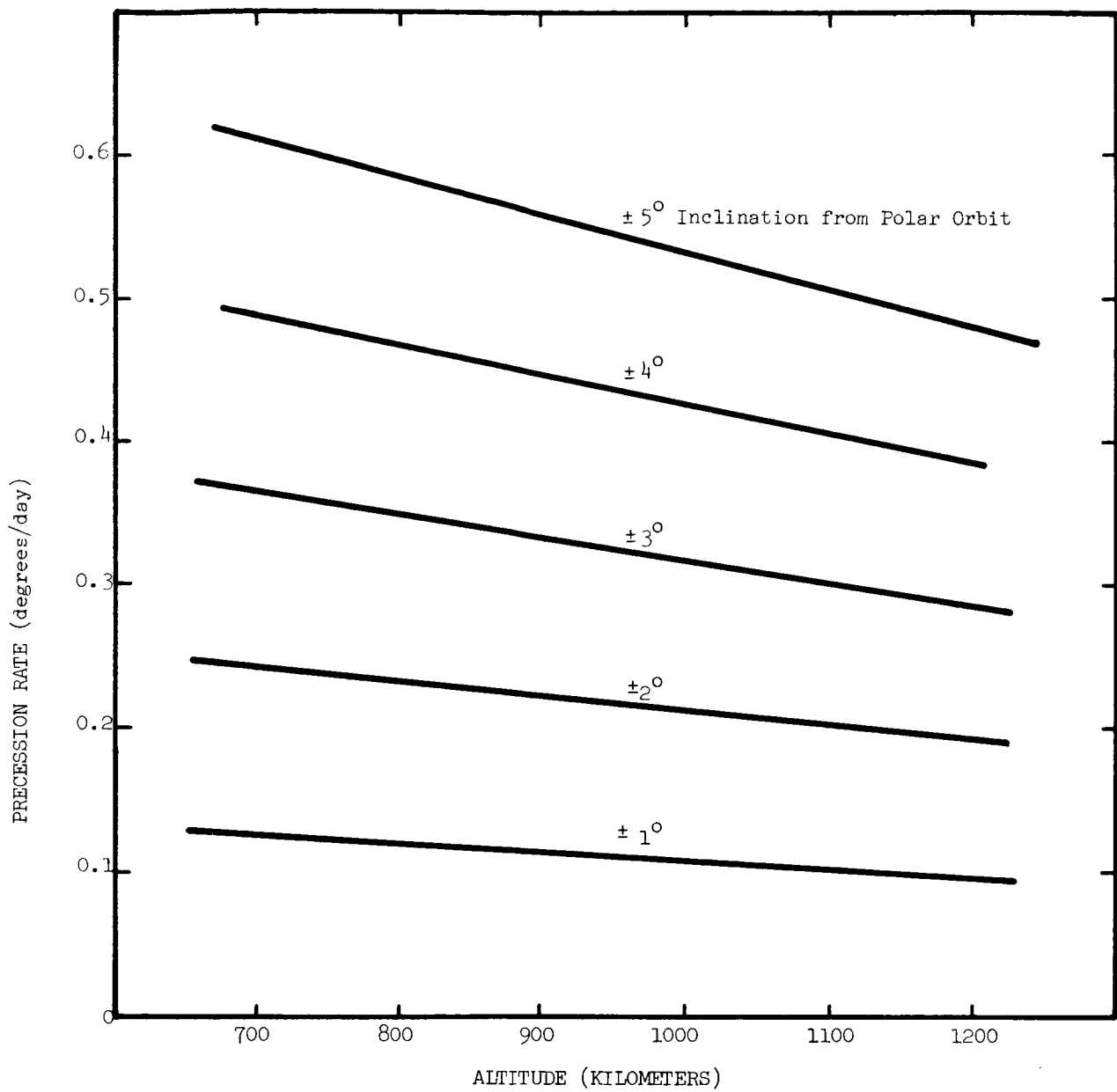
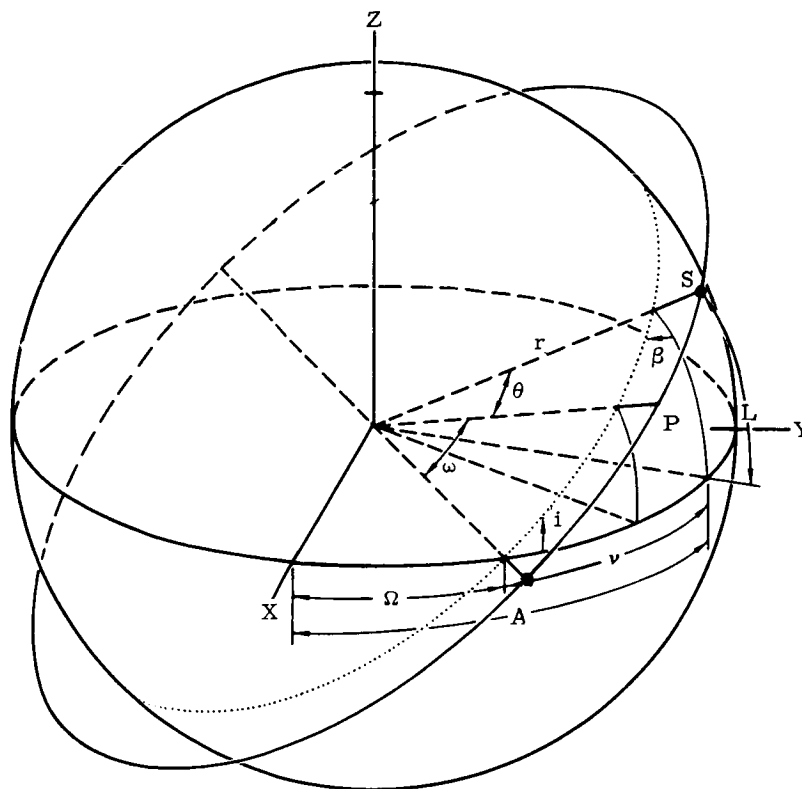


Figure 3.3.1.2-8. Jupiter Mission - Precession Rate vs Altitude



Where:

S - Satellite

$\left. \begin{matrix} X \\ Y \\ Z \end{matrix} \right\}$ Equatorial cartesian coordinates

r - Radial distance to satellite

A - Right ascension

Ω - Right ascension of the ascending node

ω - Argument of perigee

θ - True anomaly

P - Perigee

Y - Central angle measured from the ascending node

L - Instantaneous latitude geocentric

Figure 3.3.1.2-9. DSMCS Orbit Orientation

3.3.1.3 SELECTED ORBITS

Each of the orbits selected for the various missions are representative from the standpoint of orbit altitude. The required representative circular DSMCS orbit altitudes ranged from 817 to 1117 kilometers. Since the orbits were reasonably low, and provided sufficient payload, it was decided to eliminate elliptic DSMCS orbits and the related consideration of Apsidal regression.

The DSMCS/spacecraft look angles are plotted versus days in orbit after spacecraft launch for each of the missions. The look angle is defined as the angle that the DSMCS/spacecraft radial vector makes with the ascending node of the DSMCS orbit. The visibility band, described in Section 3.3.1.2 is presented below for a variety of orbit altitudes.

<u>Altitude (km)</u>	<u>Visibility Band (deg)</u>	<u>Total Field Width (deg)</u>
940	71-109	39
1100	68-112	45
1260	66-114	49
1440	64-116	53
1620	60-120	61

Mercury Flyby

The Mercury Flyby mission was the object of a more thorough investigation than any of the other missions. This was due largely to the fact that the Mercury mission served as a check case for the computer program.

To achieve a continuous line-of-sight between the orbiting satellite and the spacecraft requires trajectory shaping of five satellite orbit parameters. These are, in order of importance, longitude of the ascending node, inclination, radius of perigee, radius of apogee, and the

argument of perigee. From an examination of the Mercury spacecraft trajectory, it is obvious that the orbit plane of the satellite must be changed at least once during the 115-day mission to achieve line-of-sight, (i.e., the satellite orbit plane becomes parallel to spacecraft/earth vector in approximately 90 days). This plane change may be accomplished in two ways, either by satellite propulsive thrusting normal to the orbit plane or by allowing the node of the orbit to precess.

From the standpoint of minimum orbit altitude, maximum payload, and mission requirements, the latter method was chosen for this and all the other missions. Since the precession rate of the longitude of the ascending node is a function of both the satellite's orbital radius and orbital inclination, it is possible to determine the minimum orbital radius and resulting inclination which gives continuous line-of-sight. The optimum conditions for line-of-sight are obtained when the satellite orbit plane is no greater than $\pm 90^\circ$ from the spacecraft/earth radius vector, with this arrangement. The corresponding inclination must be such that the satellite does not move behind the earth. An inclination close to 90° with respect to the earth's equatorial plane will satisfy this requirement. In the case of circular satellite orbits, the perigee radius and apogee radius are equal and the argument of perigee is undefined.

In Figure 3.3.1.3-1, the spacecraft trajectory is described in heliocentric coordinates along with the planets Mercury and Earth as a function of days in orbit. The satellites inclination is assumed to be constant throughout the duration of the mission.

The orbits designed on the basis of the above discussion is summarized below.

Mercury Flyby (115 day transit)

Required DSMCS orbit parameter to avoid occultation:

Circular orbit altitude - 842 km

Initial longitude of ascending node (Ω_0) 159 Deg.

Inclination - 90.5 Deg.

Nodal precession rate (Ω) - .057 Deg/Day

Figures 3.3.1.3-2 and 3.3.1.3-3 show the time history of h_{\min} and look angle, respectively.

Manned Mars Mission

The spacecraft trajectory for the manned Mars round trip mission is shown in Figure 3.3.1.3-4. Due to greater DSMCS/target planet distances in this mission compared to the Mercury case, the DSMCS orbit altitude increased to 1116 kilometers. The required orbital parameters to avoid occultation are:

Mars Mission (30 day stay, 450 day total mission duration)

Circular Orbit Altitude	- 1116 km
Initial Longitude of Ascending node (Ω_0)	- 68.25 Deg.
Inclination	- 93.4 Deg.
Nodal Precession Rate	- 0.34 Deg/Day

Figure 3.3.1.3-5 presents minimum orbit altitude versus time in orbit.

JUPITER FLYBYS

The Jupiter missions consist of the three separate spacecraft trajectories listed below.

- a) 1973 opportunity - fast transit
- b) 1978 opportunity - fast transit
- c) 1978 opportunity - slow transit

The optimum launch date was provided for the 1973 opportunity whereas only an approximate date for the 1978 opportunity was available. An n-body optimizing interplanetary trajectory computer program was utilized to determine the optimum launch dates for the 1978 Jupiter opportunity. The results of this study are presented in Figure 3.3.1.3-6.

The spacecraft trajectory for the 1973 mission is shown in Figure 3.3.1.3-7. A similar analysis for the two Jupiter missions of 1978 is presented in Figures 3.3.1.3-8 and 3.3.1.3-9. Orbital altitude plots versus mission time are shown in Figures 3.3.1.3-10 through 3.3.1.3-12 for the three missions.

Jupiter Missions of 1973 and 1978

The following table gives a summary of the three Jupiter missions.

	1973 Fast Transit	1978 Fast Transit	1978 Slow Transit
Initial DSMCS Node	8.5 deg	172 deg	18 deg
DSMCS Inclination	91.1 deg	91.3 deg	90.9 deg
Nodal Precession Rate	.12 deg/day	.15 deg/day	.09 deg/day
h_{\min}	933 km	817 km	1117 km

Venus Flyby and Return

Investigation of the Venus flyby indicated that three different DSMCS nodal precession rates are required in order to avoid occultation. The method requiring the smallest velocity increment involves changing the DSMCS orbit inclination two times. As an example, with a DSMCS orbit altitude of 1100 km, initial DSMCS orbit plane of 170° , and a DSMCS inclination of 88.9° , the first inclination change would occur at 100 days after launch. The first 100 days requires a DSMCS nodal precession rate of $-.12$ deg/day. The required plane change is 7.5 degrees to a new inclination of 96.4 degrees; velocity increment for this change is .958 km/sec. This inclination will give a DSMCS-nodal precession rate of .65 deg/day. The second plane change would be made at 260 days after launch to a new DSMCS inclination of 91.5 degrees, yielding a precession rate of .22 deg/day. This second plane change through 4.9 degrees requires .575 km/sec. The total velocity increment required to produce the desired plane changes totals 1.533 km/sec.

Original study ground rules not allowing propulsive plane change maneuvers eliminated the Venus round trip mission from further study. Figure 3.3.1.3-13 presents the outgoing trajectory of the Venus mission.

Lv Earth JD 2445964.0 September 20, 1984
Ar Mercury JD 2446079.0 January 13, 1985
Transfer Time 115 Days

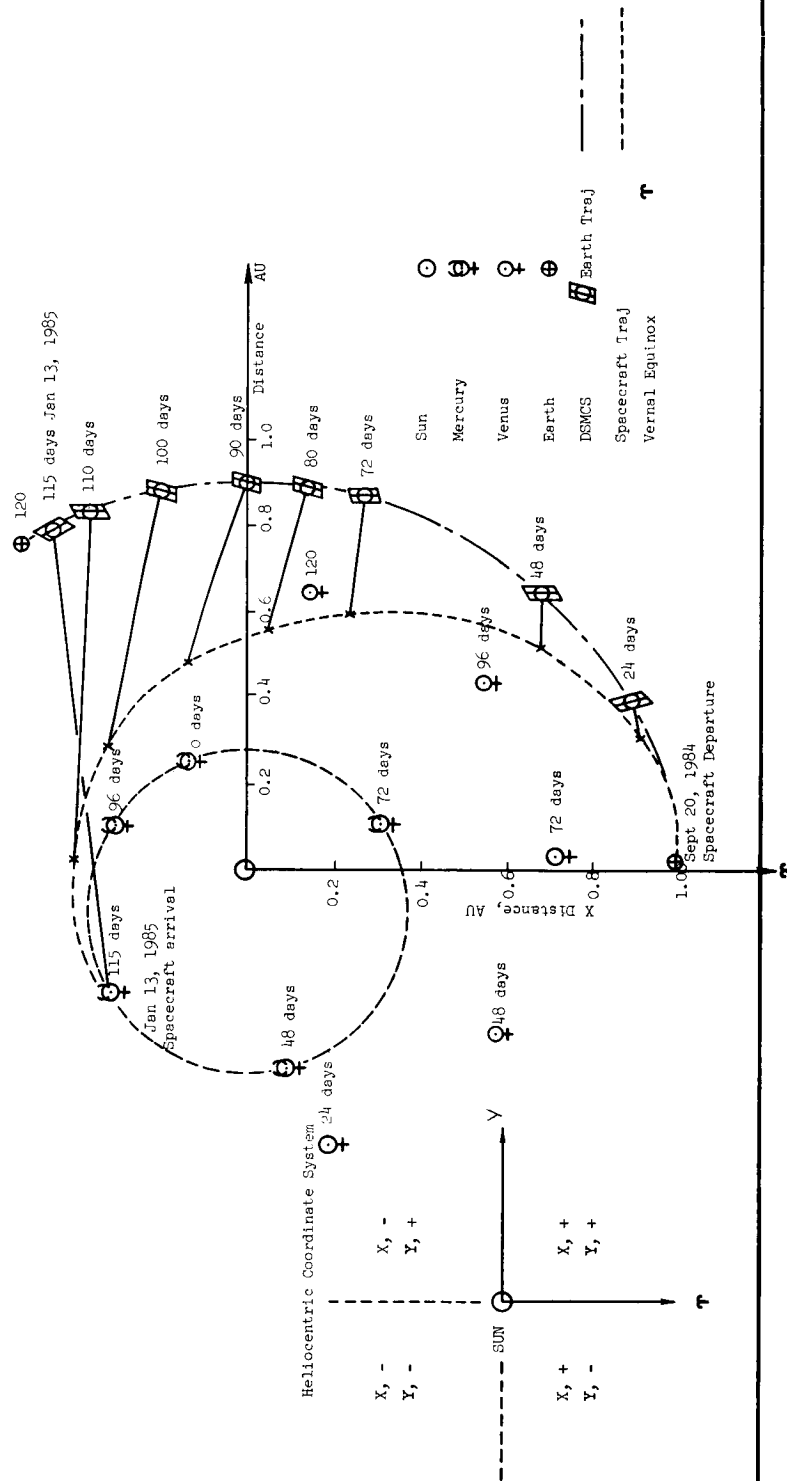


Figure 3.3.1.3-1. Mercury Flyby Trajectory

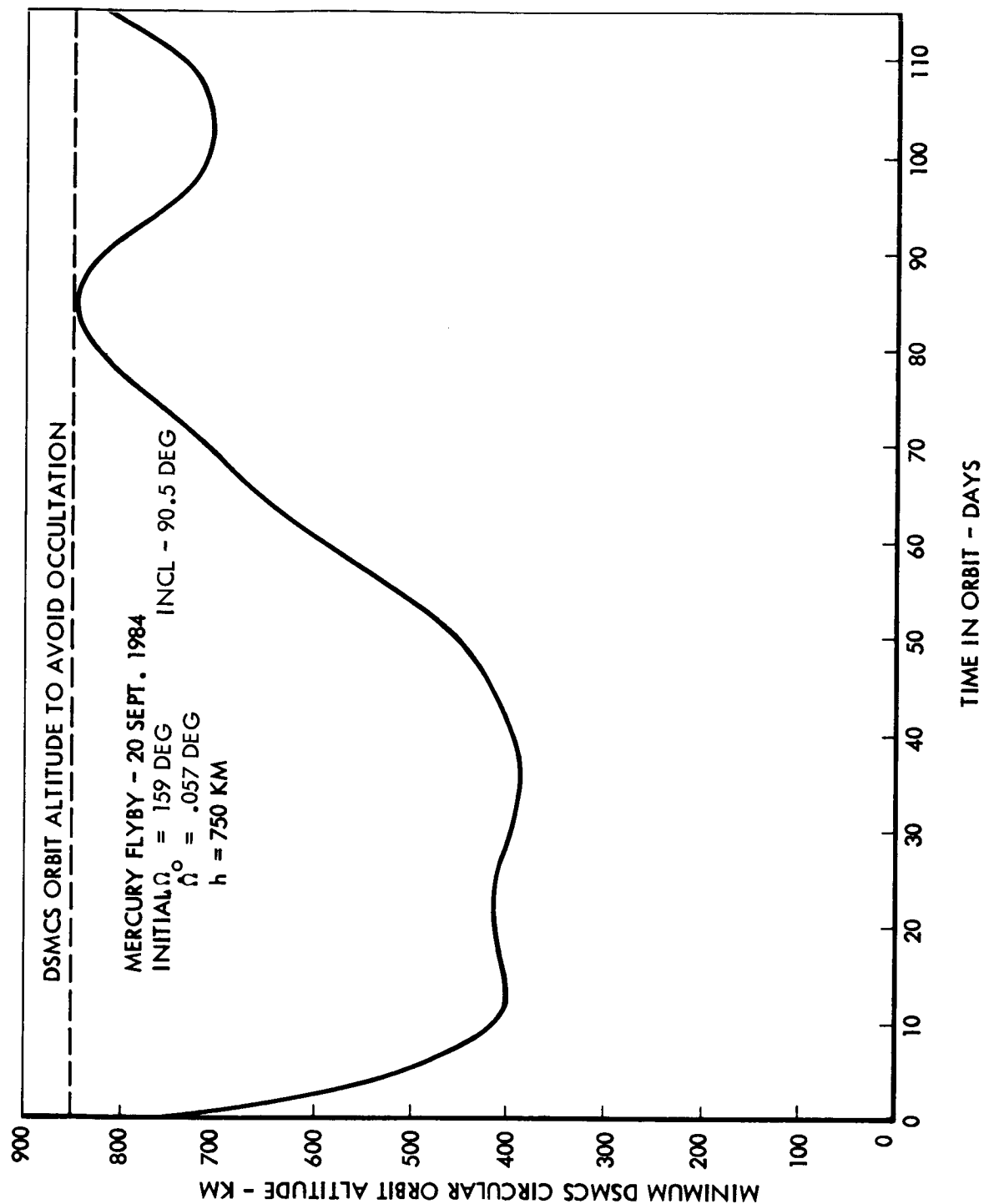


Figure 3.3.1.3-2. Mercury Flyby Orbit Altitude Envelope

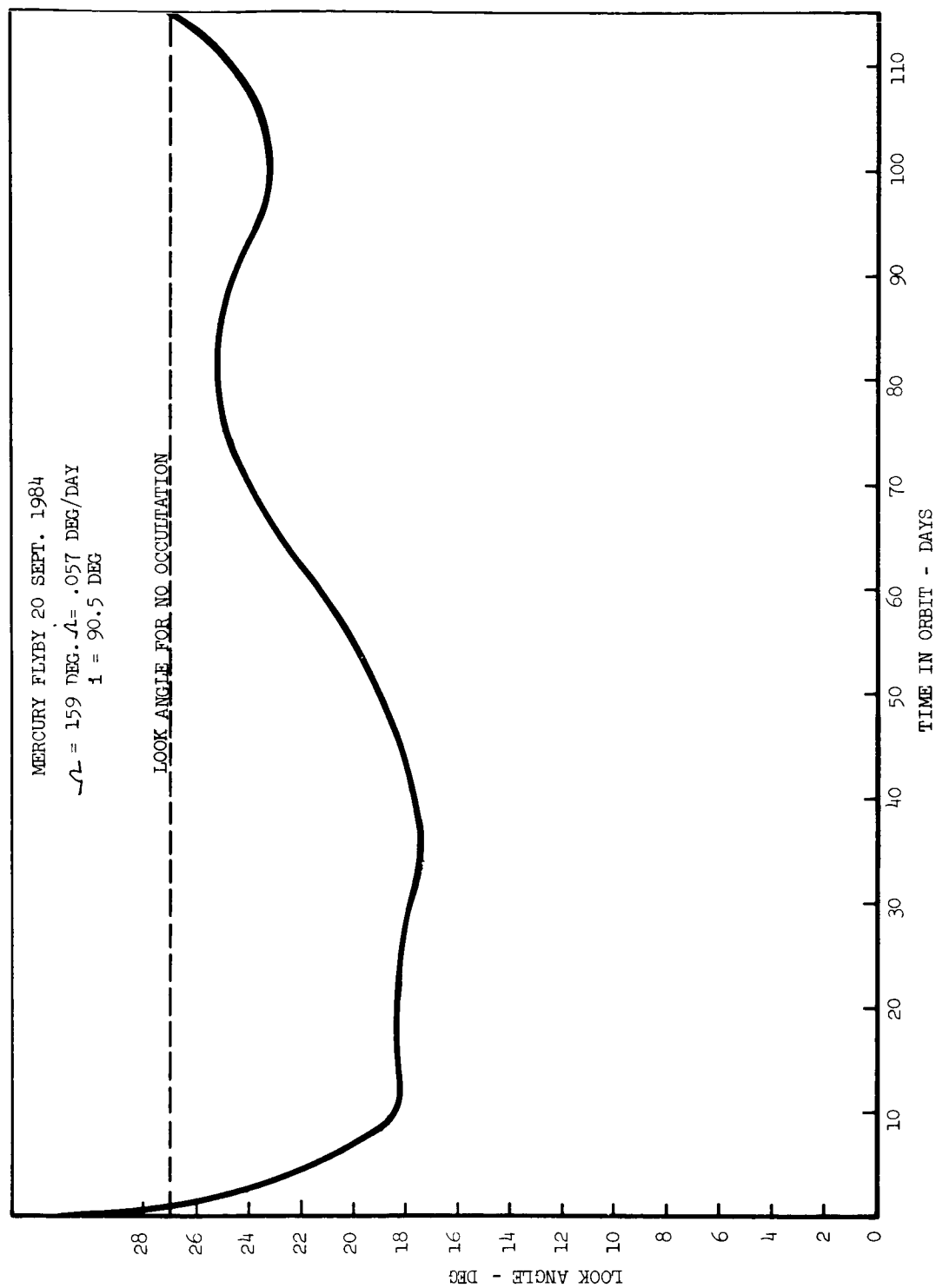
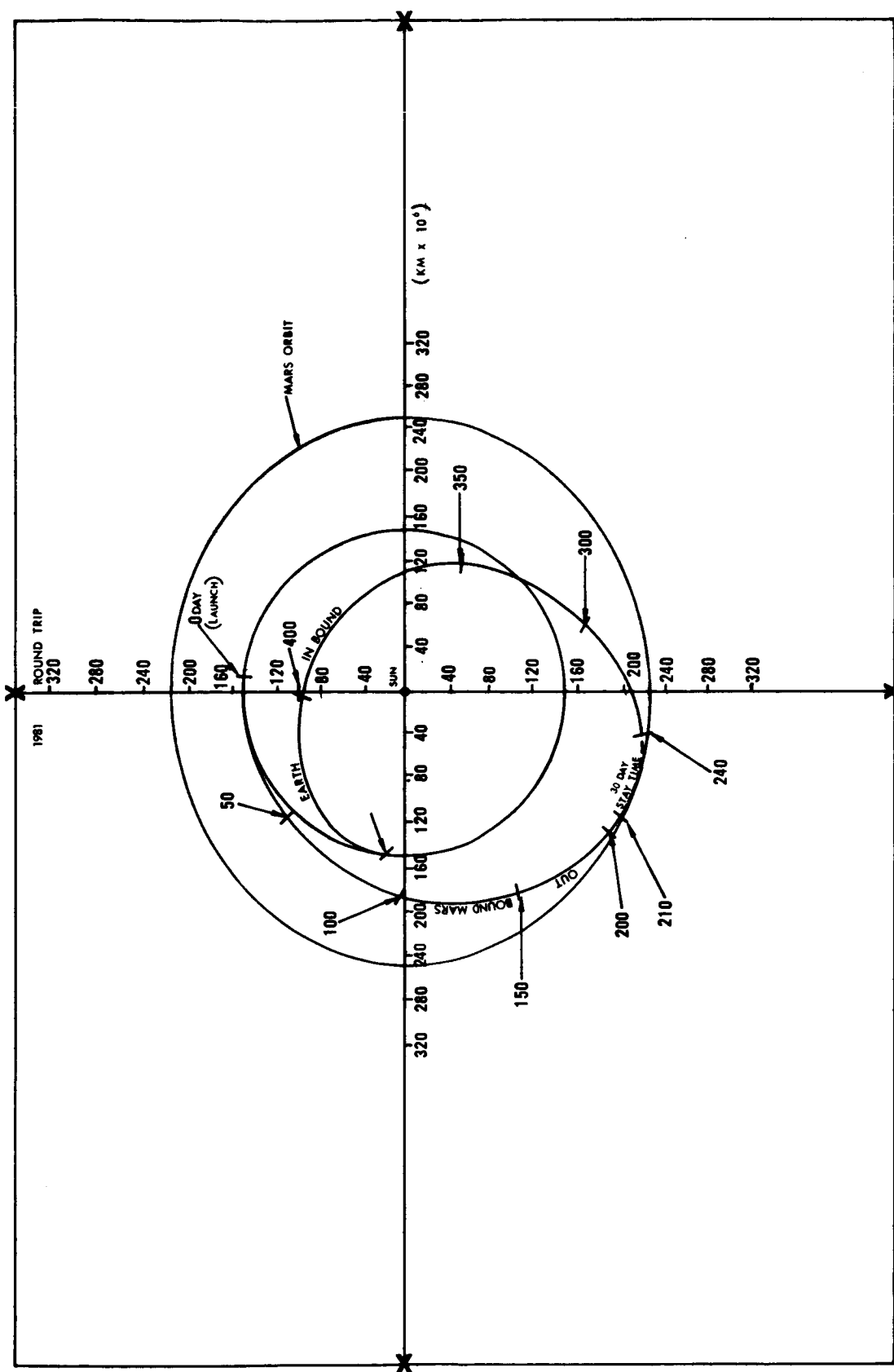


Figure 3.3.1.3-3. Mercury Flyby Orbit Altitude Envelope



*Paper, "A Manned Mars-Moon Mission" LALLY, E. Manned Planetary Mission Technology Conference, Lewis Research Center, May 23, 1963.

Figure 3.3.1.3-4. Mars Lander of 1981 Round Trip

MANNED MARS ROUND TRIP LINE OF SIGHT ENVELOPE

Launch - 16 Dec. 1981
 $\Omega_0 = 68.25^\circ$ Inclination = 93.4°
 $\dot{\Omega} = 0.34$ Deg/Day $h_{\min} = 1116$ km

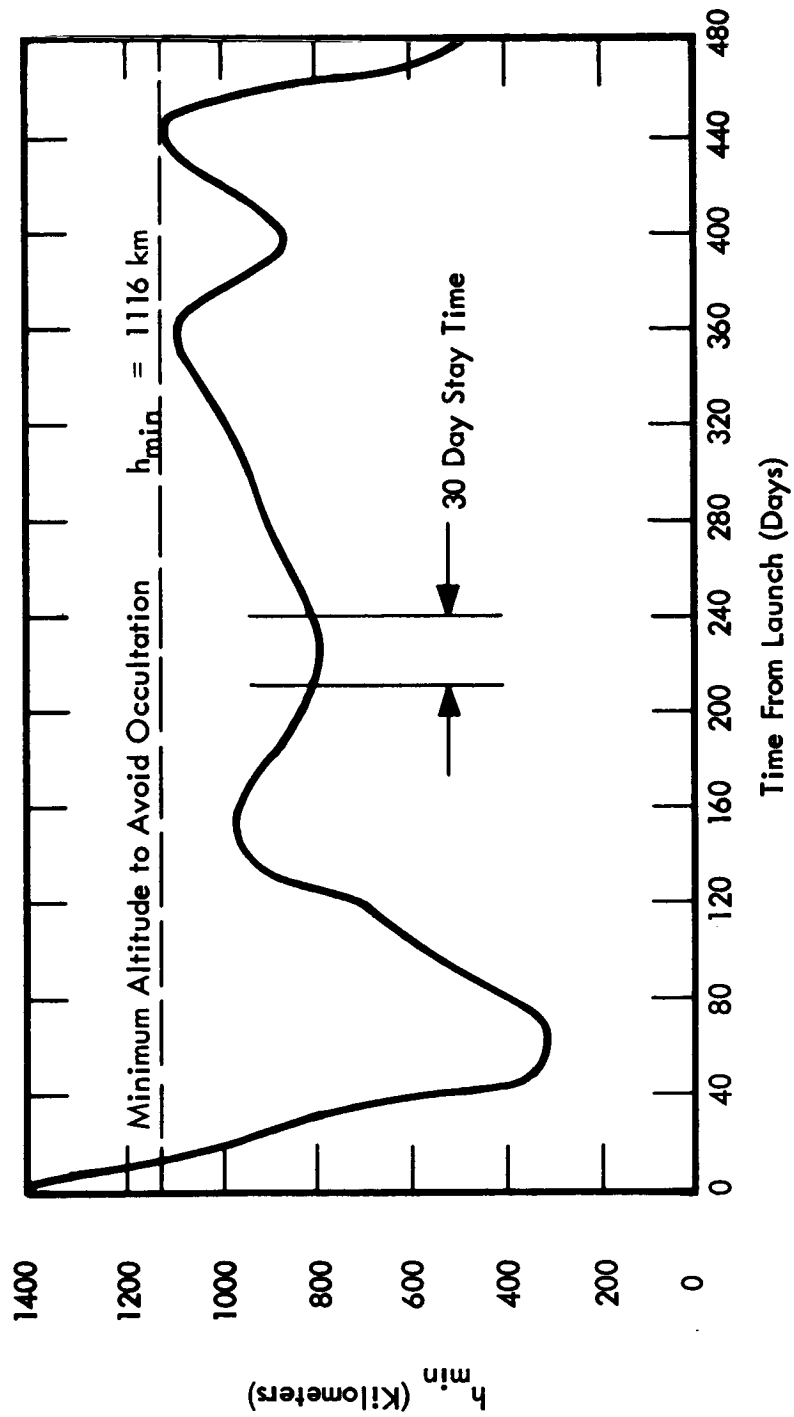


Figure 3.3.1.3-5. Mars Round Trip Line-of-Sight Envelope

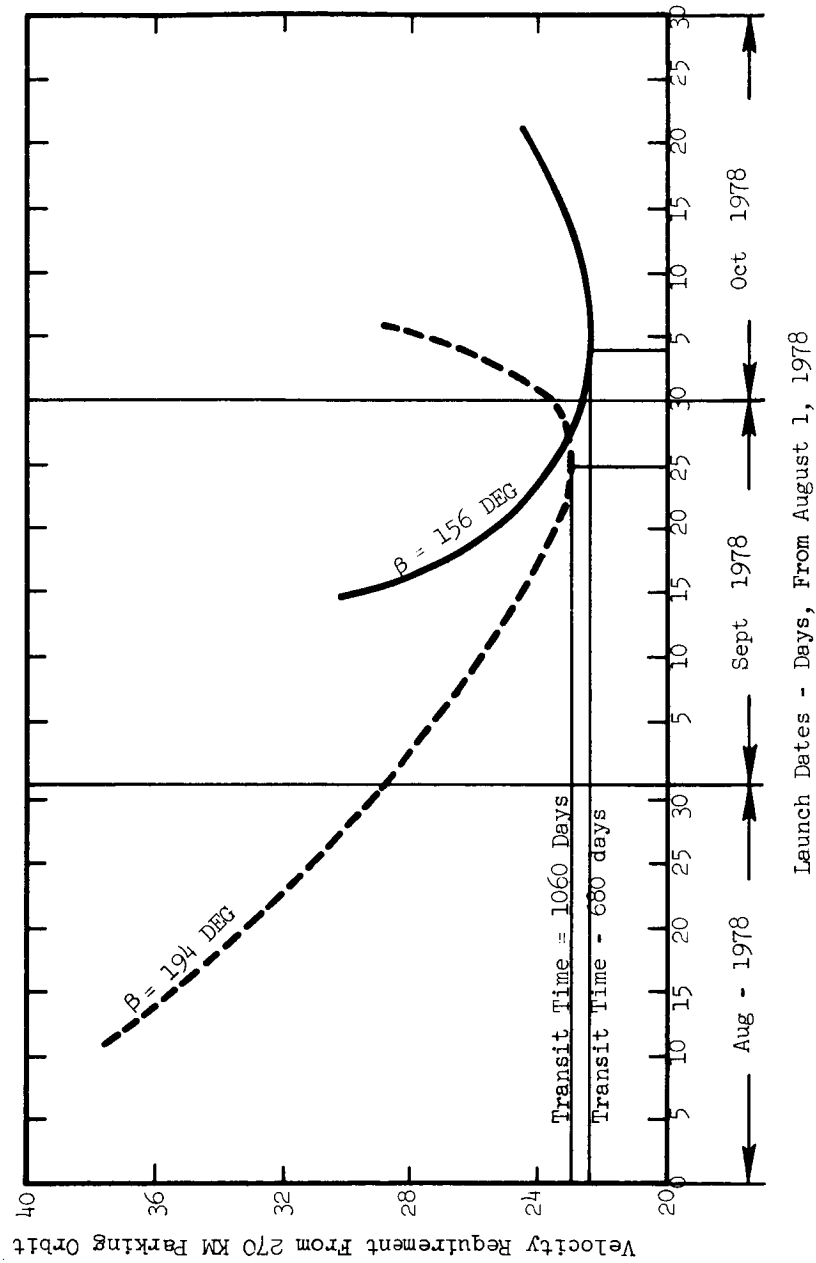


Figure 3.3.1.3-6. Optimum Launch Dates for Jupiter Flyby of 1978

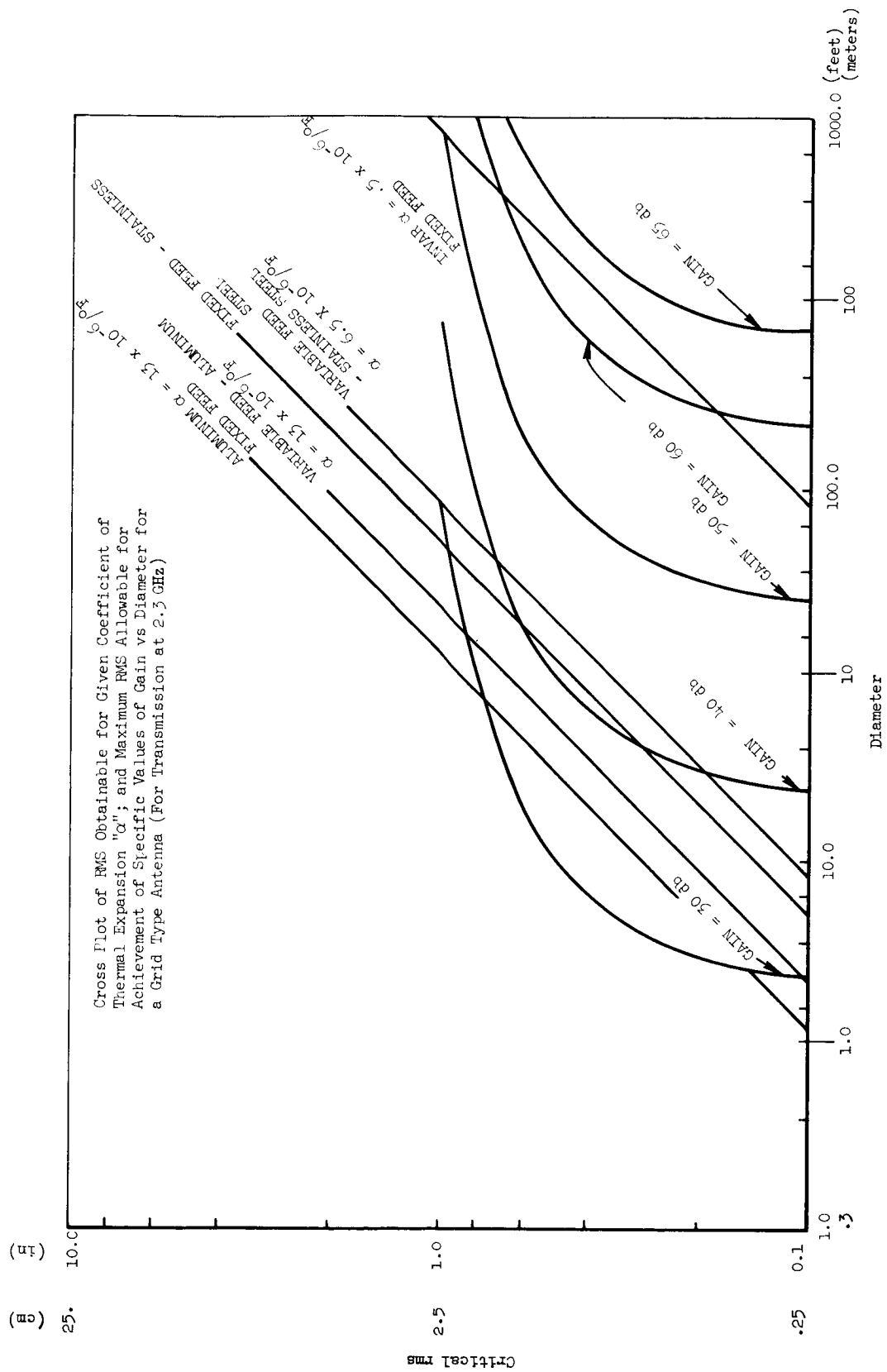


Figure 3.3.1.3-7. Satellite-Spacecraft-Jupiter Relationships
Jupiter Flyby - 1973 - Fast Transit
Trajectory 680 Days

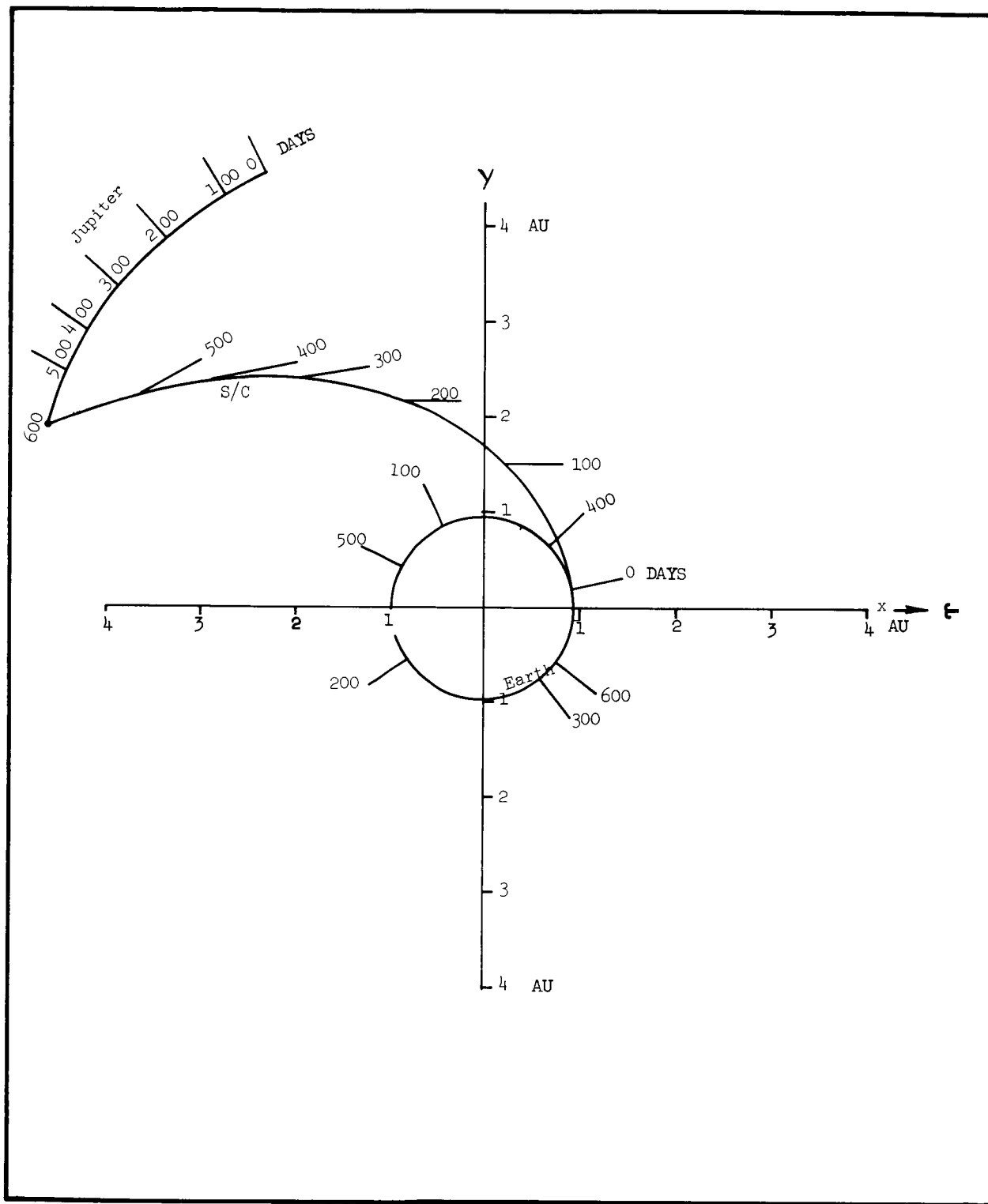


Figure 3.3.1.3-8. Satellite-Spacecraft-Jupiter Relationships
Jupiter Flyby 1978 - Fast Transit
Trajectory 680 Days

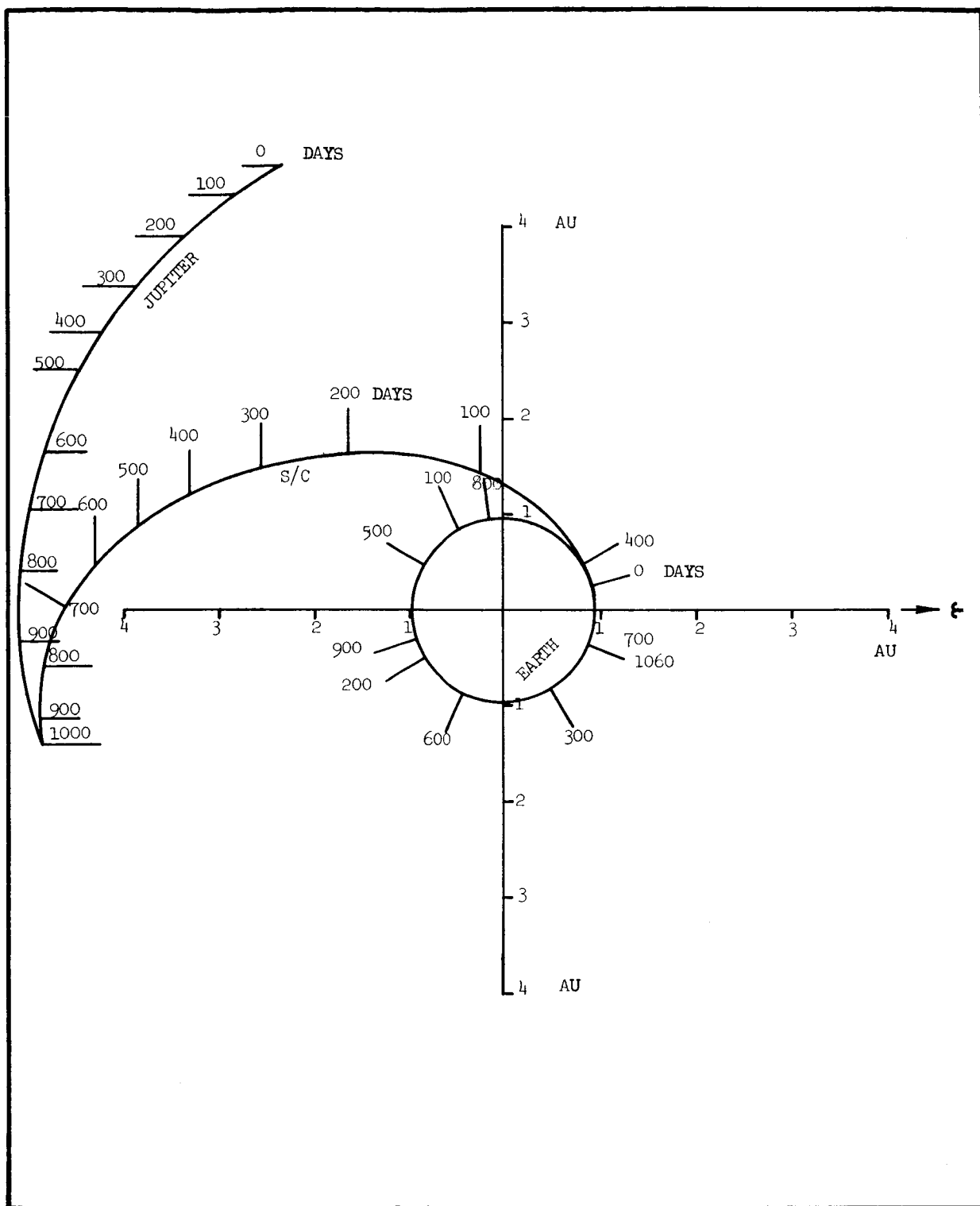


Figure 3.3.1.3-9. Satellite-Spacecraft-Jupiter Relationships
Jupiter Flyby 1978 - Fast Transit
Trajectory 680 Days

JUPITER FLYBY
1973 FAST TRANSIT (680 DAYS)

Launch - 11 April 1973
 $\Omega_o = 8.5^\circ$ Inclination = 91.1°
 $\dot{\Omega} = 0.12 \text{ Deg/Day}$ $h_{\min} = 933 \text{ km}$

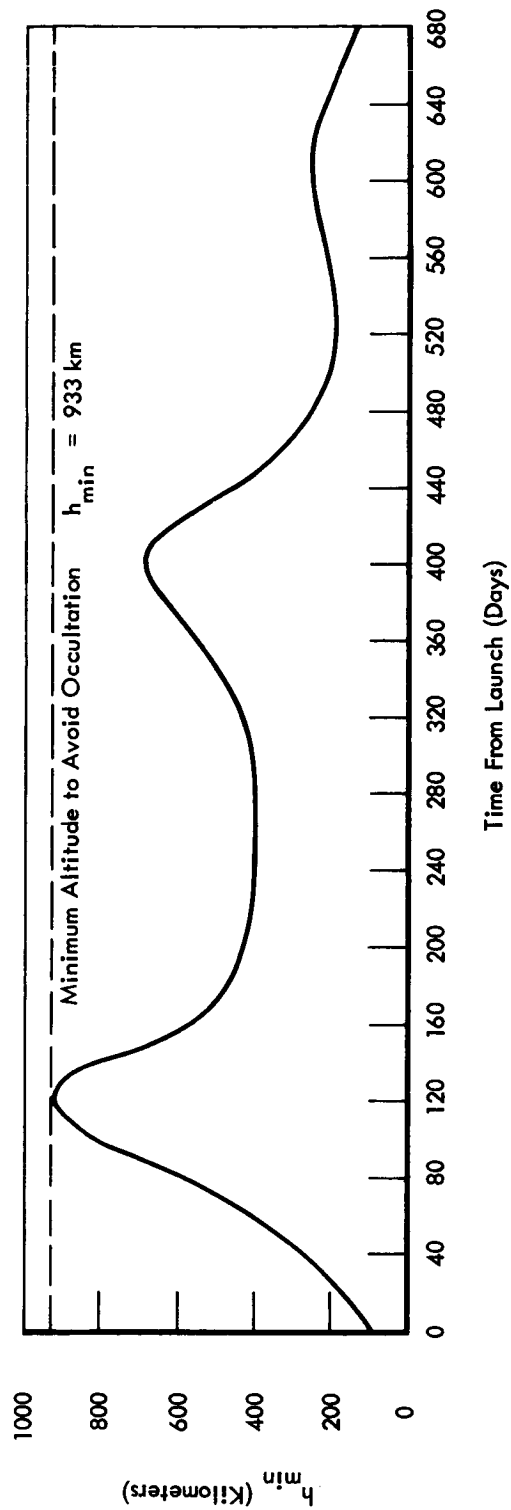


Figure 3.3.1.3-10. Jupiter Flyby Orbit Altitude Envelope

JUPITER FLYBY
1978 FAST TRANSIT (680 DAYS)

Launch - 5 Oct. 1978
 $\Omega_0 = 172^\circ$ Inclination = 91.3°
 $\dot{\Omega} = 0.15 \text{ Deg/Day}$ $h_{\min} = 817 \text{ km}$

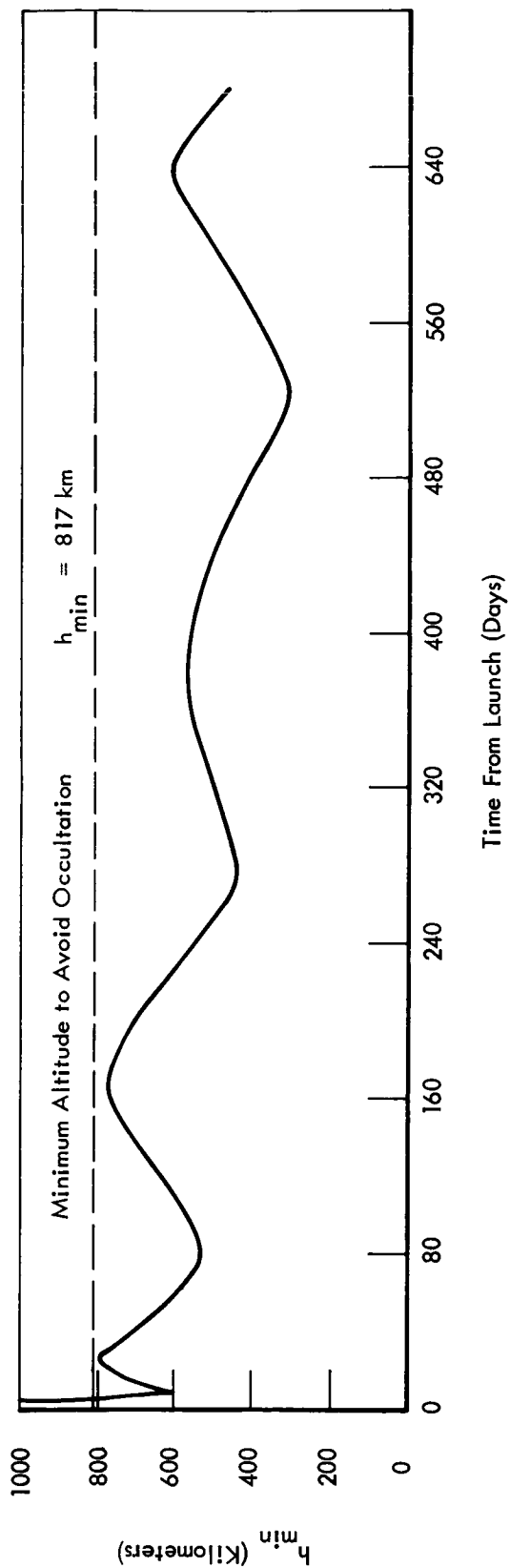


Figure 3.3.1.3-11. Jupiter Flyby Orbit Altitude Envelope

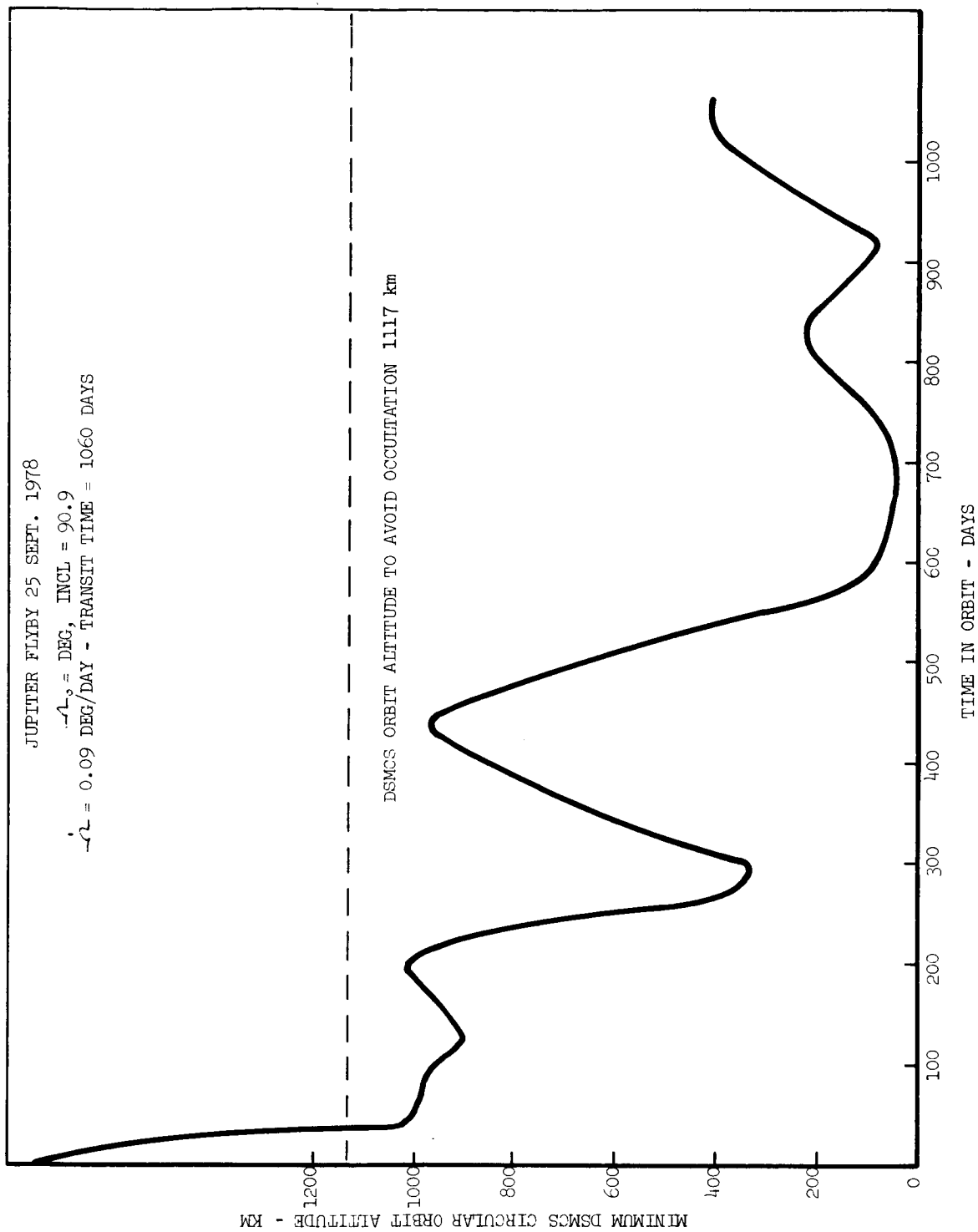


Figure 3.3.1.3-12. Jupiter Flyby Orbit Altitude Envelope

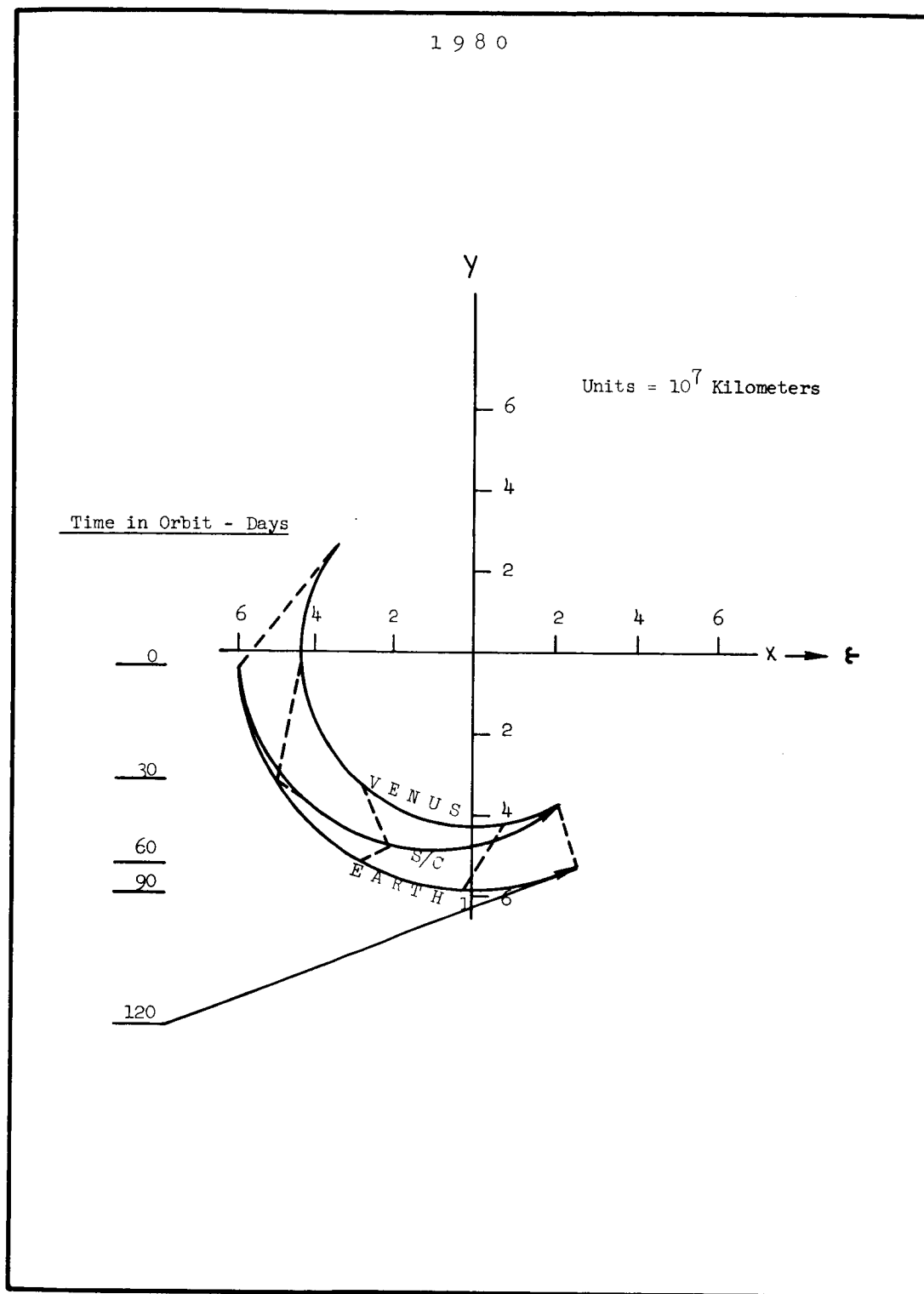


Figure 3.3.1.3-13. Venus Flyby Trajectory (1980)

3.3.2 ENVIRONMENT CONSIDERATIONS

3.3.2.1 RADIATION BELTS

Satellites in polar circular orbits traverse both electron and proton trapped radiation. The orbit-averaged flux rate densities of trapped electrons during the solar minima of 1975 and 1985 are shown in Figure 3.3.2.1-1, of trapped electrons during the solar maximum of 1978 in Figure 3.3.2.1-2 and of trapped protons valid for all years in Figure 3.3.2.1-3.

If the range of charged particles of initial energy E_1 in a shielding medium s can be expressed as

$$R(E_1) = A_s E_1^n \quad (1a)$$

(where the range is expressed in gm/cm^2). Then for a spectrum of particles shielded by a thickness R , implying no penetration by particles of energy less than E , the dose rate behind the shield may be approximated by

$$\dot{D} = \frac{1.6 \cdot 10^{-8}}{n A_s} \frac{10^{n-1}}{E^{n-1}} \Phi \text{ rads/day} \quad (2a)$$

where energy units are Mev, and flux rate density units are particles/ cm^2 -day. (Note: The 10^{n-1} factor is purely empirical to account for change in particle energy in passing through the shield.) Over the energy range of interest, for electrons shielded with aluminum

$$R_e = 0.4 E^{1.3} \quad (1b)$$

implying

$$\dot{D} = \frac{6 \cdot 10^{-8}}{E^{0.3}} \Phi_e \frac{\text{rads}}{\text{day}} \quad (2b)$$

where E is in Mev and Φ_e is in electrons/ cm^2 -day. Over the energy range of interest, for protons shielded with aluminum

$$R_p = 0.0034 E^{1.7}$$

implying

$$\dot{D} = \frac{1.4 \cdot 10^{-5}}{E^{0.7}} \Phi_p \frac{\text{rads}}{\text{day}} \quad (2c)$$

where E is in Mev and Φ_p is in protons/cm²-day. Equation 2b is approximately valid for all materials, though multiplying it by an atom-dependent factor $(\frac{Z}{13}) (\frac{27}{A})$ will improve the accuracy. Equation 2c multiplied by an atom-dependent factor of $(\frac{A}{27})^{1/3}$ will yield a rough approximation for all materials, with the accuracy improving at higher energies. (Z is atomic number. A is atomic weight.) The true ranges of particles in aluminum are shown in Figure 3.3.2.1-4.

If the orbital range of interest is no higher than 2320 kilometers (1250 n.mi.) and no lower than 740 kilometers (400 n.mi.) than for electrons above 1/4 Mev the 1975, 1985 (solar minimum) environment will be limiting. (To shield out all electrons below 1/4 Mev less than .25 mm of aluminum is required.) Using equations 2b and 2c to compare electron and proton dose rates indicates clearly by inspection that the electron environment is the limiting environment throughout the altitude range of interest for all shielding less than 2700 mg/cm² (1 cm of aluminum).

The dose rate for trapped radiation in 1975 and 1985 as a function of shielding and of orbital altitude is shown in Figure 3.3.2.1-5. (A shielding thickness of 1 mm, corresponding to a few tens of kilograms shielding weight, is typical.) The dose rate for protons is also indicated, though it is smaller than that for electrons. A modification of Equation 2b was used to calculate shielding down to 2.6 mg/cm², or 0.01 mm of aluminum. Figure 3.3.2.1-5 is believed to represent a qualitative improvement for the 1975-1985 time period over the data previously reported.

Some conclusions may be readily drawn from the figure. For a given shielding requirement in a 1853 kilometer (1000 n.mi.) orbit, there will be a few additional kilograms required in going up to a 2320 kilometers (1250 n.mi.) orbit, or a 15-25 kilogram weight savings in going down to a 1485 kilometer (800 n.mi.) orbit. This assumes the electron dose is limiting.

For successful satellite operation, the proton dose must be much less than 10^6 rad, and the electron dose must be much less than 10^9 rad. How much less may be determined by trade-offs between equipment performance and shielding requirements.

Proton doses from solar flares will be less than 10^3 rads/year and will be neglected here. Bremsstrahlung is also unimportant. Therefore only the electron and proton trapped radiation doses will be considered.

For 1 mm of aluminum shielding (weighing a few tens of kilograms at most) proton dose rates vary from 10^4 to 10^6 rads/year, while electron dose rates vary from $5 \cdot 10^5$ to $3 \cdot 10^7$ rads/year. Because of weight considerations, shielding of the entire satellite against protons is limited to about 2 to 3 mm of aluminum through individual components may be more thoroughly shielded. For shielding against electrons the economic limit will be somewhat greater.

The tolerable doses of electron radiation will usually be determined by materials for which appreciable local shielding is impractical. A dose of 10^7 rads in the satellite might be tolerable, but 10^6 rads is decidedly preferable. A dose of 10^5 rads would be desirable, while 10^4 rads is probably unnecessary. The rate of change of dose with altitude is negligible near 2320 kilometers (1250 n.mi.) but is quite significant below 1485 kilometers (800 n.mi.) Shielding on account of electron damage is relatively more difficult than for proton damage. The optimum shielding for electrons will probably consist of a 1 to 3 mm skin, while providing up to 1 cm of local shielding were required for seals, lubricants, and other critical components.

The trapped radiation dose rates as a function of shielding thickness are given only for 1975 and 1985, the solar minima. For altitudes between 817 km (450 n.mi.) and 1117 km (600 n.mi.) the electron fluxes above 0.25 Mev will be greater at solar minimum than at solar maximum. Greater solar activity results in higher atmospheric densities, which in turn depress the trapped radiation. Since even .25 mm of aluminum, shields out all electrons below 0.25 Mev, the trapped electron fluxes for the 1975 and 1985 solar minima constitute the upper limit of electron dose rate. Therefore it is unnecessary in this analysis to consider the 1978 dose rates as a function of shielding thickness. Similar reasoning is applicable to proton dose rates. For conditions outside those of current interest, the dose rates of Figure 3.3.2.1-5 multiplied by the ratio of the appropriate fluxes in Figures 3.3.2.1-1 and 3.3.2.1-2 will give a reasonable approximation to the 1978 solar maximum dose rates.

3.3.2.1.1 ALLOWABLE RADIATION DOSES

Allowable radiation dose rates for any given satellite depend upon its most sensitive components. The type of radiation may or may not affect the degradation. Such things as transistors and inorganic insulations are sensitive to proton radiation but are little affected by electron radiation. Organic substances are primarily sensitive to total dose, whether from protons or electrons. Biological substances are roughly ten times as sensitive to protons as to electrons.

Biologically, a 100 rad electron dose (or 10 rad proton dose) will make most animals sick (including man) but will kill almost none.⁽¹⁾⁽²⁾ A 1,000 rad dose will kill man and most other animals. A 10,000 rad dose will kill virtually all animals except some bats. For bacteria the lethal dose can exceed 1000,000 rad.

(1) H. Goldstein, "Fundamental Aspects of Reactor Shielding" Chapter II, Reading, Mass., Addison-Wesley Publishing Co. 1959.

(2) V.A. Rezontov and M.A. Lagun, "Role of State of Thyroid in Asthenic Syndrome after Radiation Sickness," July 1963, Soviet Physics.

Of those materials sensitive primarily to proton radiation, transistors will usually be most critical. A tabulation of allowable damage threshold (for typically 20 percent degradation in performance) doses is given below:

Table I
Proton Doses in Solid-State Devices (3)(4)

	<u>Allowable</u>	<u>Damage Threshold</u>
Si transistors	$10^2 - 10^3$ rad	$10^4 - 10^5$ rad
Ge transistors	10^4	$10^5 - 10^6$
Tunnel diodes	-	$10^3 - 10^6$

Proton damage-thresholds for other devices are suggested in Table II below:

Table II
Proton Damage-Threshold in Various Materials

Solid-state electronic devices	$10^3 - 10^6$ rad
Inorganic electrical insulations	$4 \cdot 10^6$ rad and up
Metals	10^7 rad and up
Inorganic thermal insulations	10^8 rad and up

For those materials sensitive to all forms of radiation, damage thresholds are given in Table III below:

-
- (3) L.D. Jaffe and J.B. Rittenhouse, Behavior of Materials in Space Environment, JPL, TR-32-150, Nov. 1, 1961
- (4) J. W. Gordon, "Radiation Effects Considerations in Materials in Cryogenic Systems of Nuclear Rockets, IRE Transactions on Nuclear Science, NS-9 January 1962.

Table III

Radiation Damage-Thresholds in Various Materials

Seals - fluorocarbon	$10^4 - 10^5$ rad
- most others	$10^6 - 10^8$
Thermal insulations - organic*	$10^5 - 10^{10}$
Electrical insulations - organic*	10^5 and up
- organic-inorganic*	$10^7 - 10^9$
Lubricants	10^6 and up
Adhesives	$10^7 - 10^9$

*Inorganic alternatives exist (see Table II).

3.3.2.2 SOLAR PLASMA

The steady solar plasma has no direct effect on low altitude satellites. The solar plasma does not reach into the earth's magnetosphere (1.6×10^5 kilometers diameter), but instead transmits its energy through hydro-magnetic waves to the ionosphere.

However, the indirect effects of the solar plasma largely govern altitude optimization. The variations in solar energy - whether during individual solar disturbances or through the solar cycle - are transmitted to earth by the solar plasma. During solar maximum the atmospheric (exospheric) density is 2 orders of magnitude greater than at solar minimum, over the altitude range of interest. The greater atmospheric density leads to a pronounced decrease in trapped electrons (except for low energies) in the inner radiation zone, and to a decrease in meteoroidal material orbiting the earth. The trapped electron flux in the outer radiation zone is enhanced during solar maximum, though the effect is outweighed by the decrease in the inner zone.

The significance of these indirect effects of the steady solar plasma are discussed in the appropriate sections.

The unsteady solar plasma from solar flares is another problem. In a very bad year high energy proton doses from solar flares might possibly equal those from the trapped radiation, but there is less than 1 chance in 100. Transient effects from solar flare radiation is not likely to be a problem.

The environments used in this report are based on References 1 and 2.

3.3.2.3 MICROMETEOROID FLUX

The earth-orbiting meteoroids are an important part of the total meteoroid population only for masses smaller than 10^{-5} gram. A 10^{-5} gram meteoroid will penetrate 2 mm of aluminum if the impact is normal, or on the average 1 mm if the impacts are randomly oriented. On the average, every 30 square feet of satellite surface area will be struck once per year by a 10^{-5} gram particle. Decreasing the aluminum thickness to 0.1 mm will increase the penetration rate 1,000 to 100,000 times.

If the satellite is shielded by less than 1 mm of aluminum there will be a small increase in penetrating flux as altitude increases. This increase will be a factor from 1 to 10 over a 500 km (270 n.mi.) increase in altitude. If the satellite is shielded by more than 1 mm of aluminum, earth-orbiting meteoroids may be neglected, and the penetrating meteoroid flux will be essentially independent of altitude. Since 1 mm of aluminum shielding amounts to only a few tens of kilograms, the altitude dependence of meteoroids will seldom matter and can be neglected. Moreover, for the orbits of interest trapped radiation, and not meteoroids, will be the hazard that determines the maximum altitude and the shielding requirements.

There is a small average drag due to micrometeoroid impacts. The average pressure is maximum near 1853 kilometers (1000 n.mi.) altitude with a magnitude of roughly 10^{-7} dyne/cm² ($1.5 \cdot 10^{-12}$ psi). The altitude variation is small. This micrometeoroid pressure is less than for the atmosphere until

-
- (1) W. Jenisch, Jr., and J. B. Parkinson, "Space Environment Criteria;" Aerojet-General Report 3147, dated January 1966. NAS 8-11285.
 - (2) James I. Vette, AE-2, AE-1968, and AP 1-4, Trapped Radiation Environments; Aerospace 1965-1966 (unpublished).

altitudes of 1480 to 2400 kilometers (800 to 1300 n.mi.), depending on the solar cycle and orbit orientation are reached, and it is negligible for satellite optimization work.

3.3.2.4 ATMOSPHERIC DRAG

Orbital decay rates for DSMCS orbits have been calculated from the equation:

$$\begin{aligned} \frac{\Delta r}{r-R_E} &= \frac{2\pi\rho r}{(w/C_D A)} \frac{r}{r-R_E} \text{ per orbit} \\ &= \frac{39,115\rho}{(w/C_D A)} \frac{r^{1/2} R_E^{3/2}}{r-R_E} \text{ per year} \end{aligned} \quad (1)$$

where consistent units are implied.

Atmospheric densities vary as a function of the solar cycle and of the local earth time. The Harris-Priester models (NASA TND-1444) have been adopted here, because they are believed accurate within a factor of two. The Harris-Priester "S" as a function of the solar cycle is (range of monthly averages and yearly average).

1975	95-115,100	1979	160-280,225	1983	100-150,110
1976	100-180,135	1980	130-260,180	1984	95-110,100
1977	130-300,210	1981	100-210,145	1985	95-105,100
1978	170-300,250	1982	100-180,125		

The atmospheric densities at various altitudes averaged over circular orbits are given in the enclosed table, Table 3.3.2.4-1. The orbital decay rates calculated using these densities are given in the table and in the enclosed figure, Figure 3.3.2.4-1. Examples will illustrate their use:

Consider a 1360 kilogram satellite with a 30.5 meter diameter antenna perpendicular to the velocity vector in an 800 km polar orbit. Then we may read directly its decay rates for various years between 1974 and 1985.

1975	1.2% per year
1978	88% per year
1981	7.5% per year
1985	1.2% per year

For years in between interpolation is required. (1975-1985 represents exactly one solar cycle.) Note that where the decay rate is greater than 5-10%, new values should be taken from the graphs; e.g., the 800 km orbit in 1978 would actually last for only one or two months (one month if the orbit is in the noon-midnight plane, and two months if in the dawn-twilight plane).

If instead the antenna is only 3.0 meters in diameter, the figures above must be multiplied by $\left(\frac{3.05 \text{ m}}{30.5 \text{ m}}\right)^2$ or

1975	0.012% per year
1978	0.88% per year
1981	0.075% per year
1985	0.012% per year

Averaged over 11 years time, the decay rate is roughly the average of the 1975, 1978, and 1981 values, or 0.3% per year.

If there were no (or a negligibly small) antenna, a 1360 kilogram satellite might be a sphere 1.22 meters in diameter. For this case, let $C_D = 2.4$. Then in 1978, the decay rate would be

$$\begin{aligned} \frac{\Delta r}{r-R_E} &= Y \left(\frac{1360 \text{ kg}}{W} \right) \left(\frac{d}{30.5 \text{ meters}} \right) \left(\frac{C_D}{3.0} \right) \text{ per year} \\ &= 0.88 \left(\frac{1.22 \text{ m}}{30.5 \text{ m}} \right)^2 \left(\frac{2.4}{3.0} \right) \text{ per year} \\ &= 0.0011 \text{ per year} \approx 0.1\% \text{ per year} \end{aligned}$$

which for all practical purposes is a permanent orbit.

Table 3.3.2.4-1

ATMOSPHERIC DENSITIES
(gm/cm²)

	1975	1978**	1981	1985	11-year Average
150 km	2.9·10 ⁻¹² ± 1%*	3.0·10 ⁻¹² ± 1%*	2.9·10 ⁻¹² ± 1%*	2.9·10 ⁻¹² ± 1%*	2.9·10 ⁻¹²
200	2.4·10 ⁻¹³ ± 2%	4.9·10 ⁻¹³ ± 2%	3.4·10 ⁻¹³ ± 2%	2.4·10 ⁻¹³ ± 2%	3.4·10 ⁻¹³
300	1.1·10 ⁻¹⁴ ± 10%	6.3·10 ⁻¹⁴ ± 4%	2.5·10 ⁻¹⁴ ± 10%	1.1·10 ⁻¹⁴ ± 10%	3.0·10 ⁻¹⁴
500	1.9·10 ⁻¹⁶ ± 30%	44·10 ⁻¹⁶ ± 10%	8.4·10 ⁻¹⁶ ± 20%	1.9·10 ⁻¹⁶ ± 30%	17·10 ⁻¹⁶
800	3.6·10 ⁻¹⁸ ± 35%	260·10 ⁻¹⁸ ± 20%	22·10 ⁻¹⁸ ± 40%	3.6·10 ⁻¹⁸ ± 35%	80·10 ⁻¹⁸
1100	6.4·10 ⁻¹⁹ ± 15%	285·10 ⁻¹⁹ ± 35%	20·10 ⁻¹⁹ ± 30%	6.4·10 ⁻¹⁹ ± 15%	87·10 ⁻¹⁹
1600	1.1·10 ⁻¹⁹ ± 25%	21·10 ⁻¹⁹ ± 35%	3.5·10 ⁻¹⁹ ± 35%	1.1·10 ⁻¹⁹ ± 25%	7.4·10 ⁻¹⁹
2050	3.1·10 ⁻²⁰ ± 35%	60·10 ⁻²⁰ ± 15%	12·10 ⁻²⁰ ± 25%	3.1·10 ⁻²⁰ ± 35%	22·10 ⁻²⁰

* Maximum seasonal variation for polar orbit (add for orbit in noon midnight plane, subtract for dawn-twilight plane). No seasonal variation for equatorial orbit. Seasonal variations average out over one year for all orbits.

** Values depend strongly upon solar activity; expected average is given. Values will vary temporarily by factors from 1.0 to 10.

Table 3.3.2.4-1 (Continued)

ORBITAL DECAY RATES

$$\frac{\Delta r}{r-R_e} = \frac{\Delta h}{h} \text{ per year}$$

w = 1360 kg d = 30.5 m C_D = 3.0

150 km	50,000 ± 1%*	52,000 ± 1%*	50,000 ± 1%*	50,000 ± 1%*	50,500
200	3,100 ± 2%	6,400 ± 1%	4,400 ± 2%	3,100 ± 2%	4,500
300	100 ± 10%	550 ± 4%	220 ± 10%	100 ± 10%	200
500	1.0 ± 30%	24 ± 10%	4.6 ± 20%	1.0 ± 30%	8.6
800	0.012 ± 35%	0.88 ± 20%	0.075 ± 40%	0.012 ± 35%	0.27
1100	0.0015 ± 15%	0.072 ± 35%	0.0050 ± 30%	0.0015 ± 15%	0.022
1600	0.0002 ± 25%	0.0038 ± 35%	0.0066 ± 15%	0.0002 ± 25%	0.0015
2050	0.00005 ± 35%	0.0009 ± 15%	0.0002 ± 25%	0.00005 ± 35%	0.0003

* Interpretation as in first half of this table

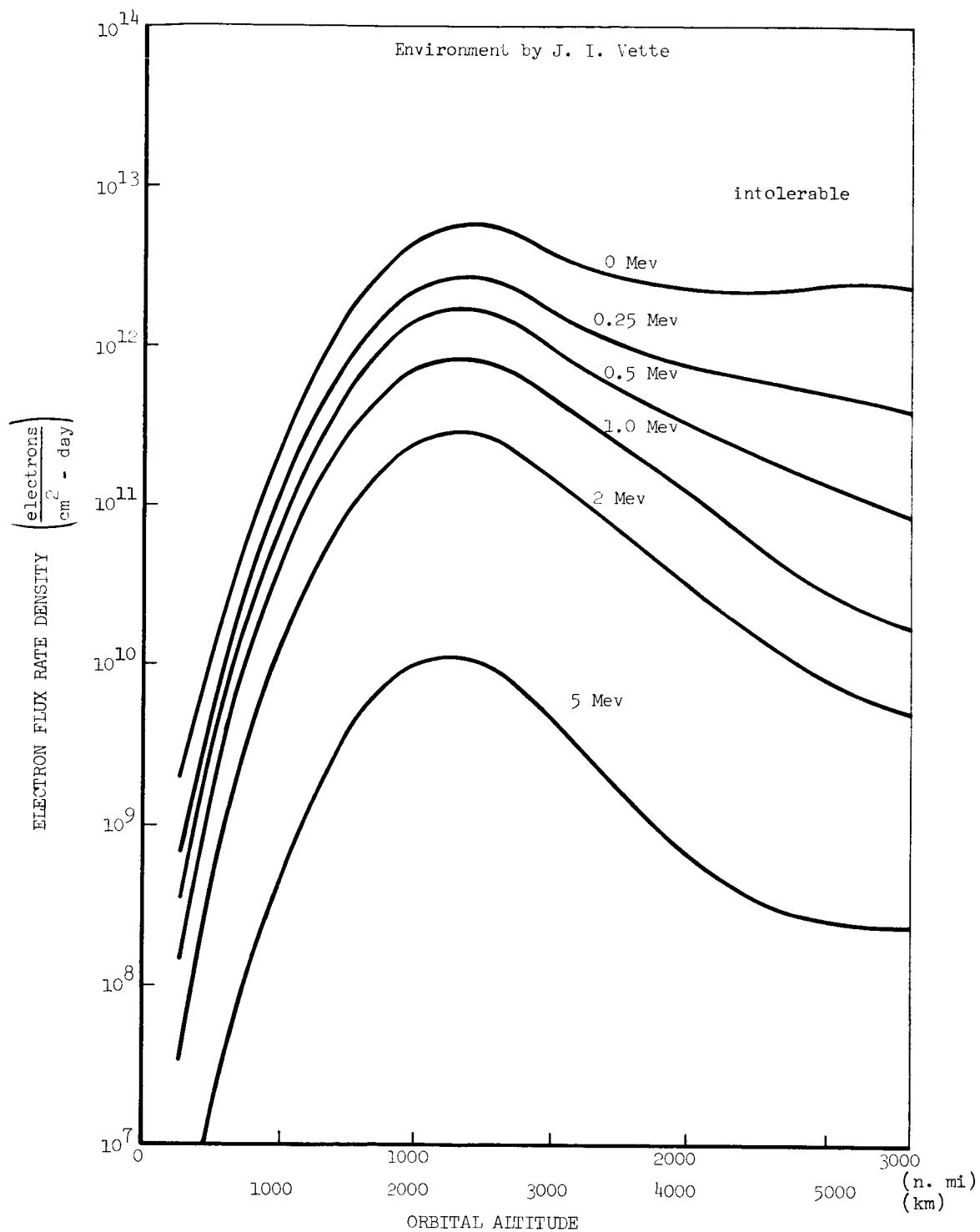


Figure 3.3.2.1-1. Trapped Electron Radiation - 1975, 1985, Polar Orbit

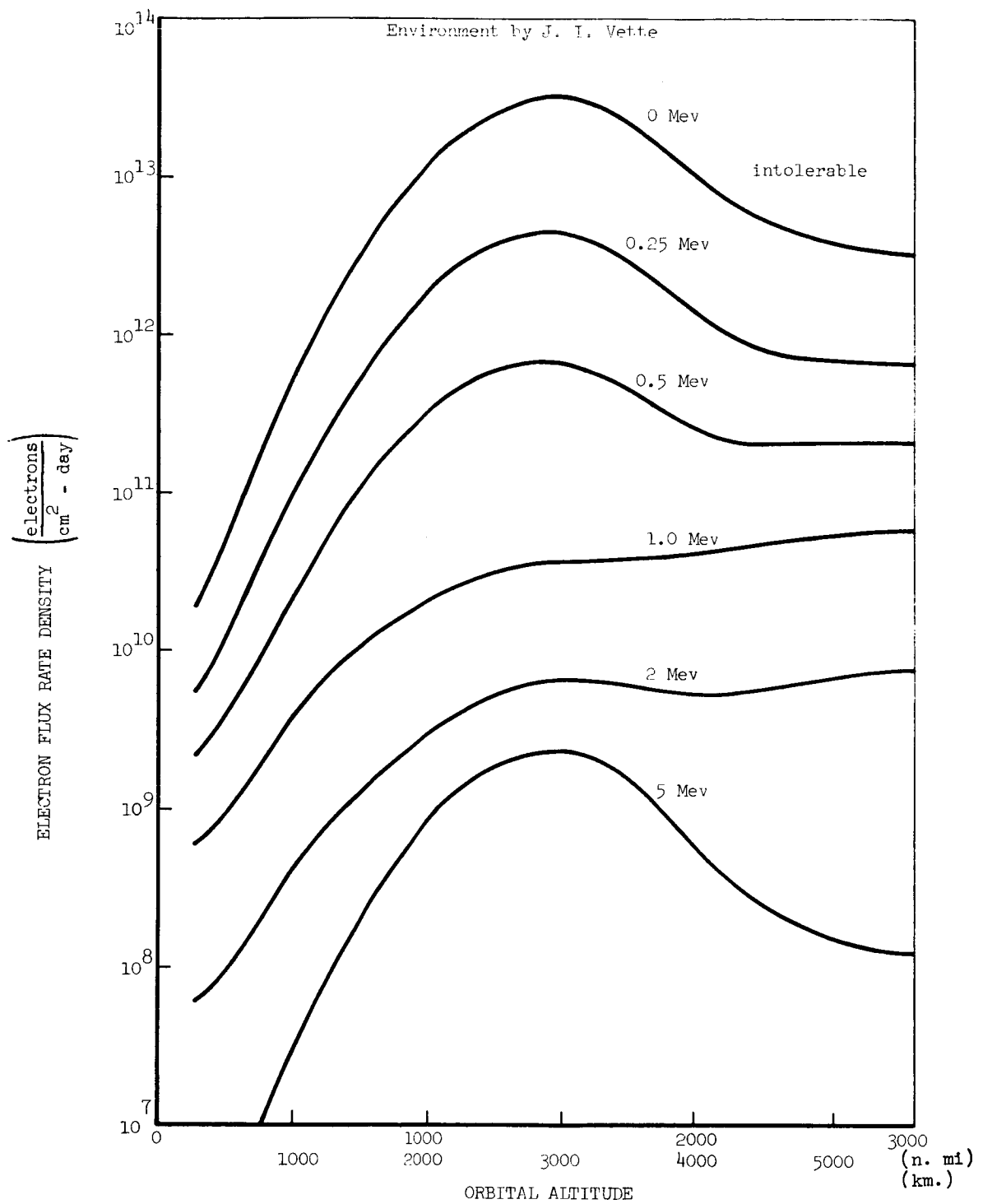


Figure 3.3.2.1-2. Trapped Electron Radiation 1978 - Polar Orbit

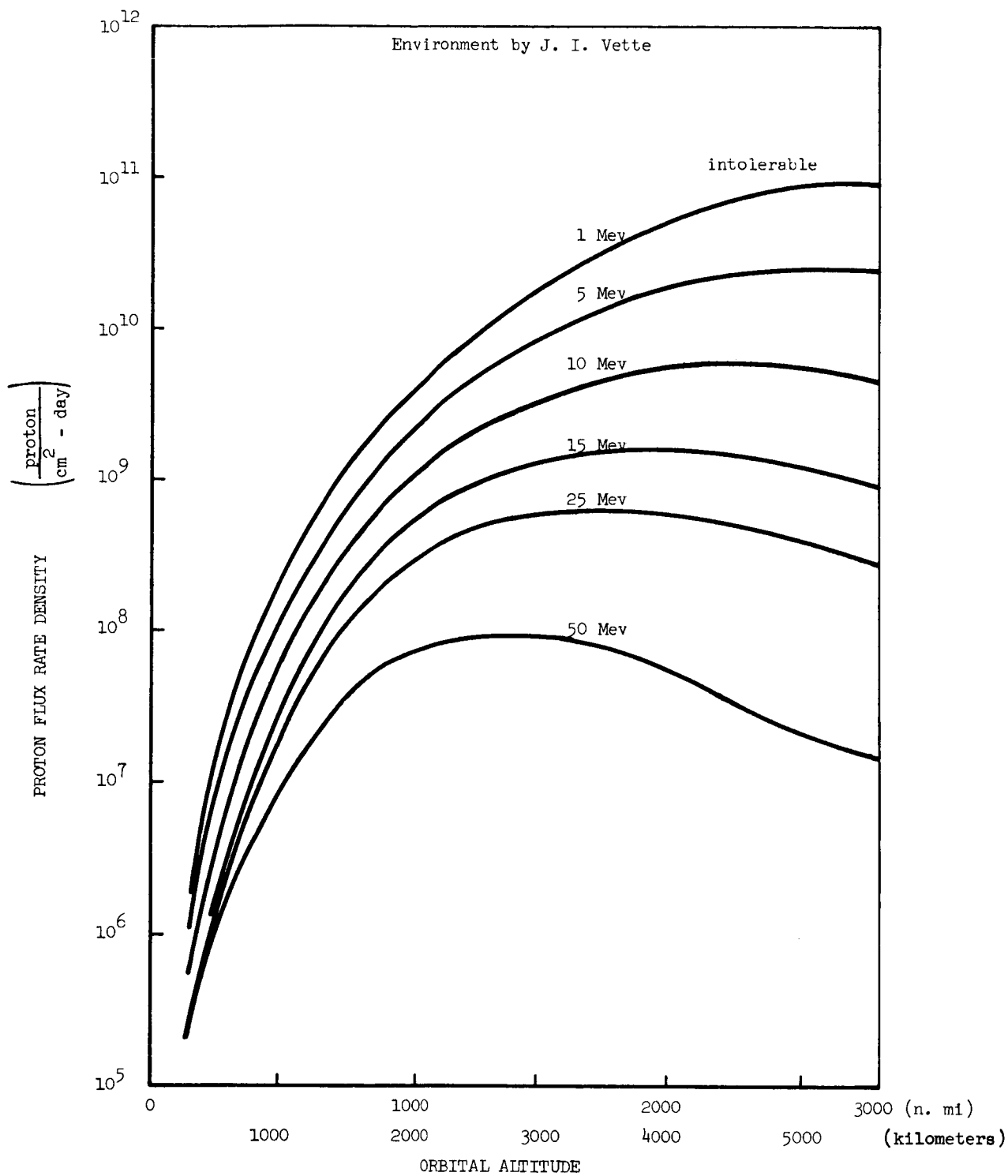


Figure 3.3.2.1-3. Trapped Proton Radiation 1975 - 1985 Polar Orbit

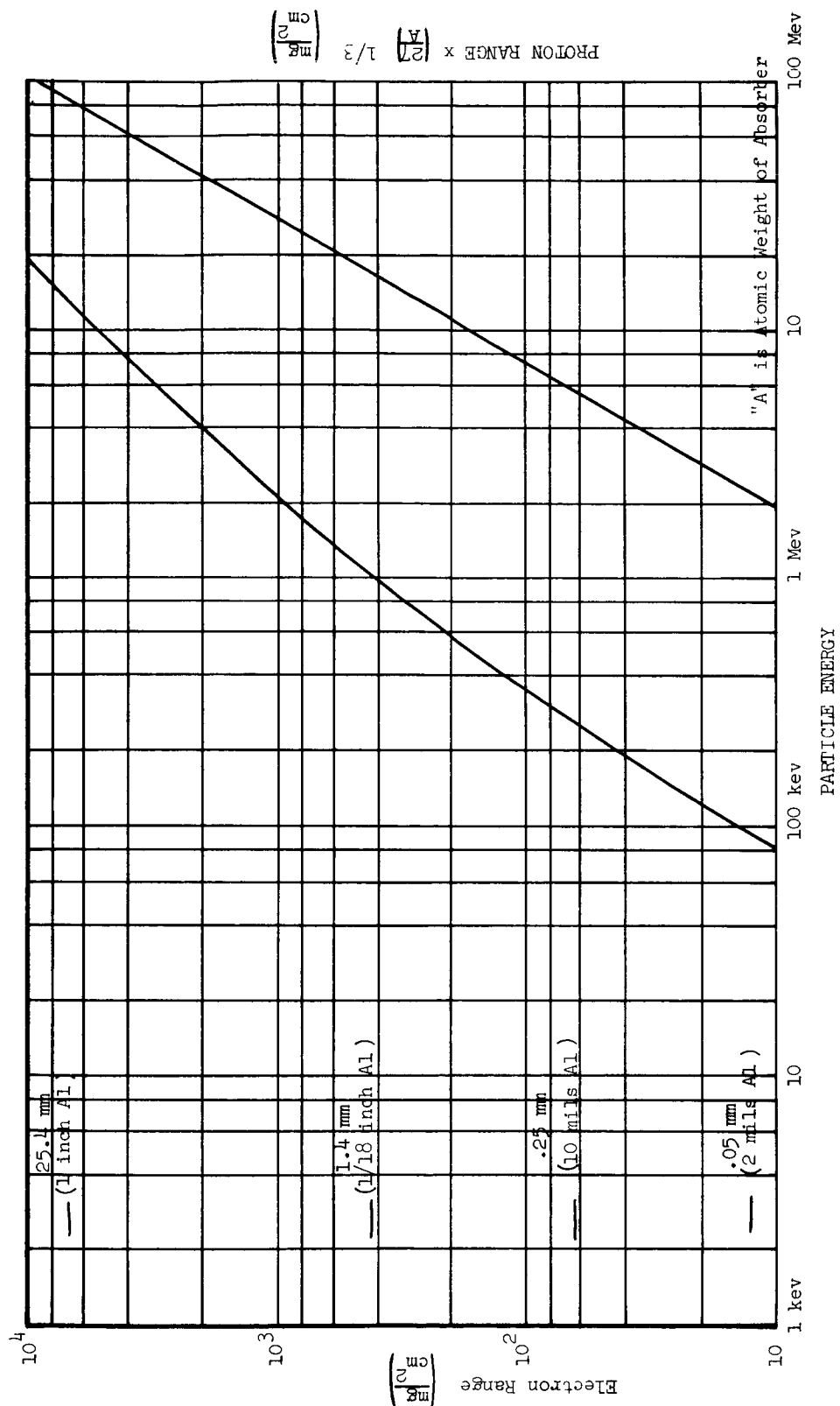


Figure 3.3.2.1-4. Charged Particle Ranges

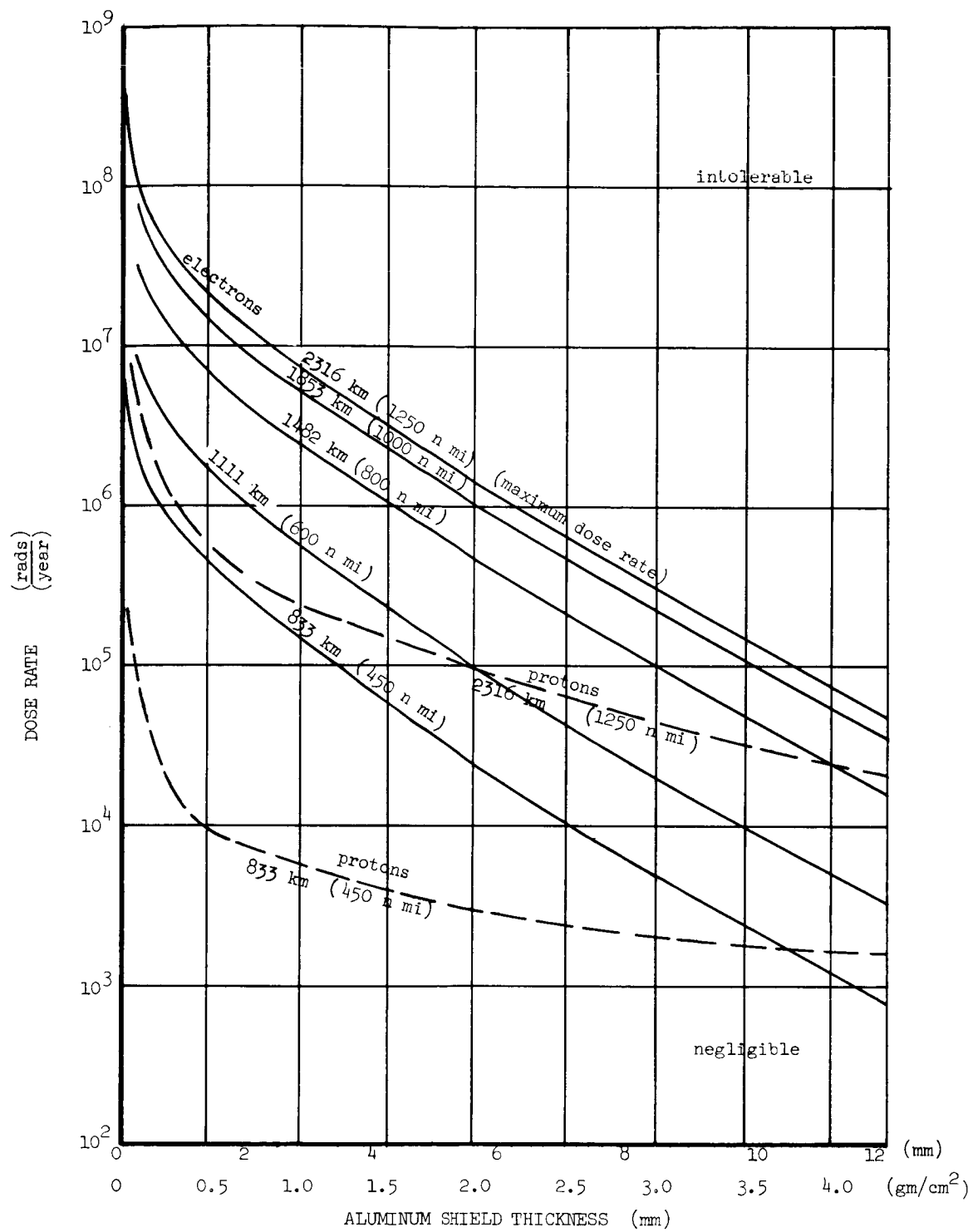


Figure 3.3.2.1-5. Trapped Radiation Dose Rates - Shielded 1975, 1985 Polar Orbit

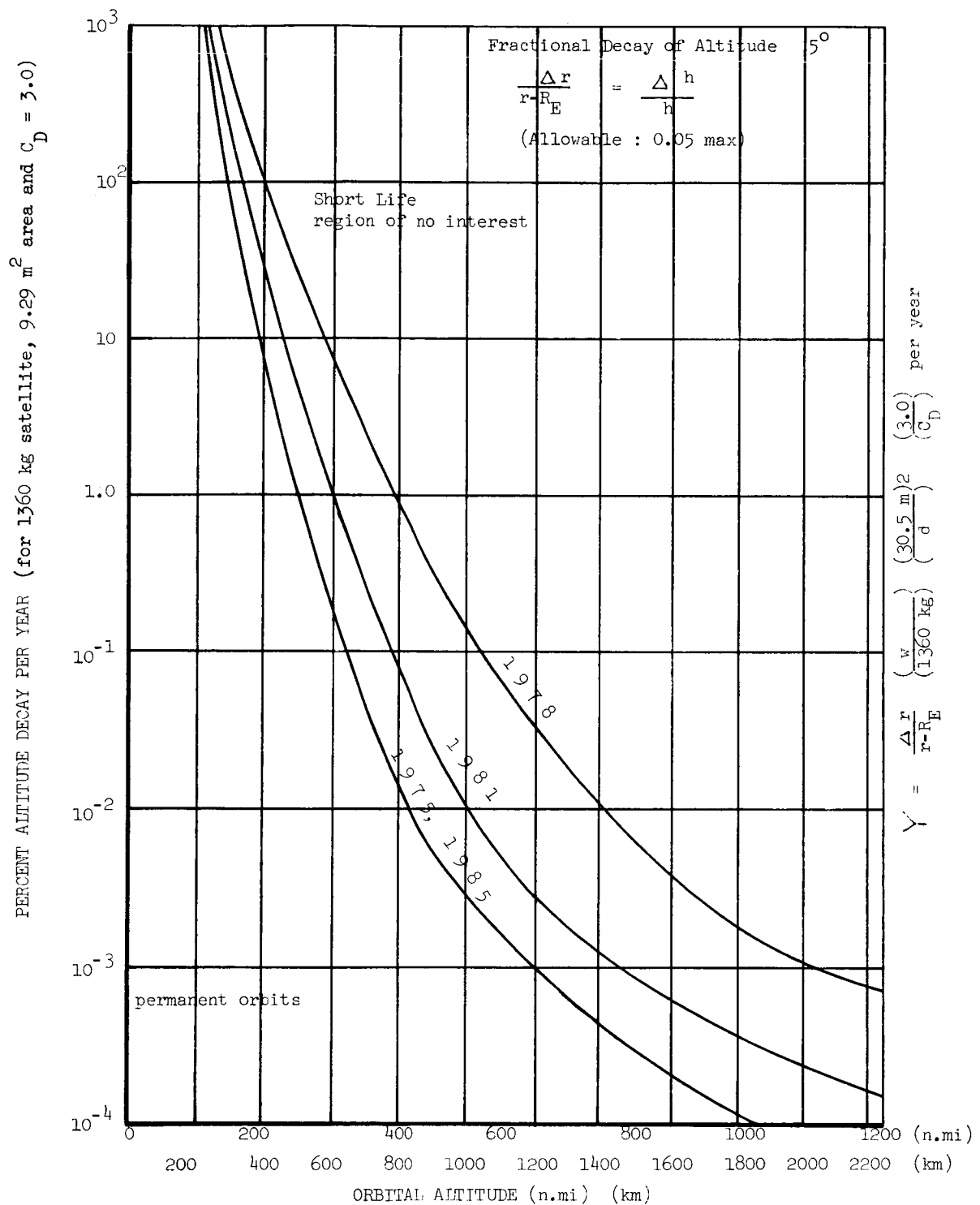


Figure 3.3.2.4-1. Orbital Decay Rates, 1975 - 1985 - Circular Orbits

3.3.3 EARTH ATMOSPHERE R.F. OCCULTATION

Due to the relatively low orbital altitude, a significant deviation of the vector normal to the orbit plane from the communications line of sight vector to the spacecraft will either cause the signal to pass through the earth's atmosphere with possibly deleterious effects or to be completely blocked by the earth itself. The purpose of this section is to discuss the atmospheric constituents and how they affect a signal passing through it so that an equivalent earth radius can be formulated which could be used in the orbit computations. Also, the conclusions drawn regarding the effect of the atmosphere, particularly at the lower elevations, may be used to demonstrate the superiority of an orbiting station over a ground station. Among the signal characteristics studied are its amplitude, direction, phase, and polarization. The reduction of amplitude or attenuation translated into noise temperature will be compared against other expected system noise temperature contributors. Signal direction, phase or path length and polarization effects which are caused by the ionosphere will be evaluated in terms of nominal system goals, beamwidth, range accuracy and polarization.

Atmospheric constituents vary as a function of altitude. Three spherical shells formed by this dependence will be considered, Troposphere, Stratosphere and Ionosphere. The particles within each shell interact with the passing wave along a nearly straight path L . The total effect of all the particles is found by integrating along the path.

$$Z = \int_0^L f(\ell) d\ell \quad (1)$$

Since this integration will be repeated several times it seems appropriate to examine the geometry to which it must be applied. Because of the general altitude dependence of the atmospheric constituents, the path length must be related to altitude as in (2) and illustrated in Figure 3.3.3-1.

$$L^2 = h^2 + 2 R h \quad (2)$$

where L is the distance from the point of interest (P) to the point of tangency (T).

GT is the radial distance from T to the earth.

R is the radial distance from the center of the earth to the point of tangency (T).

h is the radial distance from the point of interest (P) to the circle of tangency.

A is altitude, the distance from point of interest (P) to the earth.

Together Equations (1) and (2) will be used to compute signal characteristic changes caused by passing into and out of the atmosphere. A 600 KM altitude was selected to represent a realistic worst case. A lower altitude is prohibitive due to atmospheric drag and a higher altitude would permit a larger viewing angle. All path integrations will begin at this altitude. Figures 3.3.3-2 and 3.3.3-3 show path length from this altitude for various tangency altitudes.

Attention will be confined to the frequency range between 2 and 100 gigahertz. The upper limit is dictated by the available equipment and the lower by the gain that can be achieved by an aperture limited system.

Troposphere

The troposphere, which is the domain of weather, is in convective equilibrium with the sun-warmed surface of the earth. Its upper limit ranges from 6 to 18 kilometers depending on the latitude. The higher limit is in the equatorial regions. The average ceiling is 8 kilometers. Absorption of electromagnetic radiation in the 2 to 100 gigahertz band has been detected for most of the atmospheric gases including molecular oxygen, water, ozone, sulphur dioxide, nitric dioxide and nitrous oxide.¹ The nitrogen molecule has neither an electric nor magnetic moment. Only the oxygen molecule and the water molecule are of sufficient density to be distinguished at tropospheric pressures. A single water vapor absorption line exists in the frequency regime of interest. The attenuation associated with this electric moment is described by the Van Vleck expression.^{2, 3}

$$\nu_{H_2O} = 4.23 \times 10^2 \frac{f^2}{T^{5/2}} \left[\frac{\Delta f}{(f - 22.33)^2 + (\Delta f)^2} + \frac{\Delta f}{(f + 22.33)^2 + (\Delta f)^2} \right] \quad (3)$$

where f is the frequency in gigahertz

T is the air temperature in degrees Kelvin

Δf is the half width of the line at its half power point in gigahertz

γ_{H_2O} is the attenuation in decibels per kilometer for one gram per meter cubed water density.

The numerical coefficients in (3) are based on measurements made at .2 and .4 kilometers at single frequency points at 35, 70, 90, 140 gigahertz and in detail measurements between 18. and 25. and also 100 to 117 gigahertz.^{4, 5} Equation (3) is plotted in Figure 3.3.3-4 with the appropriate line widths.

The total attenuation experienced by a wave propagating to or from a 600 kilometer satellite and passing within 0, 2, 4, 6 and 8 kilometers of the earth's surface was computed as described in (1). A ground water density of 10 grams per cubic meter and an exponential altitude dependence with a one neper decrease at 2 kilometers was assumed. From the results shown in Figure 3.3.3-5 it is clear that water vapor effects are negligible for the 8 kilometer tangency point path.

Water in particle form including fog, rain, and snow also attenuate radio waves in the band of interest. The loss is due to scattering and increases with increasing frequency. No effort was made to compute the scattering loss because precipitation very rarely exists above 5 kilometers and neither precipitation nor clouds exist above 10 kilometers.⁶

A number of oxygen absorption lines occur near 60 gigahertz. As was the case with the water line, the Van Vleck expression describes the absorption frequency dependence.² The multiplicity of lines requires a more complex form, however.⁷

$$\gamma_{O_2} = 2.649 \frac{P}{T^3} f^2 \sum_{\text{ODD } K} \left[\frac{K(2K+3)}{K+1} S_{K+} + \frac{(K+1)(2K-1)}{K} S_{K-} + \frac{2(K^2+K+1)(2K+1)}{K(K+1)} S_{K0} \right] \exp \left[-\frac{2.069 K(K+1)}{T} \right] \quad (4)$$

where the same nomenclature is used as in (3) and P is the air pressure in mm Hg

$$S_{K_{\pm}} = \left[\frac{\Delta f}{(f - f_{K_{\pm}})^2 + (\Delta f)^2} + \frac{\Delta f}{(f + f_{K_{\pm}})^2 + (\Delta f)^2} \right]$$

$$S_{K_0} = \frac{\Delta f}{f^2 + (\Delta f)^2}$$

$f_{K_{\pm}}$ are the resonant line frequencies in gigahertz.

γ_{O_2} is the absorption in decibels per kilometer when the air consists of 20.94 percent oxygen by volume.

The error in the coefficient S_{K_0} of reference 7 has been corrected here. The numerical coefficients in (4) were determined from recent experiments.⁷ Also, these experiments have shown that the line half width is described by (5)

$$\Delta f = 1.58 \times 10^{-3} P \left(\frac{760}{760 + P} \right) \left(\frac{290}{T} \right)^{.9} \quad (5)$$

The coefficient 1.58 is given as 1.9 in reference 7. However, in the text, the outline states that $\Delta f = .6$ gigahertz at sea level and this leads to the coefficient used in (5). Furthermore, a line width of .6 gigahertz has been used in several other references.

The attenuation coefficient was calculated for the first 26 resonant frequencies shown in Table 3.3.3-1. The "U.S. Standard Atmosphere 1962" was used as a source for the temperature and pressure profiles. The calculations which were programmed on a 7040 are thought to be unique in that the temperature dependence was computed directly. The attenuation coefficients are shown in Figure 3.3.3-6. The total oxygen absorption computed as described in (1) for 0, 10 and 20 kilometers tangency altitude is included in Figure 3.3.3-7. It is clear from Figure 3.3.3-7 that oxygen absorption is significant over most

of the band even for the 20 km integration path.

Stratosphere

The stratosphere typically ranges from 8 kilometers to 80 kilometers, the thickness being greater at the poles. It is characterized by a nearly uniform temperature and the same proportion of constituents as occurs in the troposphere. The one exception in regard to the constituent proportions is the absence of water vapors. Atomic oxygen density becomes comparable to the molecular oxygen density at the top of the stratosphere.

The pressure and therefore the density of the constituents is, of course, much lower than in the troposphere. The lower pressure decreases the oxygen line widths as indicated in (5). The attenuation coefficient computation of (4) was programmed in five megahertz steps between 50 and 70 gigahertz in order that the fine line structures could be seen. Figure 3.3.3-8 shows the resultant attenuation coefficients up to 40 kilometers. It is clear that by moving a system operating frequency into and out of a null, system characteristics could be modified. For example, a system could operate in a null thereby reducing atmospheric blockage to a minimum while maintaining virtually perfect immunity to jamming of DSMCS or inadvertent reception of the spacecraft signal by an earth station.

Ionosphere

Beginning at approximately 100 kilometers and extending up to as high as 1000 kilometers is the region known as the ionosphere. Although the electron density is below one electron per 1000 molecules, the effect on a propagating radio wave is significant, particularly below one gigahertz. Temporal and spatial variations of ion density are the rule rather than the exception. However, sufficient data has been taken so that average electron density profiles for day and night can be effectively used to study radio wave behavior. With these profiles, the effect of the ionosphere on the amplitude, direction of propagation, phase and polarization will be examined in this section.

The effect of the ionosphere on a passing wave is measured by the medium's refractive index. The Appleton equation describes the refractive index of the ionosphere where the operating frequency is much greater than the penetration frequency. Equation 6 is the Appleton expression in conventional notation.⁹

$$\mu^2 = 1 - \frac{X}{1 - \frac{Y_T^2}{2(1-X)} + \left[\frac{Y_T^4}{4(1-X)^2} + Y_L^2 \right]^{\frac{1}{2}}} \quad (6)$$

where

$$Y_T = \omega_T / \omega$$

$$Y_L = \omega_L / \omega$$

$$X = \omega_N^2 / \omega^2$$

$$\omega_T = \omega_H \sin \theta$$

$$\omega_N = \left[\frac{Ne^2}{\epsilon_0 m} \right]^{\frac{1}{2}}$$

$$\omega_L = \omega_H \cos \theta$$

$$\omega_H = \mu_0 \frac{He}{m} \text{ gyro frequency}$$

and

ω is the angular frequency in radians per second.

θ is the angle between the wave normal and the earth's magnetic field.

N is the number density of free electrons in electrons per cubic meter

H is the earth's magnetic field in ampere turns per meter

μ is the real part of the refractive index in henrys per meter

$$\mu_0 = 1.257 \times 10^{-6} \text{ henry/meter}$$

$$\epsilon_0 = 8.85 \times 10^{-12} \text{ farads/meter}$$

$$m = 9.1 \times 10^{-31} \text{ kilogram}$$

$$e = 1.6 \times 10^{-19} \text{ coulombs}$$

$$\text{If } \frac{Y_T^4}{(1-X)^2} \gg 4 Y_L^2 \quad (7)$$

the wave is classed as quasi-transverse and if

$$\frac{Y_T^4}{(1-X)^2} \ll 4 Y_L^2 \quad (8)$$

the wave is quasi longitudinal.

At 2 gigahertz per second X is very small and therefore the breakpoint is where

$$\frac{4 Y_L^2}{Y_T} = 1$$

substituting $Y_L = \left(\frac{\omega_H}{\omega}\right) \cos \theta$

$$Y_T = \left(\frac{\omega_H}{\omega}\right) \sin \theta$$

$$\sin \theta_1 \tan \theta_1 = \frac{2\omega}{\omega_H}$$

The gyro angular frequency is near 1×10^7 radians per second and thus at an operating angular frequency of 12.56×10^9 radians per second (2.0 gigahertz)

$$\begin{aligned} \sin \theta_1 \tan \theta_1 &\cong 2500 \\ \theta_1 &= 89^\circ 58.5' \end{aligned}$$

Hence, quasi-longitudinal conditions will exist except when the magnetic fields are exactly transverse to the direction of propagation. For the condition specified by (8), (6) reduces to

$$\mu^2 \approx 1 - \frac{X}{1 \pm Y_L} \quad (9)$$

The positive and negative signs here represent the ordinary and extraordinary waves respectively. The magnetic field increases the refractive index of the ordinary wave and reduces it for the extraordinary wave relative to that for the same electron density in the absence of the magnetic field.

For ω_H near 10^7 at 2 gigahertz operating frequency, Y_L and X are much less than one and therefore (9) reduces to (10)

$$\mu \approx 1 - \frac{1}{2} X (1 \pm Y_L) \quad (10)$$

By ignoring temporarily wave splitting, (10) reduces further to (11)

$$\mu \approx 1 - \frac{1}{2} X \quad (11)$$

Let $\Delta\mu \triangleq 1 - \mu$

$$\text{and since } X = \frac{\omega^2 N}{\omega^2 \epsilon_0 m \omega^2} = \frac{Ne^2}{\epsilon_0 m \omega^2} \quad (12)$$

$$\Delta\mu = b \frac{N}{\omega^2} \quad (13)$$

where

$$b = 1.6 \times 10^3 \frac{(\text{Meter})^3}{(\text{Sec})^2}$$

With the approximate expressions derived, the effects of the ionosphere on a propagating wave can now be simply determined. The computations will be carried out at 2.0 gigahertz, since it is the most sensitive frequency in the band of interest. Also, the theoretical frequency dependence will be given for each effect.

Path Length

The phase path length through the ionosphere will increase. Equation (14) describes the path length for any wave.

$$P = \int_0^L \mu \, d\ell \quad (14)$$

The angle cosine between the wave normal and the Poynting vector is assumed to be one. The path length change due to the ionosphere is computed with (15).

$$\Delta P = \int_0^L \Delta\mu \, d\ell = \frac{b}{\omega^2} \int_0^L N \, d\ell \quad (15)$$

Consistent with earlier integrations, the path length change was computed from a 600 kilometer orbital height through the total ionosphere. Figure 3.3.3-9 shows the ionosphere idealized model.^{6, 10} Although the step model appears to be a crude approximation, the integration of (15) is across layers and thus the effect of the idealization is reduced. Integrations were made at several different tangency elevations so that the continuous plot of Figure 3.3.3-10 could be constructed. The results shown in Figure 3.3.3-10 are easily translated to other frequencies by the inverse squared relation included in (15).

Wedge Refraction

In addition to vertical gradients, horizontal gradients have been observed in ionosphere studies.¹¹ Anomalous refraction caused by these

gradients is particularly important, since the DSMCS wave will be striking such gradients at a low incidence angle and also the beamwidth may be very narrow. The wave front deviation due to a horizontal gradient can be computed with (16).

$$\tau = \frac{d \Delta P}{d s} = \frac{b}{\omega^2} \frac{d \int N d\ell}{d s} \quad (16)$$

where s is a dimension transverse to the wave front normal.

Radio astronomy research at near zenith angles has shown that a gradient of one percent per ten horizontal kilometers with a 5 degree slope is typical.¹² At grazing incidence the gradient is increased by Sec θ or 11.5.

Hence, at 2.0 gigahertz and a 10^{17} electrons per meter² column

$$\tau = \frac{b}{\omega^2} 11.5 \times 10^{-5} \times 10^{17}$$

$$\tau = 3.0 \times 10^{-5} \text{ radians}$$

$$\text{or } 1.7 \times 10^{-3} \text{ deg.}$$

Scintillation

In addition to the systematic variations in the refraction index as those causing wedge refractions, there are also many irregular variations which distort and scatter a passing wave at random. The temporal and spatial variations of the refractive index cause the apparent positions and magnitude of a source seen through them to fluctuate. Speculations still exist regarding what is the best cause model for this phenomenon.¹³ However, sufficient empirical data have been collected to reveal relative magnitudes and frequency dependence.^{14, 15} Amplitude variations are commonly described by the amplitude index S :

$$S = \frac{P_{\max} - P_{\min}}{P_{\max} + P_{\min}} \quad (17)$$

Records show that at 30 gigahertz the index is generally near unity and it is proportional to the fourth power of wavelength and the cube of the distance. Thus the amplitude fluctuation is negligible at 2.0 gigahertz. Similarly, the angle of arrival fluctuation is a few minutes of an arc at about 30 gigahertz decreasing to negligible levels at 2.0 gigahertz.

Group Path Delay

The ionosphere is a dispersive medium. As a result, the

spectrum generated by data modulated on the carrier will be retarded or advanced relative to free space transmission. The group path through the ionosphere is given in (18).

$$P_G = \int_0^L \mu_G d\ell \quad (18)$$

$$\text{where } \mu_G = \frac{d(\mu \omega)}{d\omega} = \mu + \omega \frac{d\mu}{d\omega}$$

$$\text{thus } P_G = P + \omega \frac{d\mu}{d\omega}$$

Using the approximations of (11)

$$\mu_G \approx \frac{1}{\mu}$$

therefore,

$$\Delta \ell_G = \int_0^L (\mu_G - 1) d\ell \approx \int_0^L \frac{(1 - \mu)}{\mu} d\ell = - \Delta \ell \quad (19)$$

where $\Delta \ell_G$ is the group path delay

$\Delta \ell$ is the phase path delay.

Thus the time error ΔT is positive

$$\Delta T = \frac{\Delta \ell_G}{c} \quad (20)$$

where $c = 3.0 \times 10^8$ meter/second.

Figure 3.3.3-10 shows this delay for the conditions assumed earlier in computing the phase path difference.

Polarization

The affect of the magnetic field is assumed to be very small in the signal parameter computations considered so far. It is a necessary consideration in analyzing polarization ratios, since the wave splitting into ordinary and extraordinary components is a result of it. A linearly polarized wave passing through the ionosphere can be represented by two oppositely rotating circularly polarized vectors. The rotations of the resultant wave, $d\Omega$, could, by the differing propagation speeds for the two component rotations dK_+ and dK_- over a path length L be given by

$$d \Omega = \frac{d K_+ - d K_-}{2}$$

and $d K_+ \triangleq \frac{2\pi}{\lambda_+} d\ell$

$$d K_- \triangleq \frac{2\pi}{\lambda_-} d\ell$$

where λ_+ and λ_- represent the ordinary and extraordinary wave lengths.

Hence $d\Omega = \pi \left(\frac{1}{\lambda_+} - \frac{1}{\lambda_-} \right) d\ell$

Since $\lambda = \mu_+ \lambda_+ = \mu_- \lambda_-$

and $d\Omega = \frac{\pi}{\lambda} (\mu_+ - \mu_-) d\ell$

From (10)

$$\mu \cong 1 - \frac{X}{2} + \frac{X Y_L}{2}$$

and $\mu_+ - \mu_- \cong \frac{X Y_L}{2}$

$$\therefore d\Omega = \frac{\pi}{\lambda} \frac{X Y_L}{2} d\ell \quad (21)$$

In rotationalized units

$$X Y_L = \frac{Ne^2}{\epsilon_0 m \omega^2} \cdot \frac{\mu_0 H \cos \theta}{m \omega}$$

The nomenclature is given in equation (6)

Rearranging $d\Omega = \frac{D}{\omega^2} NH \cos \theta d\ell \quad (22)$

$$D \triangleq \frac{e^3 \mu_0}{2 c \epsilon_0 m^2} = 1.15 \frac{(\text{meter})^3}{\text{sec coulomb}}$$

Integrating

$$\Omega = \frac{D}{\omega^2} \int_0^{I_1} NH \cos \theta d\ell \quad (23)$$

to be consistent with the pessimistic bias of earlier computations the $H \cos \theta$ will be estimated from the horizontal field at the magnetic equator and θ

will be assumed to be zero.⁶ Also, the field will be assumed constant over the whole ionosphere

$$H \cos \theta = 34. \frac{\text{amp turns}}{\text{meter}}$$

A more detailed analysis¹⁶ of this value showed a 45 ampere turns per meter maximum.

Integrating (23) over the same paths as the phase path length, computations show that at 2 gigahertz the maximum rotations would be one radian for a daytime profile and 3 radians for the nighttime case.

Absorption

The collision of electrons oscillating under the influence of the propagating wave with neutral and other ionized particles attenuate the wave. The absorption coefficient can be taken directly from the complete Appelton expression.⁹

$$K = \frac{e^2}{2mc \epsilon_0} \frac{1}{\mu} \frac{N \nu'}{\nu^2 + (\omega + \omega_L)^2} \quad (24)$$

where ν' is the frequency of collision of free electrons with heavy particles.

This is further simplified at the frequency range of interest by assuming

$$\begin{aligned} \mu &\approx 1 \\ \omega + \omega_L &\gg \nu' \\ \omega &\gg \omega_L \end{aligned}$$

Hence

$$K = \frac{e^2}{2mc \epsilon_0} \cdot \frac{N \nu'}{\omega^2} \quad (25)$$

and the total attenuation is computed with (26)

$$A = \int_0^L K \, d\ell = \frac{e^2}{2mc \epsilon_0} \frac{1}{\omega^2} \int_0^L N \nu' \, d\ell$$

Detailed integrations were not carried out over the probable DSMCS ray paths because of the low loss levels experienced in the VHF band coupled with the inverse frequency squared dependence. Experiments have demonstrated this dependence. The absorptions for a zenith path near 100 megahertz have been

measured near 10^{-4} decibels in the temperate zone. This level will fluctuate an order of magnitude in either direction due to solar induced ionospheric disturbances. These disturbances primarily effect the loss in the D region below 90 kilometers.

Refractions

The analysis of the normal refractions of the ionosphere have been put at the end of this section because it does not involve the simple integrations of (1). Figure 3.3.3-11 shows an exaggerated view of a wave passing through the ionosphere. The computation of the refraction through the ionosphere is a laborious task. By applying a previous analysis the job has been substantially reduced.¹⁷ The systematic refraction of a wave generated at the earth's surface passing through the ionosphere is given by Figure 3.3.3-12 assuming the profile of Figure 3.3.3-9. The wave is assumed tangent to the earth at the launch point. Figure 3.3.3-11 shows that the refraction effects of a wave launched in or above the ionosphere, passing through the ionosphere, grazing the earth, and back out are compensating. The daytime refractions of Figure 3.3.3-12 represents a worst case where the day-night line is directly above the earth tangency point. The analysis from which these data were taken were only traced out to 500 kilometers. However, the additional refractions at 600 kilometers is not considered large.

Summary

The effect of the earth's atmosphere on a signal transmitted between a near earth satellite and a deep space vehicle has been reviewed for the frequency range between 2.0 and 100. gigahertz. Efforts were made to keep the range of study parameters considered sufficiently general so that almost any system that might be proposed for DSMCS could be analyzed, but limited in scope to the probable geometry and system variables so as to reduce the unnecessary labor. With one exception, the signal characteristic computations were made over paths terminating at a DSMCS station in a 600 kilometer circular orbit. This altitude was assumed because the atmospheric drag is prohibitive below this level.

The atmospheric constituent profiles used in the water vapor and oxygen computations are average for most of the earth's surface. The fluctuations in the results due to the variations in constituent concentration is expected to be less than two. From Figure 3.3.3-5 for attenuation of the radio wave or the increase in noise temperature due to water vapor is small compared to a system noise temperature of 10 degrees Kelvin for a wave passing 8 kilometers or higher above the earth. Figure 3.3.3-7 shows that the oxygen noise temperature contributions does not reduce to 10 degrees Kelvin until an altitude of 30 kilometers is reached. This does not include the regions of 60 gigahertz plus or minus six gigahertz. In the absorption region the loss effects can be controlled by changing the frequency as suggested by the absorption coefficient fine structure shown in Figure 3.3.3-8.

The effect of the ionosphere on a propagating wave was calculated with the two profiles shown in Figure 3.3.3-9. The electron density shown is typical of temperate zone latitudes. Variation of an order of magnitude above and below the indicated densities occur with time and location. From the expressions derived it can thus be concluded that the results of the ionospheric computations are accurate only to an order of magnitude.

Phase path decrease and group path delay increase is shown in Figure 3.3.3-10 for 2.0 gigahertz and the frequency dependence in (15) and (20). Both effects are small as is also scintillation and absorption at 2.0 gigahertz. The frequency dependence is also inverse. Wedge refractions and spherical refraction for the same frequency is also probably negligible at 4.0×10^{-3} degrees. The computed rotation of a linear polarized wave was 1.0 radian for the daytime profile and .3 for the nighttime. Thus a circularly polarized antenna might be necessary at the bottom of the band.

To summarize the system implications of the findings, it can be stated that the effective earth radius is about 30 kilometers greater than the true radius for water vapor and oxygen absorption except for the 53 to 66 gigahertz band. In this band, the occultation altitude is between 60 and 100 kilometers. The specific height is largely judgement as to how narrow the line may become before they are not considered a nuisance. The order of magnitude accuracy ionospheric results indicate that the ionosphere will not significantly change the amplitude, direction or phase length and that circular polarization is preferred below about 10 gigahertz.

Bibliography

1. S. Ghoch and H. Edwards, "Rotational Frequencies and Absorption Coefficients of Atmospheric Gases," AF Cambridge Research Center, Bedford, Mass., AF Surveys in Geophysics No. 82; March, 1956.
2. J. Van Vleck and V. Wushapf, "On the Shape of Collisions Broadened Lines", Rev. Mod. Phys., Vol 17, pp 227-236; April-July 1943
3. C. Talbert, et al., "Propagation Studies between 18-0 and 25-5 KMC", EERL Report No. 110, the Univ. of Texas, (1949).
4. C. Talbert, et al., "Experimental Measurements of the Absorption of Millimeter Waves Over Extended Ranges", IRE, PGAP-5, pp 239-241; April, 1957
5. A. Stroiton, et al., "Anomalies in the Absorption of Radio Waves by Atmospheric Gases", IRE Proc., Vol 48, pp 898-903; May, 1960.
6. Handbook of Geophysics, Revised Edition, USAF Air Research and Development Command, Geophysics Research Directorate, book, Macmillan, New York, 1960
7. C. Talbert et. al., "Synopsis of Attenuation and Emission Investigations of 58 and 62 KMC frequencies in the Earth's Atmosphere", Proc. IEEE 51 1754 (1963)
8. M. Mizushrina and R. Hill, "Microwave Spectrum of O_2 ", Phys. Rev. 93, 745 (1954)
9. J. Ratcliffe, "The Magneto-sonic Theory and its Application to the Ionosphere", Cambridge University Press, Cambridge, England (1959).
10. Monograph on Ionospheric Radio, ed., W. J. G. Beyton, XIIIth General Radio Assembly URSI, London, Elsinier Publishing Company, New York, book, (1963)
11. F. Smith, "Atmospheric Refractions of 81st Radio Waves from Radio Wave from Radio Stars", J. Atmos. Ten. Phys., Vol 2, pp 350-355 (1952)

12. R. Lawen, "Ionospheric Refraction, I: Analytic Calculation for an Ionosphere Almost Spherically Stratified", J. Geophysics Res., Vol 67, pp 2339-2345; (1962).
13. G. Bowhill, "The Scattering of Radio Waves by an Extended Randomly Refracting medium". J. Atmos. Ten. Phy., Vol 20, pp 9-18 (1961)
14. H. Chevers, "The Simultaneous Observations of Radio Star Scintillations on Different Radio Frequencies", J. Atmos. ten. Phys., Vol 17, pp 181-187; (1960).
15. R. Allen, et al., "Measurement of Radio Star and Satellite Scintillations at a Subnormal Latitude", IEEE, Trans. Ant. and Prop., AP-12, No. 7, pp 812-821 (1964).
16. K. Yeh and V. Gonzalex, "Notes on the Geometry of the Earth Magnetic Field Useful to Faraday Effect Experiments", J. Geophys. Res., Vol 65, pp 3209-3214; (1960).
17. W. Pfister and T. Keneshea, "Ionospheric Effects on Positioning of Vehicles at High Altitudes", Air Force Surveys in Geophysics, No. 83, AFCRL (1956).

Table 3.3.3-1

MICROWAVE LINE FREQUENCIES (IN GHz) OF O_2 Hill⁸.

The first 26 resonant frequencies, as calculated by Mizushima and

ν_{1+} = 56.265	ν_{1-} = 118.75
ν_{3+} = 58.447	ν_{3-} = 62.486
ν_{5+} = 59.591	ν_{5-} = 60.305
ν_{7+} = 60.435	ν_{7-} = 59.164
ν_{9+} = 61.151	ν_{9-} = 58.323
ν_{11+} = 61.800	ν_{11-} = 57.612
ν_{13+} = 62.411	ν_{13-} = 56.968
ν_{15+} = 62.998	ν_{15-} = 56.364
ν_{17+} = 63.568	ν_{17-} = 55.784
ν_{19+} = 64.127	ν_{19-} = 55.222
ν_{21+} = 64.678	ν_{21-} = 54.673
ν_{23+} = 65.223	ν_{23-} = 54.132
ν_{25+} = 65.770	ν_{25-} = 53.599

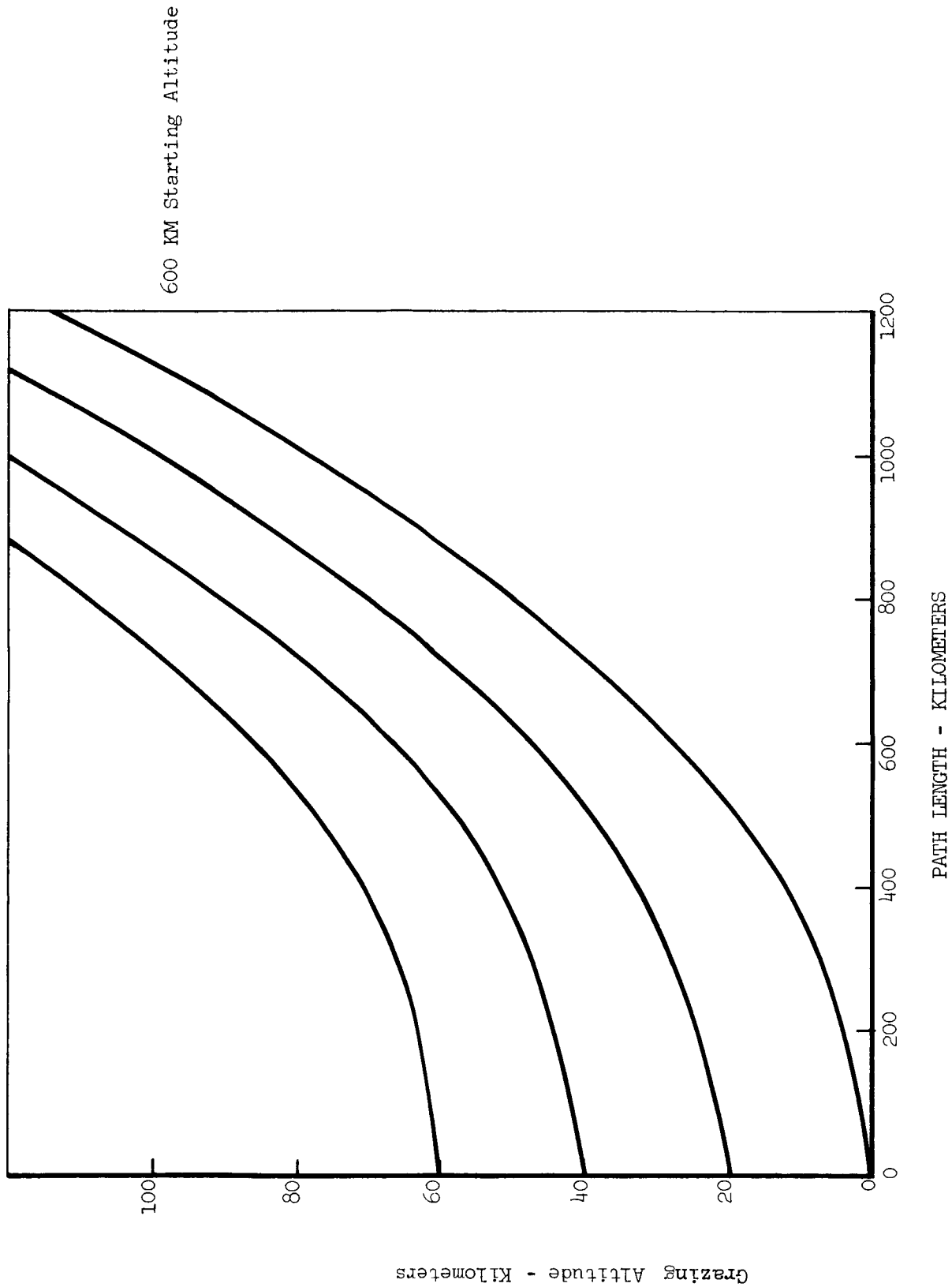


Figure 3.3.3-2. Altitude vs Path Length

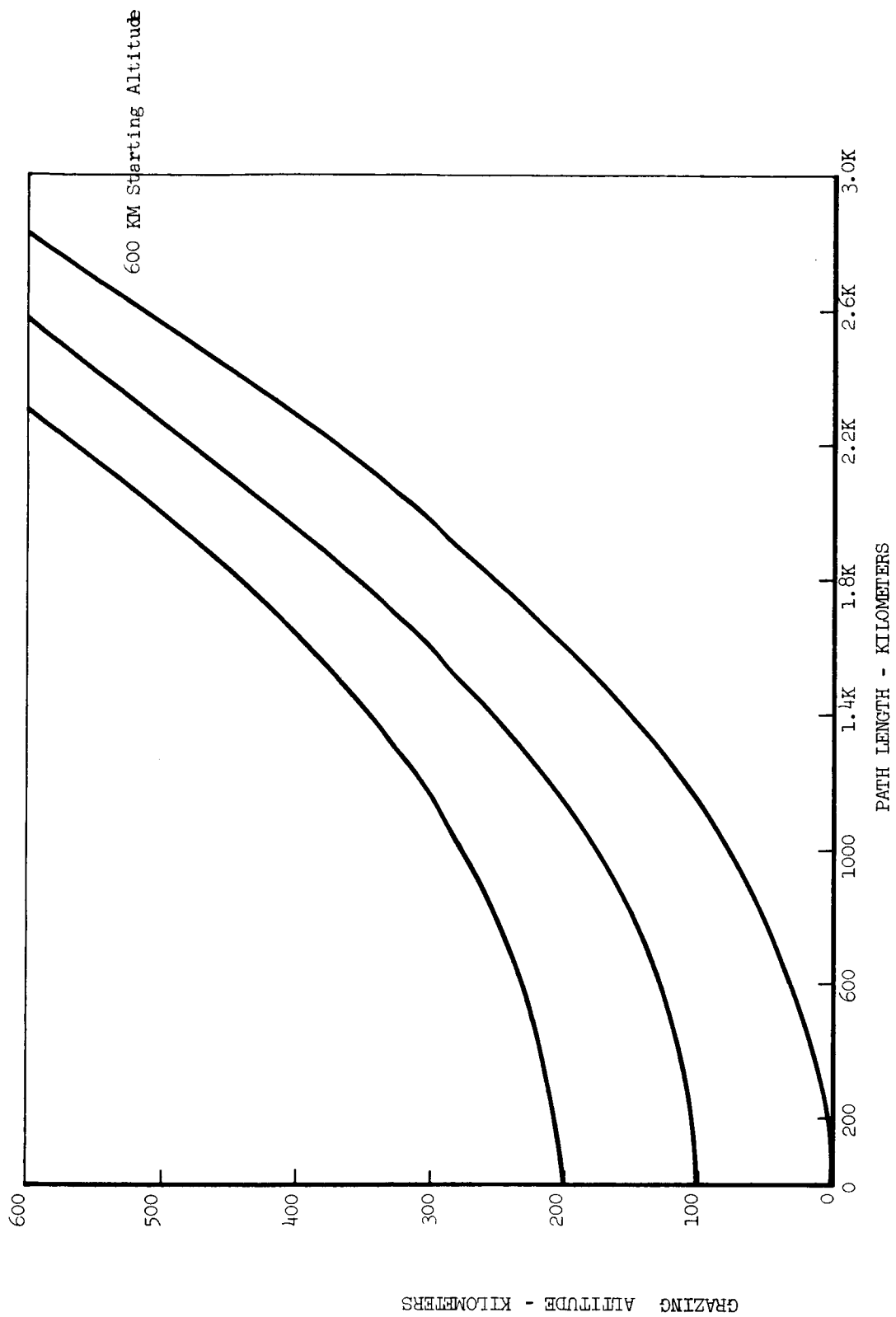


Figure 3.3.3-3. Altitude vs Path Length

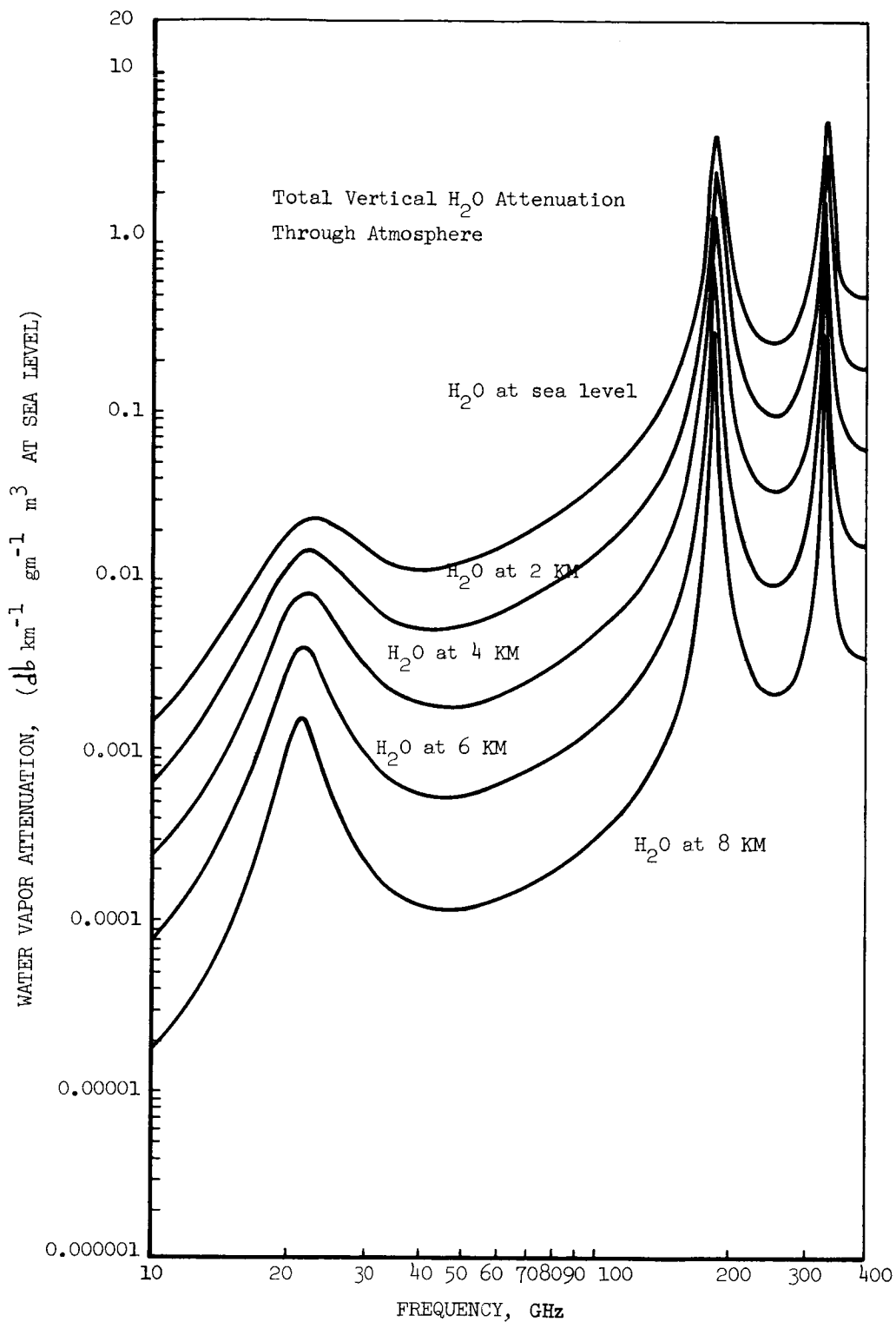


Figure 3.3.3-4. Earth's Atmosphere Water Vapor Attenuation

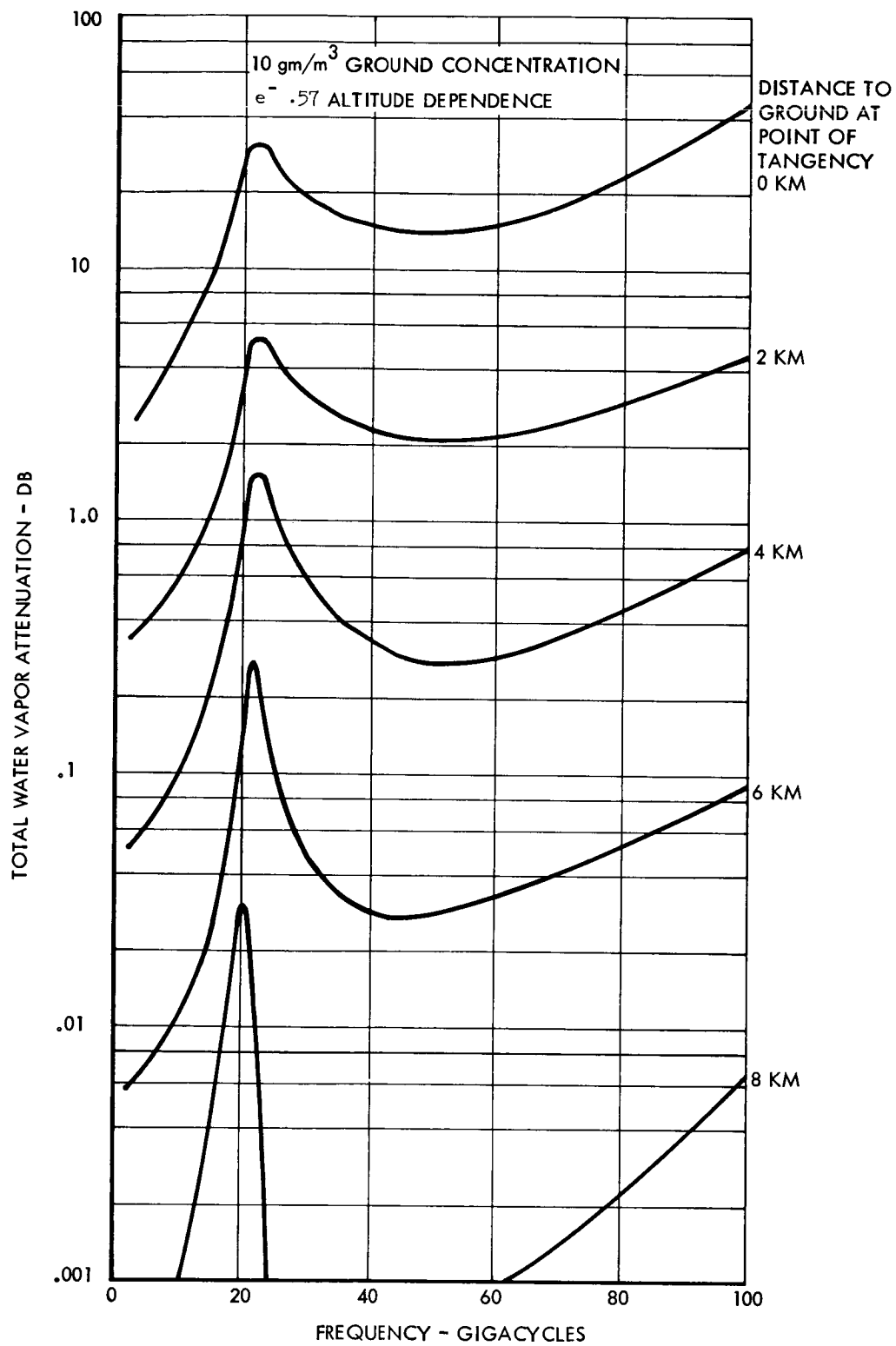


Figure 3.3.3-5. Water Vapor Effects Upon Tangency Point

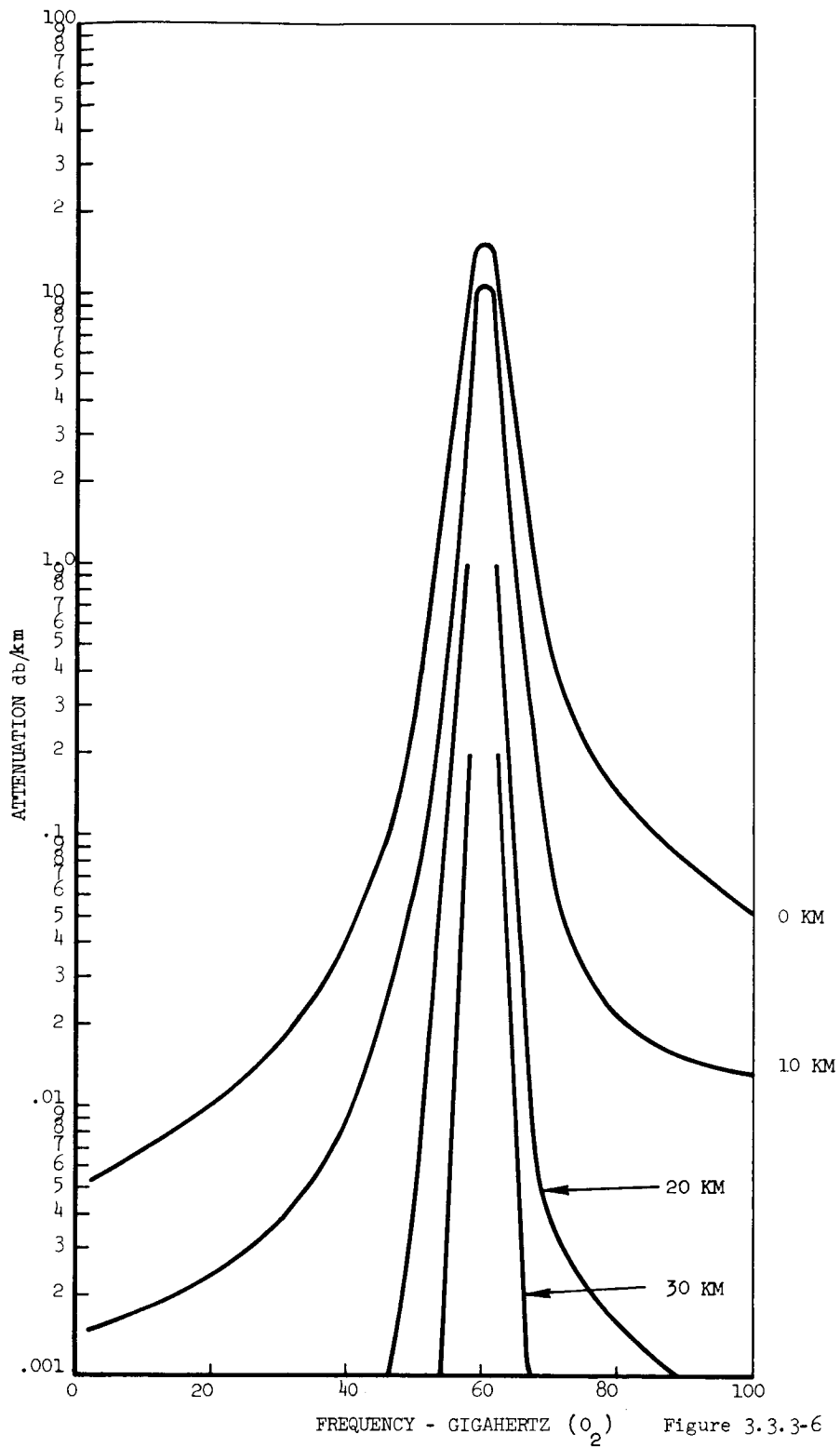


Figure 3.3.3-6. Attenuation vs Frequency

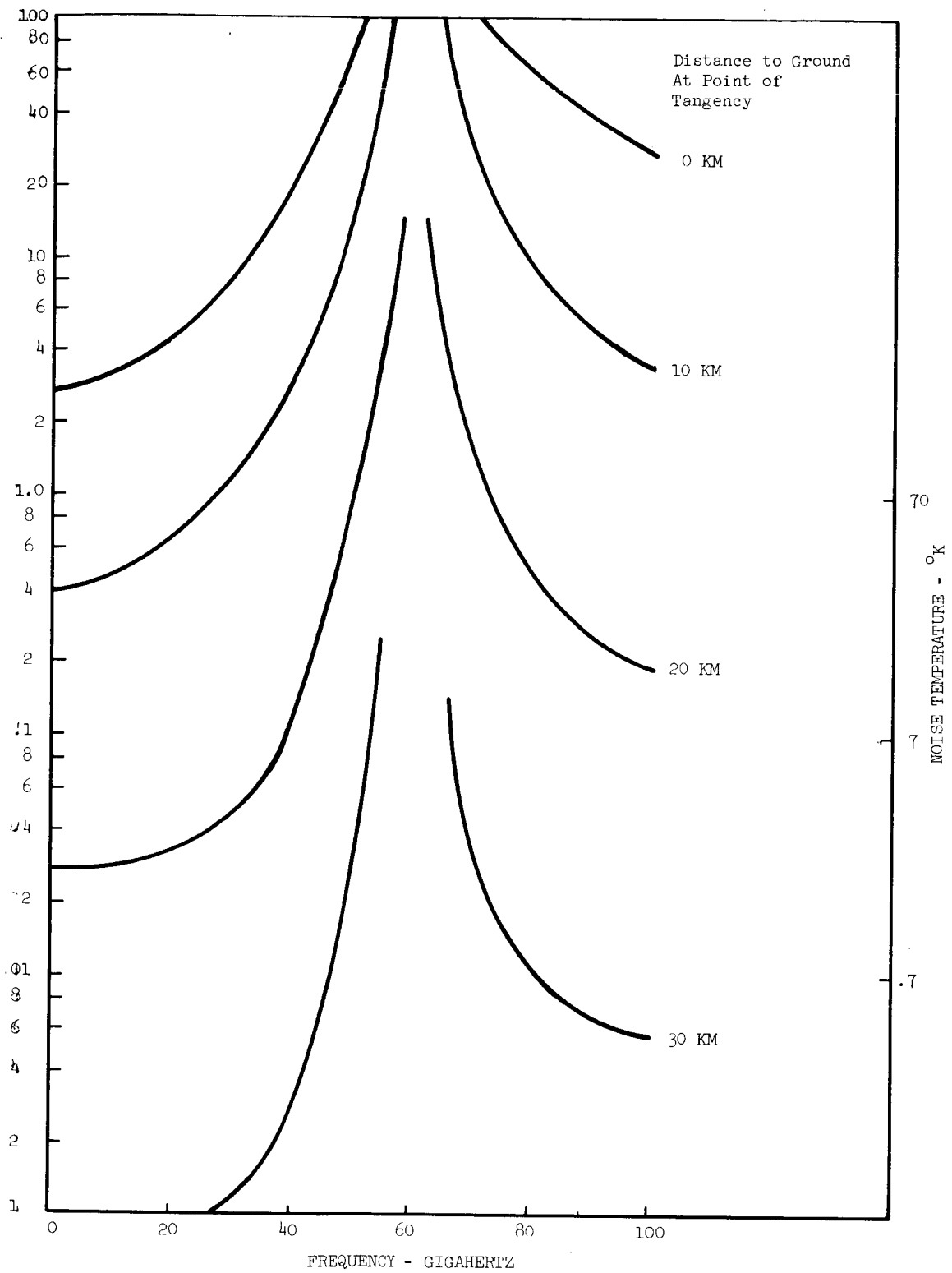
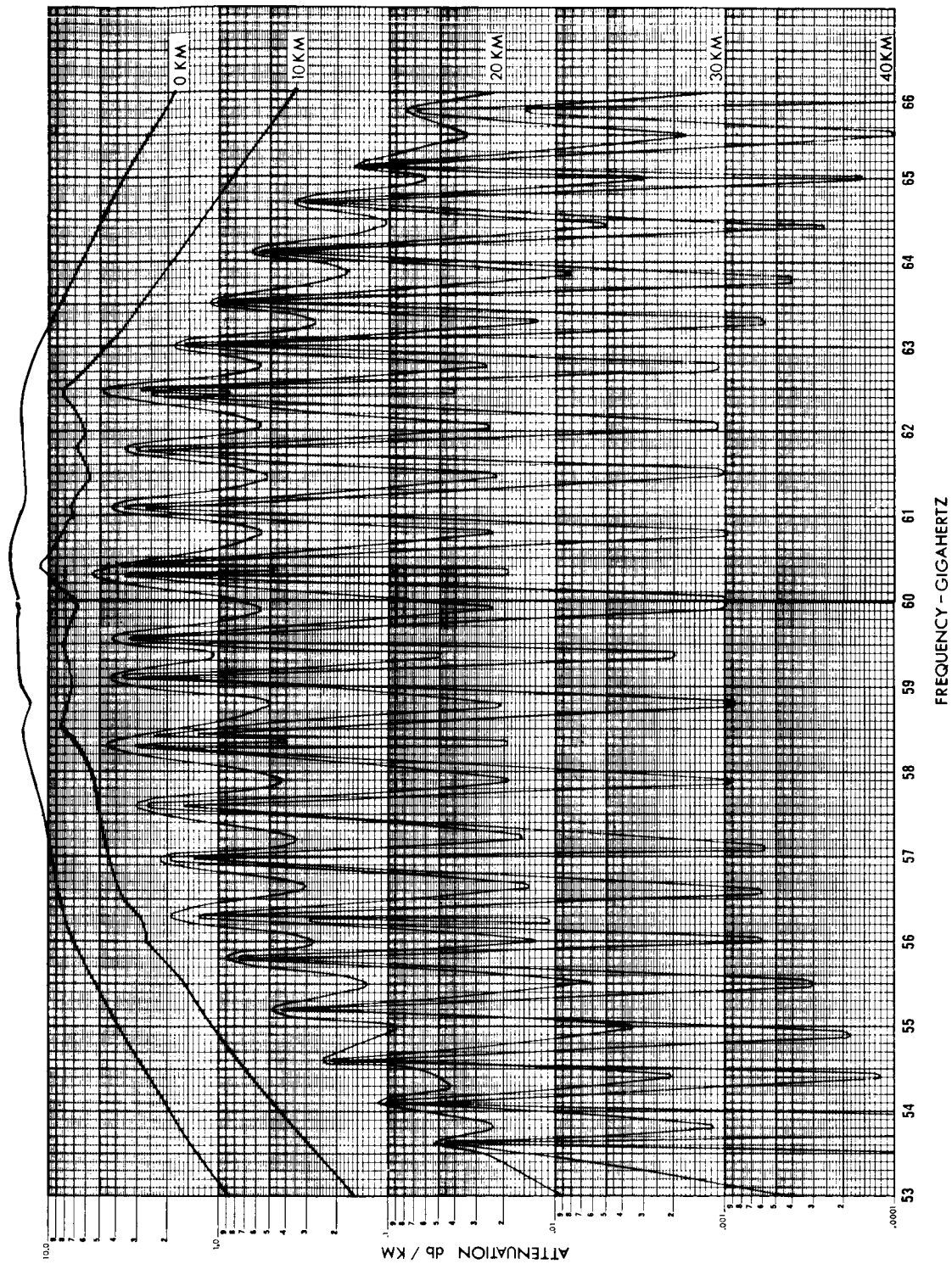


Figure 3.3.3-7. Attenuation vs Frequency



ATTENUATION VERSUS FREQUENCY

Figure 3.3.3-8. Attenuation Versus Frequency

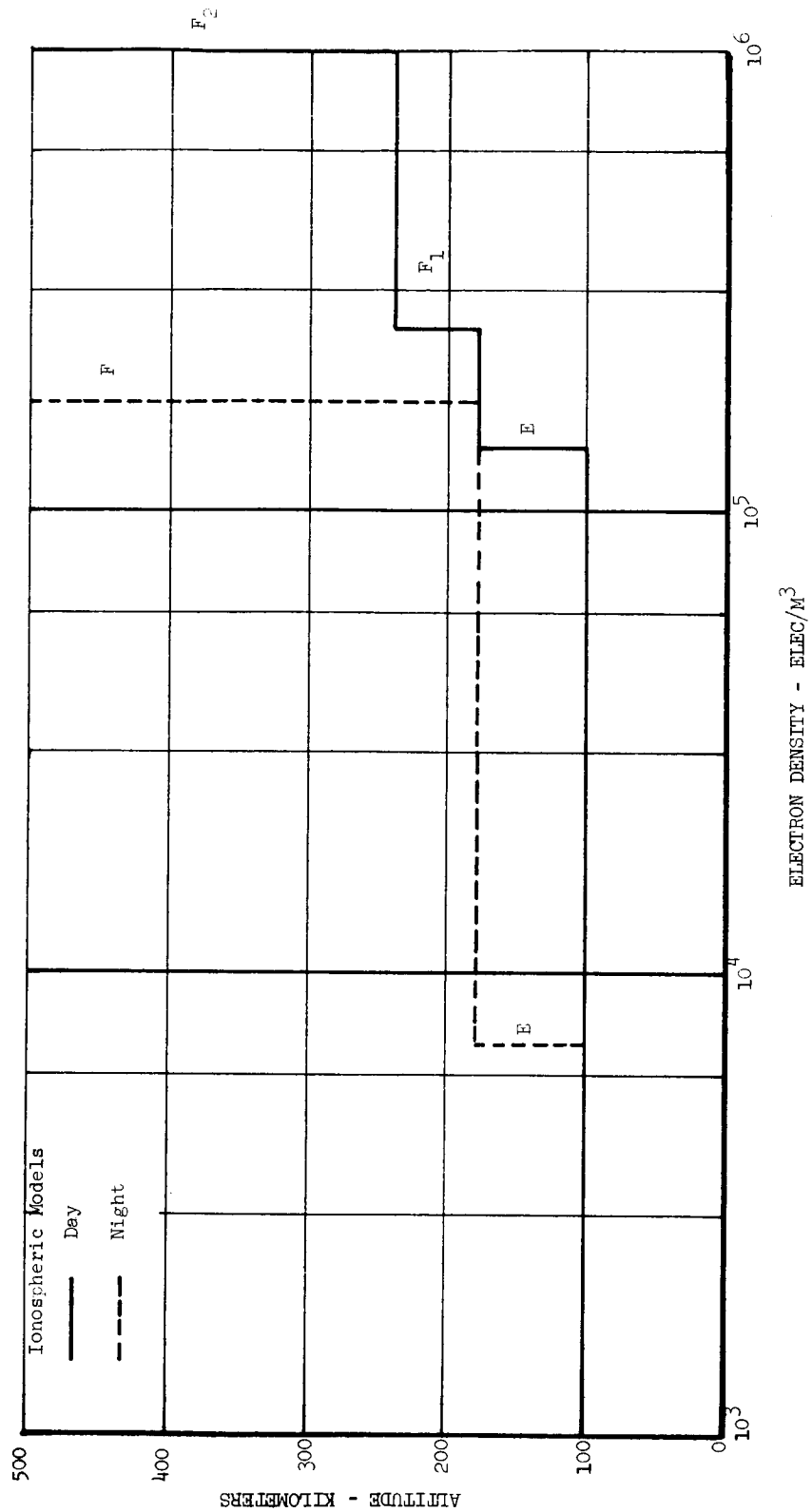


Figure 3.3.3-9. Altitude vs Electron Density

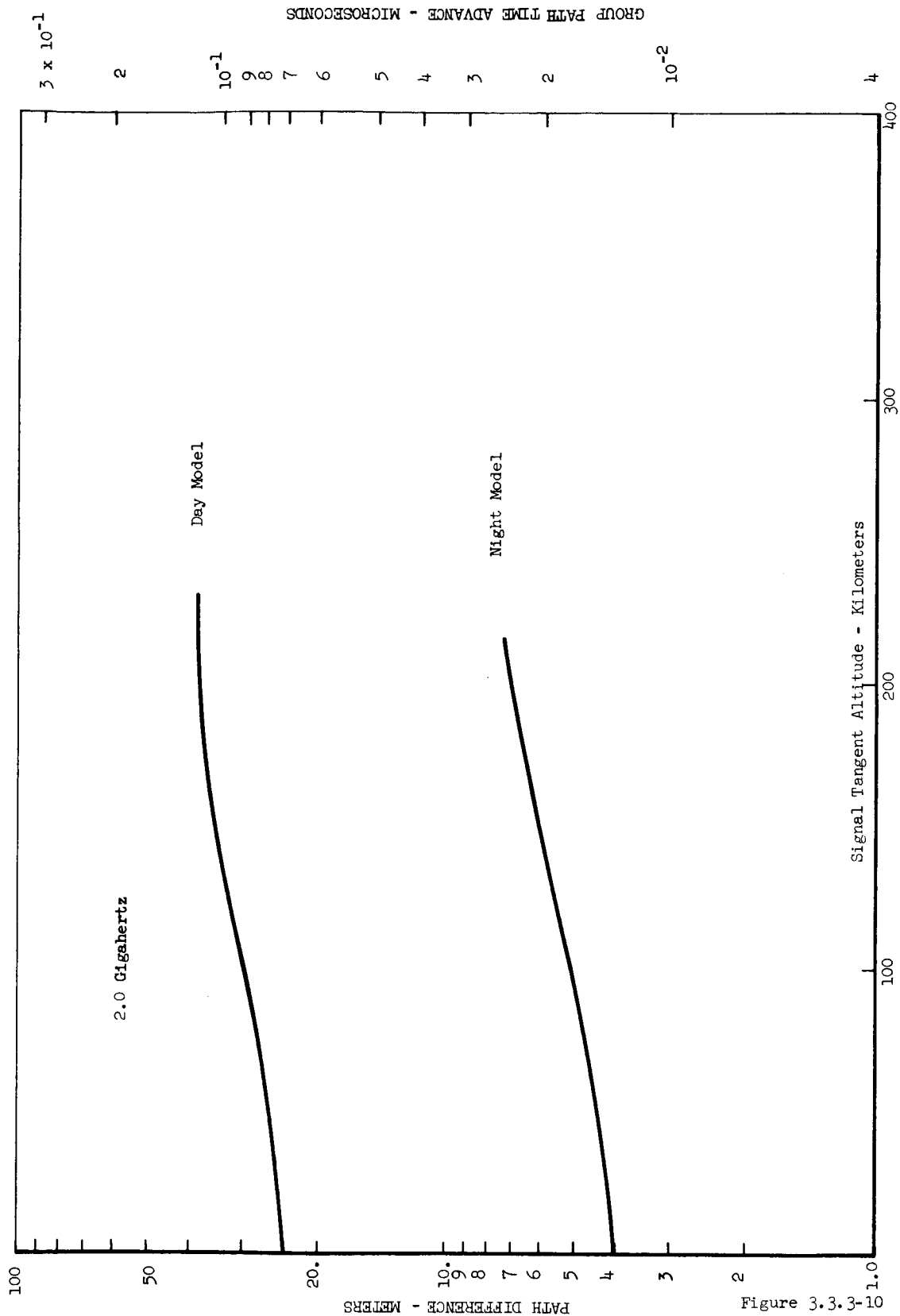
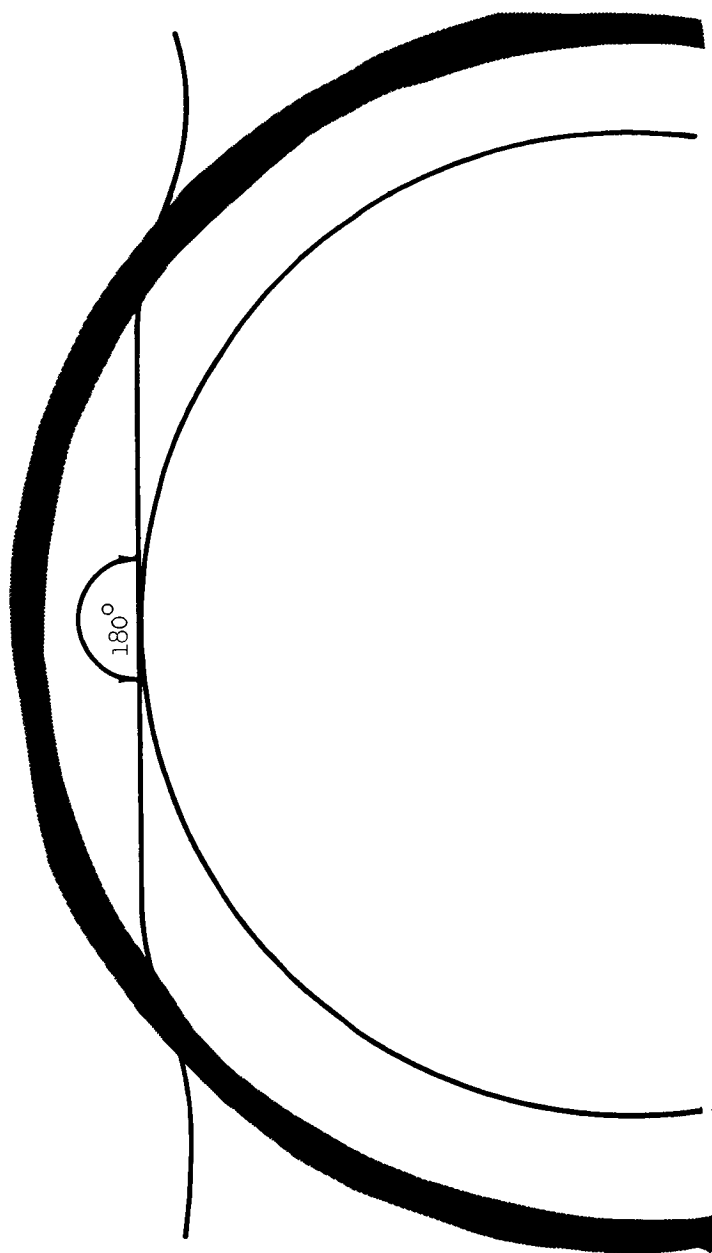


Figure 3.3.3-10. Signal Tangent Altitude - Kilometers

Figure 3.3.3-11. Wave Passing Through Atmosphere



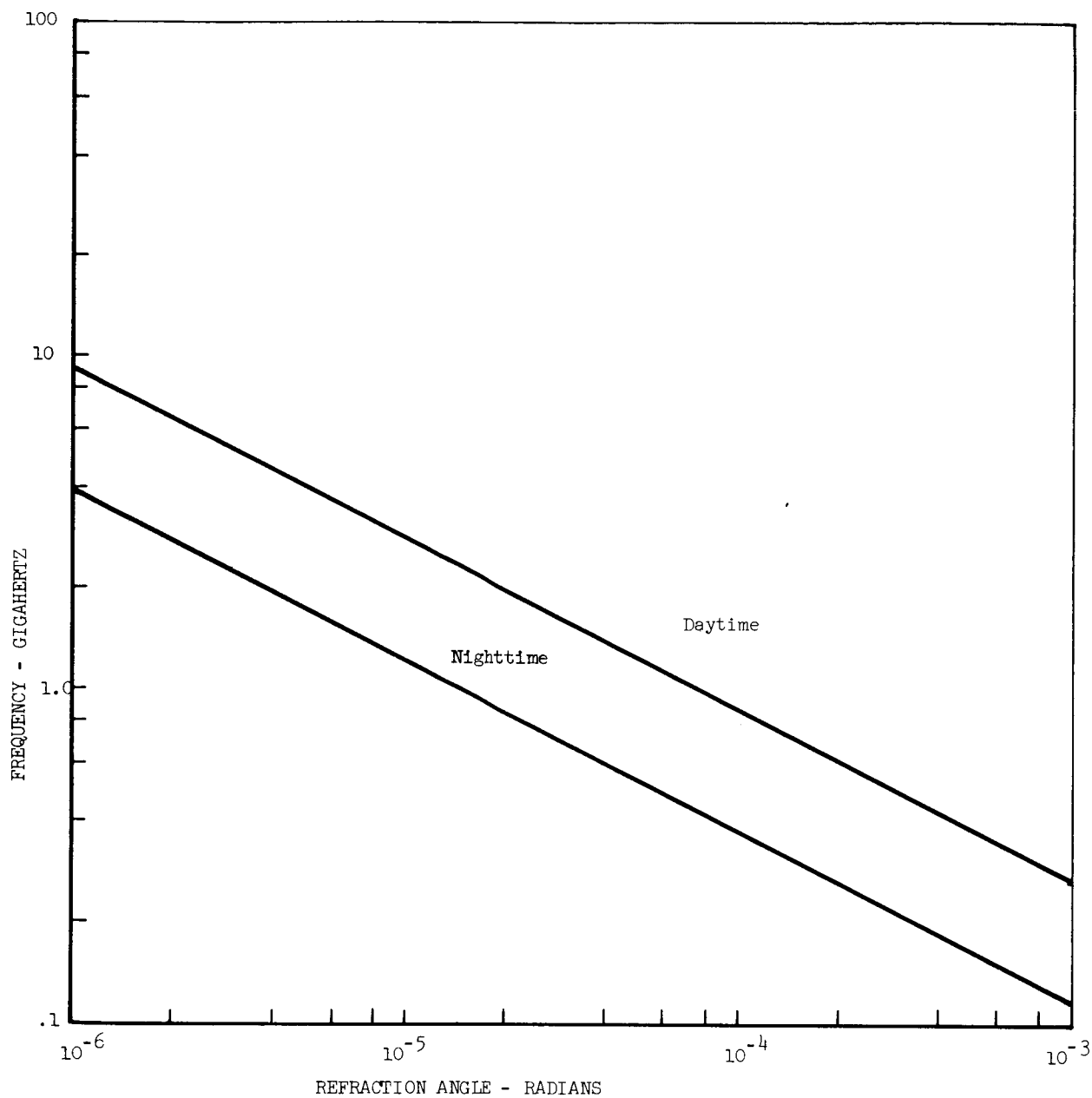


Figure 3.3.3-12. Frequency vs Refraction Angle

4.0 SATELLITE DISCIPLINE PARAMETRIC REQUIREMENTS AND DESIGN INTERFACE
CONSIDERATIONS

4.1 COMMUNICATIONS

4.1.1 SATELLITE RECEIVER

System sensitivity is described by the system noise temperature which includes background noise, side lobe noise, coupling loss noise and receiver noise. The magnitude of the receiver noise contribution for a DSMCS is reviewed here along with estimates of the size and weight of the various receiver types. Direct detectors show some promise for broadband applications such as radio astronomy in the 10 to 100 gigahertz band but are not comparable to either the parametric amplifier or the maser amplifier followed by a detector in terms of noise temperature. These detectors which include crystal receivers and bolometers of the cooled and uncooled variety perform well in radio astronomy applications because their relatively high noise temperature is compensated by their broad radio frequency bandwidth and their simplicity of operation. Similarly, tunnel diodes and traveling wave tube amplifiers exhibit low differential temperature sensitivity but their effective noise temperatures are much greater than either the parametric or the maser amplifier.

Besides a low noise temperature requirement, DSMCS receivers must be capable of remote operation thus demanding a relatively simple system of high reliability. A low noise pre-detection amplifier must provide at least 30 decibels gain so that succeeding stages do not add appreciably to receiver noise.

Of the two candidate DSMCS low noise amplifiers, the parametric amplifier is in wider use because it is a small and relatively inexpensive piece of hardware and more significantly, it can be operated at room temperatures. Figure 4.1.1-1 includes the receiver noise temperature of some of the operational parametric amplifiers at 300° Kelvin and a few below that. The cooled parametric amplifier symbols are underlined. The symbols used are referenced to the source of information at the end of the bibliography. Also shown in the figure is the parametric amplifier theoretical minimum noise temperature at 300° Kelvin, 77° Kelvin and 4° Kelvin⁽¹⁾. The theoretical noise temperature calculations were based on assumed dynamic quality factors of 20, 16, 12, 8, and 6 at 1, 2, 4, 6, 8 gigahertz and were then extrapolated above 10 gigahertz.¹ The operational noise temperatures shown include the plumbing loss to the parametric amplifier and the

calibration hardware loss. With a few exceptions, parametric amplifiers have generally been designed to operate in the region below 10 gigahertz. This can be attributed to the undesired reactances in the diode as well as those in the parametric amplifier structure above 10 gigahertz. Diode dynamic quality factors in this range have been improving steadily. Development in this direction is evidenced by the annular GaAs varactor which is expected to provide a 300°K noise temperature amplifier at room temperature. Further, only recently techniques have been implemented which use pump frequencies below the signal frequencies.^(2,3)

From the curves shown in Figure 4.1.1-1, it is clear that cooling is mandatory for DSMCS applications above 4 gigahertz if an environment limited system is to be achieved with available diodes. Parametric amplifier specialists indicate that with comparable cooling, the parametric amplifier will out-perform the maser⁽⁴⁾. An operational 50 gigahertz cooled parametric amplifier appears quite probable within a few years⁽⁵⁾. The future improvements in the parametric amplifier diodes and structures is not as clear above 20 gigahertz that it can be predicted with confidence that an environmental limited system is possible. Below this frequency, however, 20° Kelvin noise temperatures are quite probable. A parametric amplifier at the low noise temperatures would be preferred to a maser amplifier. The parametric amplifier does not require high magnetic fields as the maser, it can be tuned, with some difficulty, and is much less susceptible to saturation⁽⁴⁾. In addition, the parametric amplifier noise temperature is not as sensitive to the bath thermometric temperature. Maser gain decreases rapidly as the maser material thermometric temperature increases above 4.2° Kelvin⁽⁶⁾. Parametric amplifier liabilities include a strong sensitivity to pump source and circuit variations. Methods are being developed to stabilize this variation so that these amplifiers may be used in radiometry where gain stability is critical.⁽⁴⁾

Unlike the parametric amplifier, the maser amplifier cannot operate at 300° Kelvin ambient but must be immersed in cryogenic liquids. The particular thermometric temperature at which adequate gain is achieved is dependent on the magnetic field, host material, doping concentration, and pump frequency. In general, present masers are immersed in fluids 4.2° Kelvin or colder as was the

case for all the masers noted in Figure 4.1.1-1. The high density of maser amplifiers below 10 gigahertz can be attributed to the fact that the host material until recently was ruby with a zero-field splitting frequency of 11.4 gigahertz. Materials research is continuing in the search for host materials in which maser amplification can be achieved at higher frequencies and with reasonable magnetic field requirements. A notable result of this research is represented by the symbol M8 on the plot. The system has already been packaged for operational use. The results of this maser program demonstrate two points. First, following the discovery of a host material with the appropriate characteristics for high frequency operations, the maser and peripheral apparatus necessary for a successful operation are substantially the same in content, size, and weight as that of lower frequency systems. Secondly, pump frequencies near the channel frequency are practical since this maser was operated at 40 gigahertz with a 43 gigahertz pump. With respect to DSMCS applications, the fixed equipment character, size and weight provides a conservative estimate for future higher frequency maser systems. The low pump to signal frequency ratio indicates that higher frequency systems can be developed in the near future with present pump power levels. This low ratio was not possible in the ruby host because of cross-relaxation effects. Maser oscillation has been achieved at 96 gigahertz with only a 65 gigahertz pump⁽⁷⁾. This effort, when published, was far from producing an operational device.

The weight and size of all the existing maser amplifier systems is relatively independent of the signal frequency for comparable operation. Closed cycle systems are usually separated into two groups. The maser amplifier, Dewar, magnet and initial detector are located in a compact package at the focus of the antenna to minimize receiver noise temperature. The cryogenic compressor and high level electronics are at a more convenient location near the antenna. The focus package for operational ground based systems weighs 180 kilograms to 300 kilograms (300 to 500 lbs) and occupies .09 to .17 cubic meters (3 to 5 cubic feet). The compressor for these systems constitutes most of the weight of the ground group, from 420 to 480 kilograms (700 to 800 lbs). The most significant parameter of note is the power consumption of the present cryogenic refrigerators; 3.4 to 6

kilowatts are required to extract a continuous heat load of 1 watt of 4.2° Kelvin. A survey of state-of-the-art refrigerators reviewed in Section 4.4.3 indicates that for space application systems, specific powers of 1000 (watts power input over cooling power at 4.2° K) and specific weights of 22.6 (kilograms weight over watts cooling at 4.2° K). An accurate measure of the reliability of these developmental units is not available yet. Steady-state heat loads run near .5 watts for ground based systems. A DSMCS low noise amplifier heat load is difficult to predict because there is no comparable space system. The reduction in convective loss insulation will be offset by an increase in radiation. An alternative to a refrigeration system would be simply a large Dewar filled with cryogenic fluid which would have to be replenished periodically. In order to provide a half watt steady-state at 4.2° Kelvin for one year, 1,100 kilograms (2500 lbs) of liquid helium must be vaporized. The low density of liquid helium causes the required volume to be 10 cubic meters or a cube 2.16 meters (7.6 feet) on each side. Although a comparison of the closed loop to the open loop system seems to be strongly in favor of the closed, the additional weight costs to power the closed loop system dissolve this advantage at certain altitudes. This will be discussed in the final system tradeoff section.

Research in super conducting magnets is expected to soon provide operational, very high magnetic fields within small volumes. The obvious marriage of super conducting magnetics and maser amplifiers in cryogenic fluids is inevitable. The higher field requirements of masers that will be built above 35 gigahertz can be achieved with the magnets using much less space and weight.

RESUME

A review of the detection and predetection amplifiers in the two to one hundred gigahertz region clearly indicates that either a parametric amplifier or a maser amplifier followed by appropriate detection will out perform any other methods for a DSMCS. Below 10 gigahertz a 300° Kelvin ambient parametric amplifier noise temperature is low in comparison to other uncooled devices in that region, but it is much too high for DSMCS application, as can be seen in Figure

4.1.1-1. In order to reduce receiver noise temperature to the 10 to 20° Kelvin region where a system would be environment limited rather than receiver limited, liquid helium temperature baths are necessary. A nominal one-half watt heat load for a one-year mission can be satisfied by either a closed cycle refrigerator or a refillable Dewar. The weight of the closed cycle refrigerator is much less than the Dewar; however, the weight necessary to provide energy to operate the refrigerator is considerable. The two approaches will be compared in the final system tradeoff section where the energy source weight is considered.

Environment limited DSMCS cooled amplifiers either parametric or maser will undoubtedly be available before ten years pass. This is clear if it is remembered that the first maser amplification occurred only ten years ago⁽⁸⁾. Also the foundations of parametric amplification were made in that time⁽⁹⁾. The 20° Kelvin, 35 gigahertz system noted as M8 of Figure 4.1.1-1 is indicative of the rapid pace of low noise receiver technology. The noise temperature of low noise amplifier systems within the amplifier assembly will undoubtedly be below 20°K up through 100 gigahertz. The remaining receiver noise will be engendered by losses in the apparatus connecting the amplifier to the antenna. These may be reduced by careful design and further cooling of the transmission line.

RECEIVER NOISE BIBLIOGRAPHY

1. K. Kurakawa and M. Vinuhara, "Minimum Noise Figure of the Variable Capacitance Amplifier," Bell Systems Tech. J. Vol. 40, May, 1961.
2. Ginzberg, "Summary Report," Technical Documentary Report, RTD-TDR-64-2 AFSC Wright-Patterson, June, 1964.
3. H. Henning, "New Parametric Amplifiers for K-band and Above," Microwave Journal Vol. VI, No. 10, October, 1963.
4. M. Unohara, and J. Elward, "Parametric Amplifiers for High Sensitivity Receiver," IEEE Trans AP-12, No. 7, December, 1964.
5. Steinrecher, D., MIT, Private Communication
6. W. Higa, "Total System Noise Temperature: 15.0°K ", IEEE Trans. on MTT, MTT-12-No. 6, November, 1964.
7. W. Hughes, "Maser Operations at 96 KMC with a pump at 65 KMC", Proc of IRE, (Correspondence) Vol. 50, No. 7, July, 1962.
8. J. Gordon, et al., Phys. Rev., Vol. 99, 1955.
9. H. Rowe, "Some General Properties of Nonlinear Elements II", Proc of IRE, Vol. 46, 1958.

FIGURE 4.1.1-1 REFERENCES

- P2 University of Manchester, Jodrell Bank
- P3 National Radio Astronomy Observatory, Greenbelt
- P4 Royal Radar Establishment, Worsc. England, J. S. Hey, Nature, Vol. 190, No. 4782, p. 1150; 1961.
- P5 & P7 Mullard Radio Astronomy Observatory, University of Cambridge
- P6 Cornell, Arecibo
- P8 Jet Propulsion Lab, Pasadena, California, W. K. Victor, R. Stevens, and S. W. Golomb, JPL Tech. Report No. 32-132, August, 1961.
- P9 Harvard Radio Astronomy Station, Ft. Davis, Texas.
- P10 University of California, Hat Creek, California.
- P11 Bibliography 4
- P12 Aerospace Corporation, El Segundo, California.
- P13 Bell Telephone Laboratory, Murray Hill.
- P14 Trans of IEEE, MTT-13, No. 1.
- M1 Harvard College Obs., J. V. Jelley and B.F.C. Cooper, Rev. Sci. Inst., Vol. 32, p. 166; 1961; J. V. Jelley, Microwave J. Vol 5, p. 77; February, 1962.
- M2 Royal Radar Establishment, Worsc. England.
- M3 BTL, R. W. de Grasse, D. C. Hogg, E. A. Ohm, and H.E.D. Scovil, J. Appl. Phys., Vol. 30, p. 2013; 1959.
- M4 & M6 NRL, J. A. Giordmaine, L. E. Alsop, C. H. Mayer, and C. H. Townes, "A maser amplifier for radio astronomy at X-band," Proc of IRE, Vol. 47, pp. 1062-1070; June, 1959.; R. Novick, "The Observation of three Centimeter Radiation from Astronomical Objects with a Ruby Maser," Columbia Radiation Lab, N.Y., N.Y., Special Tech. Report, Contract DA-36-039, SC-78330, June 1, 1961.
- M5 University of Michigan, M. E. Bair, J. J. Cook, L. G. Cross, and C. B. Arnold, "Recent developments and observations with a ruby maser radiometer," IRE Trans. on Antennas and propagation, Vol. AP-9, pp. 43-49, January, 1961; J. J. Cook, L. G. Cross, M. E. Bair, and R. W. Terhune, "A low-noise X-band radiometer using maser," Proc of IRE, Vol. 49, pp. 768-778, April, 1961.
- M7 Tech Report JPL No. 32-691.
- M8 Arams and Peytaon, "Traveling-wave maser and radiometer," Proc of IEEE, Vol. 53, No. 1, January, 1965.

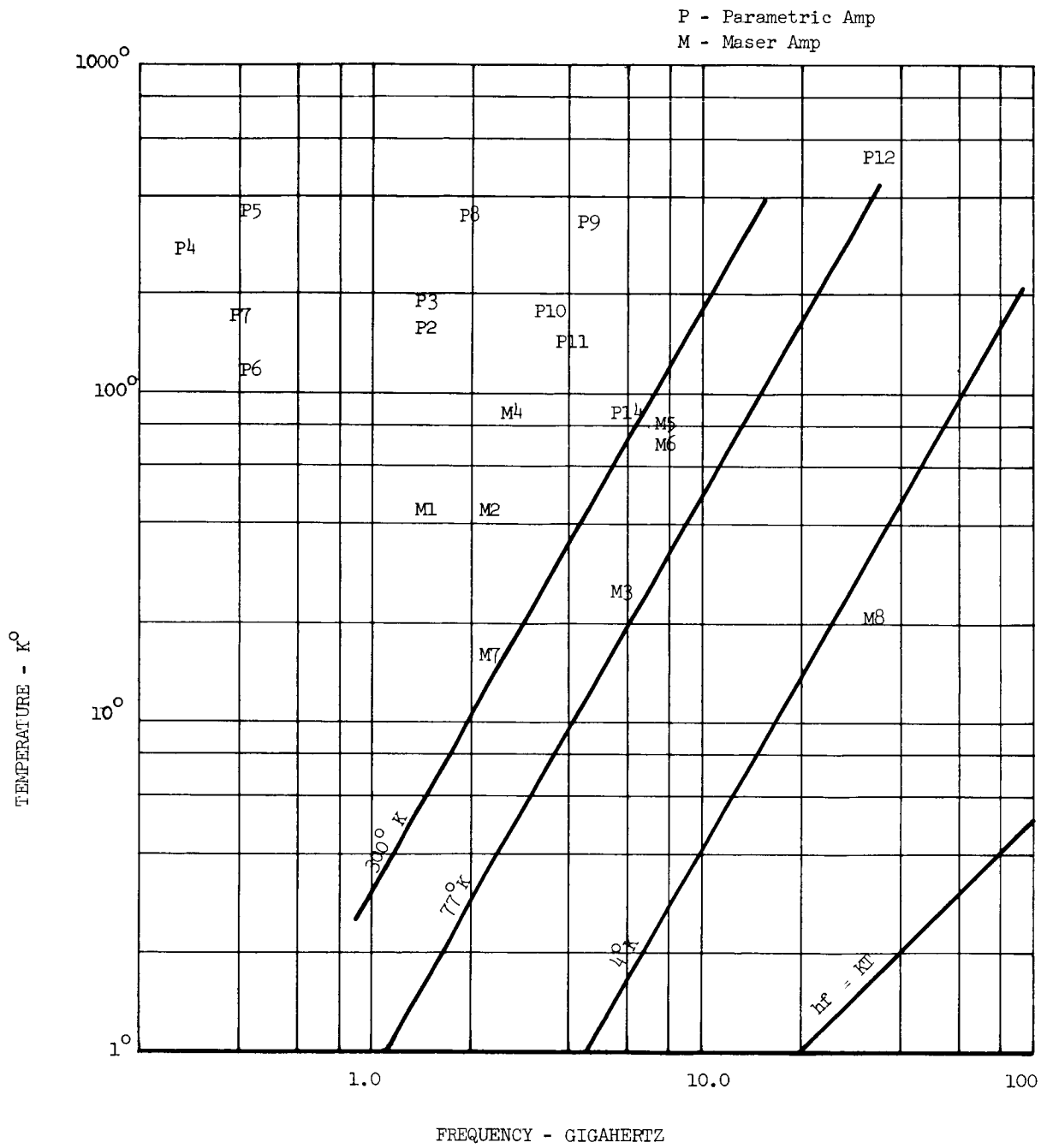


Figure 4.1.1-1. Amplifier Temperature vs Frequency

4.1.2 SATELLITE TRANSMITTER

A survey of the devices available to generate radio-frequency power in the 2 to 100 gigahertz band revealed a large combination of candidate exciters and amplifiers with characteristics of varying applicability to DSMCS. For expediency, the survey does not specifically indicate the references in the open literature, the manufacturer's specification sheets, and the private communications upon which it is based.

The average output power was assumed to be of primary importance. Consideration of the prospective rf power generators is divided into two groups, those below 10 gigahertz and those above. This dichotomy is basically historical in that the depth of effort in rf power design below 10 gigahertz far exceeds that above, due to the long use of this band within the atmospheric window. The survey is further divided into low and high power sections, because of the power limitations of certain power generation mechanisms but also because of the need for an alternate receive only DSMCS. The low power review will be of value in assessing the high-frequency spacecraft transmitter feasibility also. Following a review of each candidate device characteristic and peripheral equipment, selection for each band will be made on the basis of the DSMCS requirements.

Below 10 Gigahertz

Three vacuum tube amplifiers generate power at one watt or greater with reasonable efficiencies below 10 gigahertz, the klystron, the amplatron, and the TWT (traveling wave tube). Variations on these devices, in addition to other devices, could fulfill the exciter requirement. The exciter is not important here since it can be small compared to the amplifier and would be mated to the amplifier so that no significant addition in equipment is necessary. Also worthy of consideration is a solid-state multiplier chain. In this case the exciter would be significant both in size and weight.

The klystron amplifier is the oldest of the vacuum tube amplifiers reviewed. As in all the amplifiers considered, the gain should be 30 decibels or greater, and the reliability should be approximately 20,000 hours or greater for DSMCS consideration. The large MTBF is mandatory in order that the total system including the refrigerator with a present 9000 hours MTBF

approach one year. The average power handling capability of the operational klystron is approaching one megawatt. Its power limit has not been approached because in this linear beam amplifier only rf currents flow in the rf structure. The large power dissipation occurs at the collector which can be removed from the rf structure. Overall efficiency runs from 20 to 60 percent, the high values being at 1 kilowatt or greater. Collector depression also enhances efficiency. Simple klystrons provide .1 to .3 percent bandwidth. This is not too serious a constraint for most deep space channel rates. Because of their long development, klystrons have been designed to operate up to 15,000 hours. The frequency stability and phase linearity of the klystron are excellent.

The primary asset of the amplitron is its high efficiency. This is attributable to the direct conversion of potential energy to rf energy without the conversion to kinetic energy as in linear beam devices such as the klystron and the TWT. The amplitron is essentially a magnetron where the electron stream interacts with a backward wave non re-entrant rf structure and which includes an input port for control of the wave. The total efficiency normally runs between 40 and 55 percent, but can exceed 80 percent in a single high power (3 megawatt peak) tube. Amplitron continuous power levels are approaching 1 megawatt and thus power capability does not constitute a limit here. The gain at these levels, however, are near 10 decibels and therefore the overall efficiency with cascaded amplifiers is approaching that of a klystron. The amplitron is relatively new and therefore is relatively complex in operation. Heater power must be programmed during the warm-up cycle and some external logic is necessary to recycle the tube if input power is lost. The tube bandwidth normally runs 10 percent of the carrier. With present tubes, the gain does not meet the 30 decibel criteria because of the inherent instability of a bi-directional amplifier. However, these devices are approaching 20 decibels gain and an additional 10 decibels appears quite reasonable in the near future. A key specification of concern with the amplitron is reliability. Insufficient data exists to accurately estimate the life from the tubes recently put into service. Raytheon predicts 10,000 hour MTBF total transmitter reliability based on RADC parts failure rate and actual component part stress. A rough approximation of the reliability can be made from the experience with the similar magnetron. The magnetron at best runs approximately 5,000 hours MTBF

and therefore some doubt exists as to the reliability of the amplitron for DSMCS application.

TWT amplifiers fall between the klystron and the amplitron in terms of engineering experience with the device. Average power limits of 30 kilowatts are more than adequate for DSMCS application. The efficiency of the TWT is generally lower than the klystron and the amplitron, from 15 to 40 percent overall with the higher efficiencies occurring at higher powers. The bandwidth runs 10 to 50 percent and thus is worthy of no further consideration. The stability and support equipment specifications of the TWT also fall between the klystron and amplitron requirements. The stability difficulties of the TWT are steadily being reduced. The phase linearity per gain increment is comparable to the klystron. TWT reliability is undoubtedly the best in the vacuum tube amplifier class; 30,000 hours have been demonstrated and 80,000 hours have been predicted for low power tubes.

Solid-state power generation can be accomplished by straight amplification up to approximately 2 gigahertz and by mixing methods to higher frequencies. Transistor technology permits efficient amplification in the 100 to 500 megahertz range for low power levels and steadily decreasing efficiency at higher powers. Appreciable power can be achieved by mixing methods in the 1 to 10 gigahertz range. Through a combination of doublers and triplers, up to 10 watts of power is expected. The optimum mixing levels for efficient doubling or tripling, or whatever harmonic is desired, is a function of the drive level. By selection of the appropriate varactor, an efficiency versus frequency may be achieved as shown in Figure 4.1.2-1. A .01 watt 350 megahertz exciter level with 18 watts drive into the mixer chain was assumed for the figure. When a solid-state transmitter must be modulated, the up converter at the final stage may be used to place the information on the carrier. Bandwidth of .1 to .2 percent are generally achieved with an up converter, although an order of magnitude increase in bandwidth can be achieved at the expense of some decrease in efficiency. The reliability of semiconductor circuitry is exceptionally good. MTBF of 30,000 hours are very probable for DSMCS if sufficient shielding is provided to preclude radiation deterioration.

Low Power

The selection of the best low level power source for DSMCS is contingent on many of the parameters already mentioned in addition to the physical parameters not considered yet, such as weight, temperature, and sensitivity to g loading at liftoff. The significance of the transmitter weight for the DSMCS must be examined in relation to the total satellite weight. Total satellite weight ranges from 3,000 kg (6600#) to 7000 kg (15,400#). A 1.0 kilowatt transmitter would weigh only 25 kg (55#) plus heat dissipation apparatus. Thus, transmitter weight is a small fraction of the total. Further, since the primary function of the DSMCS is reception, there is no significant weight with which the transmitter weight may be traded. At low power levels any of the vacuum tube amplifiers or solid-state sources could satisfy DSMCS electrical performance criteria. The TWT, klystron and solid-state amplifiers of the present technology level exhibit reliability levels sufficient for DSMCS application. At low powers, however, the TWT exhibits a clearly better reliability than the klystron. Present solid-state transmitters are generally below 10 watts at 2 gigahertz and steadily decrease to approximately 1 watt at 10 gigahertz. A comparatively high sensitivity to temperature excursions could increase the complexity of solid-state thermal design but not preclude its use in the DSMCS. Although both the solid-state varactor chain and the TWT are non-linear devices, the solid-state amplifier output harmonic content is a much stronger function of drive level than the TWT. In addition, the TWT is less susceptible to radiation existing at DSMCS altitudes than the solid-state devices for the same level of shielding. Considering the present need of DSMCS, it appears that a solid-state varactor chain with a final stage up converter is most suitable up to about 5 watts and a TWT amplifier through 100 watts. The general preference for the TWT is verified by the success of the Hughes Aircraft TWT's on Mariner IV, EARLYBIRD, and SYNCOM II and III.

High Power

Above 100 watts the TWT and the klystron are the only amplifiers with reliability necessary for DSMCS. At this level the klystron verified reliability generally exceeds the TWT. Most of the ultra reliable TWT systems fall below 50 watts. Klystrons have demonstrated MTBF of 5000 hours and in some tubes have exceeded 15,000 hours above 100 watts. Above 100 watts

the weight of the source of power which runs from .5 to 1 kg per electrical watt far exceeds the transmitter weight where 5 watts out per kg is typical for ground systems. The klystron is generally simpler to operate and can generate a wide range of output levels in contrast to the TWT. Thus, the klystron amplifier appears to be most suitable for a high-powered DSMCS transmitter, although more operating experience at high power with the TWT may show its reliability to be comparable to the klystron.

Above 10 Gigahertz

In the interim region between 10 gigahertz and the millimeter band (30 gigahertz to 300 gigahertz) rf exciter and amplifiers differ very little from those below 10 gigahertz. The number of devices in this region is comparatively low because the water absorption line generally reduces the system advantages that might be achieved by raising system frequency for ground-to-ground systems. In this interim region, the designs are generally scaled-down versions of below 10 gigahertz devices. As a design scales down the mechanical tolerances and heat dissipation capacity of the elements diminish. At approximately 30 gigahertz, the tolerances and maximum power capacity are reduced to the point that the usual manufacturing and design methods cannot be utilized. It is this region above 30 gigahertz that this section is devoted. In this region, high power is considered to be that above 10 watts rather than 100 watts and will be used accordingly.

Low Power

There are numerous methods of generating milliwatt rf power levels at 30 gigahertz. These include diode mixers, tunnel diode amplifiers, maser, oscillators, and Cerenkov radiators. Each of these devices are limited for the foreseeable future to less than one watt. Between one watt and ten watts, the rf power is derived from klystron and TWT amplifiers and O-type BWO (Backward Wave Oscillator). These designs are modifications of lower frequency devices in order that reasonable power outputs can be achieved. The heat generating collectors on these devices can be relatively easily moved away from the rf structure. The intimate relation of the dc and rf fields in the crossed field device precludes moving the heat generating anode from the confined interaction area. The traveling wave tube helix has caused some difficulty in

the millimeter range but has been replaced by stronger structures intended to slow the wave down. All the linear beam devices, klystron, TWT and BWO (a single port TWT) are fairly new to this frequency range and so little has been established regarding reliability. Their characteristics are about the same as their low-frequency counterparts, with the exception of generally lower efficiency. Traveling wave tube designers have predicted that reliability in this range will be as good as the low power below 10 gigahertz devices within a few years. Any of the linear beam devices are adequate for DSMCS application if a reasonable reliability can be achieved.

High Power

Above 10 watts, tube design is experimental or at best, developmental. Liquid cooled fixed frequency klystrons have been recently introduced on the market in the 10 to 100 watt range. Above 100 watts, two experimental developments show promise for large powers in the near future. Hughes Research Laboratory has developed a traveling wave tube using coupled cavity slow wave structures which produces 6 kilowatts average power at 55 gigahertz and is expected to generate 1 kilowatt at 100 gigahertz. The overall efficiency using depressed collectors is 25 percent. A 3000 hour life test was successful in the amplifier configuration and an 8500 hour test was successful in the oscillator mode. TWT reliability equivalent to those below 10 gigahertz are considered quite possible by the designer. Another high power tube of recent success is the Ubitron, designed at General Electric. Peak powers of 100 kilowatts at 50 gigahertz have been obtained with expectation of 15 kilowatts average power. The Hughes design alone represents verification that high power can be achieved in the 30 to 100 gigahertz region with high efficiency.

Conclusion

The total transmitter weight is small compared with the total satellite weight, and therefore weight does not represent a basis for selection. Below 10 gigahertz several devices can provide the electrical characteristics as necessary for DSMCS. The selection criteria was reliability.

Below 10 watts the solid-state exciter and mixer is preferable. Between 10 and 100 watts, the TWT demonstrated reliability is best. Above 100 watts, only the klystron reliability has been verified and thus is preferred. Above 30 gigahertz little data are available to judge the reliability of the devices since the designs are relatively new. Below 10 watts, linear beam devices such as TWT's, klystrons, and BWO's appear most suitable for DSMCS application. Above 10 watts the designs are generally experimental. However, the laboratory results indicate that kilowatt power levels are possible at high efficiencies at 30 gigahertz or greater. Designers feel that both the high power and low power millimeter tubes could be designed to be as reliable as the amplifiers below 10 gigahertz within a few years. Figure 4.1.2-2 represents a realistic estimate of total TWT conversion efficiency above 100 watts. A deep space spacecraft transmitter will be at this level by the DSMCS operational era.

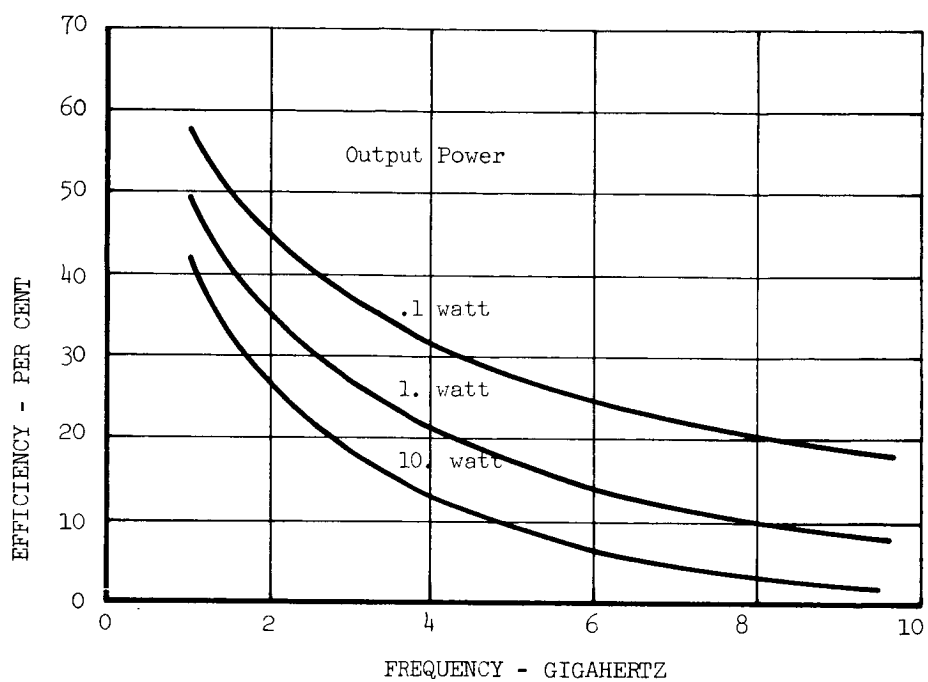


Figure 4.1.2-1. Output Power Efficiency vs Frequency

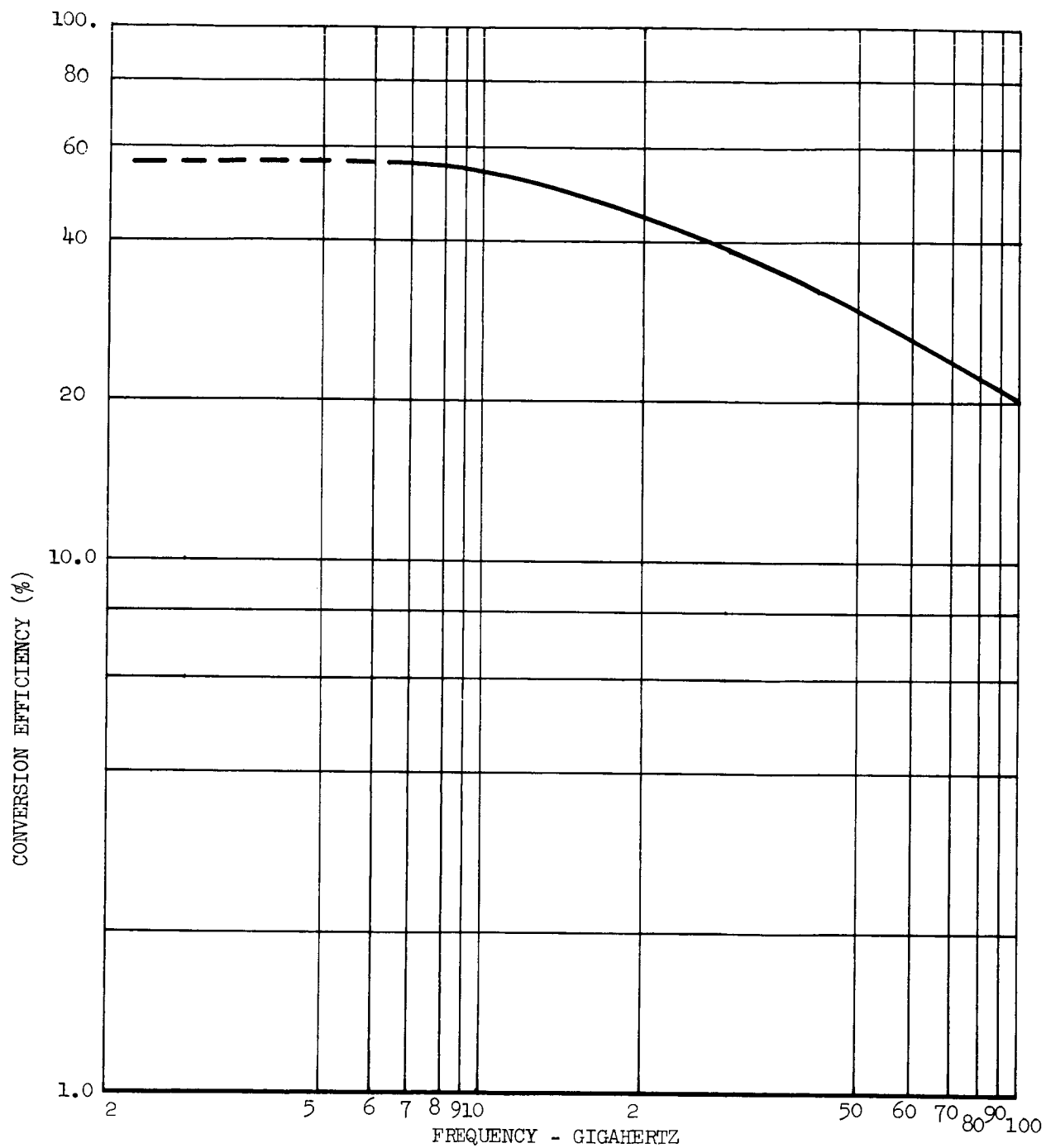


Figure 4.1.2-2. Conversion Efficiency vs Frequency

4.1.3 ANTENNA ELECTRICAL DESIGN REQUIREMENTS

Introduction

The primary result of the antenna design effort established a functional relationship between the available antenna gain and system operating frequency for a family of available antenna weights. It is the intent of this section to completely relate the antenna electrical characteristics to the mechanical tolerances. The objective of the antenna subsystem is to coherently add the signal energy of a plane wave over as large an aperture as possible. The noise induced by antenna loss must be as small as practical and at worst near that due to the receiver. Similarly, the sidelobes should be sufficiently low that the earth radiation noise is lower than the receiver noise. A variety of large aperture antennas are examined in this section in order to determine their capability to meet these objectives. The gross features of the candidate antenna types were examined initially to determine whether or not further study was warranted. The effect of surface deviations in a passive reflector was examined along with consideration of feed position tolerances. Following a review of the necessary electro-mechanical analytical relations, they will be applied to the remaining candidate antenna types in order to determine their relative and absolute performance for the generation of the gain and frequency vs weight data for the system trade-off study.

4.1.3.1 Antenna Types

Six distinct types of antennas have been suggested for consideration, Prime Focus Paraboloid, Cassegrainian Paraboloid, Multipole Parabolic, Spherical Reflector, Fresnel Reflector and Planar Array. The unique characteristics of two of the antenna types and how they effect system performance will be considered first. These two are the planar array and the array of parabolic dishes. The critical parameter of a planar array in a DSMCS application is the antenna system insertion loss. The system noise temperature which effects channel capacity increases by about 7°K for every .1 decibel insertion

loss increase when it is at a thermometric temperature near 300°K . The received plane wave may be coupled to a low noise receiver one of two ways. Either the wave may be received by an array of slots one-half wavelength apart and combined in a fixed waveguide network or a planar array of controllable time delay elements could focus the wave onto a feed point. In either case, it can be assumed that the preamplification and detection occurs after the energy has been collected since the number of separate low noise systems and support apparatus for a many wave aperture is prohibitive as is the noise temperature of a preamplifier that is not cooled to cryogenic temperatures. Antenna apertures for DSMCS consideration, by necessity, is greater than 500 wavelengths across. The loss experienced by a signal traveling through 500 wavelengths of TE_{01} standard waveguide ranges from 2 to 6 decibels for the frequency range of 2 to 25 GHz. Although the 7°K increase for each .1 db loss increase approximation is not precise at these loss levels, the noise contribution is clearly excessive and prevents their use. Oversize wave guide could half the loss but this is not sufficient. Another factor which suggests that large slotted arrays not be used is the extreme difficulty in machining arrays composed of thousands of slots. The slot position tolerances preclude implementing the rigidized, though less stiff, foam array above approximately 10 GHz.

The waveguide insertion loss penalty of a planar array could be avoided with a flat array which is illuminated via free space by feeding it at a distance from the array. The position of the feed relative to the array would be controlled by adjustable struts. The necessary time delay character of this lens can be achieved by active phase shifters or some passive delay method. The control complexity and the insertion loss of an active system for DSMCS application are also prohibited. Passive methods such as variable waveguide lengths for rods have not been built with apertures greater than 100 wavelengths because of the excessive machining tolerances. Earth radiation contributions to the system noise in a passive lens could be appreciable due to the strong scattering of the wave entering the lens. No further consideration of this type of antenna system are planned, primarily because it did not exhibit any particular superiority over single parabolic reflectors in an array and it is much more difficult to build.

Another antenna type considered was an array of parabolic reflectors. The optimum number of antenna elements in such an array is a compromise between the weight and difficulty of implementing many receivers and the improvement in channel performance due to such an increase. Three or four elemental apertures appear to be the most appropriate number considering general DSMCS requirements as well as the limited experience gained through adaptive arrays on the ground. The phase-lock loop at each array element can compensate for phase path difference to each feed from a plane wave but only if the spacecraft is in the beam of the elemental reflector. The spacecraft is maintained in the beam of each element of the array if the angle between the plane of each element is kept below $1/10$ the beamwidth of the elemental array under all expected loading conditions. The effect of thermal and inertial loading on the angle has been examined for mechanical structures established by other requirements. An extreme thermal loading condition would be a 60°K temperature differential across the support structure. This condition would produce an angular difference between adjacent parabolic elements of $.003^{\circ}$. An inertial load of $.8\text{ g's}$, which is far in excess of the expected ACS loads, was necessary to produce this same angular difference. Since this angle error combined with an uncorrelated $.0026^{\circ}$ standard deviation of erection tolerances is more than a factor of 10 below the $.04^{\circ}$ minimum beamwidth, further study of an array of paraboloids up to the $.04^{\circ}$ beamwidth was warranted. The characteristics of each elemental paraboloid are identical to those of the large single paraboloid. The relative merits of one or an array of paraboloids and other passive reflectors including the Cassegrainian, spherical and stepped paraboloids (Fresnel) will be discussed following a presentation of the general theory relating the electrical to the mechanical characteristics in a passive reflector system.

4.1.3.2 Mechanical to Electrical Relationships

The deviation from the desired antenna pattern due to mechanical distortions of a reflector can be separated into two classes, systematic and random. The systematic error is that deviation in a pattern from the ideal that can be calculated precisely for given mechanical errors. The random error is a statistical measure of the probable difference between

the actual pattern and the intended pattern induced by random mechanical deviations. The effect of the random error will be reviewed first followed by the systematic errors. For both types of error the computation of the exact pattern involves solving the integral of (1) and (2) for the antenna current distributions.¹

$$\vec{E}_\theta (\theta, \varphi) = \frac{-j\omega \mu}{4\pi R} \int_{V_{01}} \vec{J} \cdot \vec{i}_\theta \exp (jk \vec{\rho} \cdot \vec{R}) dv \quad (1)$$

$$\vec{E}_\varphi (\theta, \varphi) = \frac{j\omega \mu}{4\pi R} \int_{V_{01}} \vec{J} \cdot \vec{i}_\varphi \exp (jk \vec{\rho} \cdot \vec{R}) dv \quad (2)$$

The coordinate system for these far field approximations is shown in Figure 4.1.3-1. \vec{R} is the unit vector in the direction of observation and ρ is the source position vector. For a few simple current distributions the field can be determined but for most real antennas, the integration is a very tedious computation. The integration has been mechanized for the general case on other antenna studies on both an analog and digital computer and it is still quite tedious. The integrations for an arbitrary current distribution in the case of the digital computer is implemented by breaking the current distributions into small apertures over which the phase deviation is small, and summing. The computation required for the 500 wavelength and greater diameter antennas considered for DSMCS is large. The computation is particularly difficult for the random error case since many patterns would have to be computed to build up the necessary statistical moment accuracy of the ensemble pattern.

In order to facilitate the computation of antenna pattern distribution due to random errors, the statistical analysis of Ruze will be considered here.² This work was primarily intended for pattern errors induced in parabolic reflectors. The analysis not only avoids the tedious computation of patterns but also provides a description of the distribution of the antenna characteristics. In order to make the analysis tractable, however, a number of assumptions were required in the analysis. Their applicability to DSMCS antennas is of primary concern. There are four assumptions for the continuous aperture analysis.

- (I) The errors are uniformly distributed over the aperture. Thus, if the usual convention for computing root mean squared phase error by doubling the deviation of the reflector from a desired paraboloid is used, the result will be conservative. The validity of this assumption is a strong function of the reflector F/D (focal length to diameter ratio), the assumption being more valid at the large F/D ratios.
- (II) The local deviations from the desired surface are independent. The validity of this assumption is strongly dependent on the separation of the forcing function causing the anomaly. Also, the number of independent forcing functions such as manufacturing tolerances, deployment tolerances, thermal loads and inertial loads, effect the dependence of localized distortions over a single reflector.
- (III) The deviation of the true reflector surface from the desired is gaussian distributed and the correlation function of the phase error over the surface is of the form (3)

$$y^2(\tau) = 2 \overline{\delta^2} \left[1 - \exp(-\tau/c_1)^2 \right] \quad (3)$$

Where $y(\tau)$ is the phase difference between two points separated by τ

$\overline{\delta^2}$ is the mean square phase deviation of all points.
 c_1 is the correlation interval.

The gaussian approximation will usually be valid for any antenna which is distorted by many comparable loads due to the central limit theorem. By the same theorem, it can be shown that the correlation function does represent the autocorrelation function of the actual dish regardless of the indentation shape if the number of indentions or deviations is large.²

- (IV) The current distribution changes very little over a correlation interval.

The increase in sidelobe level due to the reflector deviations is described by the normalized antenna average pattern (4).

$$\overline{P(\theta)} = P_o(\theta) + \frac{4 c_1^2 \pi^2 \delta^2}{\lambda^2 G_o} \left[\sum_{N=1}^{\infty} \frac{[\overline{\delta^2}]^N}{N! N} \exp \left(\frac{-\pi^2 c_1^2 \sin^2 \theta}{N \lambda^2} \right) \right] \quad (4)$$

where $P_o(\theta)$ represents the pattern of an undistorted paraboloid.

$\overline{\delta^2}$ represents the phase front deviations $\overline{\delta^2} = 4 \left(\frac{2\pi}{\lambda} \right)^2 \overline{d^2}$

($\overline{d^2}$ represents the reflector distortion)

G_o is the undistorted reflector antenna gain

If $c_1 \approx \lambda$ and $[\overline{\delta^2}] < \frac{\pi}{4}$ (4) can be approximated within 1 decibel by (5).

$$\overline{P(\theta)} = P_o(\theta) + \frac{4 c_1^2 \pi^2 \overline{\delta^2}}{\lambda^2 G_o} \exp \left[\frac{-\pi^2 \sin^2 \theta}{\lambda^2} c_1^2 \right] \quad (5)$$

It is clear that the correlation interval is critical for sidelobe control. The larger correlation region has the effect of directing the sidelobe power due to distortions along the boresight axis. Also, the increase in sidelobe level with frequency is to the fourth power. If the correlation region is small ($c_1 < \lambda$) distortion induced sidelobe levels are independent of the pattern angle.

Equation (5) has been plotted with an 800 wavelength diameter aperture for three different reflector tolerances in Figure 4.1.3-2. Also, Figure 4.1.3-3 shows the average sidelobe for a family of aperture diameters as a function of the reflector error. Because the distortion induced sidelobes are inversely proportional to gain, the average sidelobe relative to an isotropic antenna is constant. Thus, the antenna noise power received through the sidelobes is relatively fixed over the range of aperture diameters.

The degradation in the average antenna gain due to reflector distortions is described by (6)

$$\frac{G_o}{G} = 1 + \sum_{N=1}^{\infty} \frac{(\overline{\delta^2})^N}{2^N N!} \left\{ 2 - \exp \left(- \frac{c_1^2 \pi^2}{N \lambda^2} \right) - \frac{N \lambda^2}{c_1^2 \pi^2} \left[1 - \exp \left(\frac{c_1^2 \pi^2}{N \lambda^2} \right) \right] \right\} \quad (6)$$

For $c_1 \ll \lambda$ this reduces to (7)

$$\frac{G}{G_o} = 1 - \frac{3 \pi^2 c_1^2 \overline{\delta^2}}{4 \lambda^2} \quad (7)$$

And for the more probable situation for DSMCS of $c_1 \gg \lambda$.

$$\frac{G}{G_o} = \exp (- \overline{\delta^2}) \quad (8)$$

This is plotted in Figure 4.1.3-4 along with intermediate values of c_1 . The analysis of Ruze further shows that the gain of a group of antennas all exhibiting the same reflector distortion statistics are distributed in a gaussian manner with the average gain reduction indicated by (6) and the second moment by (9).

$$\sigma^2 = \frac{4 c_1^2 \pi^2 \overline{\delta^2}}{\lambda^2 G_o} \quad (9)$$

This is plotted for three correlation intervals with a nominal gain of 66 decibels (4×10^6) in Figure 4.1.3-5. The spread of the distribution is clearly small even if the correlation intervals are large when the gain is high.

The accuracy of the Ruze analysis is substantiated by its wide acceptance. Many antenna designs have verified the results since Ruze made the first verification with a .76 meters (30 inches) parabolic reflector at X-band in 1952. Even in large reflectors (> 15 meters) where the assumptions two or three are not strictly valid, the gain and sidelobe relations derived by Ruze are found to accurately predict the antenna characteristics.

The reduction in the antenna gain due to surface distortions is described by (8) for most of the antennas under consideration for DSMCS. The gain of the perfect reflector with a feed accurately positioned is described by (10).

$$G_o = K_1 \left(\frac{\pi D}{\lambda} \right)^2 \quad (10)$$

where K_1 is a constant which depends on the aperture illumination, therefore,

$$G = K_1 \left(\frac{\pi D}{\lambda} \right)^2 \exp(-\overline{\delta^2}) \quad (11)$$

Using

$$\overline{\delta^2} = 4 \left(\frac{2\pi}{\lambda} \right)^2 \overline{d^2}$$

and

$$G = K_1 \left(\frac{\pi D}{\lambda} \right)^2 \exp \left[- \left(\frac{4\pi}{\lambda} \right)^2 \overline{d^2} \right] \quad (12)$$

This function increases with frequency until a maximum occurs which corresponds to the point where the reflector distortions are equal to a fraction of a wavelength and then decreases thereafter. The peak of the function is found by differentiating and setting the result equal to zero followed by a substitution.

$$G_{\text{Limit}} = \frac{K_1}{4^2} \left(\frac{D}{(\overline{d^2})^{\frac{1}{2}}} \right)^2 \exp[-1] \quad (13)$$

Using a nominal value for K_1 , .60.

$$G_{\text{Limit}} = .014 \left(\frac{D}{(\overline{d^2})^{\frac{1}{2}}} \right)^2 \quad (14)$$

The maximum gain occurs at f_o .

$$f_o = \left(\frac{c}{4\pi (\overline{d^2})^{\frac{1}{2}}} \right) \quad (15)$$

or

$$(\overline{d^2})^{\frac{1}{2}} = \frac{\lambda}{4\pi} = \frac{\lambda}{12.6}$$

let

$$(\overline{d^2})^{\frac{1}{2}} \triangleq d_{\text{rms}}$$

Figure 4.1.3-6 and 4.1.3-7 show the relation of D/d_{rms} to gain at the gain limit and the necessary relation of diameter to frequency to achieve it, respectively.

In the preceding discussion it was assumed that the reflector was illuminated from a point source located precisely at the focus. The effect of a deviation of the radiating source center from the paraboloid focus on the directivity or gain and beam position is considered next. The deviation of the source center in the direction normal to the axis will be considered first followed by the more complex axial motion. A linear distortion of the phase (φ) of a plane wave radiation from an aperture tilted by α can be described as in (16).

$$\varphi = K \alpha r \quad (16)$$

where r is the radial distance from the center of the aperture.

$$K = \frac{2\pi}{\lambda}$$

This distortion is accompanied by a change in the boresight axis of the main lobe of the antenna pattern by (17).

$$\theta = \alpha \quad (17)$$

The parabolic reflector phase front distortion due to a small deviation X normal to the paraboloid axis is not linear but is described by (18).

$$\varphi' = \left[K \cos^2 \frac{\Phi}{2} \right] X \frac{r}{F} \quad (18)$$

where F represents the focal length

Φ represents the angle subtended by the dish at the focus.

$$\Phi_0 = 2 \arctan \frac{r}{4F} \quad (19)$$

The deflection is small compared to the focal length.

$$X \ll F$$

$$\frac{X}{F} = \tan \alpha \approx \alpha \quad (20)$$

$$\varphi' \approx K \left[\cos^2 \frac{\Phi}{2} \right] \alpha r \quad (21)$$

Comparing (21) to (16) it is seen that the phase front departs from a single linear function by (22).

$$\cos^2 \frac{\Phi}{2} \quad (22)$$

At the aperture edge r_o ,

$$\phi'_o \approx \left[K \cos^2 \frac{\Phi_o}{2} \right] \propto r_o \quad (23)$$

over the whole aperture

$$\phi_r > \left[K \cos^2 \frac{\Phi_o}{2} \right] \propto r \quad (24)$$

and thus,

$$|\theta'| > \left| \propto \cos^2 \frac{\Phi_o}{2} \right| \quad (25)$$

and therefore the actual main lobe deviation must fall somewhere between the two extremes of (25) and (17).

$$\left| \propto \cos^2 \frac{\Phi_o}{2} \right| < |\theta'| < |\alpha| \quad (26)$$

The beam deviation is shown for both extremes as a function of F/D Figure 4.1.3-8. From the normalized plot it is clear that at low F/D the beam deviation can be estimated to a reasonable accuracy by selecting the center of the range. The loss in gain or directivity at gain maximum due to this motion is negligible for the small beam deviations shown in Figure 4.1.3-8.

Motion of the feed along the paraboloid axis is more probable than normal to it with some of the symmetrical support structures considered for DSMCS. The quadratic error induced by motion of the feed phase center along the axis is equivalent to the errors which occur in the near field region of any aperture. The directivity or gain and beamwidth changes in the near field are normally described by the parameter γ . For a taper circular aperture γ is described by (23)³.

$$\frac{1}{\gamma} = \frac{16 \Delta}{\pi} \left[1 - \frac{16 \Delta}{\pi} \sin \frac{\pi}{8 \Delta} + \frac{128 \Delta^2}{\pi^2} (1 - \cos \frac{\pi}{8 \Delta}) \right]^{\frac{1}{2}} \quad (27)$$

where

$$\frac{1}{\Delta} = \frac{2 D^2 / \lambda}{R}$$

The beamwidth of the antenna increases by γ and the gain reduces by $1/\gamma^2$. These results for the Fresnel region are converted to equivalent axial movement through the edge phase error of the focused antenna compared to the edge error of an improperly located feed. Figure 4.1.3-9 shows $1/\gamma^2$ for a normalized feed displacement. For purely symmetrical distortion the boresight does not move.

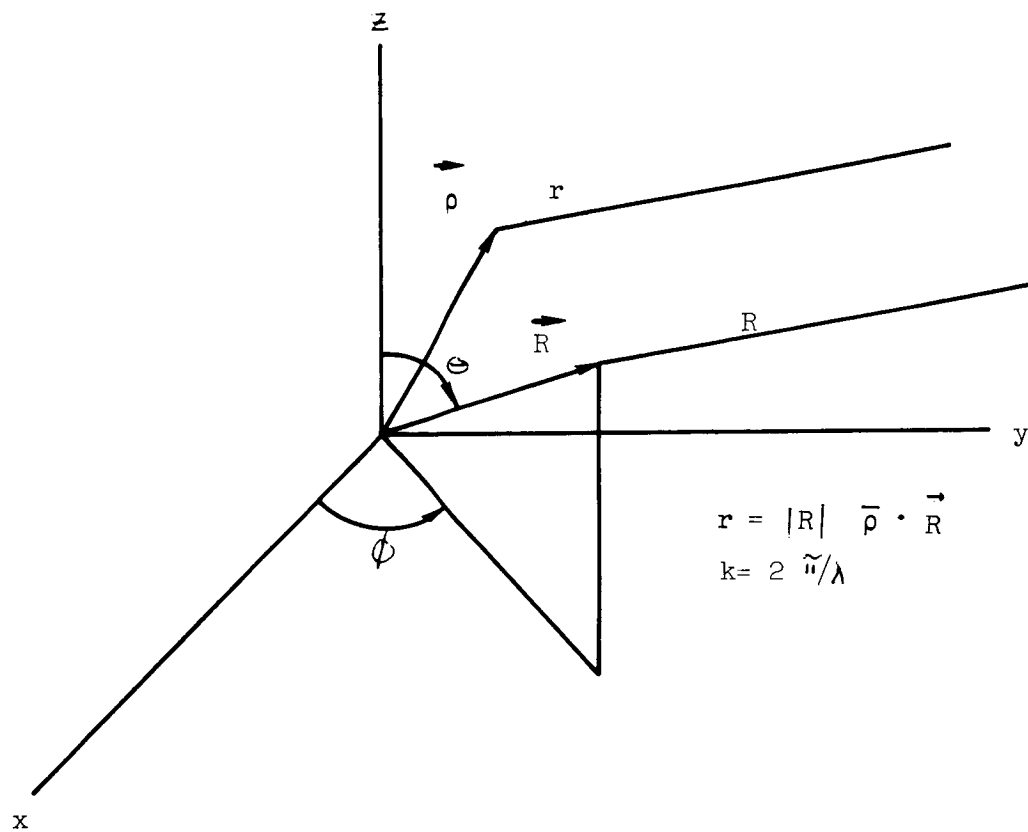


Figure 4.1.3-1. Reflector Distortion Due to Thermal Loads

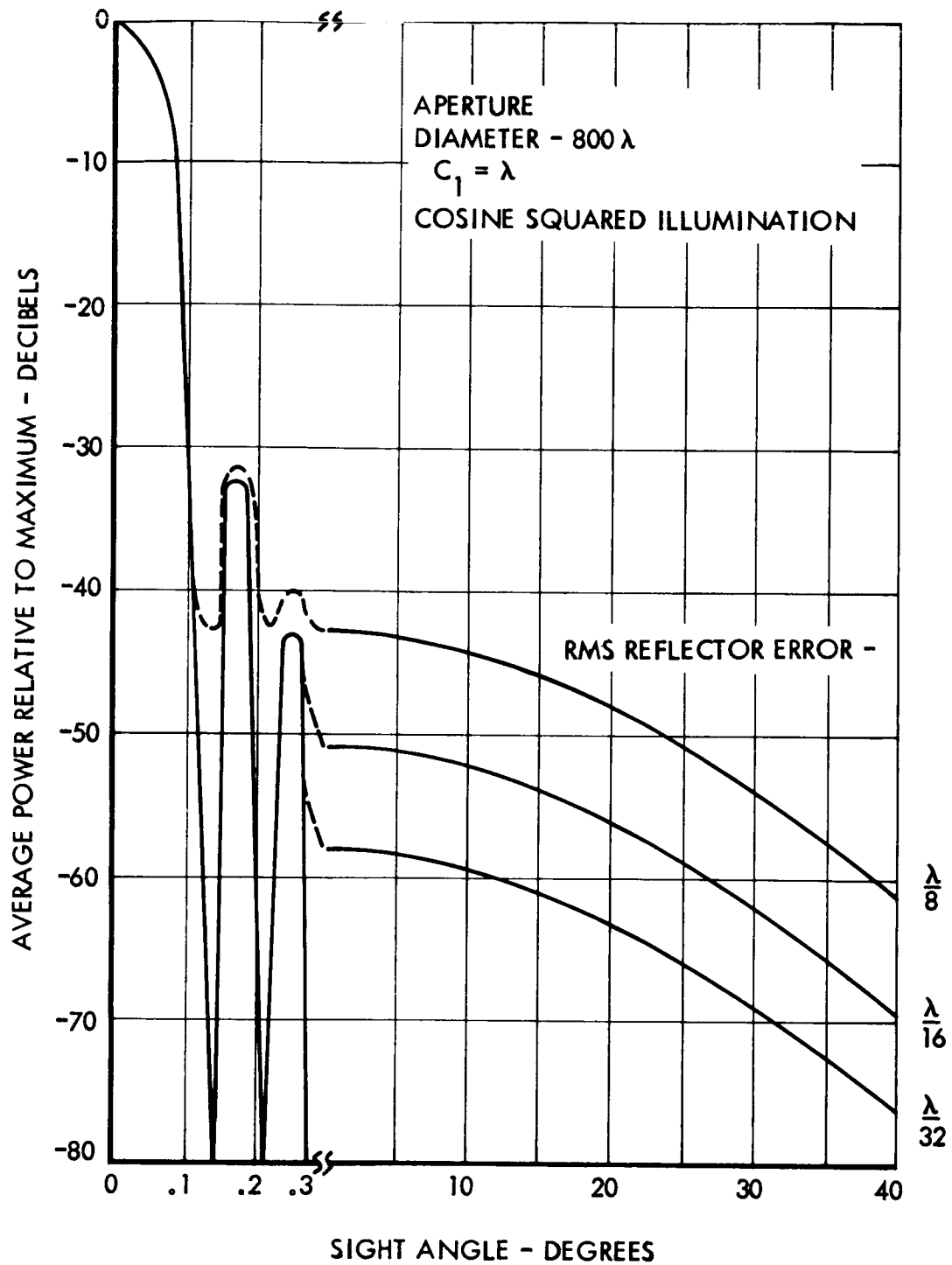


Figure 4.1.3-2. Relative Power vs Sight Angle

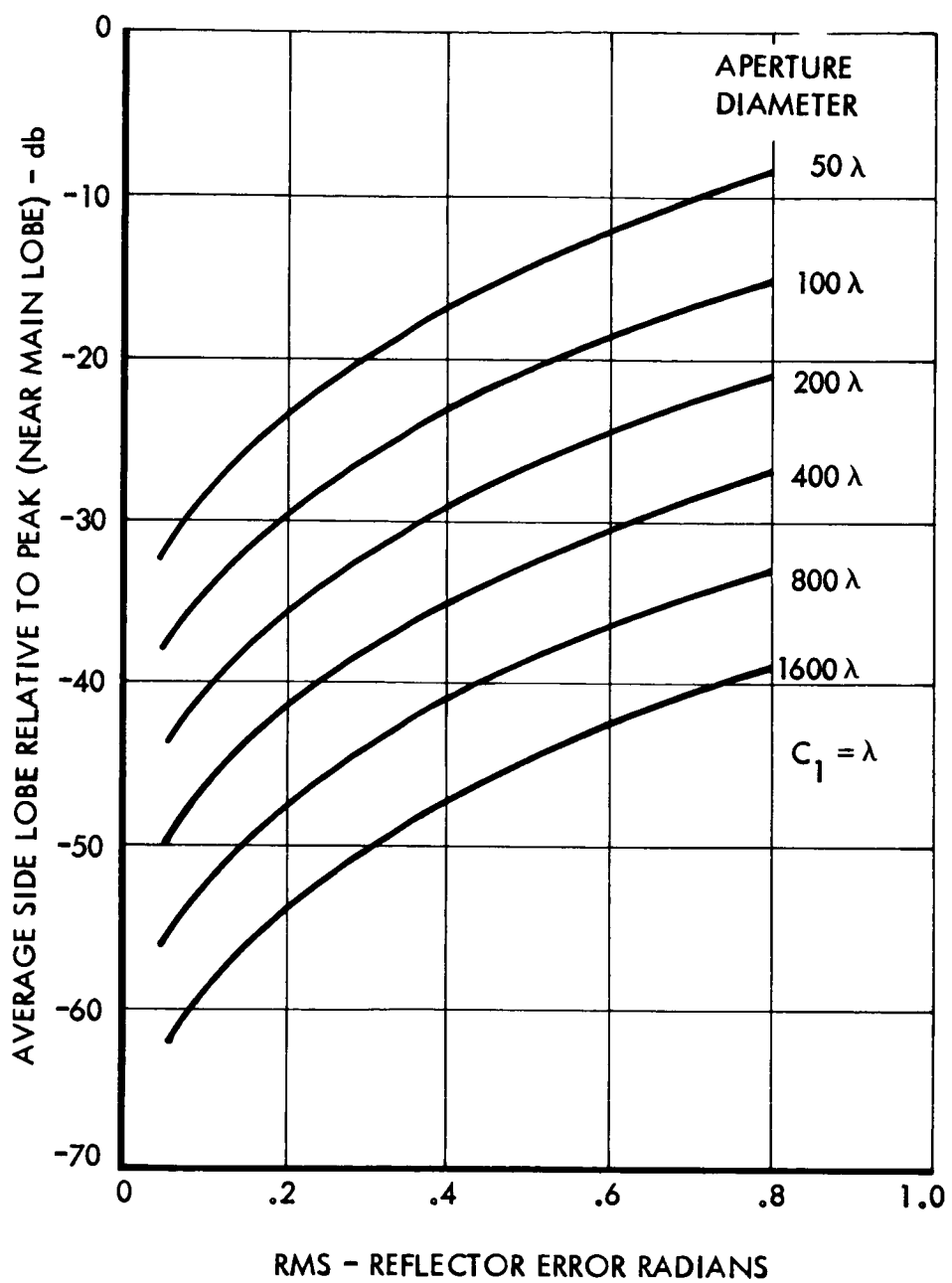


Figure 4.1.3-3. Relative Side Lobe vs Reflector Error

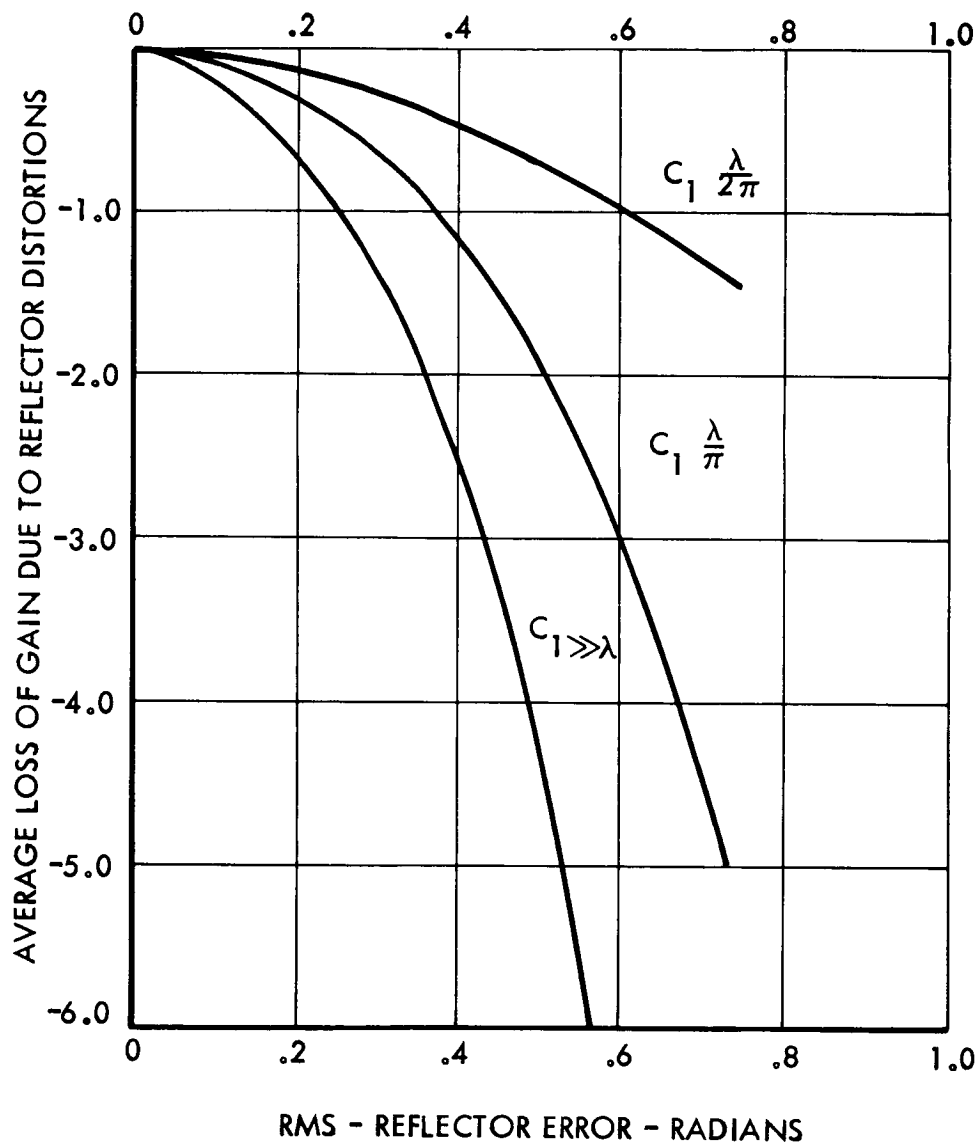


Figure 4.1.3-4. Reflector Distortion Gain Loss vs Reflector Error

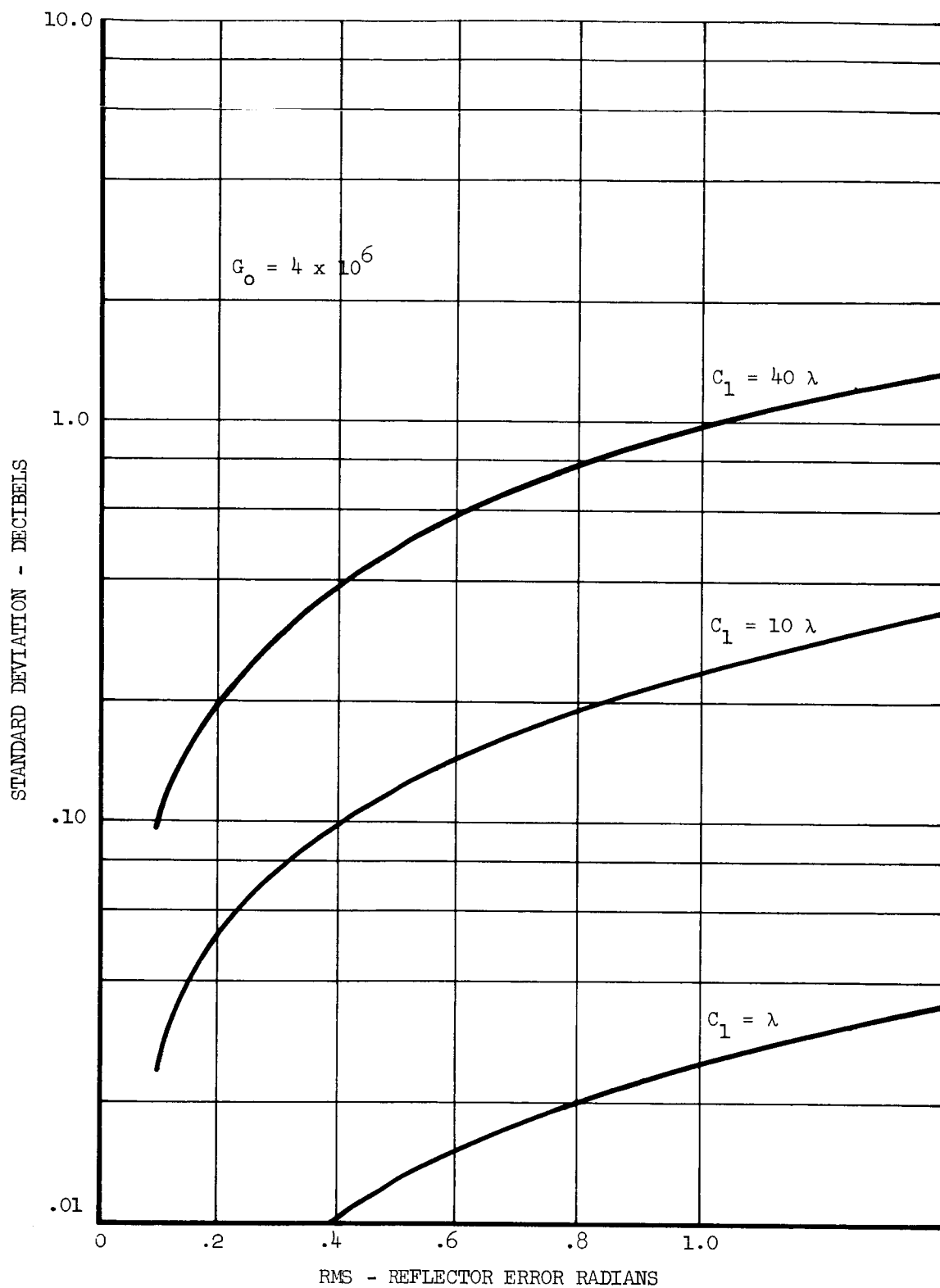


Figure 4.1.3-5. Standard Deviation vs Reflector Errors

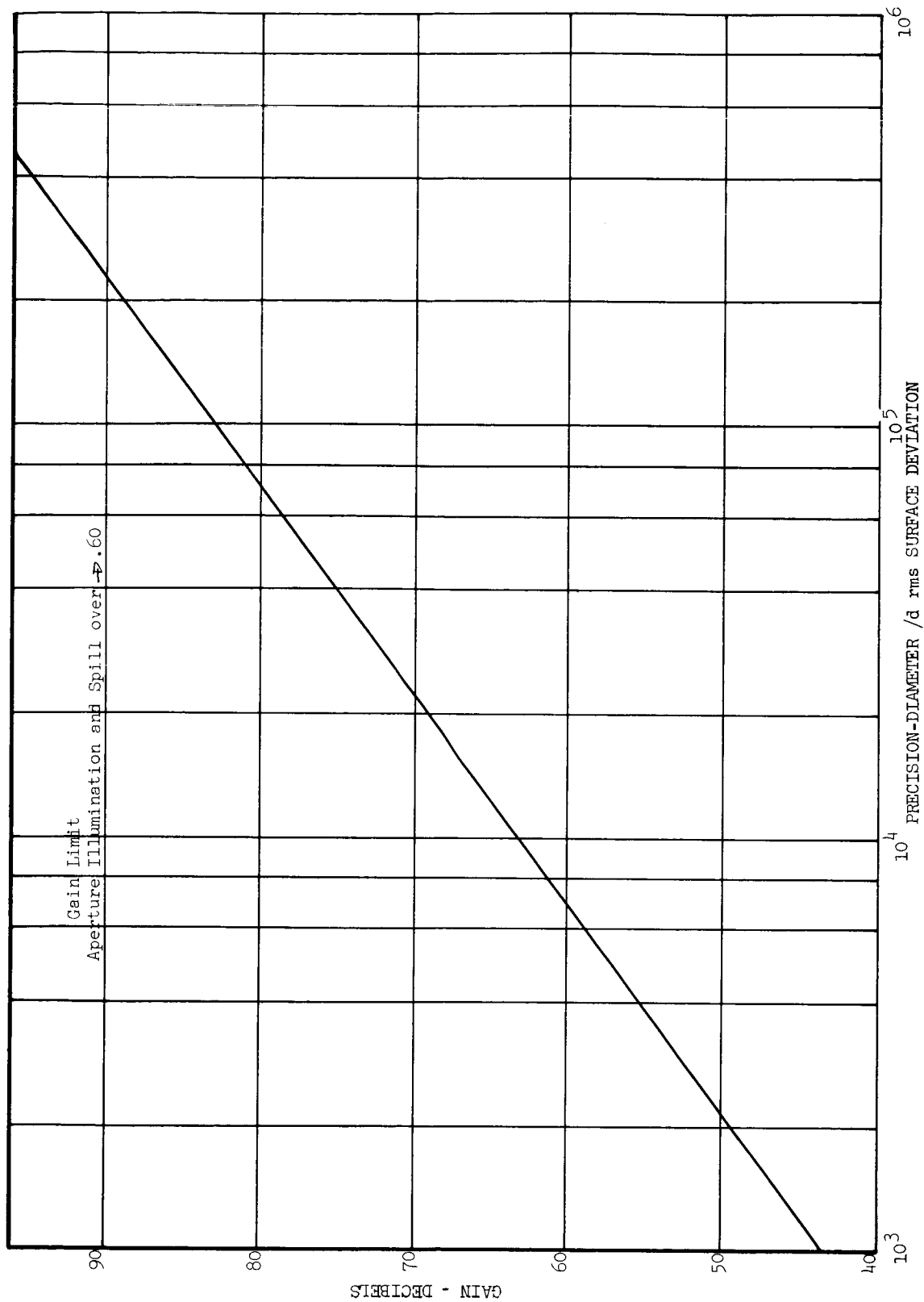


Figure 4.1.3-6. Precision Diameter/d rms Surface Deviation

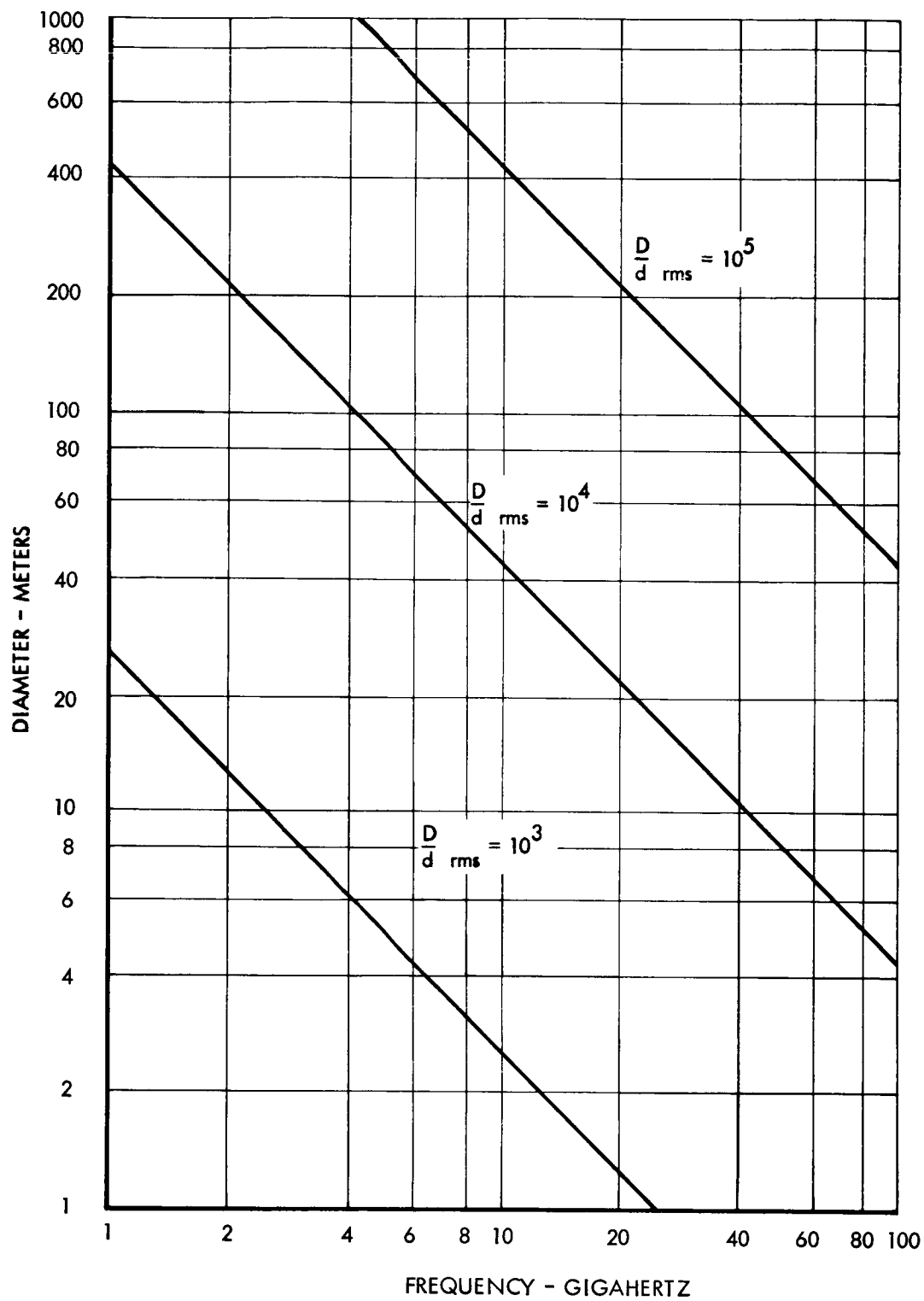


Figure 4.1.3-7. Antenna Gain Limits

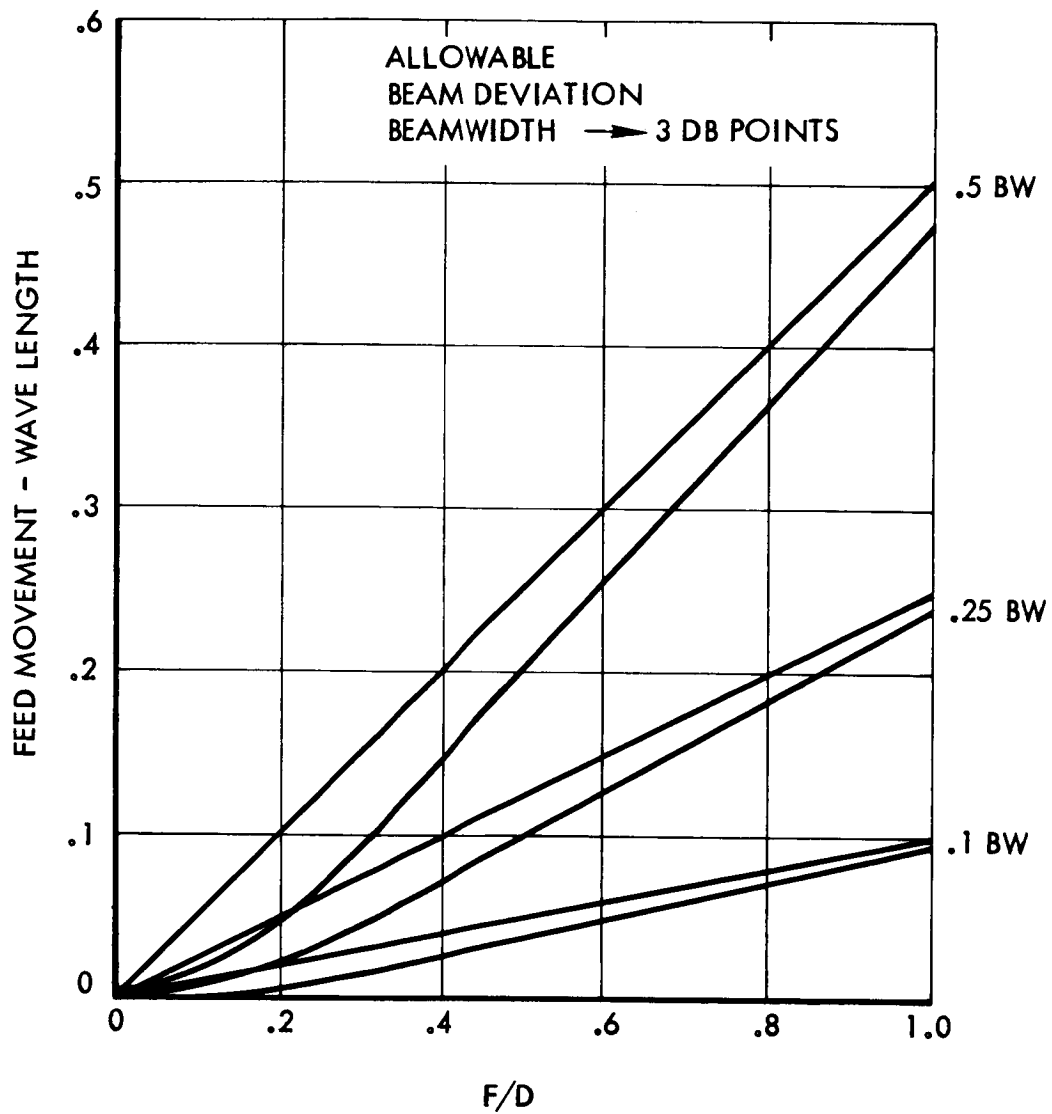


Figure 4.1.3-8. Feed Movement vs F/D

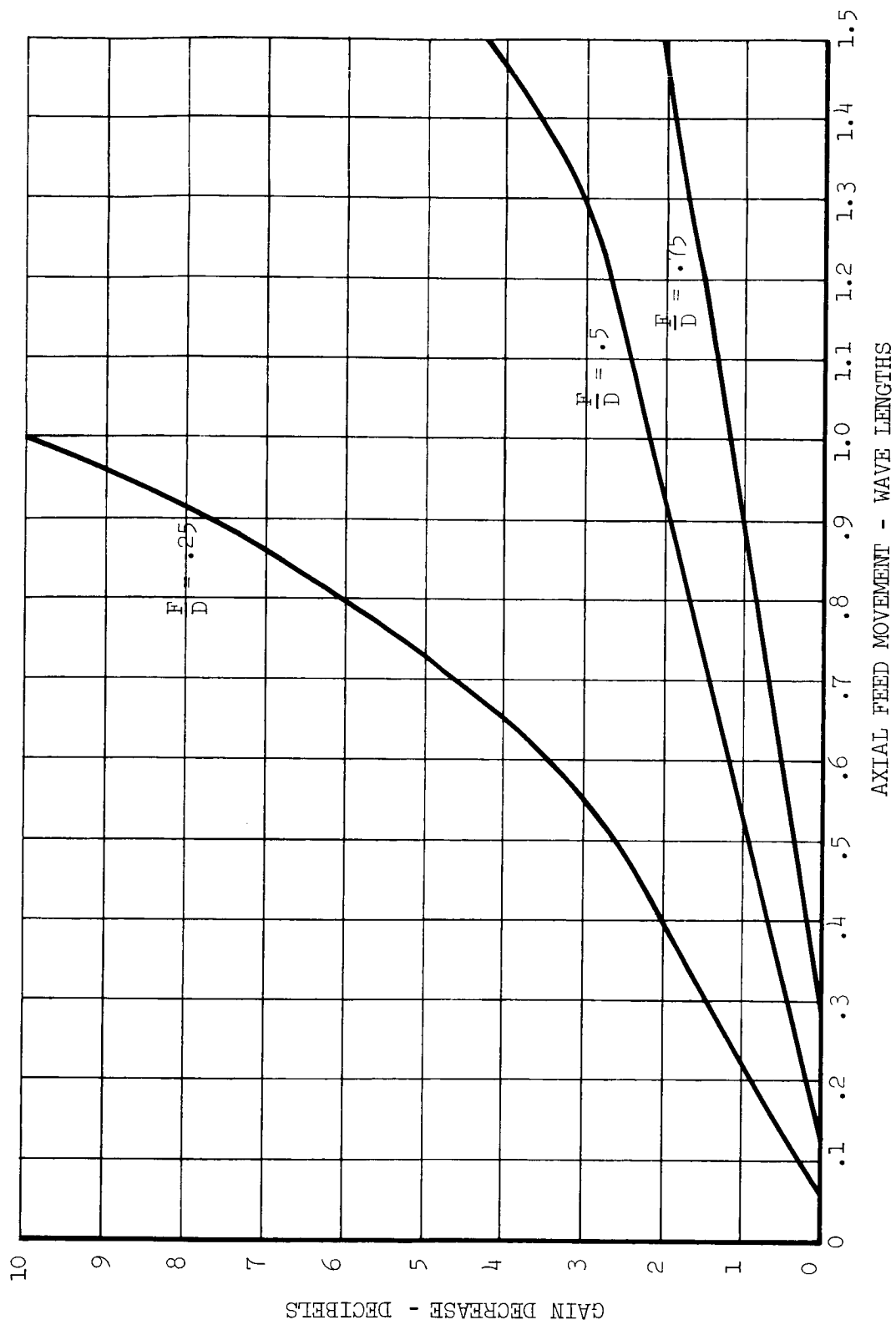


Figure 4.1.3-9. Gain/Feed Movement Relationships

4.1.3.3 PRACTICAL ANTENNA CHARACTERISTICS

In addition to the review of electro-mechanical relations of the preceding section, this final report includes a thorough review of the practical mechanical antenna tolerances in another section. With the mechanical characteristics which evolved from that effort and the electro-mechanical relations established, the characteristics of a practical antenna are determined in this section. The primary emphasis will be on the antenna gain since the other characteristics are not as difficult to control nor are as critical to the overall system performance. The parabolic reflector antenna with a feed located at the focus will be considered at length first because the results can be extended readily to other antenna systems.

The parabolic reflector antenna with the feed located at the focus is subjected to at least four major distorting forces. They are the manufacturing, erection or deployment loads, and the environment loads caused by thermal and inertial effects. These loads affect both the reflector characteristics and the accuracy and stability of the radiating feed position relative to the reflector. With the exception of the thermal loading each of these loads has a random character because of the large number of forcing functions which produce the deviation from the desired position. In order to evaluate the relative effect of the various loads, on antenna gain, a common reference system is required. Because the maximum gain is desired the axes of Figure 4.1.3-7 are considered ideal for this purpose. Figure 4.1.3.3-1 shows the D/d_{rms} ratio for the single solid paraboloid in addition to three other types due to manufacturing and erection errors in the reflector on these axes. Superimposed on this plot is the nominal gain available for a system with the same aperture efficiency as was assumed in Figure 4.1.3-6, and a perfectly located feed.

The maximum gain region for the single solid paraboloid occurs far above the diameter acceptable for a standard shroud assuming that the maximum DSMCS study frequency, 100 GHz, is utilized. Figure 4.1.3.3-2 includes the reflector distortion due to what is estimated to be a 10 thermal load. Details on the appropriate qualifiers leading to the thermal distortion computation are included in the mechanical review section. The shell analysis discussed there showed that the distortion is independent of the diameter and that for a fixed feed a D/d_{rms} equivalent to a 70 decibel gain is expected. With a backup structure to the shell an additional 4 decibels

of gain is possible. The shell analysis also computed the position of the focus for a minimum reflector distortion using a least mean squared criteria. The gain improvement with an adjustable feed is available for the larger diameter without backup structure on the shell. However, an operational sensing mechanism to determine the best position of the feed and a method of compensating for an error is quite complex and will not be considered seriously now. The effect of inertial loading is also shown in the mechanical review section. The results are not plotted in Figure 4.1.3.3-2 because the present attitude control system design loads cause reflector distortions several orders of magnitude below those of the thermal load.

The effect of moving source center of the radiating feed from the reflector focus is a function of the allowable pattern degradation and the paraboloid F/D ratio. A compromise ratio of .42 was used for the mechanical design. Ratios below .25 cause primary feed pattern problems and above .6 the feed structure tolerances becomes unwieldy. This value is typical of earth antenna design. Figure 4.1.3-8 describes the allowable feed motion normal to the paraboloid axis. Using a .1 beamwidth allowable boresight axis motion, a feed movement of about $\lambda/25$ is indicated as maximum. With this criteria the maximum allowable frequency for a given feed deviation from the paraboloid axis is plotted as a function of diameter for erectable and non-erectable feeds in Figure 4.1.3.3-3. Figure 4.1.3.3-4 shows the effect of thermal loads on the focus motion using the same $\lambda/25$ criteria. Axial motion of the feed does not move the boresight axis but does degrade the antenna gain. It is clear from Figure 4.1.3-9 that an axial feed motion of 10 times the normal to axis motion for the F/D = .42 will only degrade the gain by 1 decibel. Mechanical tolerance work for typical designs has shown that the axial beam motion due to manufacturing erection or environment loads are no greater than normal to axis motion by an order of magnitude and therefore axial movement is not the gain limiting motion.

Before examining the antenna weights some general conclusions can be made regarding the various errors distorting the reflector and feed. A general conclusion for all antenna types is that the maximum gain of an antenna is relatively flat as a function of frequency. The only exception to this is the deployment error of the erectable feed included in the Figure 4.1.3.3-3. For a single solid parabolic antenna the gain limit for a fixed feed is that due to thermal loading on the reflector. The maximum gain region for a regular or modified shroud

points towards a 50 to 100 GHz operating frequency. A backup structure to reinforce the shell would reduce the thermal induced distortion to that of the manufacturing and calibration errors.

Two other reflector material types are included in Figure 4.1.3.3-1 which could be applied to a single parabolic reflector configuration, petal structure and mesh or inflatable structure. Most of the petal structure distortion is caused by inaccuracy of the deployment process. The distortions due to deployment are comparable to and caused by thermal effects described in Figure 4.1.3.3-2. A fixed feed for the petal system would be sufficiently stable based on Figure 4.1.3.3-3 and 4.1.3.3-4 relative to the reflector gain limit. Thus, a gain of approximately 70 decibels is possible for the petal structure. The mesh or inflatable reflector of present technology is definitely manufacturing and deployment error limited. From the trace on Figure 4.1.3.3-1 it is clear that the gains are below 50 decibels. Based on anticipated improvements and technology, the mesh or inflatable errors will produce an antenna of approximately 60 decibels. At the larger diameters the feed erection degradation is comparable to the reflector degradation.

Implicit in the Figures 4.1.3.3-1 through 4.1.3.3-4 is the assumption that the antenna is gain limited as described in (13) of Section 4.1.3.2. Further, this implies that the Ruze analysis and its associated approximations are applicable to the problem. For the cases where phase front distortions are caused by either manufacturing or deployment errors such as in the inflatable or mesh structure the error characteristics are compatible with the assumptions. This conclusion is derived from the fact that the errors are caused by a large number of local effects distributed throughout the reflector area. Their independence is attributed to the many separate localized processes which caused the distortions. Similarly, the petal structure is composed of many elements, each of which are subject to the errors induced by the position mechanism.

The reflector error characteristics of a single solid reflector are largely dependent on the type of backup structure used. In the case of the unshaded shell thermal distortions dominate. The errors induced by the simple thermal environment geometry assumed in the thermal shell analysis are not independent. By adding either more backup structure or by using a more complex and more probable thermal environment the error independence across the dish will increase. In adding an additional thermal load such as the earth's albedo a higher order of distortion will be induced. Since the solid reflector must be small in order to fit into the standard shroud, a backup structure for such a small reflector will

most certainly be used. This would transfer the dominating errors from those due to thermal bending of the shell to that of the manufacturing errors on the back-up structure. Hence, the Ruze assumptions are probably valid and the gain limited lines may be used.

A Cassegrainian system pattern deterioration due to imperfect mechanical components is nearly identical to that of the focus fed paraboloid. The main reflector distortions are the same. The phase errors induced by secondary reflectors which are typically of the order of $1/10$ of the main diameter are negligible since the D/d_{rms} is constant if not improving with decreasing diameter. The sub-reflector motion normal to the axis is similar to that of the direct feed. The feed itself would be at or near the surface of the main reflector and would not be appreciably off the ideal position.

A survey of present and anticipated inflatable structure technology indicates that the manufacturing and deployment distortions of a spherical reflector are not appreciably less than those of an inflated paraboloid. Thus, since the antenna efficiency of a sphere with spherical correction is much less than the paraboloid of comparable gain, further consideration of the sphere is not justified. Also, the feed necessary for correcting spherical aberration is difficult to build at 20 GHz and lower. At 100 GHz the feed manufacturing problem would be extremely difficult particularly with a low insertion loss requirement necessary for DSMCS application.

Similarly, evaluation of the mechanical tolerances of the Fresnel antenna has shown that it provides no increase in D/σ compared to more conventional approaches, while its greater complexity raises other mechanical difficulties.

Figure 4.1.3.3-1 indicates that an array of solid reflectors provide the maximum permissible gain. For the unshaded antenna there is not justification for going to multiple parabolic arrays since the thermal distortions dominate in a single shroud limited reflector. Further, the frequency at the gain limit is beyond the DSMCS range for normal shroud configuration. Figure 4.1.3.3-2 shows that the thermal limit for each element will limit the gain to 70 decibels.

The antenna weight as a function of the antenna diameter for 5 antenna types is included in Figure 4.1.3.3-5. This information along with the gain limit error plots are sufficient data in order to complete the desired antenna gain as a function of mass and operating frequency plot. Although the mass of the mesh and inflatable types is low, they are ruled out because of in-

sufficient maximum gain. Similarly, the aluminum structures may be ruled out due to insufficient gains even though the mass is half for the same diameter. Gain limit and deflections are proportional to the thermal expansion coefficient which is 32 times greater for aluminum as it is for Invar. Thus for thermal limited configurations such as the solid reflectors and array of solid reflectors the Invar is mandatory. Invar is also required for the petal configuration because it becomes thermal limited with aluminum. Antenna gain as a function of antenna mass is given for the three configurations in Figures 4.1.3-6 and 4.1.3-7. The single solid reflector is below the gain limit at 100 gigahertz for the normal and the extended shroud. The array of solid reflectors provides 2 more decibels gain at the normal shroud diameter which is at the thermal limit for 100 gigahertz. The Invar petal reflector configuration is manufacturing and deployment error limited with present tolerances at 70 decibels for the normal shroud and 73 decibels assuming a 10 year improvement in mechanical tolerances.

BIBLIOGRAPHY

1. Silver, S., Microwave Antenna Theory and Design, Boston Technical Publishers, Inc. 1964.
2. Ruze, J., "Physical Limitations on Antennas," M.I.T. Technical Report 248, October 30, 1952.
3. Bickmore, R. W., and Hansen, R. C., "Antenna Power Densities in the Fresnel Region", Proc. I.R.E. 47, p. 2119-2120, 1959.

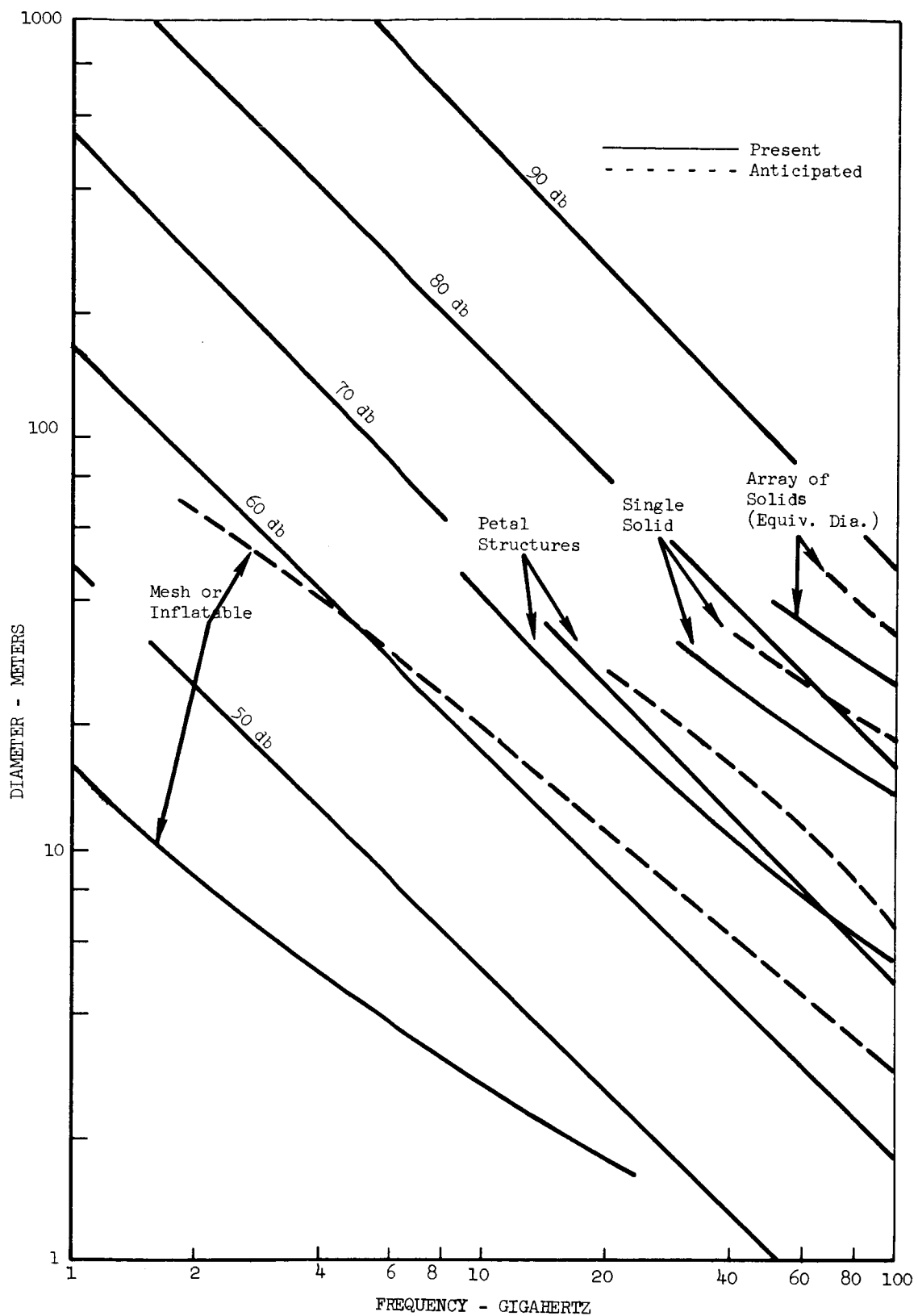


Figure 4.1.3.3-1. Reflector Distortion Due to Manufacturing and Erection Errors

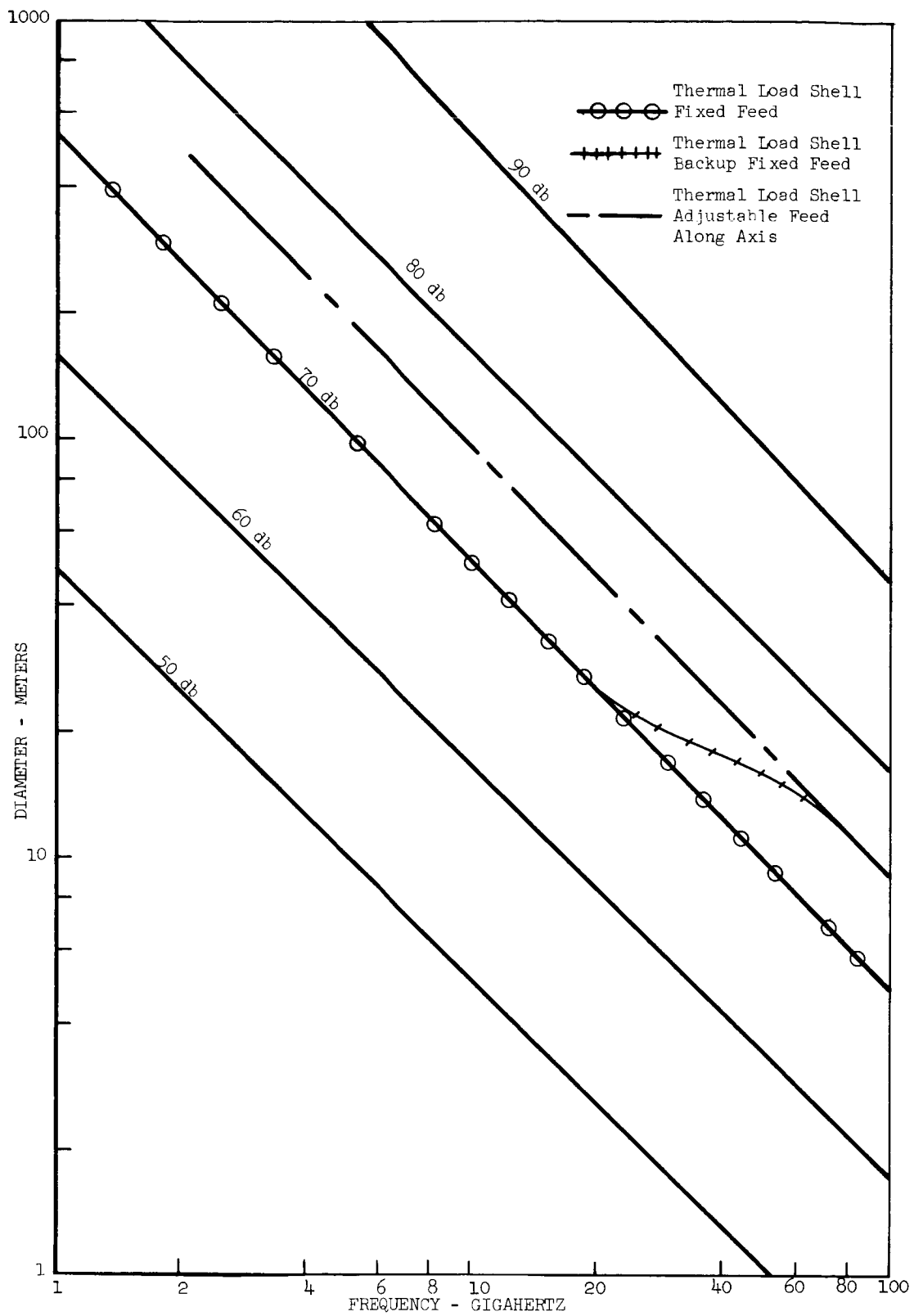


Figure 4.1.3.3-2. Reflector Distortion Due to Thermal Loads

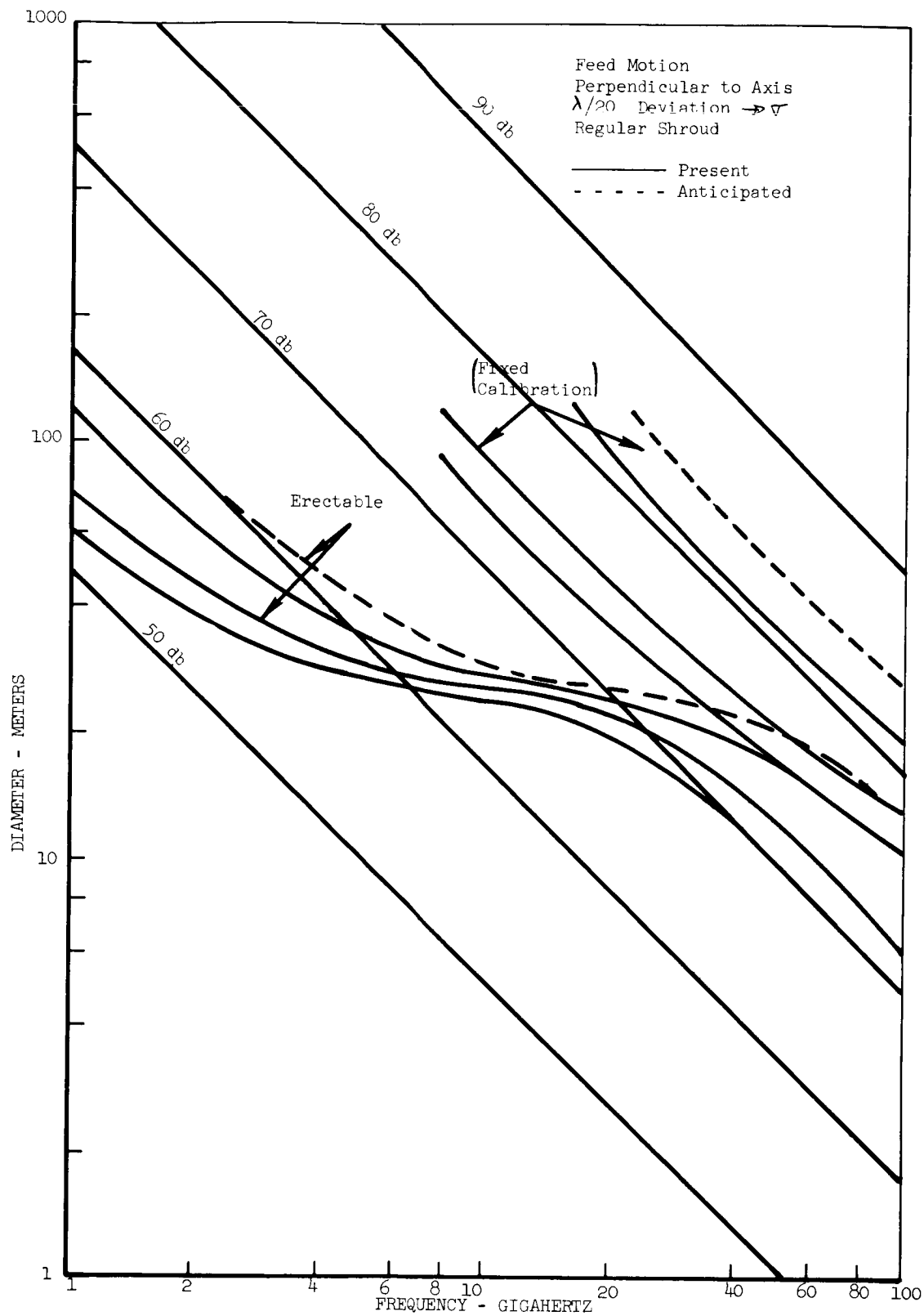


Figure 4.1.3.3-3. Diameter/Frequency/Feed Motion Relationship

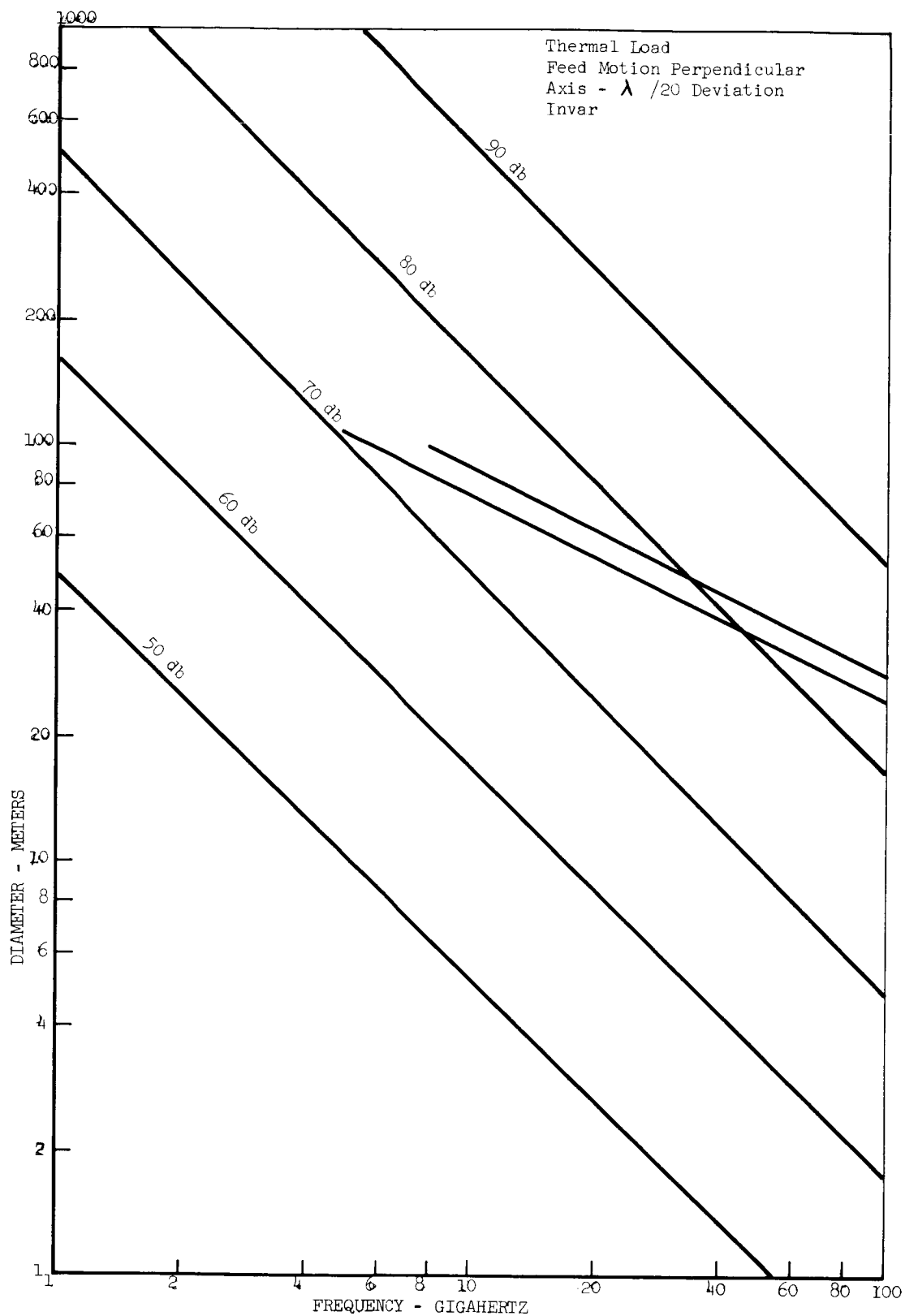


Figure 4.1.3.3-4. Diameter/Frequency/Feed Motion Relationship

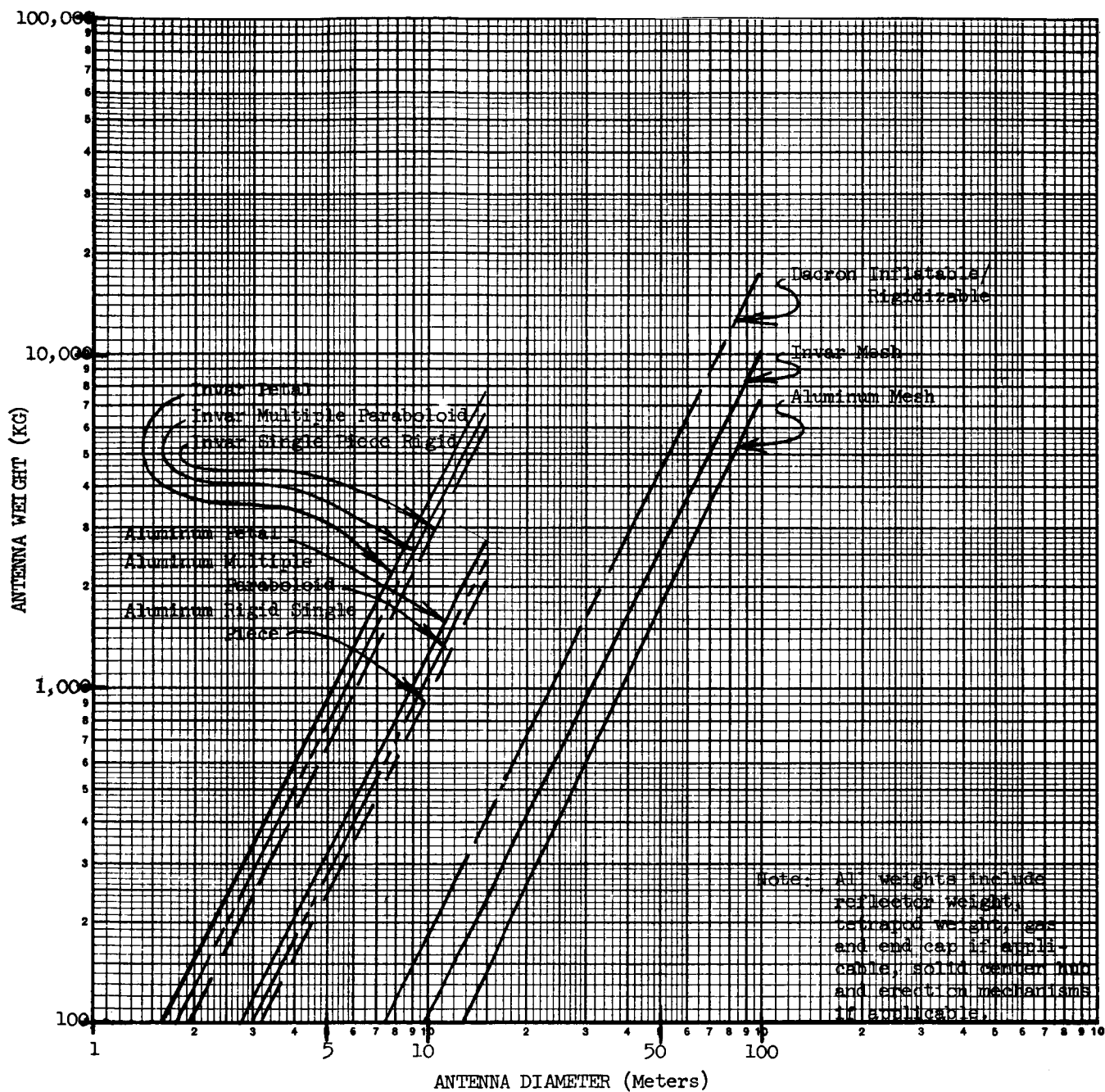


Figure 4.1.3.3-5. Antenna Weight vs Diameter

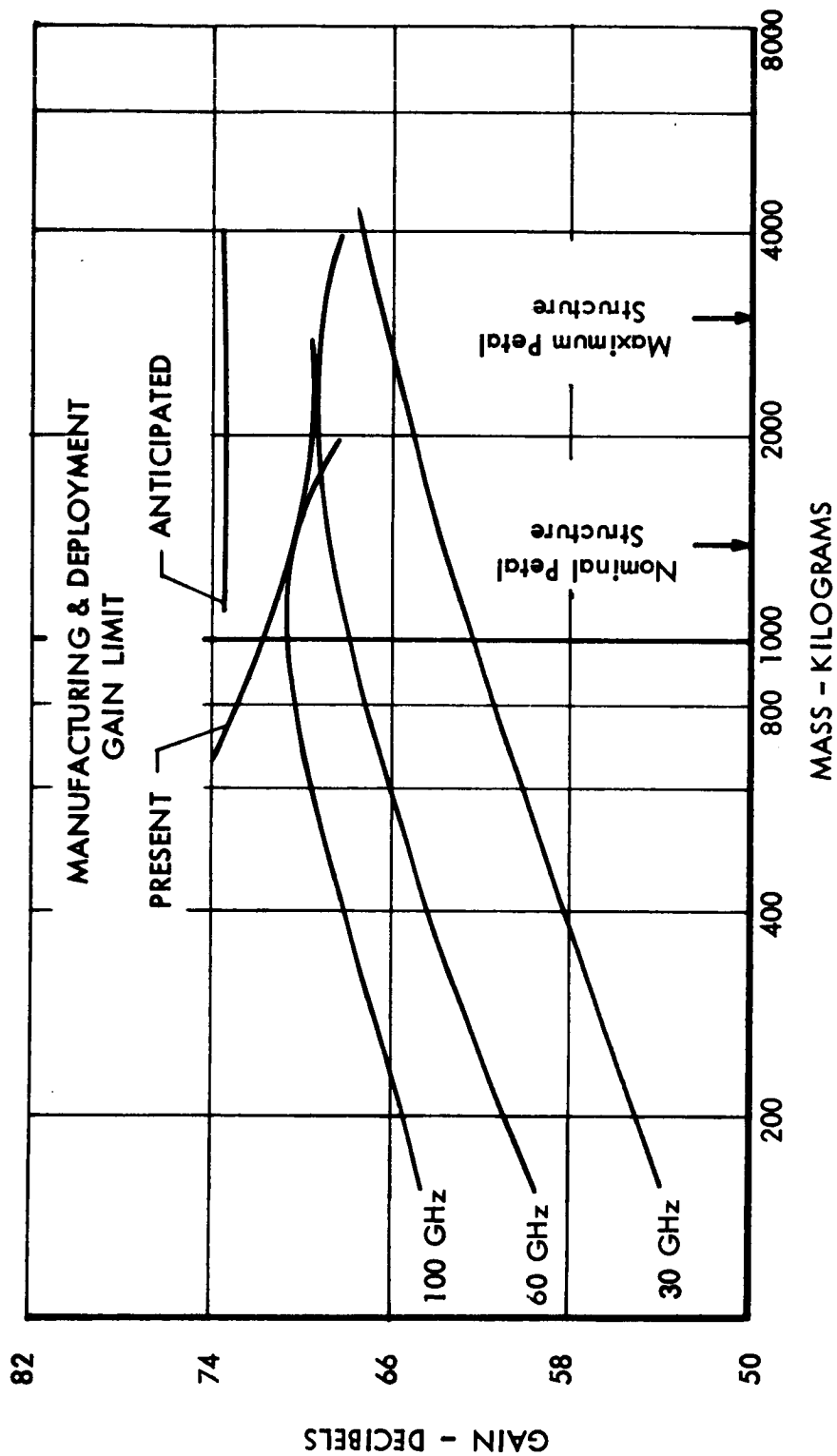


Figure 4.1.3.3-7. Petal Antenna Gain vs Mass

Two structural digital computer programs capable of analyzing deflections of antenna surfaces under inertial loadings were utilized in the study. One of these programs utilizes the finite element approach where the structural shell is approximated by a series of conical segments as shown in Figure 4.1.4-1. Arbitrary circumferential loadings may be specified by expanding the loading function in a Fourier series about the axis of symmetry of the antenna. Arbitrary radial loadings may be taken into account by varying the Fourier series from conical element to conical element. This program was developed by Dr. Stanley Dong of the University of California at Los Angeles.

In addition to these programs, a third digital program was used. This program computes the normal deflections and the root-mean-square of the beam path length error for the distorted parabola using the original parabola as a reference surface. The program will also use as a reference surface a generated parabola which is a best fit to the distorted parabola in the least squares sense. Of fundamental importance is the determination of the minimum number of conical segments which are necessary to accurately and efficiently, from the machine time standpoint, approximate the parabolic surface of the antenna. This was accomplished by calculating deflections for both an axisymmetric loading case and an asymmetric loading case, Figure 4.1.4-2, with the parabola approximated by first, three conical sections, then ten and finally thirty sections as shown in Figure 4.1.4-1. Selected points, using the critical case, are shown plotted in Figure 4.1.4-3 and 4.1.4-4 showing the horizontal, vertical and tangential deflections for the two loading conditions described above, and for the different numbers of conical segments that were used. It was described, on the basis of these curves, that thirty conical segments would be sufficient to accurately describe deflections/rms's of the parabolic shell. This was verified by computing (using the Richardson's extrapolation technique*) what the values should be if a reasonably large number of conical segments were used. In all the points tested the convergence of the deflections was rapid enough to allow the shell to be accurately approximated by thirty elements. Limiting the number of elements that are required to a reasonable value allows the program to predict the performance of various antenna systems economically.

* Salvadori and Baron, Numerical Methods in Engineering, Prentice-Hall, Inc., 1952.

The effect of thickness of a parabolic shell on its deflections is extremely critical. This is because there are two factors which determine how the shell will behave; namely, extensional stiffness and bending stiffness. The extensional stiffness is dependent on the thickness taken to its first power while the bending stiffness is dependent on the thickness taken to the third power. Thus, both the shell surface distortion pattern and magnitude can be changed by having the bending stiffness predominate, the extensional stiffness predominate, or by having both quantities of similar magnitude.

For the types of construction and materials under consideration the thickness to diameter ratio is in the range of 10^{-3} to 10^{-7} . It was strongly suspected that in this range the extensional stiffness would be predominant over bending stiffness and this was analytically proven as shown in Figure 4.1.4-5, and 4.1.4-6. The figures show the change in the rms (root mean square of path length error from best fit parabola) due to a change in thickness of three different diameter parabolic antennas. The figures were based on a constant "g" inertia loading condition of 0.1, where 1.0 is equivalent in magnitude to the gravity loading at the earth's surface. The source of this inertia loading would be the attitude control system and was arbitrarily chosen for this analysis as 0.1 g. Since for small deflections the effect of increased or decreased loading on the rms is approximately linear within the range of interest, the value for the rms may be determined for any "g" loading of the attitude control system by simple linear scaling. The figures note that thickness does not significantly effect the rms for any of the three diameters shown. This is because the extensional stiffness which is predominant, is a function of the thickness to the first power, and the weight of a unit area of surface on the antenna is a function of the inverse of the thickness. Thus, for a constant "g" level of loading the effects of change in extensional stiffness and change in loading magnitude due to the thickness (mass) change cancel out, resulting in a relatively constant rms. The slight curve in the line is due to the effects of bending stiffness and would become increasingly important as the thickness increased beyond what is shown in the charts. Figure 4.1.4-7 shows the same effect but for the thermal loading case of the antenna axis pointing directly at the sun. The same effect of extensional stiffness predominance is shown for this thermal loading case as was shown

in the inertia loading cases above. Thus, the hypothesis that bending stiffness could be neglected was substantiated by the computer shell program being used.

The effect of E (elastic modulus) is again linear and may be seen in Figures 4.1.4-5 and 4.1.4-6. Comparing these two figures it is seen that the effect on the magnitude of the distortion is approximately double for the asymmetric loading (loading perpendicular to the axis of symmetry) as for the symmetric loading (loading along the axis of symmetry). Thus, the asymmetric is the critical loading condition for the inertial type loadings.

Figure 4.1.4-7 shows the effect of thermal loading on the deflections for the symmetric condition of the antenna pointing directly at the sun. The figure shown is for a thermal expansion coefficient " α " of $13 \times 10^{-6}/^{\circ}\text{F}$ only, however, the rms will again be a linear function of " α " and hence values of rms for any " α " may be determined from this graph. It is seen by comparing this figure against Figures 4.1.4-5 and 4.1.4-6 for the inertia loading cases that the thermal loading conditions are the more critical. Hence, for a comparison of antenna gain versus size the rms due to thermal considerations will be utilized. rms due to the thermal loads will be nearly identical in either a solid shell or a rigid mesh type structure. This occurs because a very good approximation of the behavior of materials under thermal loads is obtained by using the linear coefficient of thermal expansion which considers increase in size along different perpendicular coordinates to be uncoupled. Thus, a solid square plate of side length " ℓ " will increase along both coordinates just the same amount as would a square made of only thin wires along each edge, if the squares were both the same size and made of the same material.

4.1.4.1 STRUCTURAL DESIGN ANALYSIS

The parabolic antenna was analytically studied to determine how four fundamental loadings distorted the reflector surface. These four loading conditions consist of attitude control pulses and solar heat flux vectors parallel and perpendicular to the axis of revolution.

The results of the computer analysis to interrelate gain, frequency, diameter and structural deflections concluded that the rms for grid antennas is

much higher than solid antennas, thereby causing a gain loss for any given diameter. Gains for similar diameter antennas at the same operating frequency give the solid antenna up to 30 db more gain than grid antennas. It should be noted however, that grid antennas are very appealing from a structural efficiency consideration. Most of the surface of a grid type antenna is void, which lessens the weight/unit area in direct proportion to the ratio of void area to total surface area.

The reason for the electrical inefficiency of the grid antenna is the relationship between the thermal distortion of a grid type antenna and a solid antenna and how they differ from a best fit paraboloid. The rms as determined from the JPL "RMS" computer program is calculated on the basis of the difference of beam path lengths between the distorted antenna and a best fit paraboloid to the distorted antenna in a least squares sense as shown in Figure 4.1.4.1-1. Hence, even if the original antenna undergoes large deflections in relation to the operating wavelength, a low rms can still be achieved, if the deflections are such that a translation or rotation of a best fit paraboloid can minimize the affect of most of the distortion. This is the case for both the axisymmetric thermal loading and the asymmetric solid antenna thermal loading. However, even though the magnitude of the distortions of the grid type antenna are no greater than the solid type, the rms becomes much greater due to its distortion pattern. In the grid type antenna there are two warm regions (front and back) and two cold regions (sides) making the minimization of the rms due to the shifting of the best fit paraboloid ineffective. It is because of this that the grid type antennas yield a much larger rms and hence, a much lower gain than the corresponding solid antenna.

There are several ways to overcome the thermal distortion problem posed by the grid type antennas. One would be to use a thin membrane bonded to the mesh which would be opaque to solar radiation. This membrane could also be of use in erection of the antenna if inflation techniques are utilized. Another method would be to encase the entire antenna in a thermal protective cover. One other approach would be to use a thermal compensating material to overcome the large distortions. However, there is insufficient work being performed in this area to warrant serious consideration for the antenna system being considered.

Hence, it is not expected that a solution to the grid distortions by a thermal compensating material would be available for use by the DSMCS.

From a structural point of view, operation at a higher frequency (30-100 GHz) could be more easily accomplished than operation at lower frequency (2.3-10 GHz). The interrelationship between frequency, diameter, and surface tolerance for a given gain level enters here. Higher frequency communications could utilize small (1.8 - 5.5 meter diameter) very accurate surface antennas while the lower frequencies utilize less accurate surfaces but much larger antennas (18 - 90) meter diameter). Very accurate small (under 5.5 meter) antennas could be fabricated by accurately machining the surfaces; and the thermal problem could easily be circumvented by a covering as proposed above. However, operation at frequencies at or near 100 GHz may not be desirable. In this case, two avenues are open. One, the larger antennas may be used with additional investigation into overcoming the thermal distortions and two, hybrid antennas may be used. A hybrid antenna would combine the advantages of a very accurately machined center hub region (up to 5.5 meter) with an erectable skirt. The skirt could be constructed of panels, petals or grid materials. The outer skirt would be subject to the distortions mentioned above but their smaller size plus the large support perimeter afforded by the center hub could, when combined with a lower frequency lead to a more optimum system.

4.1.4.1.1 THERMODYNAMIC ANALYSIS

Critical conditions affecting antenna surface rms (root mean square of surface distortion) are from thermal radiation emanating from the Sun. Examples of axisymmetrical thermal flux (Sun vector along axis of revolution of the antenna) problems and asymmetric (Sun vector perpendicular to the axis of revolution of the antenna) thermal flux problem were investigated. Comparison of results shows the latter to be the critical loading condition considering both thermal and inertial loads in both the axisymmetric and asymmetric modes.

Thermal Model of Antenna:

The following assumptions for the thermal analysis of the antenna were made:

1. Radiation effects were predominant over conductive effects, i.e., conduction was assumed to be zero.
2. The temperature was uniform throughout the thickness of the antenna.
3. Neither " α " or " ϵ " vary with the angle of incidence or temperature.
4. The energy impinging on the antenna is a direct function of the projected area.
5. The ratio of " α " to " ϵ " equals unity (obtainable with special thermal coatings).

4.1.4.1.2 AXISYMMETRIC THERMAL CONDITIONS

This case corresponds to the direction of the incident thermal energy being parallel to the axis of revolution of the antenna as shown in Figure 4.1.4.1.2-1a.

The absorbed energy per unit area will be

$$E_a = \alpha H \cos \theta \quad (1)$$

where

α = absorptivity

H = solar radiation at 1.0 AU

θ = angle that tangent to antenna makes with aperture plane

The radiated energy per unit area (both surfaces) will be

$$E_r = 2\epsilon \sigma T^4 \quad (2)$$

where

ϵ = emissivity

σ = Stefan-Boltzmann constant

T = temperature in degrees Rankine

At equilibrium the absorbed energy equals the radiated energy and hence,

$$T = \sqrt[4]{\frac{H \cos \theta}{2\sigma}} \quad (3)$$

The above equation specifies the temperature for the axisymmetric thermal loading condition along a meridian as a function of the tangent angle of the antenna and is presented in Figure 4.1.4.1.2-2. The temperature does not vary circumferentially for the axisymmetric case. The computer program was originally written to provide Fahrenheit outputs rather than Centigrade and in order to maintain continuity in the analysis, conversion to Centigrade was not acceptable.

4.1.4.1.3 AXISYMMETRIC THERMAL CONDITIONS

This case corresponds to the direction of the incident thermal energy being perpendicular to the axis of revolution of the antenna as shown in Figure 4.1.4.1.2-1b.

On the half of the antenna exposed to the direct rays of the sun the absorbed energy will be

$$E_a = \alpha H \sin \theta \sin \phi \quad (4)$$

where ϕ = angle that tangent to antenna makes with the sun position vector (see Figure 4.1.4.1.2-3)

The radiated energy will be

$$E_r = \epsilon \sigma T^4$$

Hence at equilibrium

$$T = \sqrt[4]{\frac{H \sin \theta \sin \phi}{\sigma}} \quad (5)$$

The above equation specifies the temperature for the asymmetric loading condition on the half of the antenna that is exposed to direct sunlight. The backhalf (half not exposed to direct sunlight) presents two separate cases. One case considers the class of antennas that are solid and do not allow sunlight to pass through the frontside to strike the backside. The other case considers the class of antennas that are constructed of wire grids or meshes and do allow direct sunlight to impinge on the backside. These two cases will be considered separately.

4.1.4.1.3a SOLID ANTENNAS

The backside will not receive any direct solar energy but will receive a heat flux from the radiation of the frontside surface. It was calculated that the average energy impinging on the backside was 2.3% of the amount of energy radiated by the frontside. The assumption was made that the energy radiating from the front side fell uniformly over the backside. This causes a temperature gradient as shown in Figure 4.1.4.1.3a-1.

4.1.4.1.3b GRID ANTENNAS

The grid or mesh type structures present a completely different thermal profile because of the solar energy that passes through the frontside and impinges directly on the backside. This causes a temperature distribution that has a warm section on the center of the backside as well as the center of the frontside.

From Figure 4.1.4.1.3b-1 it is seen that the thermal energy impinging on the backside is a function of wire size to grid hole size. For a wire diameter to hole width ratio of 9:1 the solar energy striking the backside will be in ratio to the radiation striking the frontside as

$$\frac{E_{\text{back}}}{E_{\text{front}}} = (.81) \sin \theta \sin \phi \quad (6)$$

Taking (4) into account yields

$$E_{\text{back}} = \alpha H \left[(.90) \sin \theta \right]^2 \quad (7)$$

The backside will also be subjected to radiation energy due to frontside radiation, this will be

$$E_{\text{rad}} = (k)(.023) \alpha H \quad (8)$$

where k is a constant depending on the amount of void space that is present in the frontside surface. For this case taken above k = .19 (81% void area versus 19% wire area).

The radiated energy will be

$$E_r = \epsilon \sigma T^4$$

Hence, at equilibrium the temperature will be

$$T = \sqrt[4]{\frac{H}{\sigma} (.81 \sin^2 \theta \sin^2 \phi + .0043)} \quad (9)$$

The above equation specifies the temperature for the backside surface when the antenna is constructed of a grid or mesh material. This temperature distribution is shown in Figure 4.1.4.1.3b-2.

Other methods to limit deflections due to solar radiation were sought in addition to those already presented. The most hopeful solution found was selection of materials with a lower coefficient of thermal expansion. There is a class of such materials called "Low Expansion Alloys" whose properties are presented in the American Society of Metals Metals Handbook. Of these, the material Invar seemed the most promising with the following properties:

Composition: iron-nickel alloy of 36% Ni with minor amounts of Mn, Si, and C;

Coef. of Thermal Expansion: 0.5 to $10^{-6}/^{\circ}\text{F}$ ($0.9 \times 10^{-6}/^{\circ}\text{C}$) -
Increases if temperature reaches 200°C .

Elastic Modulus: 21.4×10^6 lbs/in.² ($1.5 \times 10^{10} \frac{\text{Kgs}}{\text{sq. meter}}$)

Density: .29 lbs/in.³ ($.805 \times 10^4 \frac{\text{Kgs}}{\text{cu. meter}}$)

Elastic Limit: $20-30 \times 10^3$ lbs/in.² ($14-21 \times 10^5$ Kgs/sq. meter)

Yield Point: $40-60 \times 10^3 \text{ lbs/in.}^2$ ($28-42 \times 10^5 \text{ Kgs/sq. meter}$)

Tensile Strength: $65-85 \times 10^3 \text{ lbs/in.}^2$ ($45.5-60 \times 10^5 \text{ Kgs/sq. meter}$)

Since the deflections of the antenna are directly proportional to the coefficient of thermal expansion, the use of Invar represents an order of magnitude decrease in expected thermal deflections. This gain in accuracy is not without penalty, however, because the elastic limit of Invar is approximately the same as aluminum, but its weight is three times greater.

Surface distortions have been presented as a value called rms, related to a best fit paraboloid. Since the best fit paraboloid changes both shape and orientation for different loading conditions, the relation of the rms to this varying reference infers that an adjustable secondary reflector (or feed) must be positioned. With the electrical problems inherent in commanding a continuously tracking secondary reflector, it was concluded that an optimum DSMCS design should not consider a continuously adjustable feed. Hence, additional computer calculations were made to determine the effect fixing the feed had on the rms. The results of these calculations are presented in Table 4.1.4.1.3b-1 along with the values for an adjustable feed based on the use of Invar. It is seen that fixing the feed increases the rms from one and two orders of magnitude depending on the loading condition. Cross plots relating rms obtainable for different structural materials and for both adjustable feed and fixed feed are presented in Figures 4.1.4.1.3b-3 through 4.1.4.1.3b-6.

4.1.4.2 MANUFACTURING AND DEPLOYMENT SURFACE CHARACTERISTICS

4.1.4.2.1 RIGID SINGLE PIECE ANTENNAS

This type of antenna would be similar in construction to the standard ground-based antenna and would consist of a rigid reflecting surface supported with a back-up space-truss and would present similar manufacturing problems. Figure 4.1.4.2.1-1 shows the manufacturing tolerances held on some of the high precision ground-based antennas and would also represent the manufacturing tolerance that could be held on similar sized rigid space antennas. An anticipated line is shown also and represents what are conservative estimates for 1975. Table 4.1.4.2.1-1 and Figure 4.1.4.2.1-2 present a comparison of the

rigid single piece antenna versus the other structural types discussed. It is seen that D/σ (ratio of aperture diameter to the root-mean-square of the surface deviations) values of 83,000 can be achieved for a 5.5 meter (18-foot) antenna (maximum diameter possible due to shroud restrictions). A D/σ of 93,000 can be achieved if the diameter is decreased to 4.3 meters (14 feet) which is the maximum diameter possible due to shroud restrictions for an antenna stowed in the upright position in Saturn shrouds.

4.1.4.2.2 MULTIPLE PARABOLOID ARRAYS

A configuration of this type is shown in Figure 4.1.4.2.2-1. Since the multiple paraboloid arrays would utilize several rigid single piece antennas in combination, the surface characteristics of the total array would relate directly to the surface characteristics of the individual paraboloids. It has been shown the maximum size that could be packaged using the present Saturn IB shroud is a set of four paraboloids each 4.3 meters in diameter. This yielded a total aperture area equal to that of a single paraboloid 8.6 meters in diameter.

Each of these 4.3 meter diameter antennas could be manufactured to a D/σ of 93,000 and hence the D/σ of the multiple system based on the total effective diameter would be 186,000. Even though a higher effective D/σ can be achieved for the multiple paraboloid array than for a single dish, it must be remembered that the multiple paraboloids will have loss associated with their individual erection tolerance build-up. It was calculated that the four-paraboloid antennas could be erected co-planar to within a deviation of 30 arc sec (three sigma). A tabular presentation of this is shown compared to other structural antenna types in Table 4.1.4.2.1-1 as a function of diameter.

4.1.4.2.3 ERECTABLE PETAL PARABOLOID ANTENNAS

This type of antenna would consist of large numbers of radial slices (petals) of a paraboloid that are erected mechanically into a configuration easily packaged during launch.

The deviation of a petal type antenna from a true paraboloid is composed of two principal components. The first consists of the surface

deviations of each individual petal due to manufacturing error. The second consists of petal deviations from the true paraboloid due to erection misalignment. Two types of erection deviations were studied. The first considered the deviations that would occur for a purely mechanical erection and locking system, with no effort made to calibrate individual petals once erected. The second considered the deviations that would occur if each petal was first erected then aligned through a servo operated system.

It was assumed for the calculations of the portion of the rms that was due to erection misalignment that the petals were distributed about the mean in accordance with a normal distribution. The results of this study are presented in Table 4.1.4.2.1-1 and Figure 4.1.4.2.1-2 compared to other structural antenna types.

4.1.4.2.4 INFLATABLES AND MESH TYPE STRUCTURES

This type of construction consists of the expansion of a thin-wall inflatable structure. The structural material could consist of an expanded mesh or a material similar to Echo II material.

Figure 4.1.4.2.4-1 presents both present and anticipated values of D/σ and rms versus diameter. The present values are based on manufacturing and erection deviation data supplied by Viron Corporation and Schjeldahl Corporation for the small sizes (3 meter diameter) and by data on the Echo balloons for the large size diameters. Information on structures of the type being considered in the intermediate size regime is not available and hence values for this region must be interpolated. It is expected that a full order of magnitude increase in D/σ is obtainable within the next 10 years. This is reflected in Figure 4.1.4.2.4-1 for the anticipated values.

4.1.4.2.5 FEED POSITION

Antenna mechanical characteristics have thus far been referenced only to the deviations of the antenna surface. Of equal importance to the electrical performance are the deviations from the nominal position of the feed (prime focus system) or the secondary reflector (Cassegrainian system). The

deviation of the feed or secondary reflector must be kept nominally at or below 1/20 of a wavelength or severe defocusing will occur. An analysis was made of a representative erectable tetrapod and is presented below.

4.1.4.2.5a ERECTION TOLERANCE

From Figure 4.1.4.2.5a-1 the following relationships are evident:

$$d_i = L\varphi_i \quad (1)$$

$$\varphi_i = \frac{\delta}{\ell} (i-1) \quad (2)$$

$$d_{\text{total}} = \sum_{i=1}^N d_i + \frac{\delta}{2} (i-1) \quad (3)$$

substituting (1) and (2) into (3) and closing the summation yields

$$d_{\text{total}} = \frac{\delta}{\ell} L + \frac{\ell}{2} \frac{N(N-1)}{2} \quad (4)$$

where the following nomenclature is used

C = compressed packaged length

d_i = deviation caused by "i" segment

d_{total} = summation of all d_i

D_i = diameter of "i" segment

δ = minimum clearance between the I.D. of the "i" segment and the O.D. of the "(i+1)" segment

φ_i = angular difference between "i" segment and the "(i-1)" segment

ℓ = engaged length

L = extended length of each segment

N = total number of segments

$R = \frac{C}{S}$ = ratio of package length to extended length

S = total extended length of tetrapod

Again from Figure 4.1.4.2.5a-1 the following relationships are obtained

$$S = NL + \ell \quad (5)$$

$$C = L = \ell \quad (6)$$

then

$$L = \left(\frac{S - C}{N - 1} \right) \quad (7)$$

defining $\frac{C}{S} = R$ the ratio of packaged length to extended length and substituting (7) and (6) into (4) yields non-dimensional form:

$$\frac{d_{\text{total}}}{S} = \left[\frac{(NR - 2R + 1)(NR)(N - 1)}{4(NR - 1)} \right] \quad (8)$$

This equation is shown graphically in Figure 4.1.4.2.5a-2. It is seen that for a given value of C/S (compressed length/extended length) there is an optimum number of boom segments to use based on a minimum value of d_{total}/S (ratio of the tip deflection to the extended length). On the basis of the figure, and using packaging ratio restrictions as imposed by the Saturn IB, shroud computations were made to relate the feed (or secondary reflector) structural support tip deflection to aperture diameter. These erection tolerance build-ups combined with calibration tolerance build-ups are presented in Figure 4.1.4.2.5a-3.

4.1.4.2.5b OPERATION TOLERANCES

An analysis was also performed as to the normal deflections an erectable feed or secondary reflector support would make under operational

loading. The results of this are presented in graphical form in Figure 4.1.4.2.5b-1 and are based on the assumption that with proper thermal design the temperature gradient of the erectable feed support structure can be kept at or below 20°F.

4.1.4.3 ANTENNA WEIGHTS SUMMARY

Antenna weights were calculated as a function of antenna diameter for the different types of antenna under consideration and are presented in Figure 4.1.4.3-1. The weights as shown in this figure include the primary reflector, gas and end cap system if applicable, solid center hub, structural attachment to the satellite and any necessary erection mechanisms.

The types of antennas shown are the single piece rigid antenna, the multiple parabolic array, multiple petal antenna, inflatable/rigidizable antenna and expandable mesh antenna. The diameter of the multiple parabolic array is for the purpose of this figure taken to mean an "equivalent diameter", where the surface area of all the multiple paraboloids are lumped together into one equivalent large paraboloid. The Fresnel antenna was also given consideration but it was determined that no significant increase in the diameter to rms deviation (D/σ) would be obtained compared to the more conventional approaches, while its greater complexity raised other mechanical difficulties.

Two different basic materials are shown for each type of antenna, namely aluminum and Invar. The Invar antennas have been shown to possess superior thermal deflection characteristics because of the low coefficient of thermal expansion of Invar metal ($0.9 \times 10^{-6}/^{\circ}\text{C}$). However, the aluminum antennas may be constructed to a lighter weight due to the greater strength/weight ratio of aluminum. A thermal shade or protective cover would have to be provided for the aluminum antennas in order that the antenna performance not be seriously degraded.

It is noted from Figure 4.1.4.3-1 that the expandable mesh antennas can be made lightest for any given diameter. This is followed in order of increasing weight/unit area by the inflatable/rigidizable, rigid single piece antennas, multiple parabolic arrays, and multiple petal antennas.

Table 4.1.4.1.3b-1

RELATIONSHIP BETWEEN DIFFERENT LOADING CONDITIONS,
FEED FIXITY, AND RMS

Loading Condition	Aperture Diameter Meters (Feet)	rms Referenced To "Best Fit" Parabola		rms Referenced To Fixed Parabola	
		Fixed Focal Length	Variable Focal Length	Fixed Focal Length	Variable Focal Length
Axisymmetric Inertia Loading 0.01 "g's"	3.05 (10)	-	-	-	-
	18.3 (60)	.0002	.0002	.0018	.0009
	30.5 (100)	.0005	.0005	.0051	.0027
	91.4 (300)	.0042	.0041	.0460	.0239
Asymmetric Inertia Loading 0.01 "g's"	3.05 (10)	-	-	-	-
	18.3 (60)	.0003	.0003	.0242	.0242
	30.5 (100)	.0008	.0008	.0673	.0673
	91.4 (300)	.0075	.0075	.6057	.6057
Axisymmetric Thermal Loading	3.05 (10)	.0005	.0005	.0057	.0030
	18.3 (60)	.0031	.0031	.0342	.0178
	30.5 (100)	.0052	.0052	.0571	.0297
	91.4 (300)	.0156	.0155	.1712	.0891
Asymmetric Thermal Loading	3.05 (10)	.0001	.0001	.0037	.0037
	18.3 (60)	.0003	.0003	.0219	.0219
	30.5 (100)	.0006	.0006	.0366	.0366
	91.4 (300)	.0017	.0017	.1097	.1097
Asymmetric Thermal Loading For Mesh Antenna	3.05 (10)	.0087	.0083	.0118	.0117
	18.3 (60)	.0523	.0499	.0706	.0703
	30.5 (100)	.0872	.0832	.1178	.1171
	91.4 (300)	.2616	.2496	.3532	.3513

Table 4.1.4.2-1
COMPARISON OF D/σ VERSUS DIAMETER FOR
DIFFERENT TYPES OF ANTENNA
CONFIGURATIONS

Type	Diameter Meter (ft)	Manufacturing & Erection Surface Characteristics D/σ		Remarks
		Present	Anticipated	
Single Piece Solid	3.05 (10)	100,000	120,000	1) Tolerances held on this type of antenna similar to ground-based antennas.
	18.3 (60)	50,000	75,700	
	30.5 (100)	40,000	66,700	
	91.4 (300)	25,700	51,500	
Multiple Parabolic Arrays	3.05 (10)	300,000	300,000	1) Presently multiple antennas could be held co-planar to an alignment band of 30 arc-sec (three sigma) 2) Anticipated value is improvement to 20 arc-sec
	18.3 (60)	133,000	180,000	
	30.5 (100)	109,000	160,000	
	91.4 (300)	66,700	120,000	
Petal Antennas (Calibrated after Erection)	3.05 (10)	52,300	67,000	1) Individual panel erection tolerance for single-hinged panel 30 arc-sec. 2) Individual panel erection tolerance for double-hinged panel 42 arc-sec. 3) Anticipated value for single-hinged panel is 20 arc-sec and 28 arc-sec for double-hinged panel.
	18.3 (60)	38,000	48,200	
	30.5 (100)	33,100	36,300	
Petal Antennas (Not Calibrated after Erection)	3.05 (10)	19,700	28,600	1) Individual panel erection tolerance for single-hinged panel is 1.5 minutes. 2) Individual panel erection tolerance for double-hinged panel is 2.1 minutes. 3) Anticipated value for single-hinged panel is 1.0 minute and 1.4 minutes for double-hinged panel.
	18.3 (60)	18,300	25,400	
	30.5 (100)	17,600	23,700	
Mesh and Inflatables	3.05 (10)	1,000	10,000	
	18.3 (60)	720	7,200	
	30.5 (100)	650	6,500	
	91.4 (300)	530	5,300	

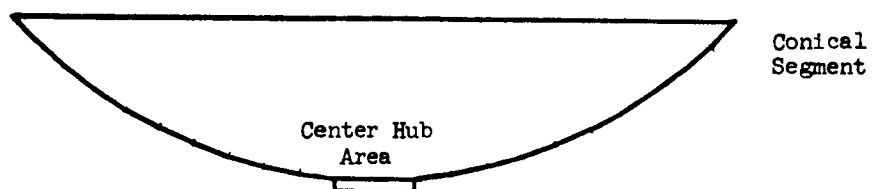
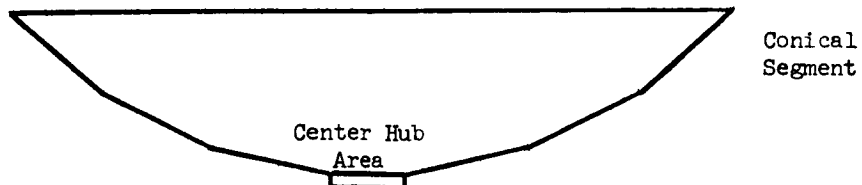
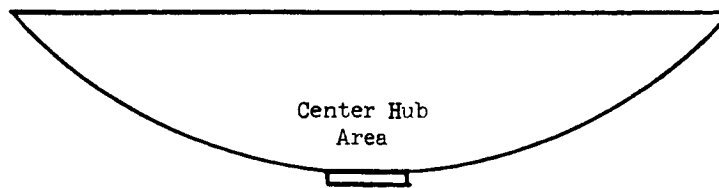
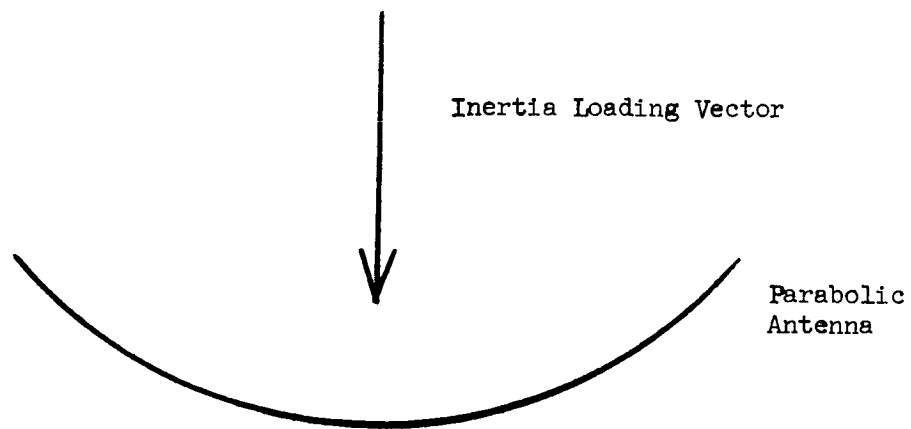
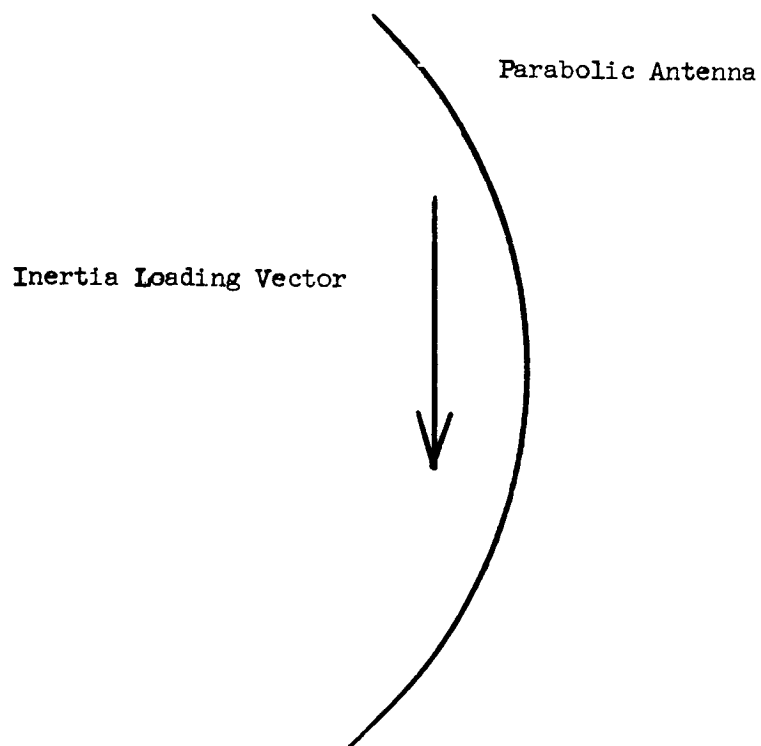


Figure 4.1.4-1. Paraboloid of Revolution Approximation

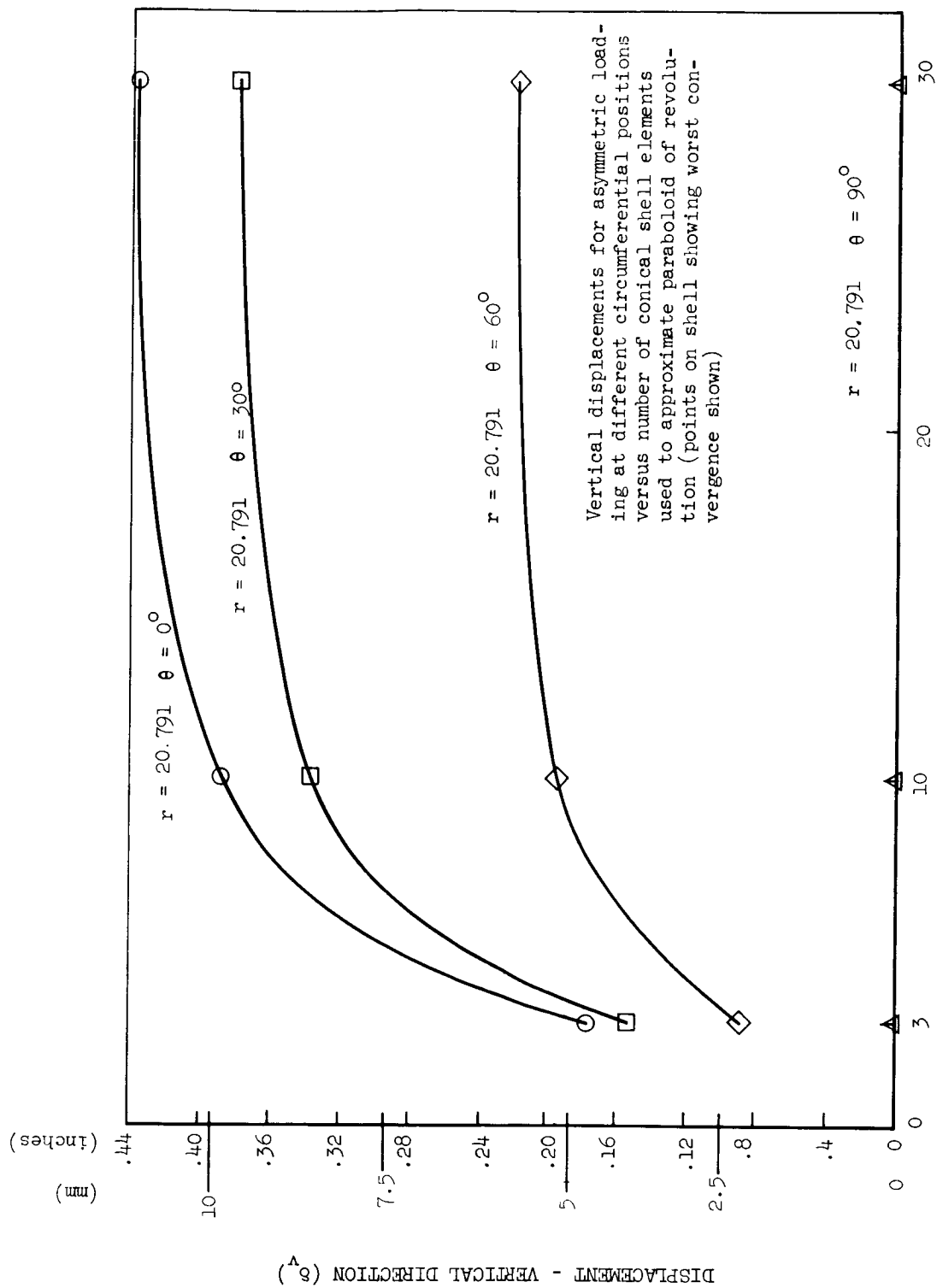


ZENITH DIRECTION --Axisymmetric Loading



HORIZONTAL DIRECTION--Asymmetric Loading

Figure 4.1.4-2. Loading Cases



N - NUMBER OF CONICAL SHELL ELEMENTS USED TO APPROXIMATE PARABOLOID OF REVOLUTION

Figure 4.1.4-3. Vertical Displacement vs Number of Conical Shell Elements

Horizontal displacements for asymmetric loading at differential circumferential positions versus number of conical shell elements used to approximate paraboloid of revolution (points on shell showing worst convergence shown)

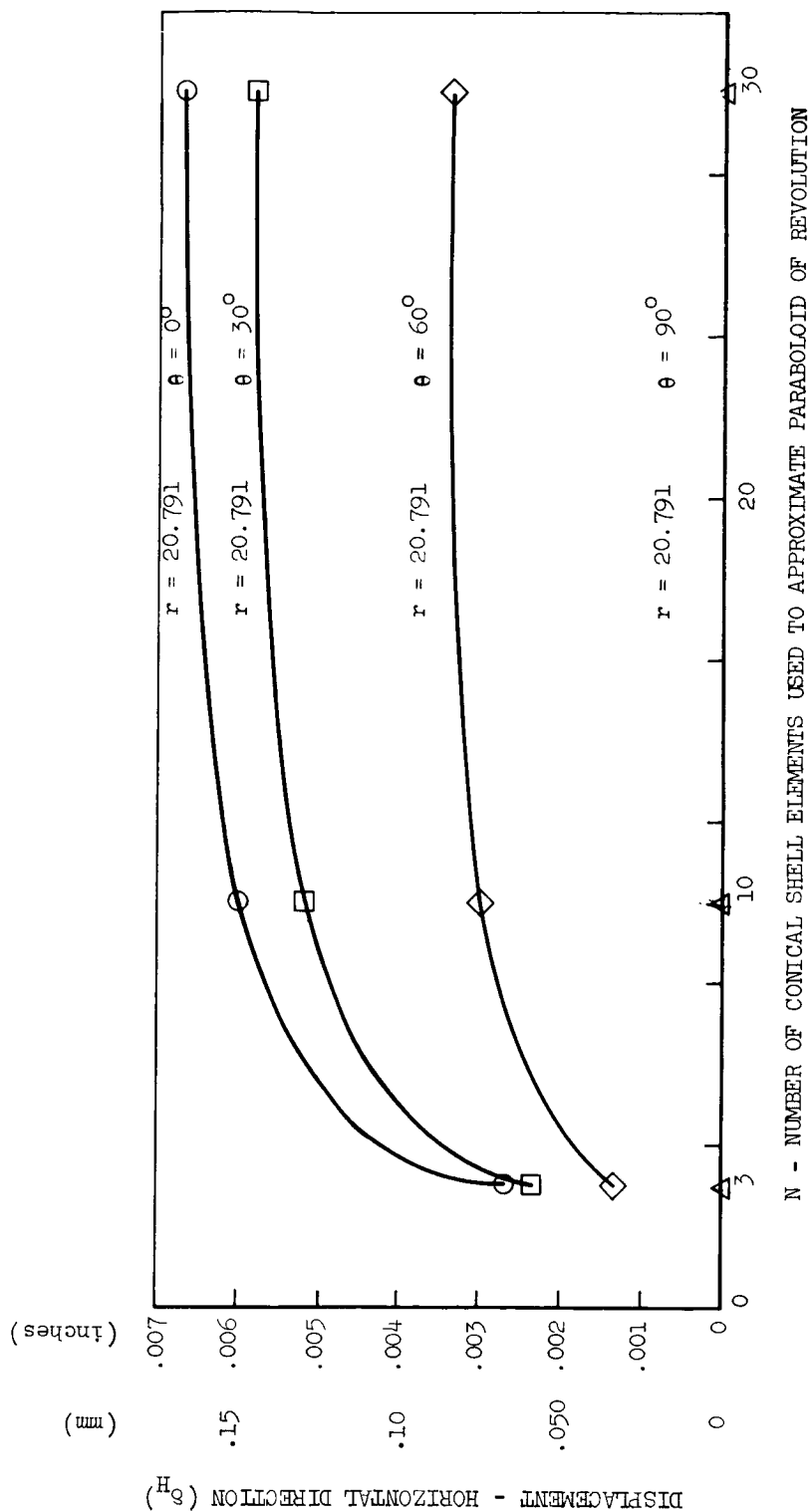
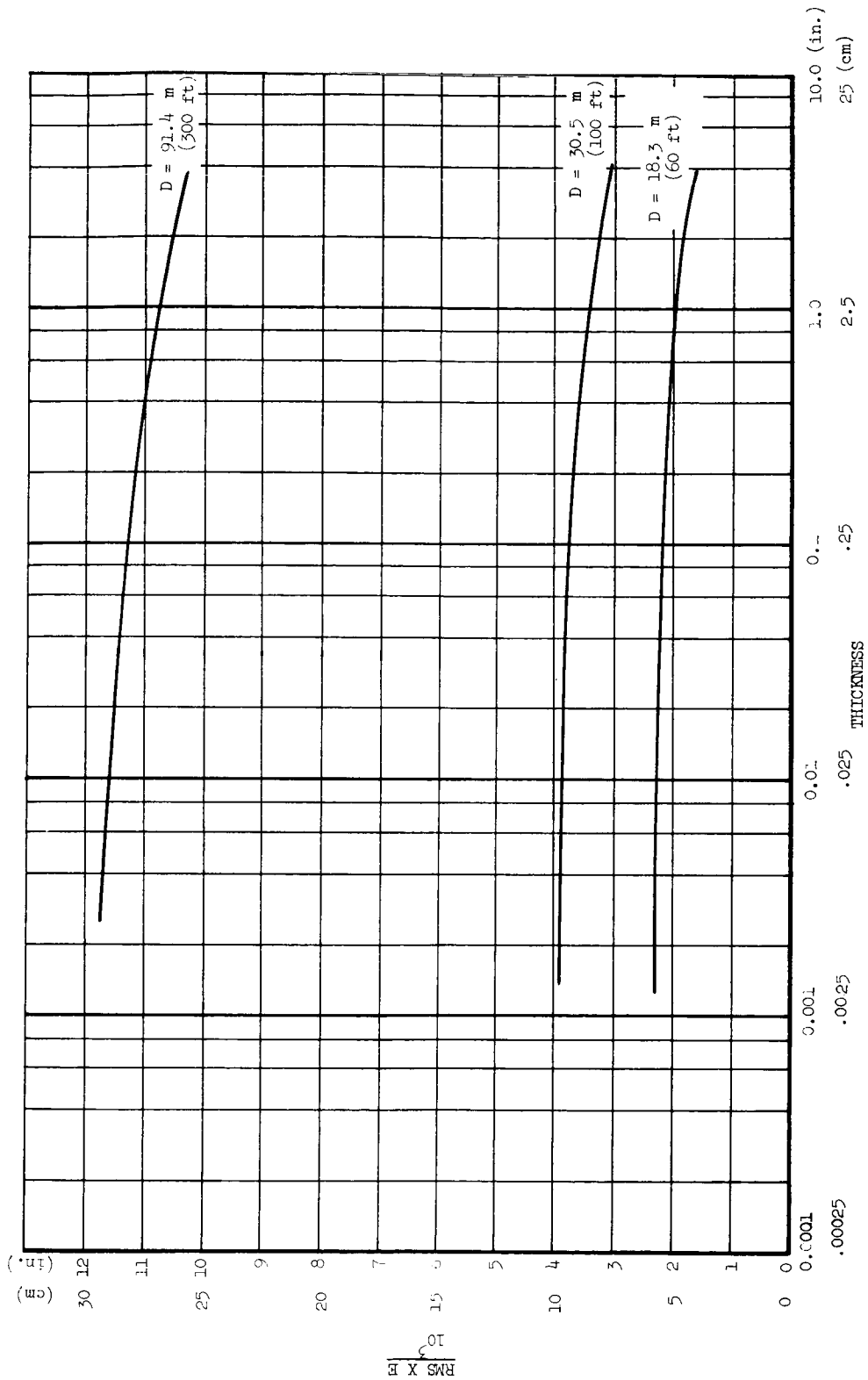
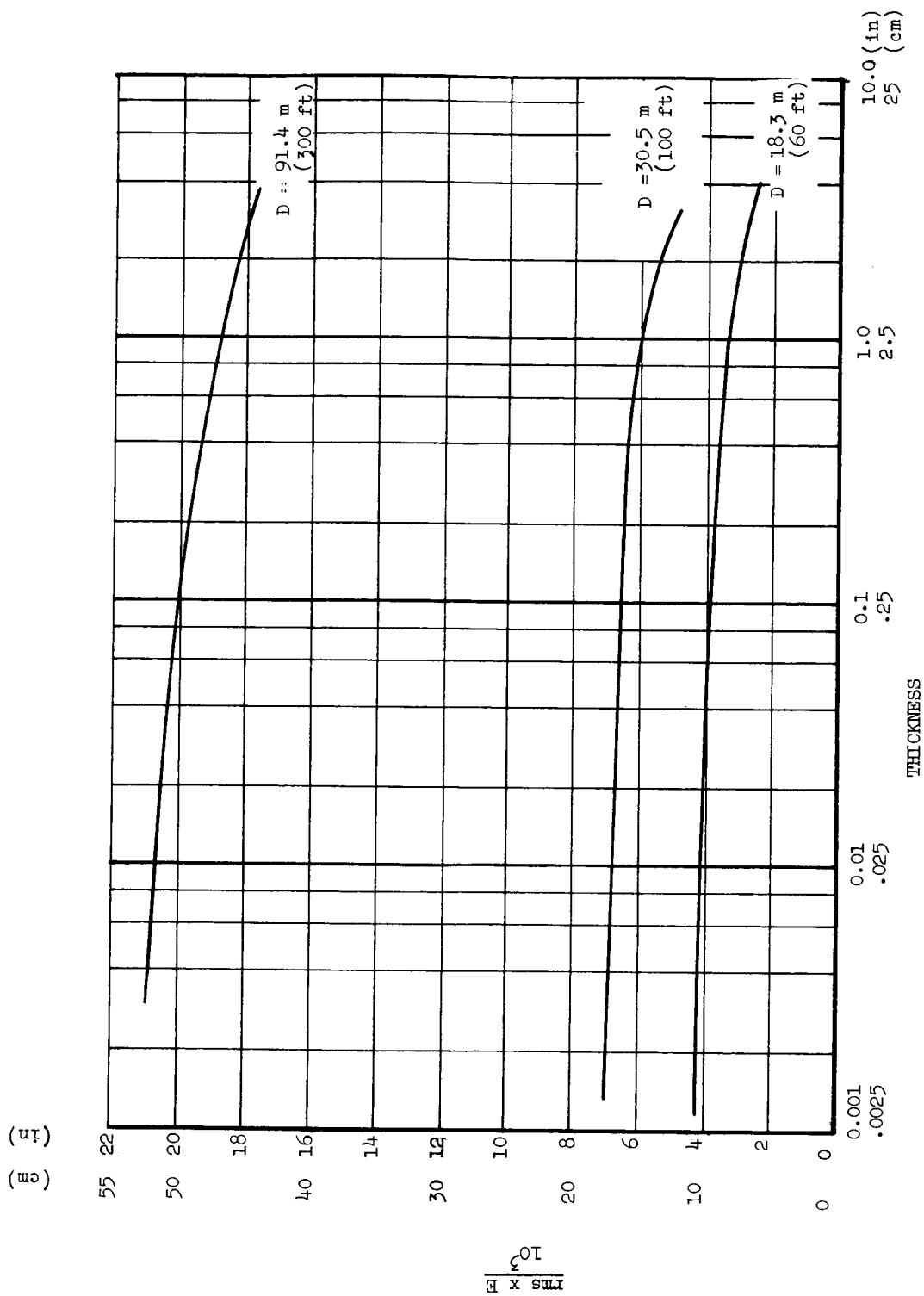


Figure 4.1.4-4. Horizontal Displacement vs Number of Conical Shell Elements



rms vs Diameter for Various Diameters
and Various Values of Elastic Modulus

Figure 4.1.4-5. Inertial Axisymmetric Loading of 0.1 g



rms vs Diameter for Various Diameters
and Various Values of Elastic Modulus

Figure 4.1.4-6. Inertial Asymmetric Loading of 0.1 g

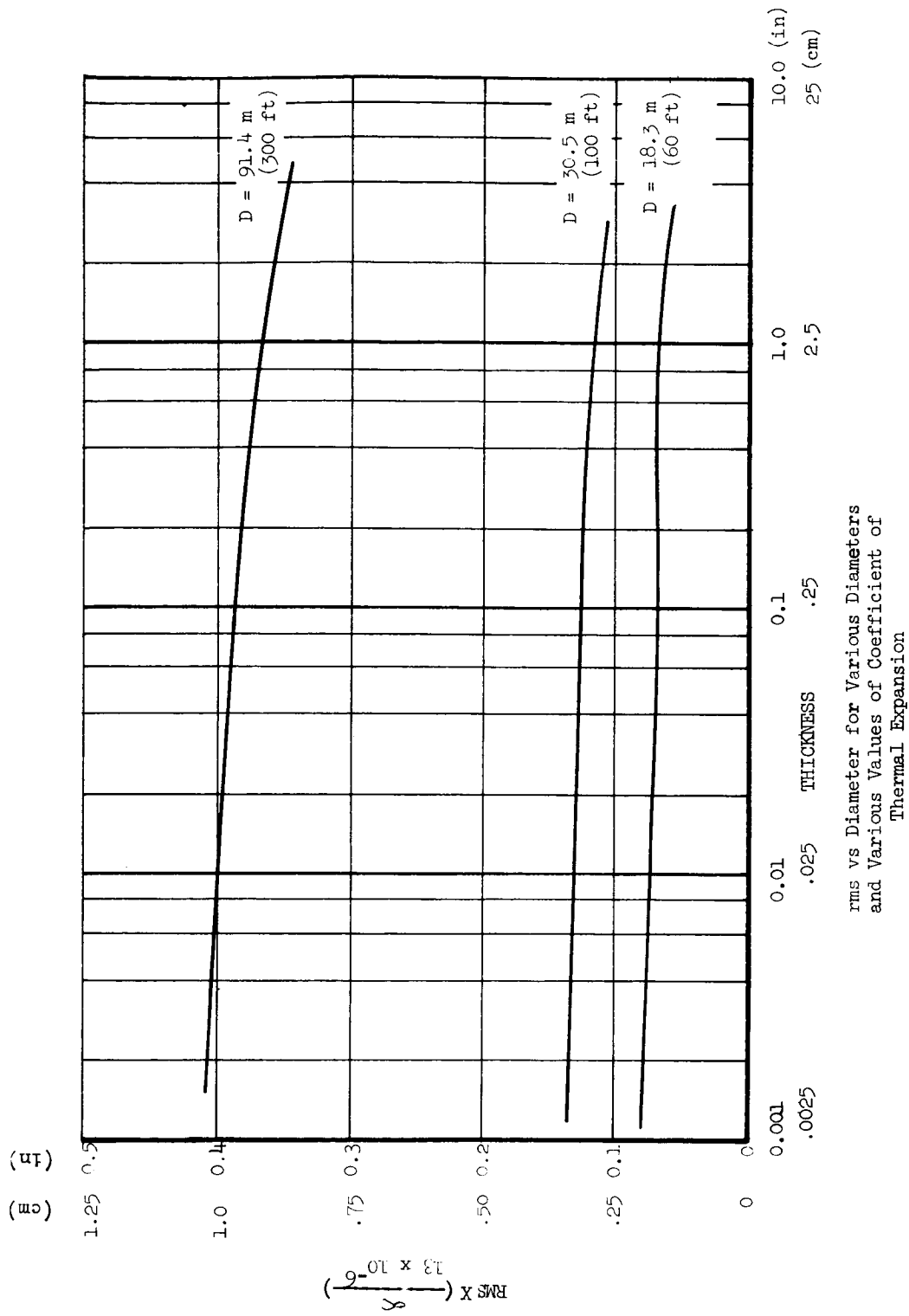
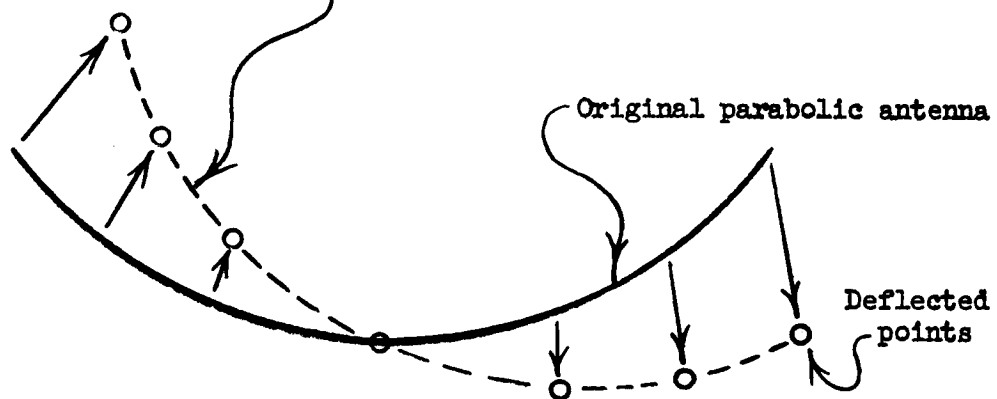


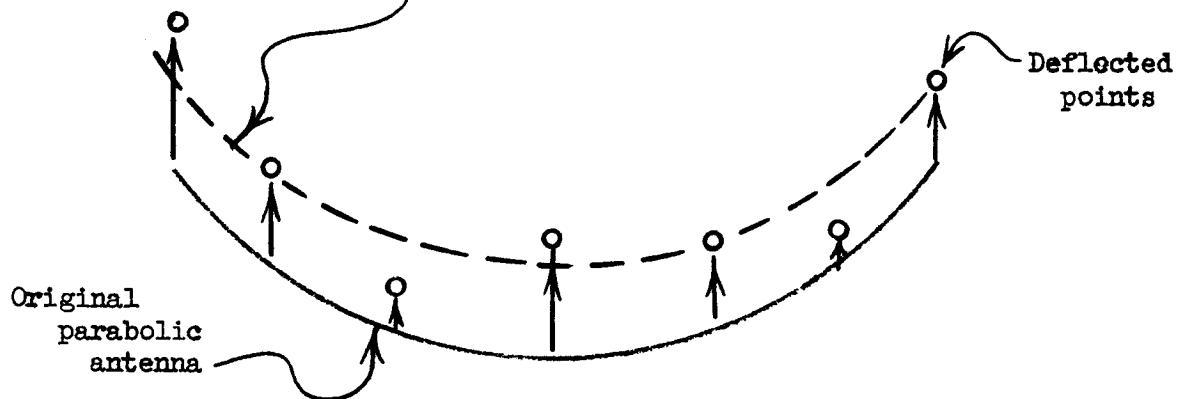
Figure 4.1.4-7. Axisymmetric Thermal Loading

Best fit parabola in least squares sense
to distorted points



Example of Low RMS Achieved Because Deflected Points Could
be Minimized by a Rotation of the Original Antenna.

Best fit parabola in least squares sense to
distorted points



Example of Large RMS Achieved Because Deflected Points Could
Not be Minimized as Effectively as Above.

Figure 4.1.4.1-1. Achievable RMS's

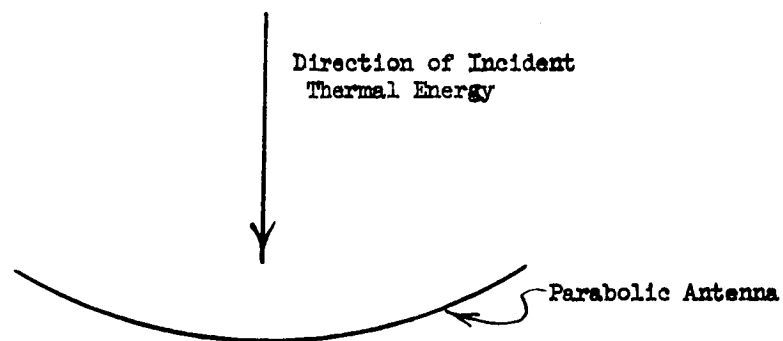


Figure 4.1.4.1.2-1a. Axisymmetric Thermal Condition

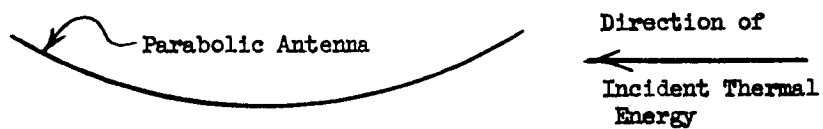


Figure 4.1.4.1.2-1b. Asymmetric Thermal Condition

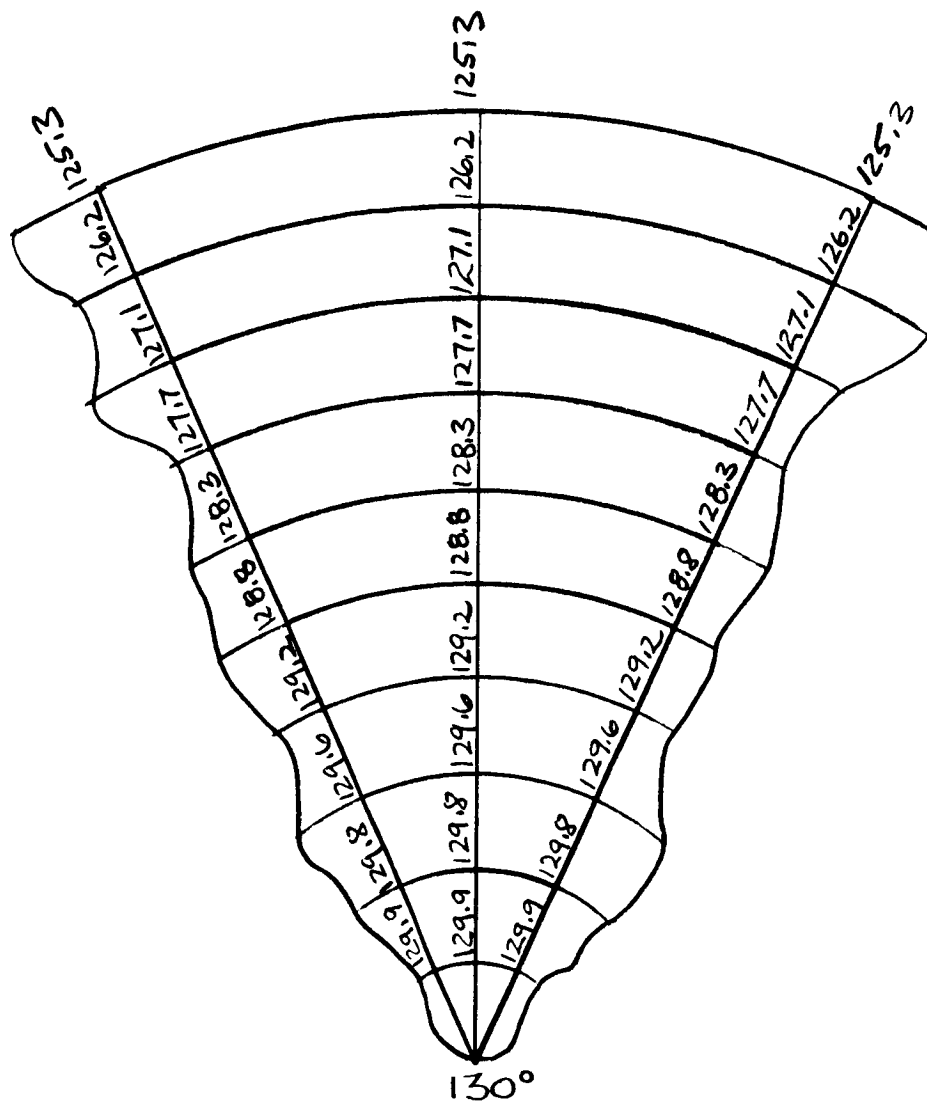


Figure 4.1.4.1.2-2. The Temperature Distribution Along a Meridian for The Axisymmetric Thermal Condition (Degrees Fahrenheit)



Diagram Showing " θ " - The Angle That a Tangent to the Antenna Along A Meridian Makes With the Aperture Plane

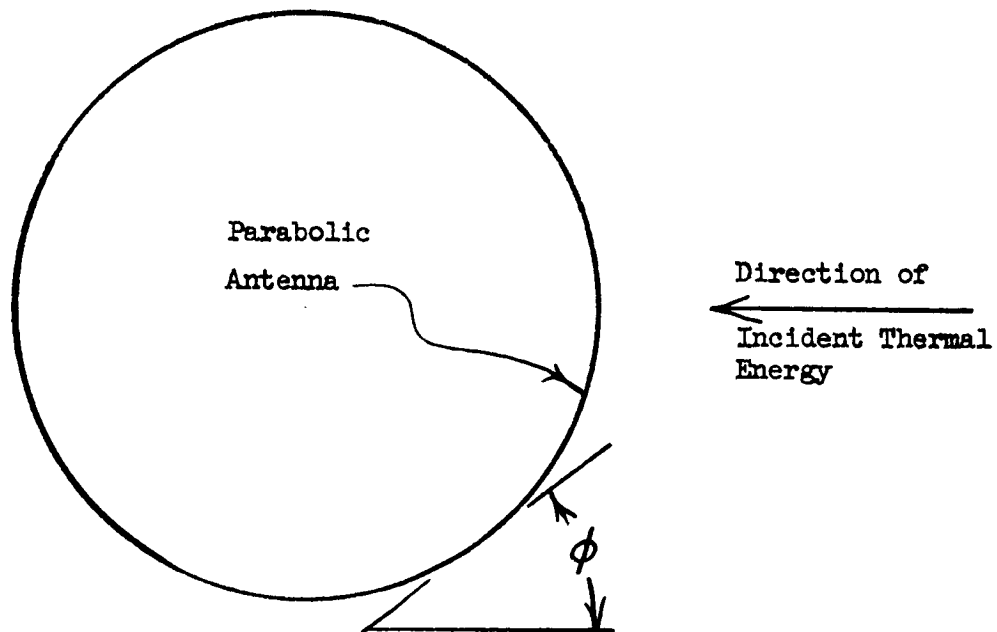


Diagram Showing " ϕ " - The Angle That a Circumferential Tangent to the Antenna Makes with the Sun Position Vector

Figure 4.1.4.1.2-3. Antenna Angle Definitions

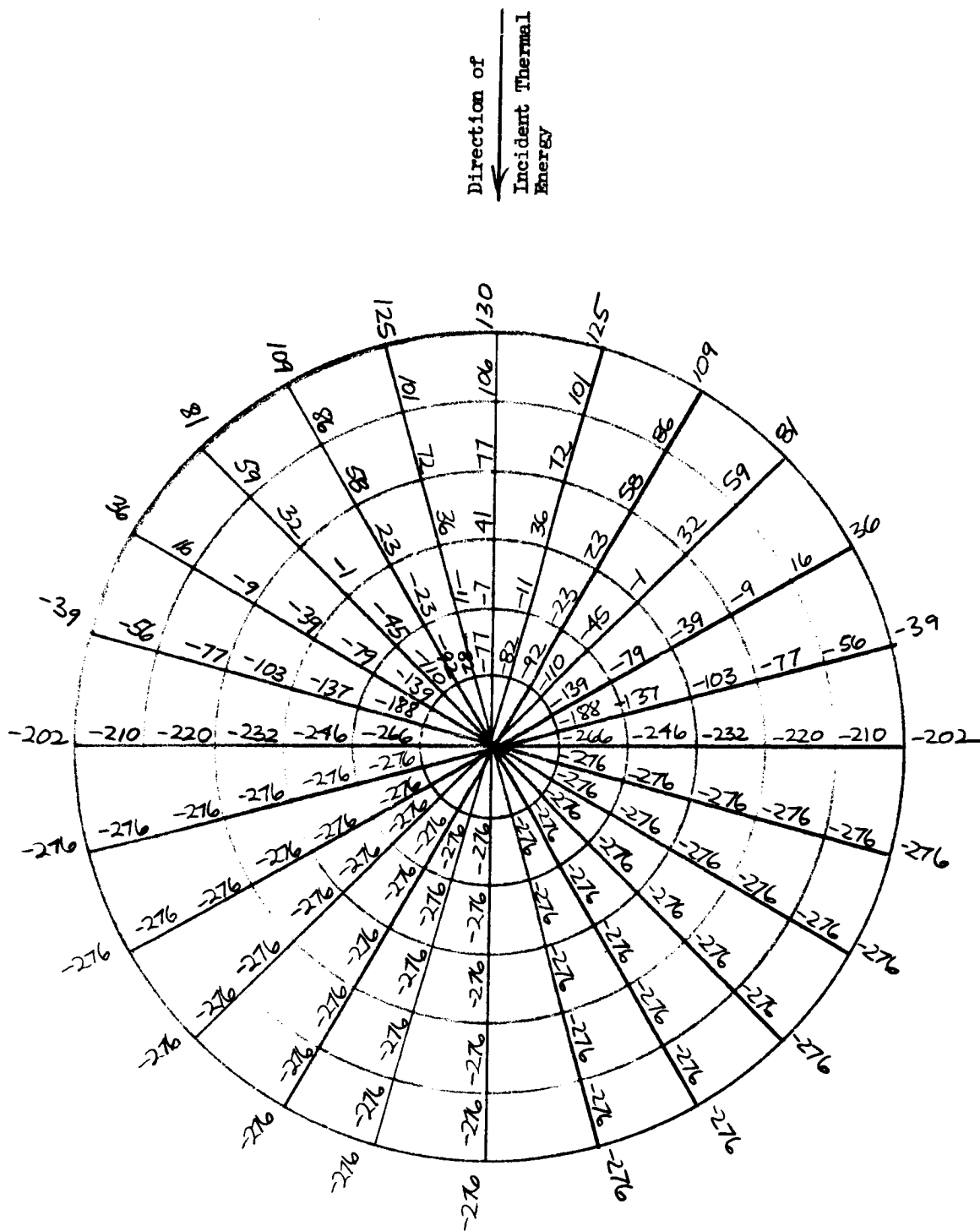


Figure 4.1.4.1.3a-1. The Temperature Distribution on The Solid Parabolic Antenna for the Asymmetric Thermal Condition (Degrees Fahrenheit)*

* Computer Program printed out Fahrenheit Degrees.

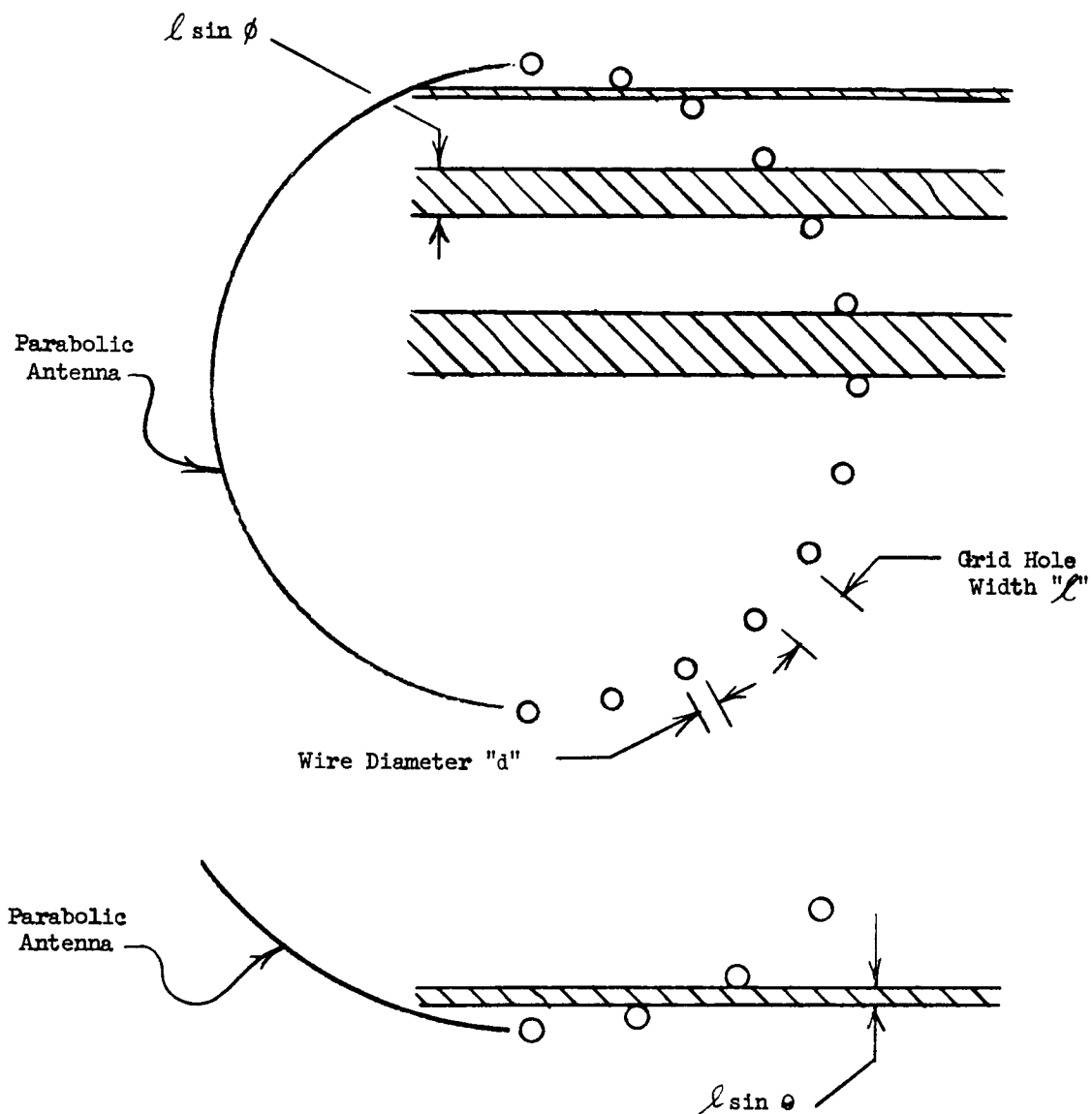
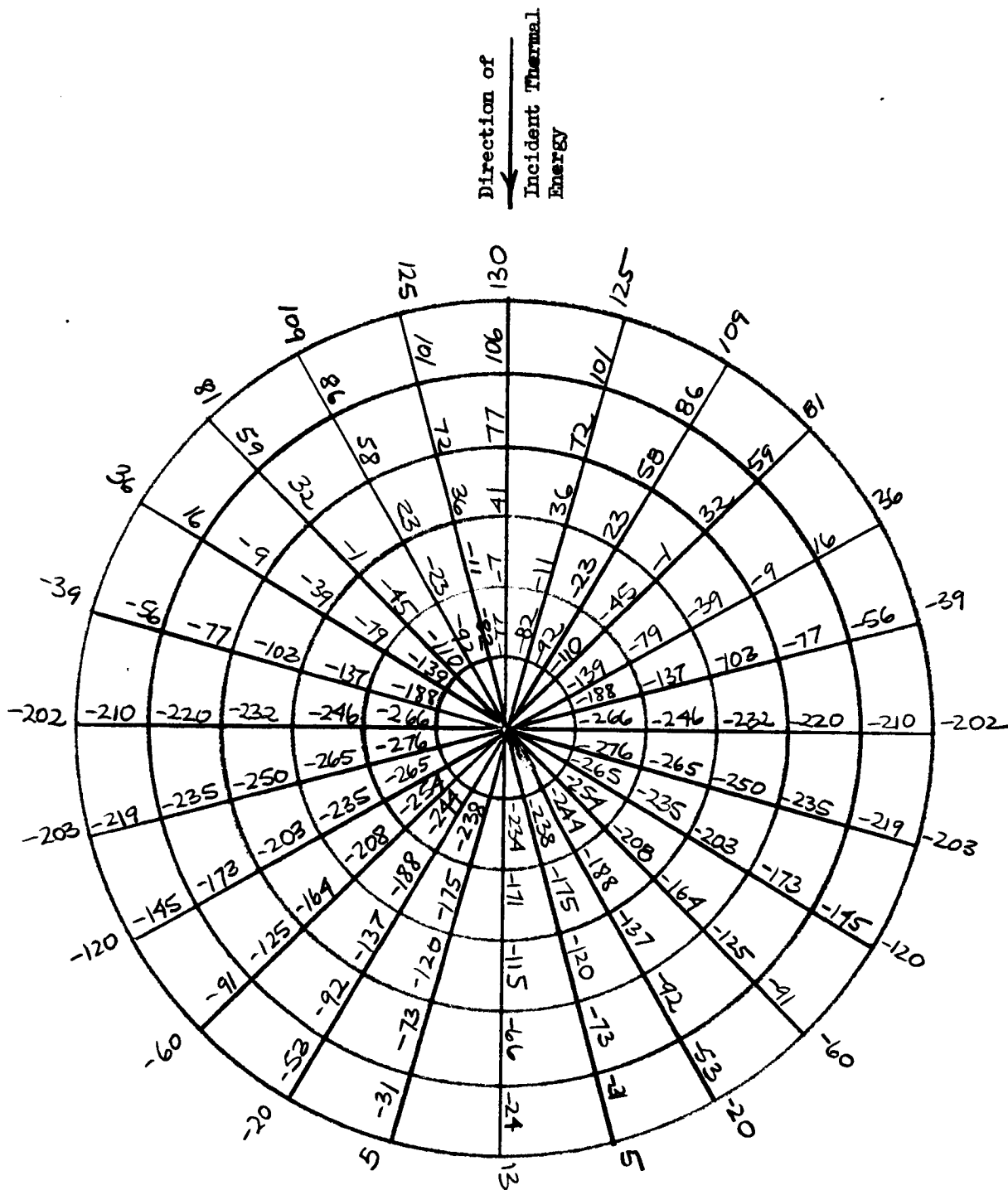


Figure 4.1.4.1.3b-1. Diagram Showing That the Thermal Energy Impinging on the Side of the Antenna Away from the Sun is a Function of the Ratio of the Wire Size to Grid Hole Width



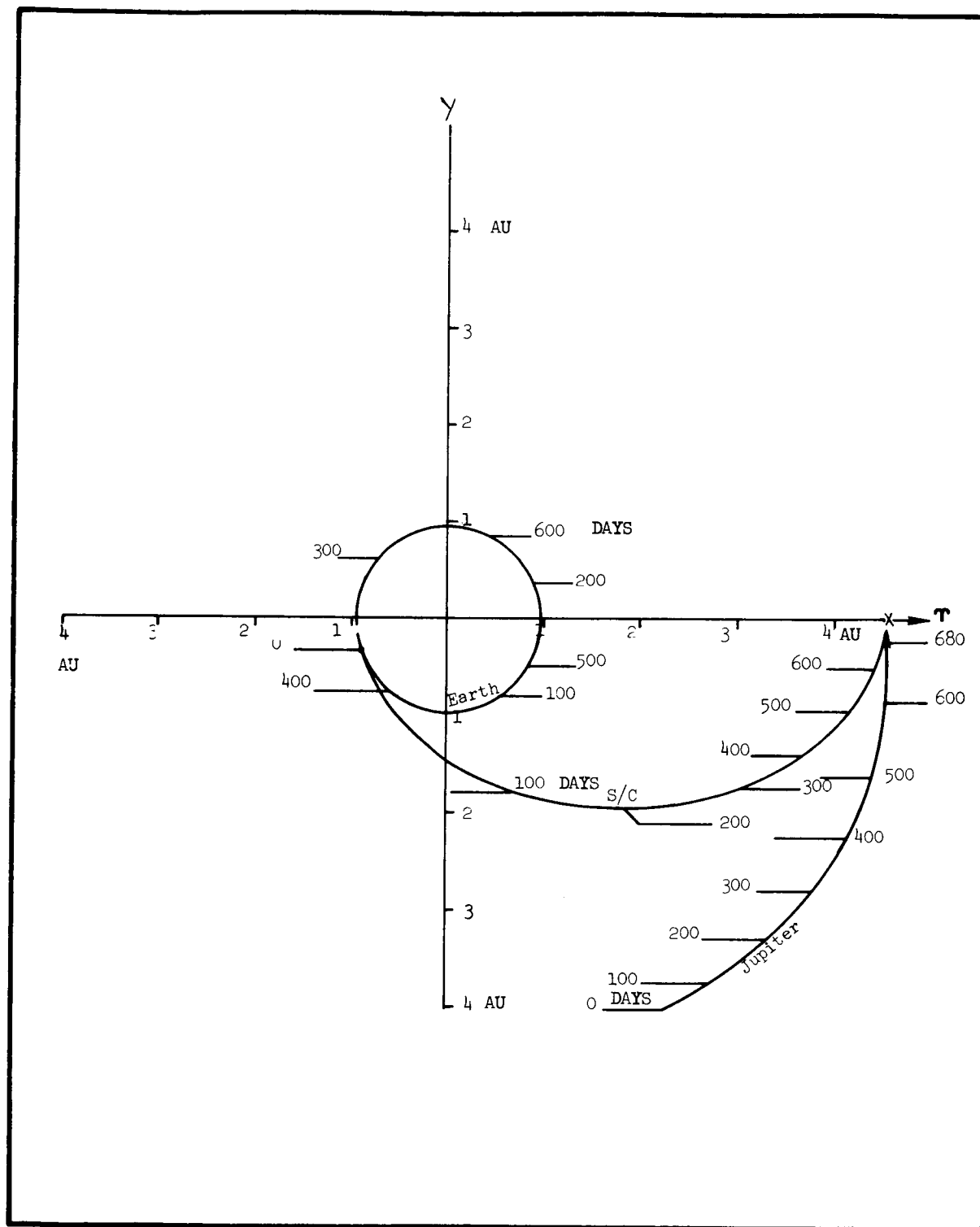


Figure 4.1.4.1.3b-3. RMS Cross Plot at 2.3 GHz

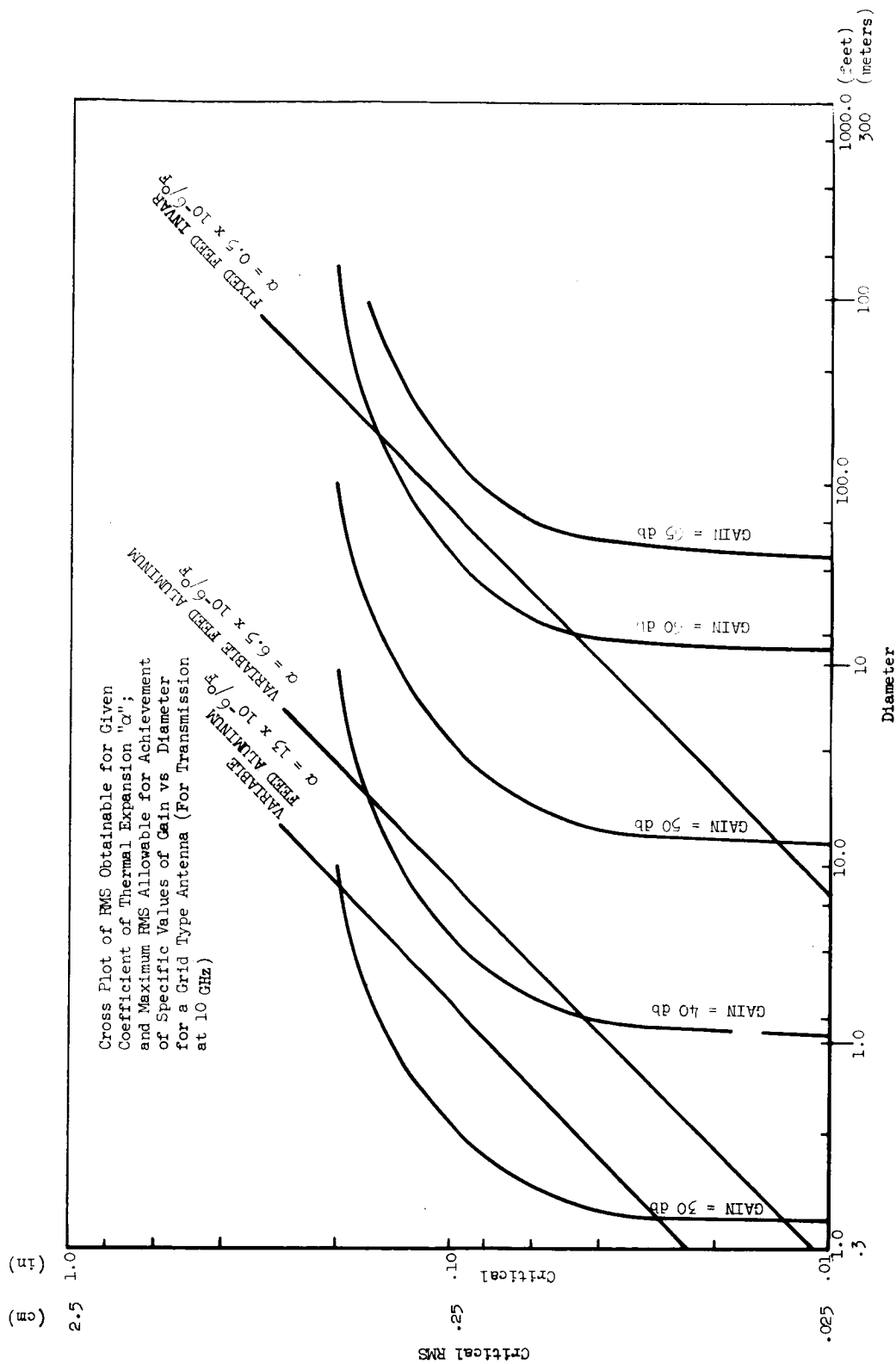


Figure 4.1.4.1.3b-4. RMS Cross Plot at 100 GHz

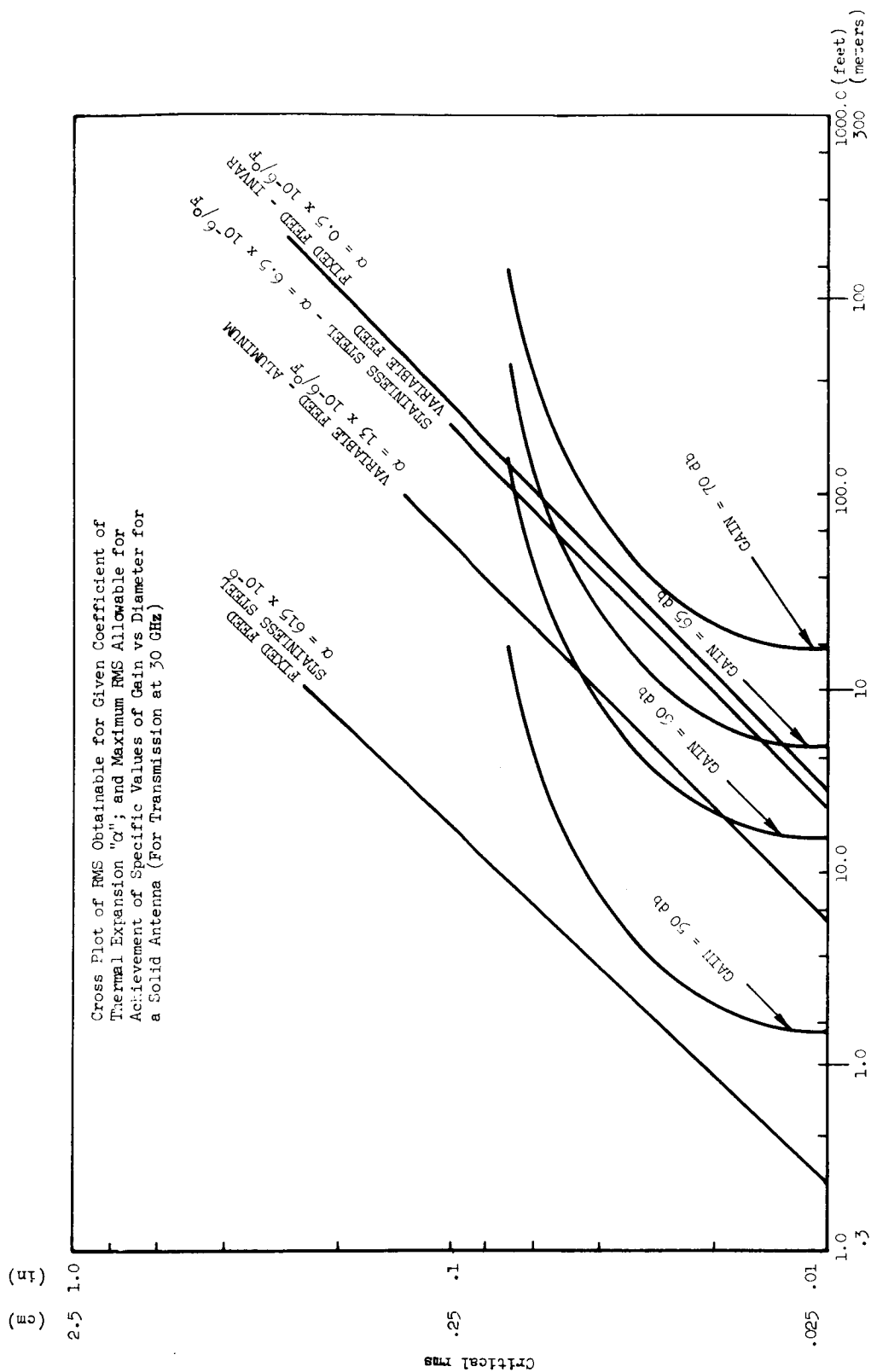


Figure 4.1.4.1.3b-5. RMS Cross Plot at 30 GHz

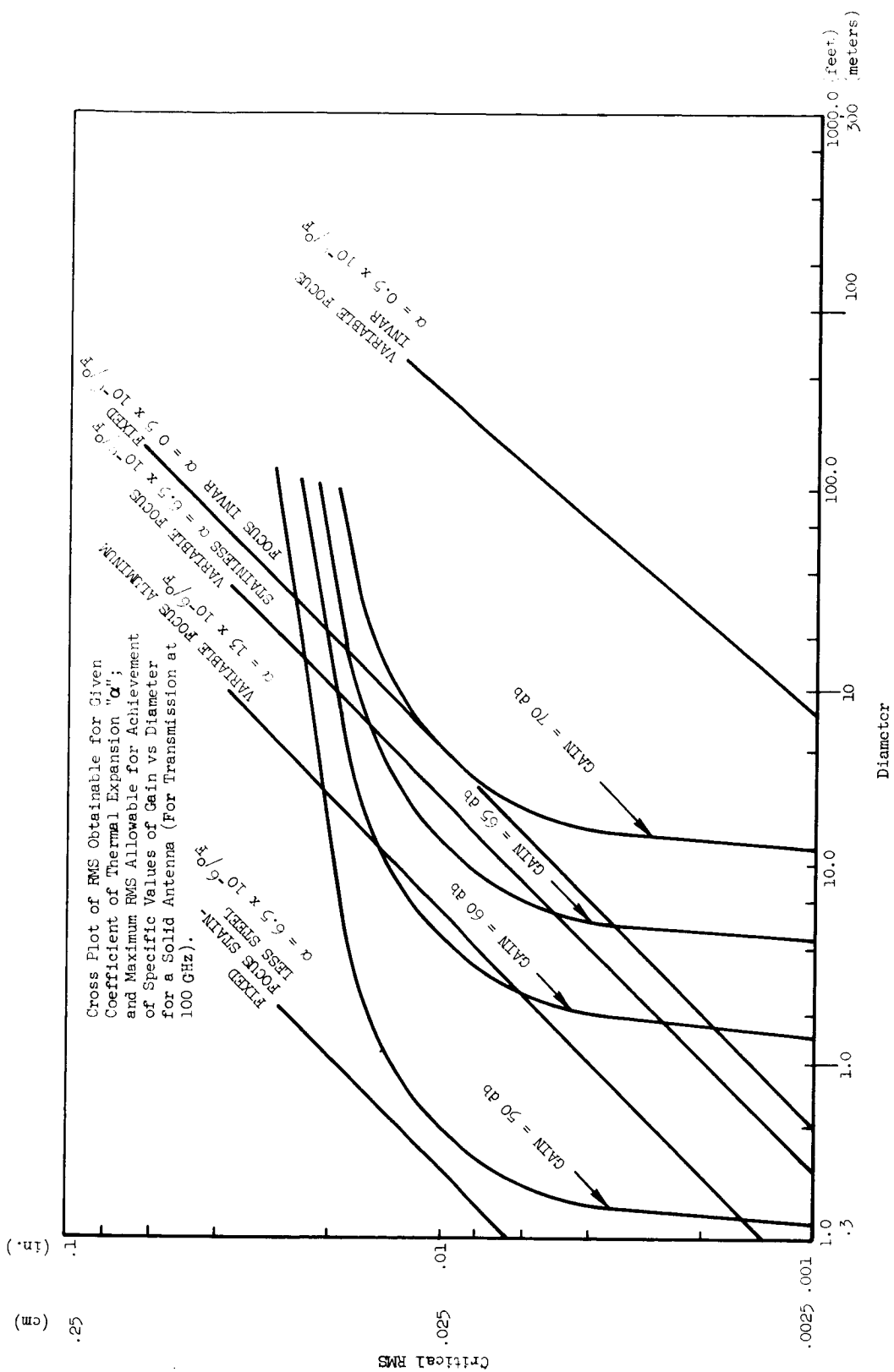


Figure 4.1.4.1.3b-6. RMS Cross Plot at 100 GHz

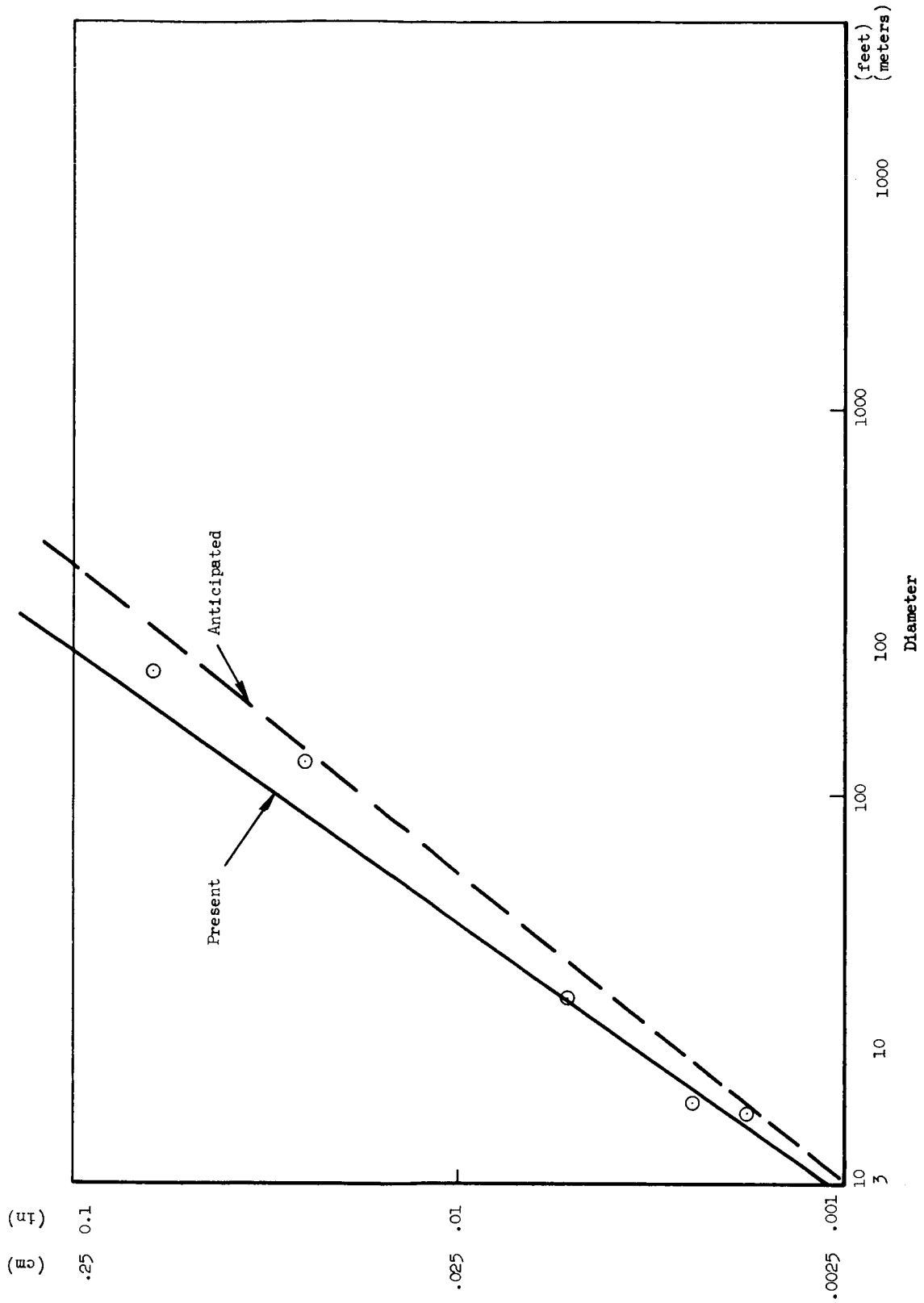


Figure 4.1.4.2.1-1. Relationship Between Manufacturing Tolerance and Antenna Diameter (Solid Rigid Antenna)

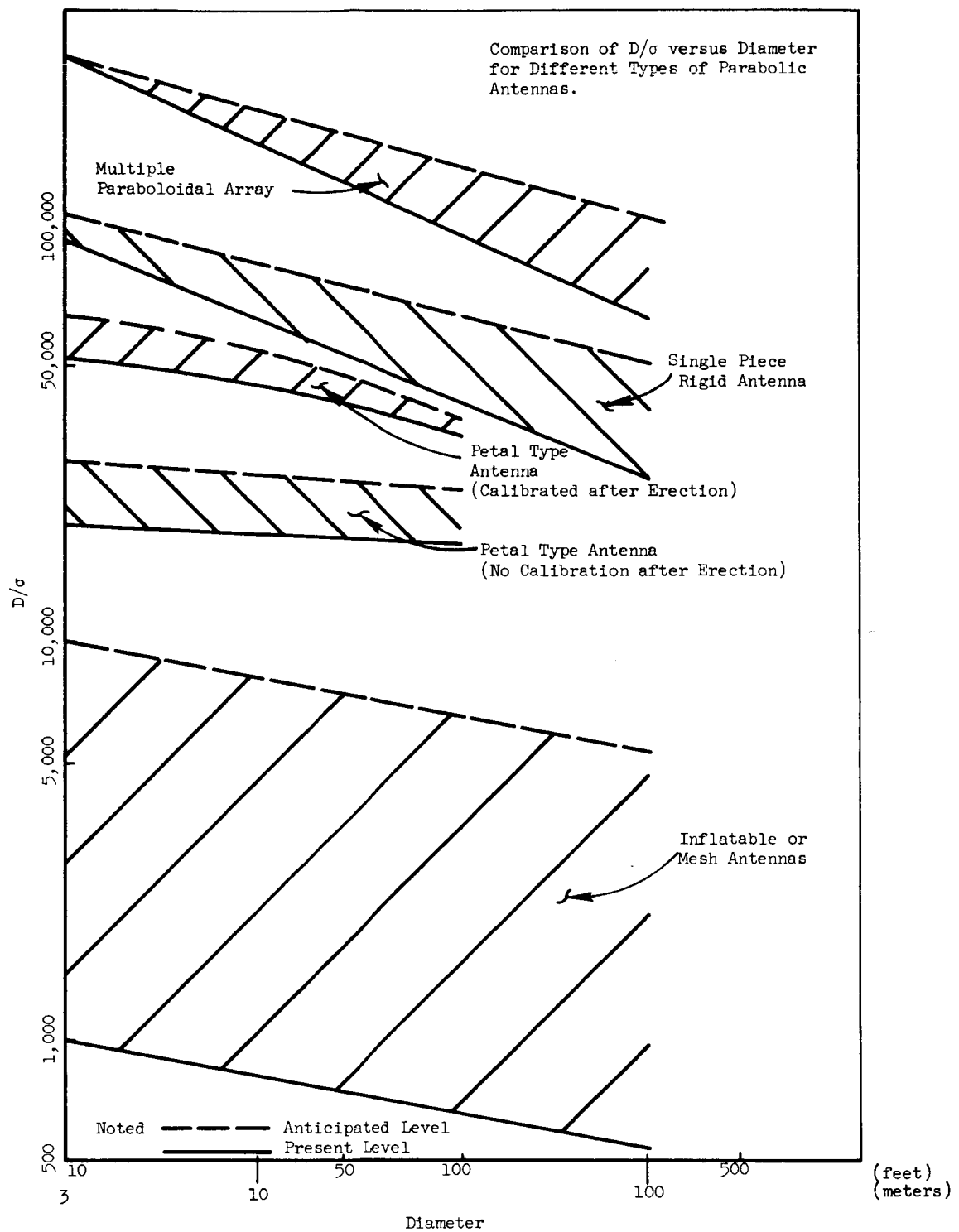


Figure 4.1.4.2.1-2. Comparison of D/σ Versus Diameter for Different Types of Parabolic Antennas

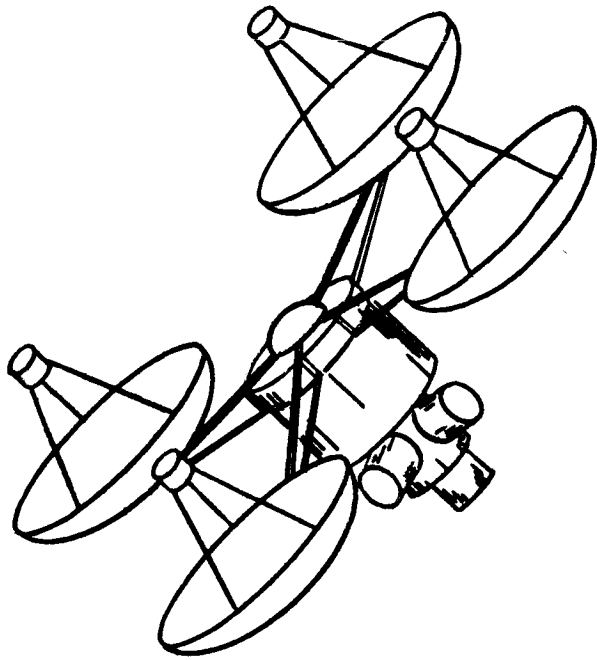


Figure 4.1.4.2.2-1. Typical Multiple Paraboloidal Antenna Array

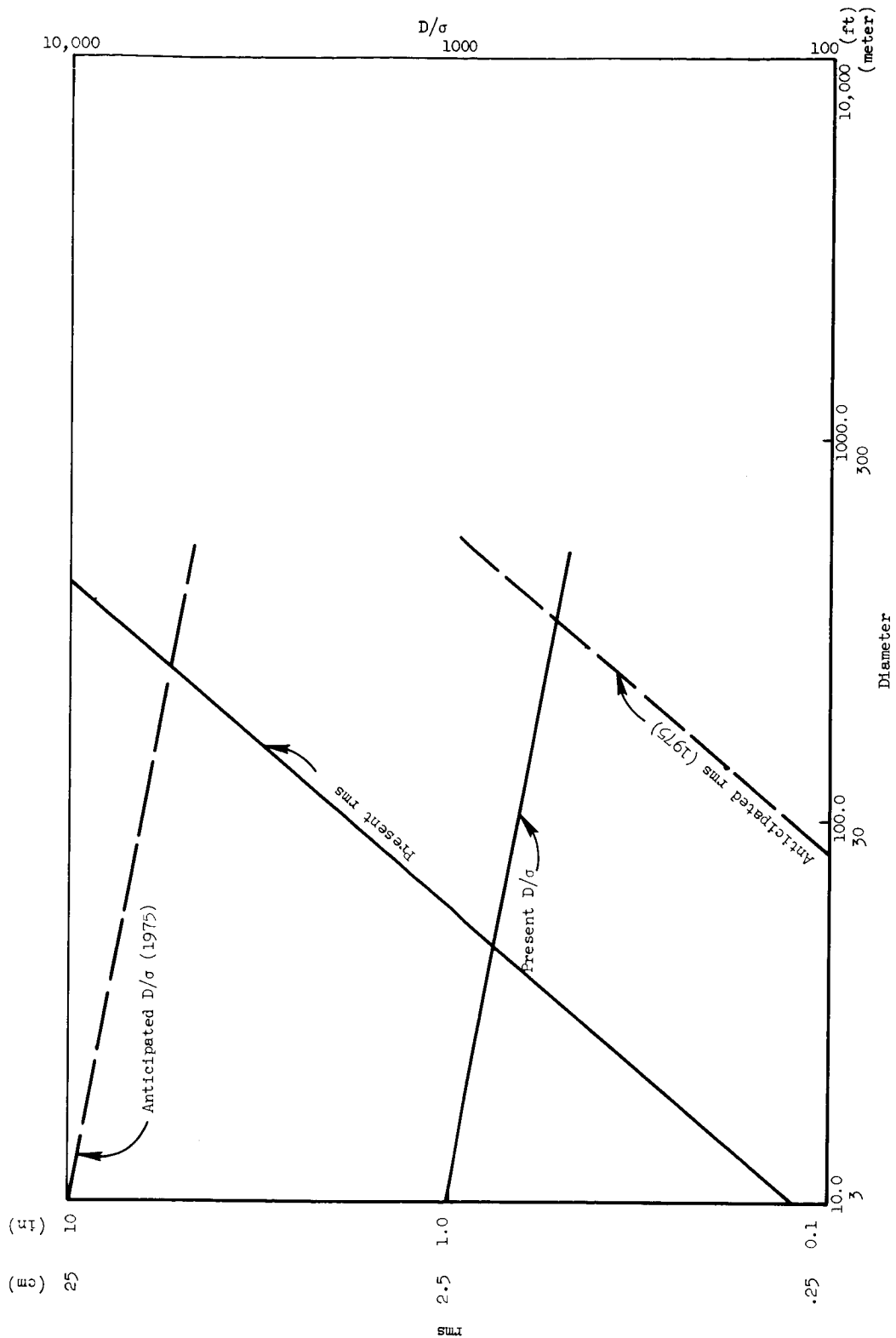


Figure 4.1.4.2.4-1. Present and Anticipated Manufacturing and Erection Tolerances for Mesh Type Antennas

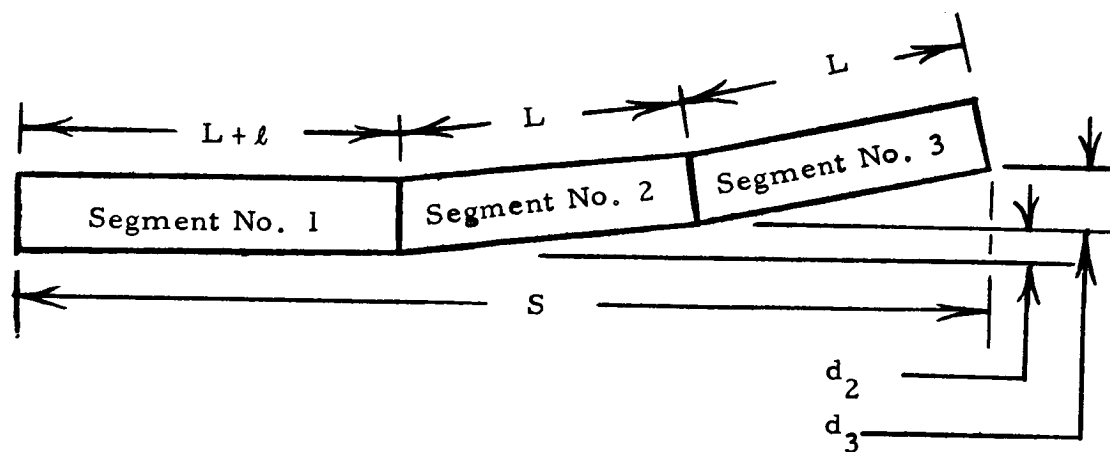
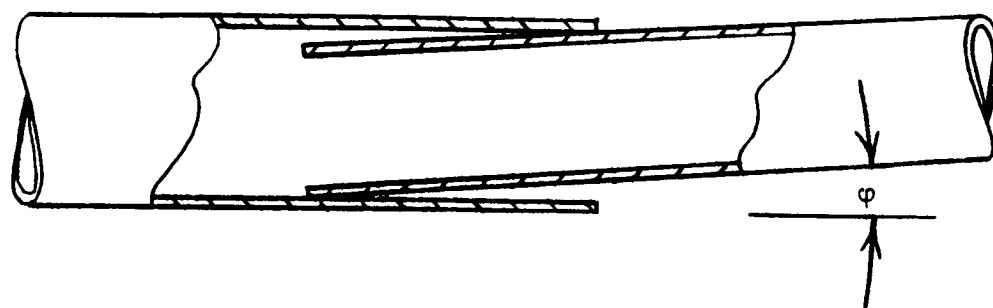
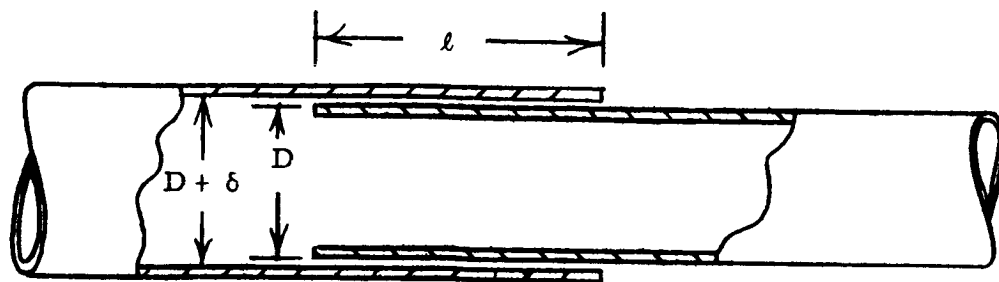


Figure 4.1.4.2.5a-1. Diagrams Showing Relationships Between Segments of Erectable Feed or Secondary Reflector Support

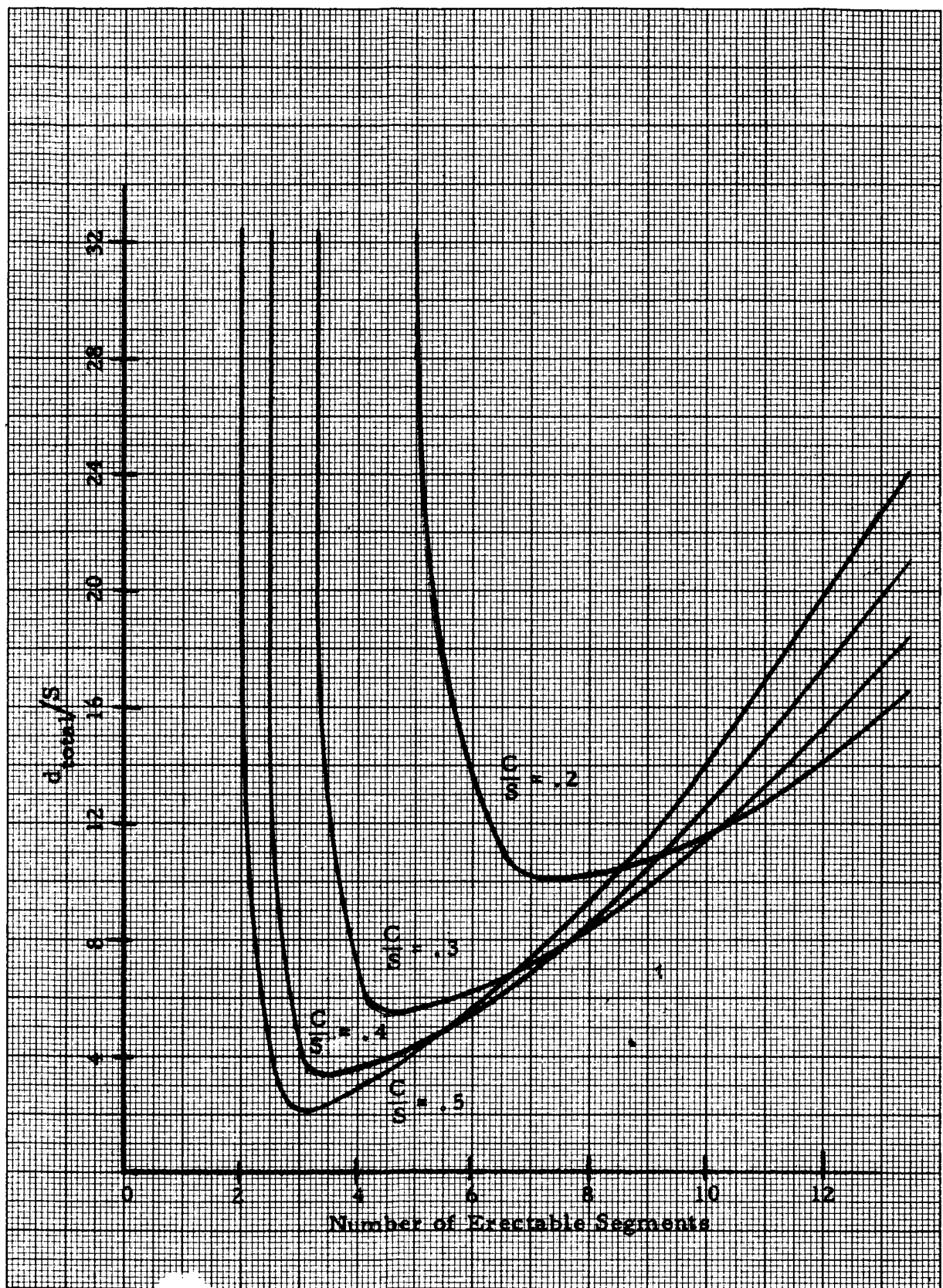


Figure 4.1.4.2.5a-2. Comparison of the Ratio of the Tip Deflection d_{total} to the Extended Length (S) of an Erectable Feed or Secondary Reflector Structure with the Number of Erectable Segments Used....for Various Ratios of Extended Length (S) to Compressed Length (C)

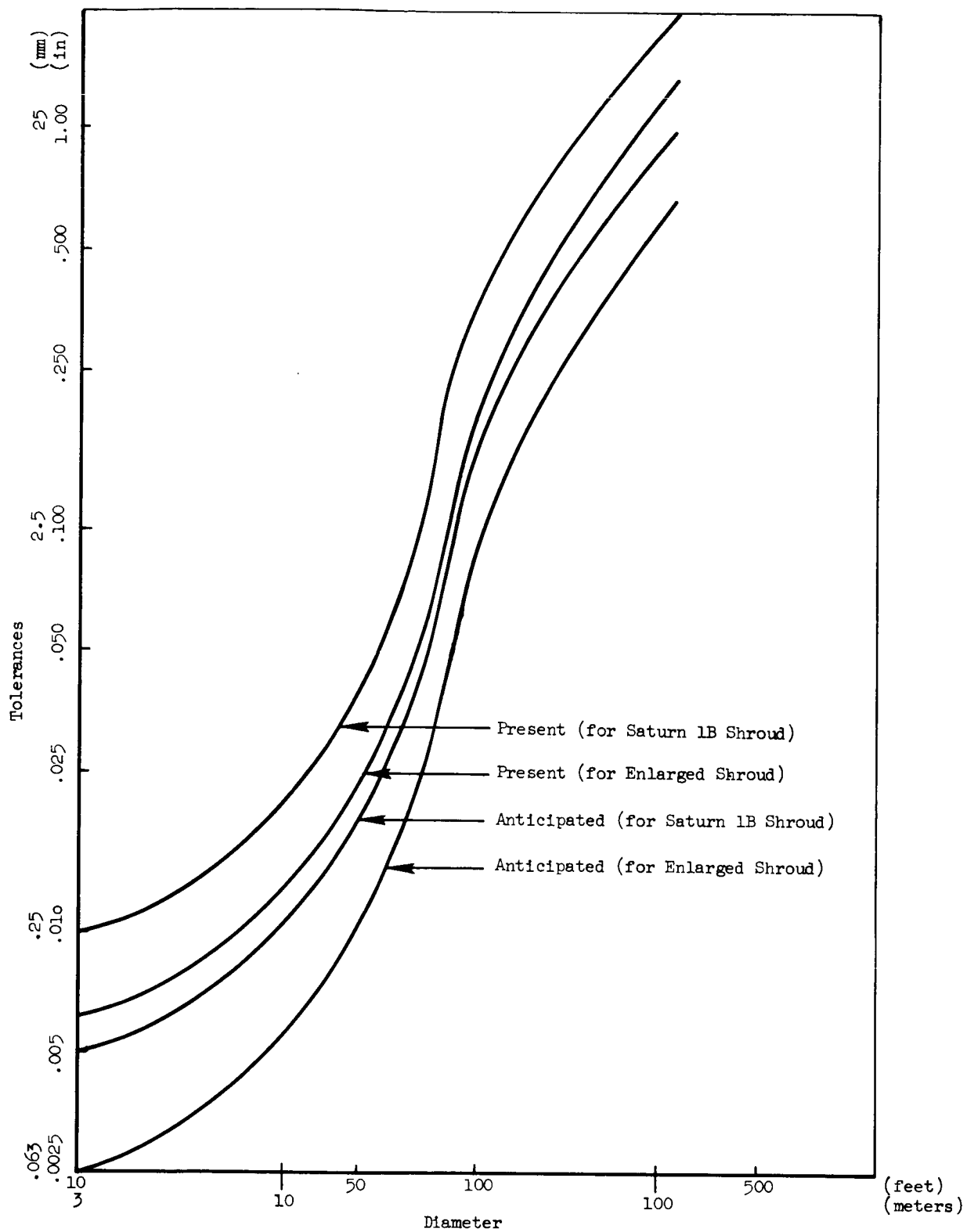


Figure 4.1.4.2.5a-3. Erection and Calibration Tolerances for Erectable Feed vs Antenna Diameter

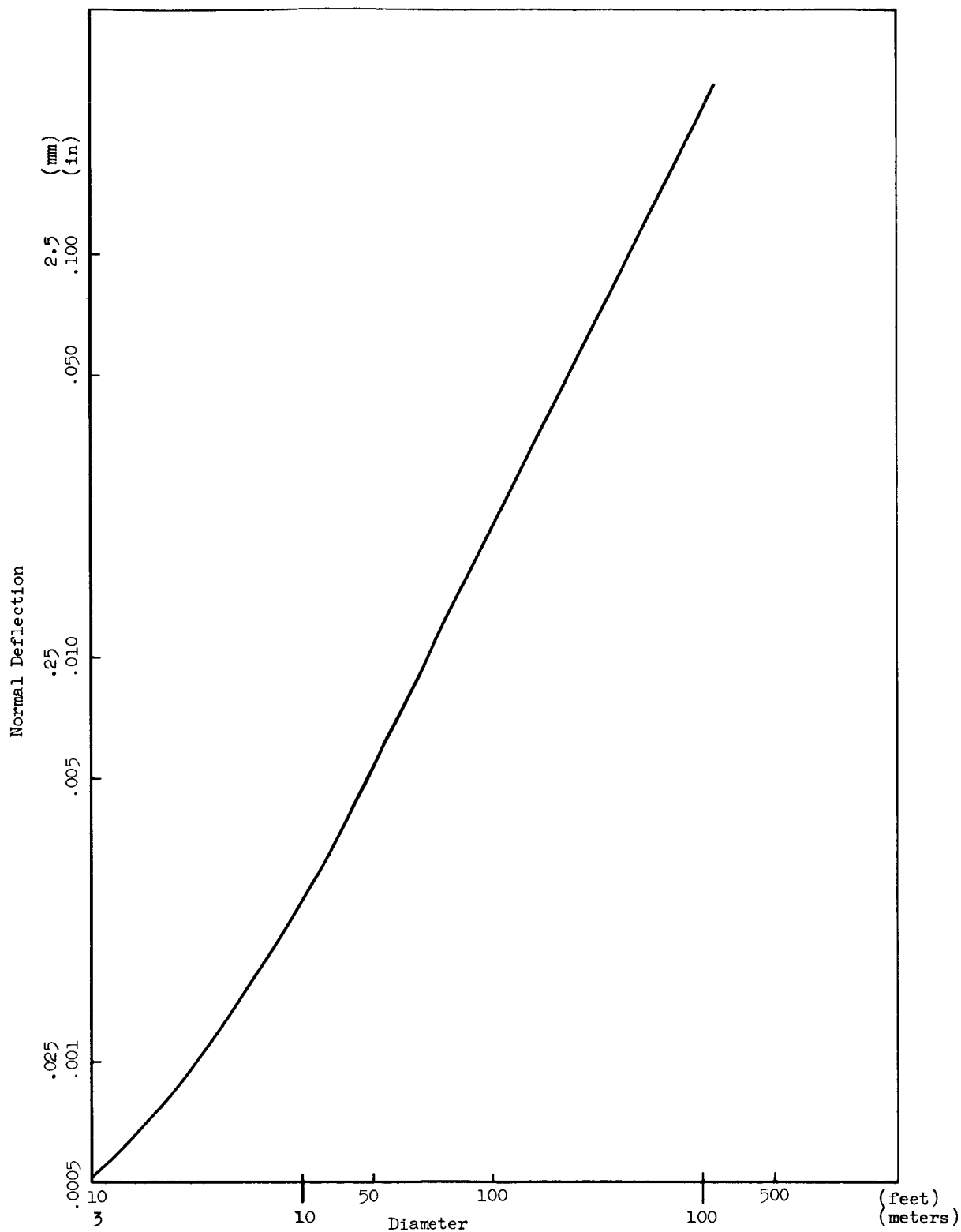


Figure 4.1.4.2.5b-1. Normal Deflection of Secondary Reflector (or Feed) vs Diameter Caused by Thermal Gradient

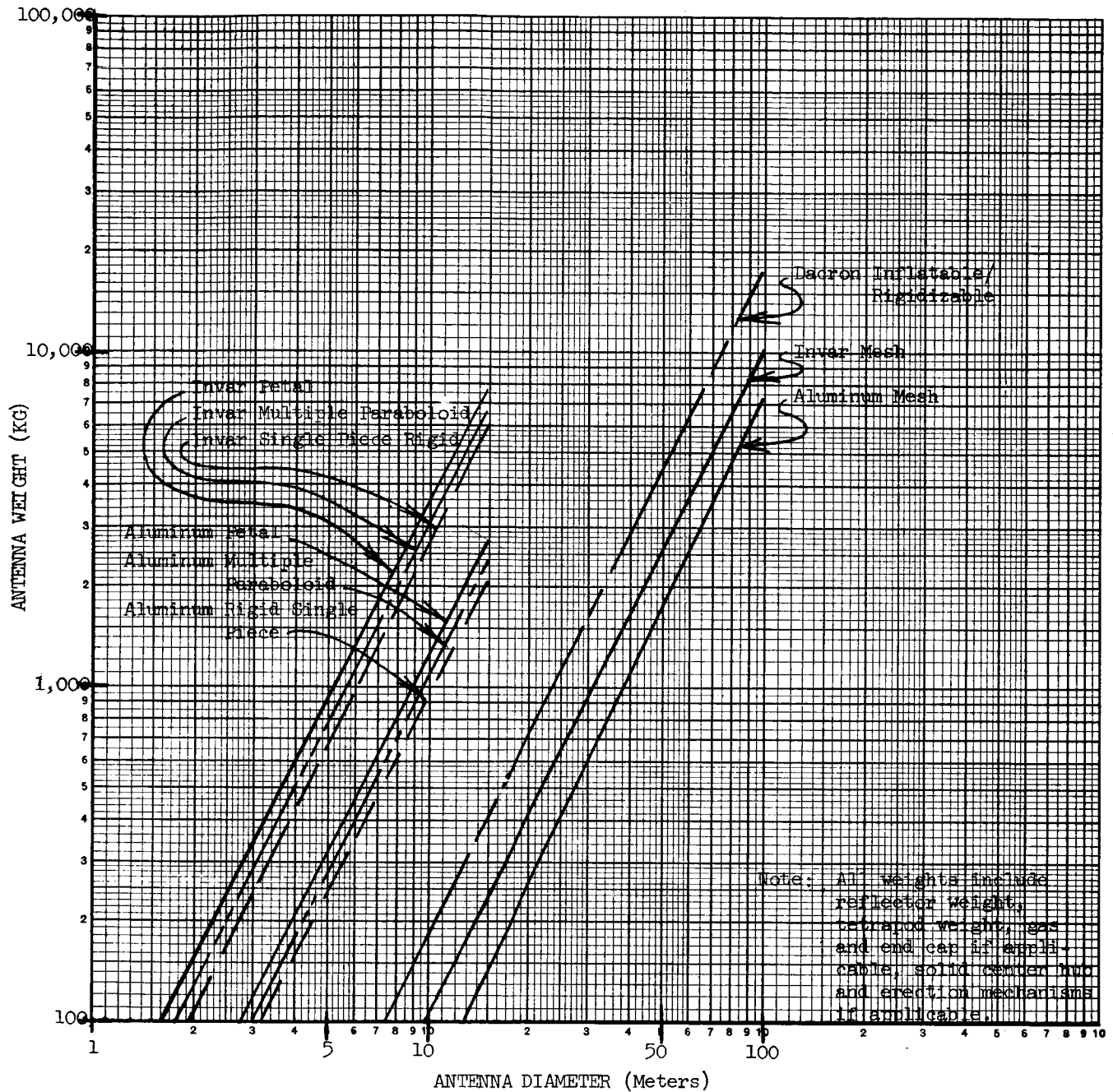


Figure 4.1.4.3-1. Antenna Weight vs Diameter

Selection of suitable power supplies for DSMCS requirements were established through energy management tradeoffs.

Combinations of power systems investigated included:

1. Solar cells and batteries
2. Fuel cells and batteries
3. Radioisotope thermoelectric generators (RTG's)
4. Reactor/thermoelectric-thermionic and batteries
5. Reactor-dynamic systems

A listing of power system design considerations follows:

1. Average power level
2. Peak power level > > Average power level
3. Lifetime > 1 year
4. Total energy
5. Sunlight geometry (day/night cycles in orbit, energy collector orientation)
6. Power transient response
7. Radiation constraints
8. On-board g-level (fuel cells)
9. Lead time (Availability)

Power profiles established in Volume II Section 5.2.2 as example cases are shown in Table 4.2-1. Three primary power loads used in the profiles are shown in Table 4.2-2. They are divided into transmitting, receiver refrigeration and satellite housekeeping. Operational conditions were arranged to provide eight example power profiles including two receive only conditions. Boundary conditions for the three primary power loads are described in Table 4.2-2. Transmitter power input for satellites with command capability varied from 92.5 kWe to 30 kWe corresponding to approximately 30 kW and 10 kW respectively of radiated power. Receive only satellites did not require transmit

power except to Earth. 6 kWe for maser refrigeration or 1 kWe for parametric amplifier partial refrigeration were assigned. Partial refrigeration refers to a level of refrigeration not optimum for system performance. Housekeeping functions such as attitude control electronics and valve actuation, receivers, command memory updating, data processing and any active thermal controlling were assigned power levels of 1500 and 500 watts.

After investigation of DSMCS requirements, fuel cell power systems were rejected because of the excessive fuel weight. Dynamic power systems were also rejected on the basis of required lifetime, anticipated launch date and appropriate power level. The criterion for consideration was that the achievement of maintenance-free operation of a power system for one year in space at a power level of 1 kW or more be demonstrated by 1970 to an acceptable degree. It does not appear that any dynamic power system will achieve such a demonstration by this date. Therefore, unless the DSMCS mission is combined with a power system demonstration mission, a dynamic power system is not appropriate.

Table 4.2-3 presents a general account of power system types versus mission requirements.

4.2.1 NUCLEAR POWER SYSTEMS

4.2.1.1 RADIOISOTOPE THERMOELECTRIC GENERATORS (RTG's)

The applicability of radioisotope thermoelectric generators (RTG's) was investigated and found encouraging. Requirements for RTG units included 10 KWe total power availability from static thermoelectric or thermionic elements. A three year lifetime was also required as was shielding for electronic components. A launch rate of one satellite every two years beginning in 1975 was assumed to estimate fuel availability and cost. Present and pessimistic element efficiencies follow.

	<u>Nominal Efficiency</u>	<u>Pessimistic Efficiency</u>
Thermoelectric	10%	8%
Thermionic	15%	12%
Cascaded-Thermoelectric/ Thermionic	20%	16%

Fuel Availability

Candidate	T 1/2 (yr)	1975 (\$/W)	Available Number Of Satellites	Power (kW)		Fuel Cost (10 ⁶ \$)
				(@ 125 kWt)	(@ 100 kWt)	
Co - 60	5.27	~15	80	185	(148)	2.78 (2.2)
Sr - 90	27.7	~15	6	135	(109)	2.02 (1.6)
Cs - 137	26.6	~18	5	135	(109)	2.43 (1.96)
Pu - 147	2.62	~300	not enough	255	(200)	76.5 (60)
Pu - 238	89.6	~500	2*	127.5	(1 or .5)	63.8 (51.3)
Cm - 244	18.4	~200	4	140	(112)	28.0 (22.4)

*Competition with other missions

It was assumed that flight units would use hot-side solid state coupling and NaK plus electromagnetic (EM) pumps or heat pipes on the cold side.

Heater Size and Weight Estimates

Fuel	Core Diameter (cm)	Shield Thickness (cm Uranium)	Heater Diameter (cm)	Power
				System Weight (kilograms)
Co - 60	25.4	13.5	52.3	2040
Sr - 90	63.0	6.9	76.5	7150
Cs - 137	116.7	4.1	125.0	20000
Pu - 238	58.3	0	68.0	160
Cm - 244	32.5	36.0	105.0	1350

The cores are 50% iron equivalent, with the core representing over half the total system weight. With core redesign, the power system weight could conservatively be reduced to one half. Co-60, Sr-90, Cs-137, Pu-238 and Cm-244 are acceptable systems. Co-60 and Sr-90 are most economical considering fuel and launch vehicle associated costs and will be used for this example.

The size of multiple RTG's for Profile B were estimated on the basis of current state-of-art for temperatures and efficiency. The RTG's may be visualized as heat sources suspended inside a double-walled can. Heat is radiated from the source to the inside wall, conducted through thermoelectric elements between the walls, and radiated from the outside wall to space. The inter-wall

spaces between the thermoelectric elements are filled with insulation. The following temperatures are appropriate:

Fuel capsule surface	975°K
Inside wall (hot junction)	875°K
Outside wall (cold junction)	590°K

Location of these temperatures are shown in Figure 4.2.1.1-1 while a 3 unit configuration for Profile B (3500 watts/unit) is presented in Figure 4.2.1.1-2. Each RTG is approximately 1.5 meters in diameter x 1.5 meters in length. Additional information on thermoelectric elements is found under SNAP-10A.

A single 20 kWe RTG investigated for Profile H was considered far beyond what has been considered a practical design limit.

Additional cost and availability information is shown in Table 4.2.1.1-1 while Table 4.2.1.1-2 presents a history and performance summary of SNAP radioisotope systems.

4.2.1.2 SNAP-1 (System for Nuclear Auxiliary Power) Isotope Rankine

The SNAP-1 system is in effect the pioneer system for the SNAP-2 and SNAP-8 systems directly and indirectly, the reactor-powered Rankine cycle liquid metal turbo-alternator systems which follow. Although it was planned for an isotope thermal source, the system was carried through its entire development with electrical source testing.

SNAP-1 is a Rankine cycle mercury system delivering 500 watts from its turbo-alternator. Although this unit was driven on hydrosphere bearings as opposed to the journal bearings of SNAP-2, it served to supply basic information regarding mercury as a lubricant. Advances were made in the technology of mercury as a working fluid, of mercury containment materials, and of static and dynamic seals for liquid and vapor mercury. Both the alternator and mercury pump served as archetypes upon which to pattern the design of their SNAP-2 counterparts.

The SNAP-1 rotating unit, at design speed and design operating conditions, experienced an uninterrupted run of 2300 hours. Based upon this performance, and the advances in technology since that time, it seems reasonable

to expect a high degree of reliability from this system. Its growth potential, however, seems rather limited. The use of rotating machinery in dynamic systems will probably require a pair of contra-rotating turbo generators to maintain roll stability. The rotating system is on the same order of size as that of SNAP-2, and yet delivers one-sixth the power. Its 500 watt output is a small margin over its combined bearing, pump, windage, seal and electrical losses. A variation in any of these becomes important, particularly with a decaying power source.

Thus, it would seem that the major contribution of the SNAP-1 program has been to establish a base for the SNAP-2 and SNAP-8 extensions.

4.2.1.3 SNAP-2 Reactor Dynamic

The SNAP-2 concept has seen little change since its initiation in 1957. It is a two-fluid, two-loop system powered by a zirconium hydride reactor similar to that of SNAP-8 except for power level. Originally, sodium was designated as the reactor coolant; but it was soon replaced by NaK with its superior thermodynamic characteristics. The NaK trade-off, however, was made at the expense of the rotating unit design, since the shaft-mounted NaK pump is larger and heavier than its sodium counterpart.

The mercury loop contains the CRU (combined rotating unit), the condenser which radiates to space, and the boiler which gains its thermal energy from the reactor coolant. Mounted on the CRU shaft, in an integrated rotating assembly, are the turbine, the alternator, the mercury pump, and the NaK pump. Bearings are of the sliding type and are lubricated by the working fluid mercury

With the exception of weight, there has been little change in the performance objectives of the SNAP-2 system. The original requirements are listed below:

1. 3 kWe net output.
2. One year unattended operation.
3. 270 kg. maximum system weight.
4. 10 sq. meters maximum radiator area.
5. Operation in hard vacuum and zero-gravity.
6. Operation in micrometeoroid environment.
7. Orbital startup.
8. System burnup if re-entry becomes necessary.
9. Packaging to withstand launch conditions.

SNAP-2 Weight Estimates

Listed below are the 1962 estimates for the SNAP-2 system, including shielding for equipment protection only.

Boiler	45 kilograms
Rotating unit	22 kilograms
Radiator plus inventory	90 kilograms
Controls	10 kilograms
Structure	22 kilograms
Piping	15 kilograms
Orbital startup system	45 kilograms
Reactor	110 kilograms
Shield	<u>150</u> kilograms
Total	509 kilograms

Note: A more recent estimate places the total system at 700 kilograms.

Present SNAP-2 Performance Specifications

Electrical

Power output	5 kW
Frequency	2000 Hz
Voltage	500 volts RMS 3 Phase
Reactor Coolant Outlet Temperature	925°K
Radiator Inlet Temperature	590°K
Radiator Surface Area	10m ²
System Net Thermal Efficiency	9%

Size

The SNAP-2 power conversion system is housed within the radiator. The radiator fits into or is integrated with the vehicle cone. Its surface area is 10m² and is approximately 1.5 meters in diameter at its base. The reactor is held in the apex of the cone beyond the condenser. In the present concept, approximately 4 meters separate the reactor from the payload.

Reliability

Apparently, the major factor in the evaluation of reliability for the SNAP-2 system is the combined rotating unit. The unit is credited with an accumulation of over 2500 hours of running time at or near design operating conditions, while it has continuously run for 500 hours. The Sunflower rotating unit, which is similar to the SNAP-2, ran for 3100 hours. The Sunflower unit shaft, since it does not mount a NaK pump as does its SNAP-2 counterpart, is shorter and is unburdened by a cantilever section. The absence of the NaK pump eases the thermal condition at the turbine bearing and permits a modified bearing housing assembly.

The SNAP-2 power conversion system has been planned to for one year endurance capability. The conditions which qualify this requirement to the extreme are of continuous unattended operation and probable orbital start-up.

The critical criteria for endurance are as follows:

1. Dynamic loading in the rotating unit.
2. Corrosion, erosion and mass transfer.
3. The NaK-Hg seal.
4. Reactor.
5. Reactor effect upon system.

4.2.1.4 SNAP-8 Reactor Dynamic

The components shown in Figure 4.2.1.4-1 plus a working fluid Mercury, comprise the bare necessities of the Rankine Cycle SNAP-8 system. The working fluid enters the boiler in its liquid state. There it absorbs heat and stores this energy by changing to a vapor under pressure. This vapor then flows to the turbine where it gives up a part of its energy by expansion, a process which drives the turbine mechanically. The Mercury is still mainly in vapor form when it leaves the turbine but its useful energy has been expended. Now it must be returned to its liquid state at a proper pressure so that it can again be capable of drawing boiler energy. Thus the turbine exhaust vapor flows to the condenser for cooling to the liquid state. The heat dissipated by the vapor in the condenser is an inevitable thermodynamic loss. The liquid from the condenser is then pumped back to the boiler to renew its cycle. The sole form of input energy is heat. The output is mechanical energy plus heat. The mechanical energy may be transformed, as in SNAP-8, to electrical energy.

The prime requirement of the heat source is that it furnish an adequate and controllable supply of heat continuously for 10,000 hours. This makes a reactor the indisputable choice. As a result of the interrelationships in the reactor, turbine, and condenser, mercury is the selected working fluid. Mercury, because of its effect upon reactor operation, must be isolated from the reactor. Thus, a primary loop, with NaK as the fluid, acts as the buffer. It extracts heat from the reactor to supply the mercury boiler. A NaK pump is added to maintain primary loop flow.

The SNAP-8 Electrical Generating System (EGS) will deliver, unattended, 35 electrical kW continuously and constantly. Since power demands will vary, a device to protect the alternator during low power demand periods is necessary. A parasitic load resistor serves this purpose by accepting and dissipating excess power as it is sensed by the electrical control circuit. Speed regulation is also attained by control circuitry which, again utilizing the parasitic load resistor, controls by varying the electrical load.

Startup of the system takes place in space upon ground command. Successful startup demands a minimum temperature of 31.3°K in both the NaK and lubricant radiators for proper fluid viscosity. The reactor is first brought to operating temperature. Then the primary loop NaK and bearing lube pumps are battery-driven through inverters to start flow. When the NaK flow heats the boiler to the required level, the liquid mercury is injected into the boiler, which then builds up vapor to start the turbine. When required, the NaK heat rejection loop flow is started. Finally, the turbine attains the speed to produce enough alternator power to drive the pumps. The batteries are disconnected and the system builds up to full power.

Working System Weight Summary

The flight article weight of 2925 kilograms is the target for SNAP-8 designs. The breakdown weight shown below should not be interpreted as the attainable value but only the target values.

Power Conversion System

Primary Loop	110* kilograms
Boiler	240* kilograms
Mercury Loop	65* kilograms
Condenser	30* kilograms
Turbine-Alternator	130* kilograms
Heat Rejection Loop	105* kilograms
Cool and Lube Loop	40* kilograms
Startup Equipment (including batteries)	170 kilograms
Electrical Assembly	225 kilograms
SNAP-8 and Satellite Attach Structure	<u>300</u> kilograms
	1415 kilograms

Nuclear System

Reactor	200 kilograms
Shield	<u>500</u> kilograms
	700 kilograms

Flight Radiator Assembly

	<u>810</u> kilograms
Total	2925 kilograms

*Includes Inventory

4.2.1.5 SNAP-10A Reactor Thermoelectric

Snap-10A design requirements consisted of: (a) production of 500 watts at 28 vdc for one year in the space environment, (b) capability of remote startup in orbit by ground command, (c) capability for handling, transport, and launch within acceptable safety criteria and currently accepted launch base procedures, (d) no requirement for long-term dynamic control, (e) sufficient instrument capability on the SNAPSHOT launch to fully monitor system performance, and (f) radiation shielding to attenuate reactor leakage to acceptable levels within the spacecraft. The reactor is the ZrH type with about 4.8 kg of fully enriched U²³⁵ fuel. The fuel-moderator is in the form of 3.17 cm diameter, 31.13 cm long rods clad with Hastelloy and densely packed within a 23 cm diameter by

40 cm long vessel. Surrounding the core vessel is a beryllium neutron reflector containing four semicylindrical control drums. These drums affect startup of the reactor by varying the neutron leakage. Long-term system control is achieved through the inherent stability associated with the reactor type. The reactor is cooled by a circulating loop of liquid metal, NaK-78, a eutectic of sodium and potassium. Liquid metal is used as the coolant because of its negligible vapor pressure at required operating temperatures and because it is virtually noncorrosive to available containment materials.

The SNAP-10A converter had an objective of operating in space for a year at temperature of approximately 825°K with an efficiency degradation of less than 10%. In the case of the SNAP-10A converter, the early contending materials were PbTe and SiGe alloys. SiGe was ultimately chosen for the final system, despite its lower figure of merit and efficiency, because: (a) SiGe alloy is metallurgically stable to well above 825°K (PbTe sublimates at temperatures above approximately 700°K and would require encapsulation, complicating the device); (b) stable low resistance electrical contacts can be made of SiGe by metallurgically bonding (experience with PbTe indicated only relatively unstable higher resistance mechanical contacts could be achieved); and (c) the mechanical properties of SiGe are more uniform and less restrictive design-wise.

SNAP-10A represents a first generation reactor thermoelectric space power plant. Its technology is conservative. The present SNAP hydride reactors will support more advanced systems operating at temperatures in the 975°K to 1025°K range. Because the specific power output of a thermoelectric system is approximately proportional to the absolute temperature to the fifth power, operation at these higher temperatures will dramatically improve system performance. Since the reactor power source and shield weight are virtually independent of small changes in power level, the obtainable outputs per unit system weight increase substantially at larger system power levels. Table 4.2.1.5-1 summarizes SNAP-10A operational characteristics. SNAP-10A related advanced reactors under development are presented in Table 4.2.1.5-2.

Operational lifetime of thermoelectric systems has been intimately related to the thermocouple operating temperature, the higher the temperature the

shorter the lifetime. Even in the case of SNAP-10A systems, reasonable thermocouple lifetimes were obtained by operating the devices below the maximum available reactor temperature. Recent thermocouple diode development has extended reliable device operation to keep pace with the SNAP-10A reactor temperature level. Figure 4.2.1.5-1 presents a thermoelectric performance growth curve showing SNAP-10A couples operating at 0.4 watts/couple and 775°K compared to advanced couples operating at over 1.2 watts/couple at 975°K. Operation of the advanced couples has been satisfactorily established and their use in conjunction with a SNAP-10A reactor could increase system output from 500 to 1500 watts. The 1500 watt thermoelectric system has been designated SNAP-10B. Weights versus power levels for the SNAP-10A/10B reactor, for thermoelectric SNAP-8 systems and for intermediate power levels are included in Figure 4.2.1.5-2.

Acceptable radiation dose rates for unmanned equipment are related to SNAP-10B shield weight and reactor-payload separation distance in Figure 4.2.1.5-3. A general curve covering power levels to 15 kWe relating separation distance to power levels is found in Figure 4.2.1.5-4. Direct radiating and compact converter system schematics are shown in Figure 4.2.1.5-5. (Reference 1) A 2 kWe reactor thermoelectric power system is depicted in Figure 4.2.1.5-6. This unit is approximately 4 meters in length. A cluster of these units to satisfy Power Profile B would be incompatible with shroud constraints. Table 4.2.1.5-3 presents reactor thermoelectric performances for systems from 0.5 to 3 kWe. The units, however, could be packaged in long Titan shrouds for Profile E.

4.2.1.6 SNAP-50

Concept

This power system concept is included for historical value. Development has been discontinued and it is doubtful that further work will be accomplished in the near future. The scarcity of published reports regarding the SNAP-50

(1) Nuclear Power Systems for Advanced High-Powered Communications Satellites, J. D. Gylfe AIAA Communications Satellite System Conference, Washington, D. C. May 2-4, 1966.

program allows very little detailed description of the system. Apparently, the studies made in the Spur program established the basis for SNAP-50 feasibility. These studies coupled with the prior work done at their CANEL facility by Pratt and Whitney, plus their efforts with a lithium cooled, uranium carbide reactor, provided the beginnings of SNAP-50.

It was expected that the system would be capable of 300 kWe to one megawatt output. Lithium was the reactor coolant while potassium was considered for the Rankine cycle working fluid. A direct condenser radiation was considered for heat rejection.

SNAP-50 Weight Estimates and Performance Specifications

A typical weight estimate for SNAP-50 follows:

Boiler	228 kilograms
Power Conversion Group	340 kilograms
Radiator	450 kilograms
Reactor	270 kilograms
Shield	<u>350</u> kilograms
Total	1638 kilograms

A typical performance specification is listed below:

Power Output	300 kWe
Reactor Coolant	Lithium
Reactor Outlet Temp.	1325° - 1375°K
Turbine Working Fluid	Potassium
Turbine Inlet Temp.	1325° - 1375°K
Radiator Inlet Temp.	925° - 975°K
Radiator Surface Area	90 m ²
System Net Thermal Efficiency	12-15%

Although the above estimates seem reasonable, some weight increase should be expected as design progresses. Radiator changes would obviously increase weight, particularly if it should be decided that condensation occur by heat transfer to another fluid which in turn would reject heat in an all-liquid radiator. Also, the high heat rejection temperature may require a preheat of

the radiator, leading to increased weight of the startup system. The reactor, and consequently the shield, will probably see negligible weight or size increase even if power is increased.

Everything considered, the present specific weight estimate of 5.5 kg per kWe seems reasonable, particularly for one megawatt output systems, in spite of the fact that increased radiator surface implies at least a proportionate increase in weight required for meteoroid protection.

Growth Capability

Based upon the estimates given here for the 300 kWe system, the 5.5 kilograms per kWe for system specific weight may be reduced to 4.5 kilograms per kWe for the one megawatt system. This follows from the reasoning that increased radiator weight would be more than overcome by the negligible increase in the reactor and shield.

The SNAP-50 system contained opportunities equal to that of the SNAP-8 system for the use of multiple component modules in various combinations. Achievement of long-term operation, providing the one year goal is reached, involves improvement which is interwoven with the problems of high temperature materials. Development to the next logical advance in liquid metal dynamic systems with nuclear sources seems contingent mainly upon increasing temperatures.

4.2.2 NON-NUCLEAR POWER SYSTEMS

Introduction

The applicabilities of non-nuclear power systems to unmanned space missions are compared, primarily with respect to their anticipated specific energy/power capabilities in the 1970-1985 period. Power sources from 2 to 50 kWe with durations up to 3 years have been considered.

The types of applicable non-nuclear power systems can be broadly divided into those that derive their energy from the sun and those that utilize the chemical energy of on-board fuels. The anticipated performances of the solar power systems are compared to each other on the basis of system specific power. Solar power systems are more susceptible to damage from the space environment than are the chemical systems, and in earth-orbiting missions they must

include some form of energy storage device for power while the spacecraft is in the earth's shadow. Photovoltaic systems are particularly susceptible to damage from the trapped radiation belts at the orbital altitudes required in this study. At the power levels under consideration, the energy collecting surfaces of the solar power systems are large and must be fully oriented toward the sun. The size of these collectors and constraints on launch configuration will require that they be erectable. Inflatable structures of adequate size, with sufficiently accurate surface contours, and capable of the necessary orientation control will be required for the DSMCS.

Chemical energy systems suffer none of the above disadvantages of the solar derived power systems and they are comparatively independent of the space environment. System performances are time-dependent and they are compared to each other on the basis of system specific energy.

Comparison of solar systems to chemical systems must consider both distance from the sun and duration. The comparison is essentially independent of power level for the power range considered.

4.2.2.1 CHEMICAL SYSTEMS

4.2.2.1.1 BATTERIES

Primary batteries provide a very reliable energy source. Silver-zinc batteries are well developed and currently yield specific energies of 36 watt hours per kg. For very large batteries, it appears that packaging could be improved to produce 45 watt hours per kg. Battery temperature, during use, should be maintained at about 295°K for maximum energy output. Performance is degraded at lower temperatures by increased internal resistance and at higher temperatures by increased internal leakage current.

Now being developed is the Mg-MnO_2 battery which is expected to be operational by the early '70's. Anticipated storage life for this battery is about four years at $245^{\circ} - 305^{\circ}\text{K}$. With organic depolarizers, specific energies of 45 watt hrs/kg are expected. The Li-AgCl battery is also expected to produce 45 watt hrs/kg in the next decade.

The projected state-of-the-art for primary storage batteries is about 45 watt hrs/kg with improvements in storage life and operational temperature range. Batteries are simple power sources and are rugged, but for the ranges of power and duration being considered, they are excessive. Throughout the 2-50 kWe power range, chemical dynamic systems weigh less for durations exceeding a few hours. Primary and secondary space batteries are summarized in Table 4.2.2.1.1-1 and Table 4.2.2.1.1-2.

4.2.2.1.2 CHEMICAL-DYNAMIC SYSTEMS

Chemical-dynamic systems have relatively good specific power capabilities but their energy conversion efficiencies, from chemical to mechanical to electrical, are poor. Therefore, they are best suited for missions requiring high power for short durations which is not the DSMCS power profile. Systems utilizing liquid hydrogen and liquid oxygen should be available at about 10 kg/kW for the conversion components plus 0.6 kg/kW hr. for the fuels and tankage. Table 4.2.2.1.2-1 presents a survey of chemical dynamic system performances.

4.2.2.1.3 FUEL CELLS

Fuel cells are the most efficient devices for converting chemical energy into electrical energy, with conversion efficiencies of 80% rather easily achieved. It is expected that by 1970, hydrogen-oxygen fuel cells with ion exchange membranes or solid electrolytes will be operating at specific weights of 30 kg/kW for the cell and its controls plus 0.5 kg/kW hr. for the fuels and tanks. Because of their higher conversion efficiency, fuel cell systems would weigh less than chemical dynamics systems for duration of about 100 hours or more but for DSMCS applications their system weight is excessive. The specific fuel consumption of hydrogen-oxygen fuel cell is about 0.5 kg per

kW hr. The power profile of minimum energy is Profile "F" and this energy is 13,130 kW hrs. Thus, it is evident that the fuel weight for this chemical systems is prohibitive.

4.2.2.2 SOLAR-POWERED SYSTEMS

4.2.2.2.1 Solar Collectors

In an earth orbit, the size of solar collectors will be approximately $10 \text{ m}^2/\text{kW}$ of system power output. Collector size is the most crucial technological problem of solar power systems using the collector approach. The development of large inflatable or unfurlable collectors will be required and in view of work already started in this direction, is a reasonable expectation.

This approach also requires that the collector be oriented to the sun. Attitude control will be required to point the satellite antenna at the spacecraft, but additional considerations are required to point the collector at the sun. The complexity of this orientation requirement cannot be ignored, but for the purpose of this comparison, the weight involved is considered small with respect to total power system weight.

4.2.2.2.2 SOLAR-DYNAMIC SYSTEMS

Solar-dynamic systems concentrate the sun's radiant energy so that it can be absorbed by a thermodynamic working fluid at a high temperature. The collector is a mirror and it requires precise orientation to the sun. The optical quality of the mirror surface will degrade with time due to micrometeoroid erosion and to sublimation. The present state of development affords only small confidence in system availability of competitive efficiencies and substantial life-time in operational status during the 1970's.

For comparative purposes, however, system efficiencies are assumed. System efficiencies of about 18% may be achievable with furnace temperatures of about 1700°C . The Sunflower program leads to a specific power prediction of about 28 kg/kW and from the Astec program, about 32 kg/kW. The collectors of these systems represent about one-third of their total weights. With further

development of inflatable collectors this fraction should be reduced, but for now let it be assumed that this reduction will be absorbed by the orientation controls. A survey of solar dynamic system performances is shown in Table 4.2.2.2.2-1.

4.2.2.2.3 PHOTOVOLTAIC SYSTEMS

Solar cells convert solar energy directly into electricity with efficiencies up to 13% for individual cells and 10% for panel arrays. Substantial improvements in conversion efficiency are not anticipated in the next several years. However, the development of thin-film solar cells that will have the same efficiency as the present silicon cells is anticipated. These will have improved resistance to radiation damage, will be of less weight, and will be more easily applied to large area applications.

As with solar-dynamic systems, the development of large area inflatable or unfurlable panels will be required. The problem for solar panels is less stringent than for solar mirrors, however. Also since solar cell output follows a cosine function with respect to solar orientation, the pointing accuracy need not be especially precise nor is surface flatness as important as contour control in collectors. Methods of stowing the panel compactly during launch and in a manner that will avoid solar cell damage by the stowing and erecting processes must be devised.

For this comparison, it is assumed that thin-film solar cells on a flexible substrate will have the same weight per unit area as present crystalline silicon solar cells including cover glasses, adhesives, connecting tabs, and wiring but not including panel structure. This figure is 1.9 kg/m^2 . No improvement in temperature characteristics is assumed.

The output of solar cells increases with increased illumination intensity but decreases with increased temperature. The temperature of a flat solar panel normal to the sun vector as a function of distance from the sun is shown in Figure 4.2.2.2.3-1. This characteristic is based on present optical properties of solar panels using reflective coatings on the solar cell cover

glasses. The solar absorptivity is 0.78 and the thermal emissivity is 0.83. An 85% packing density is assumed and the area between the solar cells is painted white. The space environment will degrade the optical properties of the white paint. Allowing for such degradation, the assumed optical properties of the inter-cell areas are 0.4 solar absorptivity and 0.8 thermal emissivity. The back side of the panel would be treated for high thermal emissivity and a value of 0.90 is assumed. The effect of temperature on solar cell power output is shown in Figure 4.2.2.2.3-2.

Secondary batteries must be used with the solar cells to provide power while the DSMCS is in the earth's shadow and during peak power periods. The use of silver-cadmium batteries at a maximum discharge depth of 50% and at an energy density of 15 watt hours per kilograms is assumed. This is state-of-the-art although it has not yet been demonstrated in space. The solar array must not only provide direct power, but also power to recharge the batteries. The batteries and the solar array must be sized to operate the DSMCS when the orbital plane is parallel to the earth-sun vector, at which time the orbital shadow period will be the longest.

The design goal for current studies of erectable solar panel structures is 10 watts/kg for normal incidence of sunlight at air mass zero.

Solar cell assemblies currently weigh 0.45 grams per 1 x 2 cm cell. This includes:

- .154 mm thick glass filters
- .38 mm thick silicon solar cell
- .127 mm thick insulation layer of epoxy impregnated scrim
- cloth silicon rubber adhesive
- interconnecting wiring

The use of thinner silicon cells has been investigated by J.P.L. The breakage rate increases rapidly as thickness decreases, and performance decreases. A reduction to .305 mm thickness would probably be advantageous, with

respect to power-to-weight ratio, but a reduction to .203mm thickness would probably not. If the panel structure were non-conductive, the insulation layer could be eliminated.

Radiation Damage

Data for n-on-p cells indicates the radiation damage threshold for electrons above 54 kev is 5×10^{12} electrons/cm² or for protons above 1.2 mev is 2×10^9 protons/cm². For both electrons (> 54 kev) and protons (>1.2 mev) an acceptable power ratio is:

$$\frac{P(\Phi_e \Phi_p)}{P_0} = 1.00 - 0.15 (\log \Phi_e - 12.7) - 0.15 (\log \Phi_p - 9.3) \quad (1)$$

where the concentrations Φ , are measured in particles/cm² and $\log \Phi_e > 12.7$ and $\log \Phi_p > 9.3$. For a simplified approximation, it will be assumed that the damage is directly proportional to total dose (energy absorbed), but that the surface dose, which is only important in solar cells, is independent of particle energy. This assumption should be reasonably good in the kev range for electrons and the mev range for protons. Thus, Equation (1) will be assumed valid for all threshold energies of electrons and protons. Note that the use of particle concentrations for the solar cell analysis differs from the dose ("rad") analysis used for other materials. Cell degradation as a function of electron and proton flux is shown in Figure 4.2.2.2.3-3. The endurance of solar cells in the radiation environment as a function of altitude is shown in Figure 4.2.2.2.3-4.

The effect of shielding on solar cell endurance for 1, 2, and 3 year lifetimes is shown in Figures 4.2.2.2.3-5, -6 and -7. In the second year, the solar cell output is degraded an additional 9%, and in the third year it is degraded an additional 5%. It will be noted that a 1 mm thick cover glass is approximately equivalent to 0.2 gm/cm². Cover glass thicknesses above this value are usually not considered practical. Figure 4.2.2.2.3-5 points out that this amount of cover glass protecting cells in a 1100 km circular orbit for 1 year will maintain power output to a level of 82.5% of the original output.

Solar panel and RTG power systems are the primary candidates for the DSMCS mission. Table 4.2.3-1 compares system performance and weights for the two systems and all the power profiles. State-of-the-art solar panel system weights compare favorably to advanced development RTG weight expectations. Improvements in the 7.35 kg/m^2 state-of-the-art number for solar panel weight per unit area would reduce the solar panel system weight and give that system a decided weight saving advantage over RTG's on the strength of power supply requirements alone. However, Volume II points out the power system interface considerations with other satellite disciplines that influence system selection other than the power system weight criteria by itself.

The solar panel systems noted in the table represent one year duration systems operating at the worst altitude case, from shielding considerations, of 1620 kilometers. Solar panels sized for specific output levels and zero time in orbit must have sufficient additional area to allow for radiation produced cell degradation. For example, Figures 4.2.2.2.3-5, -6 and -7 note that as time in orbit is increased from 1, 2 and to 3 years, at a constant altitude of 1100 km, cell area must be increased 21.2%, 92.3% and to 194% respectively to provide the required power level at the end of the mission. Required solar panel areas would not be considered excessively large if the Pegasus micro-meteoroid detector panel configuration were applicable to the DSMCS. The large length/width ratio of the Pegasus panels, however, would require unwieldy attitude control systems to provide DSMCS antenna pointing. Lightweight expandable solar panel technology could reduce attitude control requirements on DSMCS missions.

RTG system weights in Table 4.2.3-1 are representative of SNAP-10B power system weights. The large SNAP-10B volume requirement would however not allow the use of the required number of units in the Saturn shroud. The long Titan shroud would permit their packaging.

Table 4.2-1

POWER PROFILES

Designation	Power Loads	Profile
A	30 KWe transmitter input power 6 KWe maser refrigeration 1.5 KWe housekeeping	7.5 KWe minimum full time 37.5 KWe 15 minutes/day
B	30 KWe transmitter input power 6 KWe maser refrigeration 1.5 KWe housekeeping	7.5 KWe minimum full time 37.5 KWe 5 minutes/hour
C Receive Only	6 KWe maser refrigeration 1.5 KWe housekeeping	7.5 KWe minimum full time
D	30 KWe transmitter input power 1 KWe parametric amplifier partial refrigeration 500 watts housekeeping	1.5 KWe minimum full time 31.5 KWe 15 minutes/day
E	30 KWe transmitter input power 1 KWe parametric amplifier partial refrigeration 500 watts housekeeping	1.5 KWe minimum full time 31.5 KWe 5 minutes/hour
F Receive Only	1 KWe parametric amplifier partial refrigeration 500 watts housekeeping	1.5 KWe minimum full time
G	92.5 KWe transmitter input power 6 KWe maser refrigeration 1.5 KWe housekeeping	7.5 KWe minimum full time 100 KWe 15 minutes/day
H	92.5 KWe transmitter input power 6 KWe maser refrigeration 1.5 KWe housekeeping	7.5 KWe minimum full time 100 KWe 5 minutes/hour

Table 4.2-2
SATELLITE PRIMARY POWER LOADS

Load	Upper Boundary	Lower Boundary
Transmitter	92.5 KWe (\approx 30 KW Radiated)	30 KWe (\approx 10 KW Radiated)
Receiver Refrigeration	6 KWe	1 KWe
Housekeeping	1.5 KWe	.5 KWe

Table 4.2-3
POWER SYSTEM TYPES VS MISSION REQUIREMENTS

Operational Aux. Power Systems to be available in 1969 Power Type	Operational Date	0-35 w		40-100 w		100-500 w		500-1000 w		1-2 kwe		3-5 kwe	
		Duration (months)	Duration (months)	Duration (months)	Duration (months)	Duration (months)	Duration (months)	Duration (months)	Duration (months)	Duration (months)	Duration (months)	Duration (months)	Duration (months)
Batteries	1964	X	X	X	X	X	X	X	X	X	X	X	X
Solar Cells/Batteries	1964	X	X	X	X	X	X	X	X	X	X	X	X
Fuel Cells	1966	?	?	X	X	X	X	X	X	X	X	X	X
RTG - standard	1965	X	X	X	X	X	X	X	X	X	X	X	X
- advanced	1968	-	-	X	X	X	X	X	X	X	X	X	X
Chemical APU	1966	-	-	-	-	-	-	-	-	-	-	-	-
Batteries		?	-	-	-	-	-	-	-	-	-	-	-
Solar Cells/Batteries		X	X	X	X	X	X	X	X	X	X	X	X
Fuel Cells		-	-	?	-	X	X	X	X	X	X	X	X
RTG - standard		-	-	-	-	-	-	-	-	-	-	-	-
- advanced		-	-	-	-	-	-	-	-	-	-	-	-
Chemical APU		-	-	-	-	-	-	-	-	-	-	-	-

X - requirement filled ? - possibly filled - unfilled * - < 250 Watts

Table 4.2.1.1-2
RADIOISOTOPE SNAPS AND ASSOCIATED SNAP WORK*

Unit	Status	No. of Units	Type	Application	Power Wt. (We)	Size (Inches)	Isotope	Syst Den Life	Misc.	Contractor	Power Source	Contr. System	Customer	Date Cont Start	Date Cont End	Cont. Value (less fuel)
SWAP 1	Demo	-	Tu/E	Initial radioisotope dynamic generator	500	-	-	-	-	-	-	-	AEC	1956	1958	-
1A	Demo	-	T/E	Rerouted from S-1 which was TV-E demo	125	200	Ce-144	60d	T _H 1050F T _C 335F	MM	MM	3M	"	6-59	6-61	200k 152(61)
3	Demo	4	T/E	Demonstration	4	4	4-3/4x5-1/2	90d	T _H 621F T _C 116F	MM	MM	3M	"	7-58	6-61	4.8k/unit + fuel
3A	Demo	2	T/E	Proof of principle	2.4	-	-	-	-	-	-	-	-	-	-	-
3B	Op 6-11-61	2	T/E	Transit A + 4B (USAF)	2.7	4.6	4-3/4x5-1/2	5y	T _H 900 T _C 235	MM	MM	3M	"	7-58	6-61	4.8k/unit + fuel
"7"	Op 8-61	1	T/E	Axel Heiberg weather station terr	5	1680	18x20	2-5y	T _H 950 T _C 140	MM	MM	3M	"	8-61	---	---
7A	Op 12-63 (12-61)	1	T/E	Navigational buoy - Coast Guard - 5w system	11.6	1870	21x20	Syst 2y Fuel 10y	T _H 950 T _C 140	MM	MM	3M	Sr-90 fm Hartford	12-61	12-63	---
7B	Op 5-64	1	T/E	Fixed navigational light - Coast Guard - 30w system	68	4600	22x34-1/2	Syst 2y Fuel 10y	T _H 950 T _C 140	MM	MM	3M	Sr-90 fm Hartford	12-61	12-63	620k AEC
7C	Op 2-62	1	T/E	Antarctic weather station	11.6	1870	21x20	Syst 2y Fuel 10y	T _H 950 T _C 140	MM	MM	3M	Sr-90 fm Hartford	12-61	12-63	---
7D	Op 1-64	1	T/E	McMurdo - USN - 5w system (boat) - USN - 30w system	68	4600	22x34-1/2	Syst 2y Fuel 10y	T _H 950 T _C 140	MM	MM	3M	Sr-90 fm Hartford	12-61	12-63	---
7E	Op 7-64	1	T/E	Ocean bottom sonar beacon - 15,000 ft - 5w system	6.5	6000	20x21	Syst 2y Fuel 10y	T _H 950 T _C 140	MM	MM	3M	Sr-90 fm Hartford	12-61	12-63	---
7F	Op 1-65 (Phillip Pet)	1	T/E	Navigational aid - oil drilling pilot - 30w system	60	4600	22x34-1/2	Syst 2y Fuel 10y	T _H 950 T _C 140	MM	MM	3M	Sr-90 fm Hartford	12-61	12-63	N/A (app 100k)
9	Demo	1	T/E	Satellite demonstration	10	20	20x9-1/2	5y	T _H 900 T _C 235	MM	MM	3M	"	8-61	6-62	260k
9A	Op 3/9-12/63 USN 3 NASA 1	3	T/E	Use in operational proto	25	27	20x10	5-10y	T _H 900 T _C 235	MM	MM	3M	"	3-62	8-64	700k
11	Del. Spring 65	4	T/E	Transit (USN) - 5 Surveyor Program - flight acceptable	25	30	10x12	120d	N/A	MM	MM	3M	"	1-62	In proc	1550k
13	Demo program End FY 65	1	T/I	Demonstration to begin flight type in late FY 65	12.5	4	3x6	130d	N/A	MM	MM	N/A	"	9-61	1-65	1520k
13A	Proto delivered	15	T/E	Fuel proto gen - milliwatt - nuclear weapons	.001	1	3x3.5	5y	N/A	MM	MM	GA	"	4-63	In proc	800k
13B	Proto being tested	Several	T/E	Fuel proto gen - milliwatt - nuclear weapons	.001	1	3x3.5	5y	N/A	MM	MM	Gen Instr Corp --	"	4-63	--	---
13C	Proto delivered	"	T/E	Fuel proto gen - milliwatt - nuclear weapons	.15	1-1.5	1-1/2x4.7	2y	N/A	MM	MM	--	"	6-63	11-64	600k
13X	PPR	-	T/E	Broad usage other than weapons app.	.1	-	-	5y	Replaces 15C	-	-	-	"	1966	In proc	250k

* Martin Marietta

#Reference 4.2.1-1 Power Plant Study, Aerojet-General Nucleonics, July 1965

Table 4.2.1.1-2 (Continued)

RADIOISOTOPE SNAPS & ASSOCIATED SNAP WORK

Unit	Status	No. of Units	Type	Application	Power Wt. (W)	Size (inches)	Isotope	Syst Den Life	Misc.	Contractor Power Source	Contr. System	Customer	Date Cont Start	Date Cont End	Cont. Value (Less fuel)
SNAP 17A	Program completed	N/A	T/E	USAF medium altitude communication satellite program	25-35	28-30	N/A	5y	AMP doing fuel handling	* MM	N/A	AEC	1-64	1965	865k (MM-AEC)
17B	"	N/A	T/E	USAF medium altitude communication satellite program - 2nd contractor	25-35	28-30	N/A	5y	U.S. Steel doing hdig	GE	N/A	AEC	1-64	1965	780k (AEC)
170D	Initial development stage		T/E	DOD space program	100	100	-	3y	Same as A+B	Same as A+B	AEC	AEC	1964	In proc	2,940k thru 66
19	In Ph. III proto funded	2-3	T/E	NASA IMP + Nimbus - system was 2-20w, now 2-30w	25-30w	30	22.4x10.5	3y	N/A	MM	3M	"	2-63	12-65	2,370k) for both
19X	Operational proto flight in GFI 66			Nimbus B & DOD space program	30w	30	22.4x10.5	3y	-	MM	3M	"	1964	In proc	
21A	Design complete	N/A	T/E	Ocean bottom (8-10% T) - 10w	500	140x20	Sr-90	5y	Depth to 1000 psi	MM	N/A	"	2-64	3-65	496k
21B	Design complete	N/A	T/E	Ocean bottom	10w	500	140x20	5y	8-10% T	3M	N/A	"	2-64	3-65	468k
21X	Prelim. design	Numerous	T/E	Adv. ocean bottom generator family based on ZIA+B	20-60w	-	-	5y	Oper. GFI 67	-	N/A	"	1964	In proc	1,200k thru 66
23	In design	N/A	T/E	Will rely on S-21B heavily	60w	1000	N/A	5y	7.5% T	3M	N/A	"	6-64	6-66	430k
23X	Prelim. design	Numerous	T/E	Adv. generator family for sea surface based on 23	25-200w	-	-	5y	-	-	-	"	1965	In proc	400k thru 66
25	PDP	-	T/E	Adv. space generator for Nimbus D, Adv. Tirox & DOD space program	75w	40-50	-	3-5y	-	Lockheed-Rumec	RCA	"	4-65	In proc	5,750k tot. value
"27"	"SNAP-27"		T/E	R1 power supply for Surveyor - Lunar Rover (Initial flight proto 67)	40-50w	30	4500 in ³	120d	Single contractor selection in late 65	GE Valley Forge	-	AEC DRD	6-63	9-64	1,600k thru 66
"27"	"SNAP-27"		T/E	"	40	30	4500 in ³	120d	-	-	-	AEC	6-63	11-64	
"27"	"SNAP-27"		T/E	Instrument package to be left by Apollo (prior to RCA 79k study)	50w	-	-	-	-	CE	-	NASA Houston + JPL	1-65	8-65	70k
"27"	"SNAP-27"		T/E	Lunar power supply - NASA - Surveyor	40-50	30	24x10	1yr	-	RCA	-	NASA	1-65	-	79k
SNAP-7	Prelim. design		T/E	Adv. space generator	250w	-	-	-	-	-	-	AEC	1965	In proc	450k thru 66

* Martin Marietta

Table 4.2.1.1-2 (Continued)
RADIOISOTOPE SNAPS & ASSOCIATED SNAP WORK

Unit	Status	No. of Units	Type	Application	Power Wt. (W)	Size (Inches)	Isotope	Syst Dur Life	Misc.	Contractor Power Source	Contr. Conv. System	Customer	Date Cont Start	Date Cont End	Cont. Value (less fuel)
Study	Proto - prog. completed	-	T/E	Mixed fission products generator - underseas	5	-	-	10y	-	-	-	AEC	-	-	-
Study	"	-	T/E	Early generator - underseas	5	-	Cs-137	10y	-	Royal Industries	-	"	-	-	-
Study	Demo - prog. completed	-	T/I	Proof of principle thermionic space generator	.2	-	Tm-170	-	preceded SNAP-13	GE	-	-	-	-	AF funded
Study	Design - prog. completed	-	T/E	High power space generator	500	-	Pu-238	-	-	Martin	-	AEC	-	-	-
Study	Proto - prog. completed	-	T/E	Early terrestrial space generator	100w	-	-	-	NAP-100	Westinghouse	-	-	1957	-	AF funded
Study	-	-	All T/E + Tv/E	Study for MOSS (Langley MORL)	4kw	-	Some Po-210	-	-	* MM	-	NASA Lewis	6-62	5-64	75k
Study	-	-	-	Fuel study for space heat - Prom-147, Sr-90, Ce-137, Po-210	-	-	-	-	-	MM	-	NASA Goddard	5-64	1-65	44k
Study	Proto build Electrically heated	-	T/E	Light weight 2w/#	4-10	2-5	-	-	-	GA	-	AEC	3-63	In proc	215k
Study	-	-	RTG	Uses high temperature segmented lead telluride & germanium silicon	50	25	-	Pu-238	-	Battelle MI	-	NASA Goddard	3-64	9-64	43k
Study	-	-	T/E	Preliminary design - MORL power supply	-	-	-	-	-	Douglas	-	NASA Langley	1-65	-	375k
Study	-	-	T/E	Solar probe power supply	-	-	-	-	-	RCA	-	NASA	1-65	-	22k
Study	-	-	Turbo- electric	Rankine & Brayton Dynamic Mars/Venus Fly-by, Mars Landing	4-8000	-	-	Pu-238	600dy	NAA/AI	N/A	NASA Houston	1-65	8-65	91k
Study	Develop prog.	-	T/E	SNAP using mixed fission products	-	-	-	-	-	Gen. Instr. Corp.	N/A	AEC	1-62	In proc	300k
Study	-	-	T/E	Tubular compact thermo- electric modules	-	-	-	-	-	Westinghouse	-	AEC	4-64	1-65	50k
Study	Awarded 8-64	-	RTG	MOSS Micrometeoroid deep space satellite: Using Atlas & Titan	PDE	-	-	-	-	MM	-	NASA Langley	5-65	-	269k
Study	-	-	T/I	Thermionic power sources - evaluation	100-1500	1/2-1 1/4/w	-	-	-	MM	-	NASA Langley	5-65	-	319k
Study	-	-	T/E	Sub from Douglas on MORL study - 10 kw - argon as working gas, turbo machine	2kw	-	-	-	-	NAA/AI	-	NASA Houston & JPL	2-64	3-65	40k
Study	-	-	-	-	-	-	-	-	-	AiResearch	-	Douglas	-	-	130k

* Martin Marietta

Table 4.2.1.5-1

SNAP 10A OPERATIONAL CHARACTERISTICS

Initial Power (w)	565
Reactor Power (kwt)	~ 38
Over-all Length (cm)	348
Base Diameter (cm)	127
Total Weight (cm)	246
Radiator Area (m^2)	5.8
Maximum Coolant Temperature (K°)	333
Design Life (yr)	1
Power Conversion System	Thermoelectric, "n" on "p" SiGe
Material - Structure	Ti
Liquid Metal System	316 and 405 SS
Radiation Levels at Vehicle Mating Plane	Neutrons $\sim 10^{13}$ n/cm ² /yr
	Gammas $\sim 10^7$ rad/yr

Table 4.2.1.5-2

ADVANCED REACTORS UNDER DEVELOPMENT

	<u>SNAP 10A/2</u>	<u>SNAP 10B</u>	<u>SNAP 8</u>
Power (kWt)	30 to 200	30 - 325	200 - 600
Max. NaK Temp. (K°)	925 to 975	925 to 975	925 to 975
Lifetime (yrs)	1 to 5	1 to 5	1 to 5
Control Mode	Active or Static	Static	Active or Static
Reactor/Reflector Wt (kg)	135 to 145	148 - 157	272
Shield Diameter(cm)	47 to 49	37	69 (48)*
No. of Fuel Elements	37 to 85	37 to 85	211
Date Available	July, 1967	1969 - 70	1970 - 72

* For Advanced Design with Tapered Reflector

Table 4.2.1.5-3

REACTOR THERMOELECTRIC SYSTEM PERFORMANCE (0.5 to 3 kWe)

System Level	0.5 kWe	1.0 kWe	2.0 kWe	3.0 kWe
Reactor Power (Thermal) (kW)	28.4	47.1	84.8	122.4
Reactor Outlet Temperature ($^{\circ}$ R)	975	975	975	975
Design Life (Rated Power) (yr)	3	3	3	3
Gross Radiator Area (m ²)	2.2	4.5	9.1	13.6
Base Diameter	86 cm	110 cm	147 cm	178 cm
Overall Height	2.36 m	3.1 m	4.1 m	5.1 m
Unshielded System Weight (kg)	232	280	378	490
Reactor - Payload Separation Distance (m)	13.7	13.9	14.8	22.9
Shield Weight (kg)	55	70	78	82
Boom and Cable Weight (kg)	17.3	19	22.6	26.6
Total Shielded System Weight (kg)	303	367	490	595
Specific Power (watt/kg)	0.33	0.55	0.84	1.03

SGC 920FR-1
Volume III

Page 232

***Reference 4.2.1-1. Power Plant Study, Aerojet-General Nucleonics, July 1965

	I	II	III
Anode	Cd	Cd	Zn
Cathode	Ni	Ag	Ag
Electrolyte	KOH	KOH	KOH
Separator(s)	Pellon, polypropylene, or "semi-permeable membrane"	ion-exchange membrane, Nylon + cellophane, or cellulosic	same as Ag/Cd; also Visking
Seal	mechanical, glass or ceramic	mechanical, plastic or ceramic	same as Ag/Cd
Case	stainless, plastic or nylon	stainless, plastic or nylon	same as Ag/Cd
Theoretical Performance at 25°C:			
voltage/cell	1.30	1.16 - 1.38 ^{1/}	1.59 - 1.82 ^{1/}
watt-hr./lb (active materials only)	1.30	1.16 - 1.38 ^{1/}	1.59 - 1.82 ^{1/}
watt-hr./cubic inch (ditto)	148	79 - 143 ^{1/}	124 - 230 ^{1/}
	27	22 - 40 ^{1/}	31 - 61 ^{1/}
Actual performance at 25°C and 50% discharge: ^{2/}			
voltage/cell	1.24 - 1.25	1 - 1.1	1.4 - 1.55
watt-hr./lb.	6 - 9	7 - 15	4 - 8 } ^{3/} 16 - 35
watt-hr./cubic inch	0.6 - 0.9	0.9 - 1.8	1.2 - 3
Life, number of cycles:			
10% discharge, 100-min. orbit			3000+
at 0°C,			
25% discharge, 100-min. orbit	10,000	7000+	500 - 600
24 hour orbit	4/	900+	500+
50% discharge, 100-min. orbit	5,000	4000+	300+
24 hour orbit	4/	900+	300+
65% discharge, 100-min. orbit	4,000	1500+	150+
24 hour orbit	4/	900+	150+
at 25°C			
25% discharge, 100-min. orbit	10,000	3,000 - 12,000+	300+
24-hour orbit	4/	600+	300+
50% discharge, 100-min. orbit	4,000	1,500 - 7,000+	150+
24-hour orbit	4/	600+	150+
65% discharge, 100-min. orbit	2,500	1,000 - 1,800	50+
24-hour orbit	4/	600+	50+
at 50°C			
25% discharge, 100-min. orbit	3,000	1,000+	100+
24 hour orbit	4/	75 - 120+	75+
50% discharge, 100-min. orbit	2,500	500 - 600	50+
24 hour orbit	4/	75+	40+
65% discharge, 100-min. orbit	1,000	250+	20+
24 hour orbit	4/	75+	20+
Shelf life, days:	[Ni/Cd]	[Ag/Cd]	[Ag/Zn]
at 0°C, discharged	3,000	1,000 - 1,500	500 - 1,000
charged	3,000	800 - 1,000	365
at 25°C, discharged	3,000	800 - 1,500	365 - 1,000
charged	3,000	500 - 700	200 - 270
at 50°C, discharged	1,500	150 - 1,000	150 - 180
charged	1,500	90 - 365	75 - 90
Cost, \$/watt-hr. (at 25°C and 50% discharge)	1 - 3; 20 - 50 ^{5/}	1.20 - 4	0.75 - 3.50
Mean time to failure in service	more than 1 year	---	---
Available amp-hour sizes	0.5 - 50	0.1 - 300	0.1 - 300
Available shapes	rectangular & cylindrical	rectangular & cylindrical	rectangular & cylindrical
^{1/} Lower voltage for argentous, higher for argentic oxide. ^{2/} For silver, only argentous data are given. ^{3/} Lower range for 100-min. cycle, higher for 24-hr. cycle. ^{4/} Not recommended for 24-hour orbit. ^{5/} Estimated ranges by two different sources.			

* Reference 4.2.1-1. Power Plant Study, Aerojet-General Nucleonics, July 1965

CHEMICAL DYNAMIC SYSTEMS *

*Reference 4.2.1-1. Power Plant Study, Aerojet-General Nucleonics July 1965

Table 4.2.2.2.2-1

[illegible]

*Reference 4.2.1-1. Power Plant Study, Aerojet-General Nucleonics July 1965

Table 4.2.3-1

POWER SYSTEM REQUIREMENTS AND SYSTEM WEIGHTS
(STATE OF THE ART SOLAR CELL SYSTEMS - ADVANCED DEVELOPMENT RTG'S*)

	POWER PROFILE							
	A	B	C**	D	E	F**	G	H
Solar Panel Output								
(1 year duration at 1620 km)	17.0	23.8	16.1	4.1	11.2	3.2	18.7	40.6
Conversion and Regulation Efficiency	85	85	85	85	85	85	85	85
Regulated Power Level	14.4	20.2	13.7	3.5	9.5	2.7	15.9	34.5
Solar Panel Projected Area	257	360	245	62	170	48	284	616
Solar Panel Weight	1880	2640	1790	360	1240	350	2080	4500
Panel Deployment Mechanism Weight	55	75	50	15	35	13	60	130
Battery Capacity	21.5	14.5	9.5	16.0	6.9	1.9	52.0	24.9
Battery Discharge Level	50	50	50	50	50	50	50	50
Battery Weight	600	410	265	460	200	55	1500	710
Other Component Weights	50	50	35	35	25	25	75	75
Total System Weight	2585	3175	2140	870	1500	443	3715	5415
RTG Output								
Conversion and Regulation Efficiency	9.4	13.2	8.8	2.4	6.1	1.7	10.6	22.2
Regulated Power Level	85	85	85	85	85	85	85	85
Number of Units	8.0	11.2	7.5	2.0	5.2	1.5	9.0	18.9
Size of each unit (Dia., and Length)	3	3	3	1	3	1	3	3
Total RTG Weight	1.4	1.6	1.3	1.4	1.1	1.2	1.5	2.2
Battery Capacity	2130	3000	2000	550	1380	385	2400	5000
Battery Discharge Level	14.8	4.4	0	14.8	4.4	0	45.5	13.5
Battery Weight	50	50	-	50	50	-	50	50
Other Component Weights	220	65	-	220	65	-	685	205
Total System Weight	35	35	25	35	35	25	65	65
	2385	3100	2025	805	1480	410	3150	5270

* RTG Total System Weights are also representative of SNPA-LOB Power System
** Receive-only Satellite, no transmitting power required

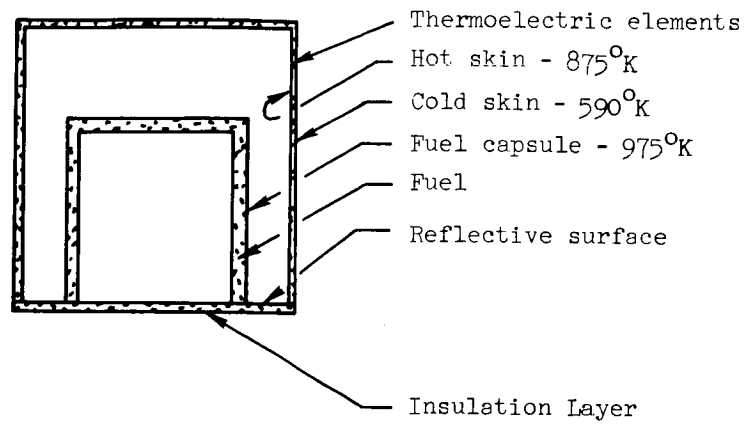


Figure 4.2.1.1-1. RTG Fuel Configuration

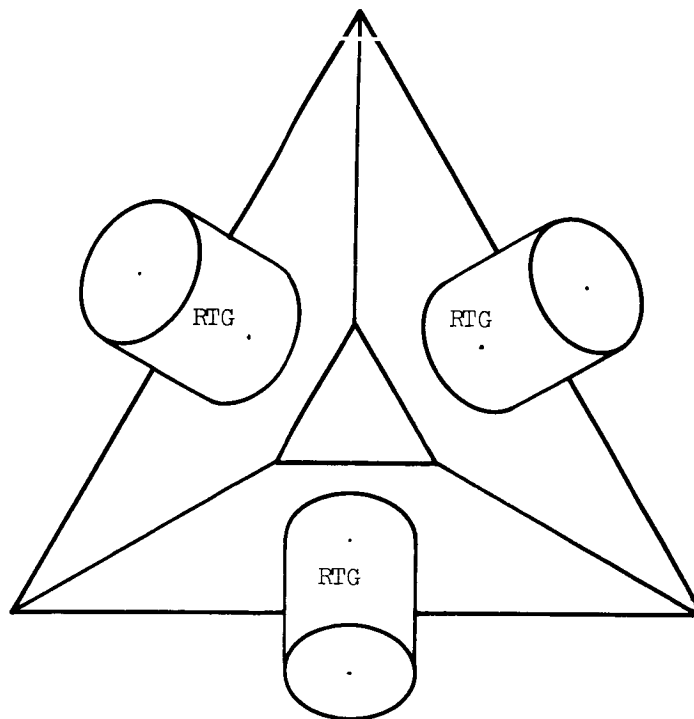


Figure 4.2.1.1-2. RTG Configuration

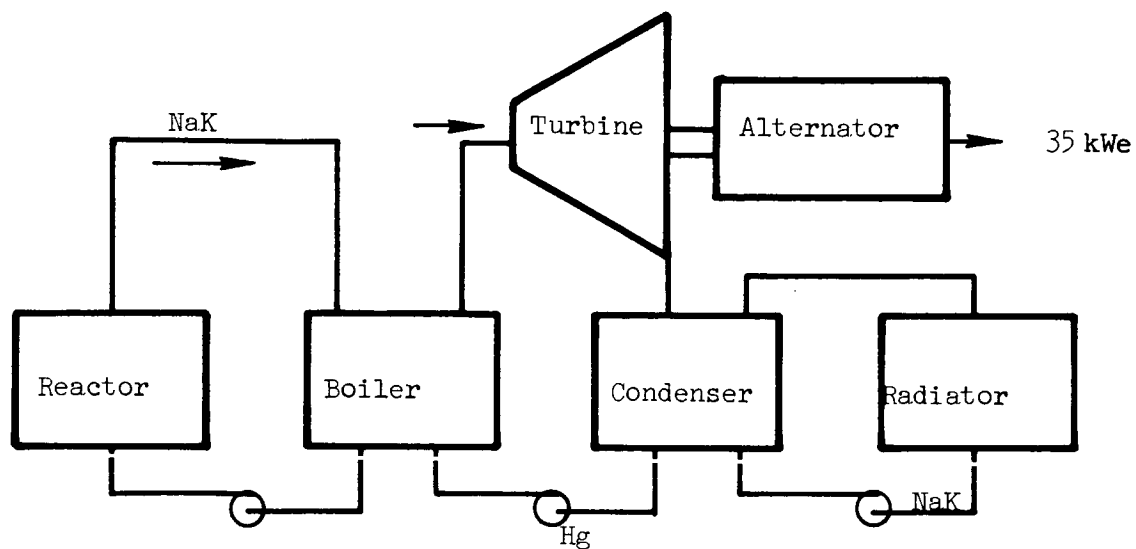


Figure 4.2.1.4-1. SNAP-8 Power System

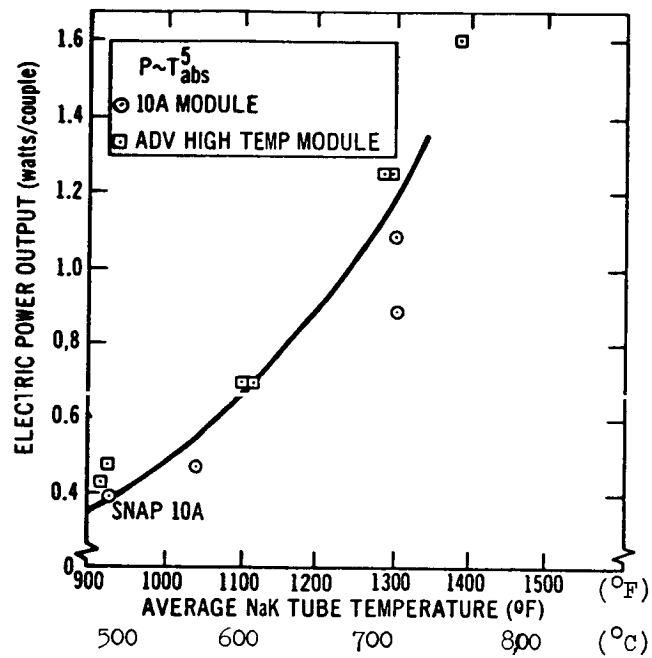


Figure 4.2.1.5-1. Thermoelectric Performance vs Temperature

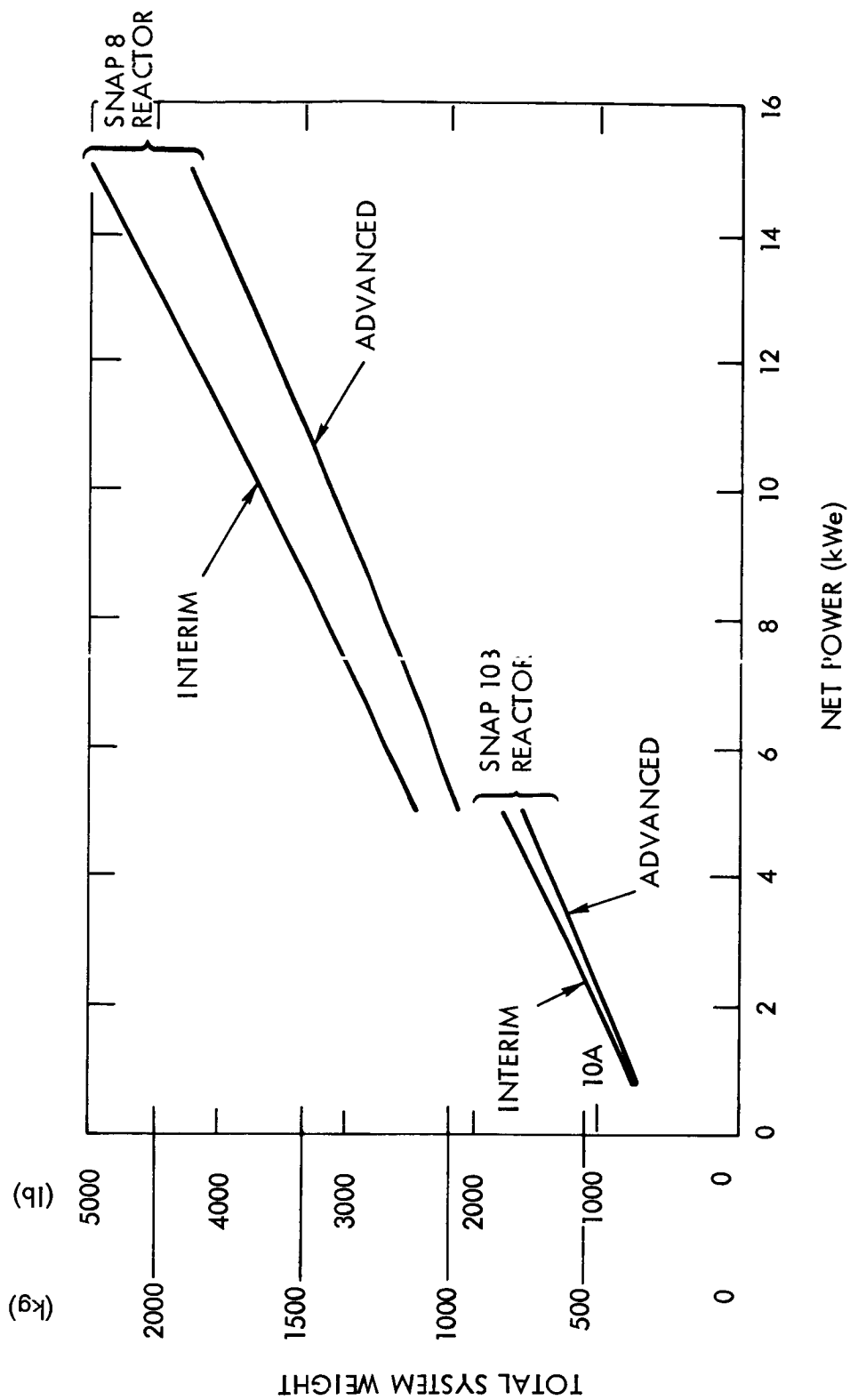


Figure 4.2.1.5-2. Advanced Reactor Thermoelectric System Weight vs Power Level

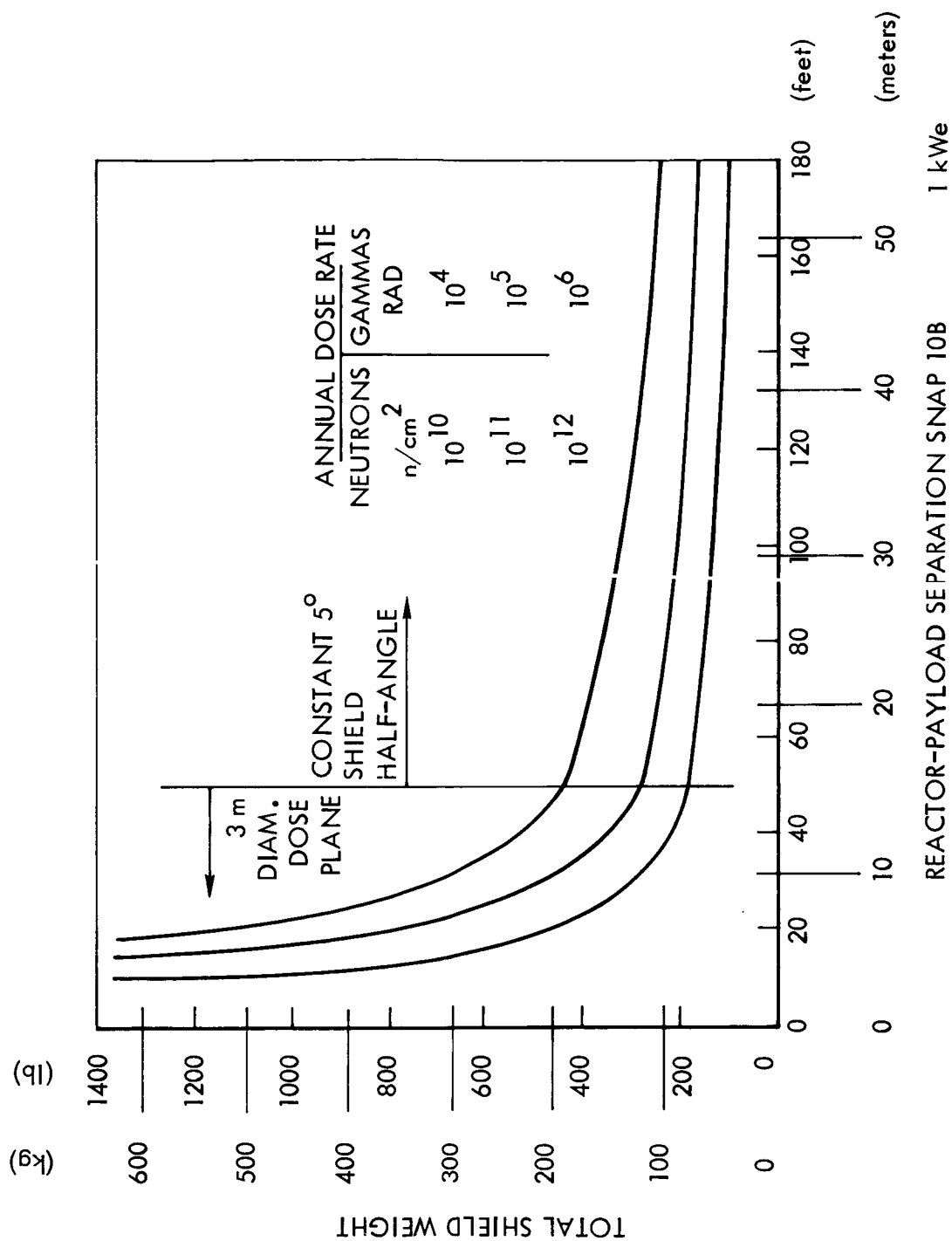


Figure 4.2.1.5-3. Shield Weight vs Separation Distance

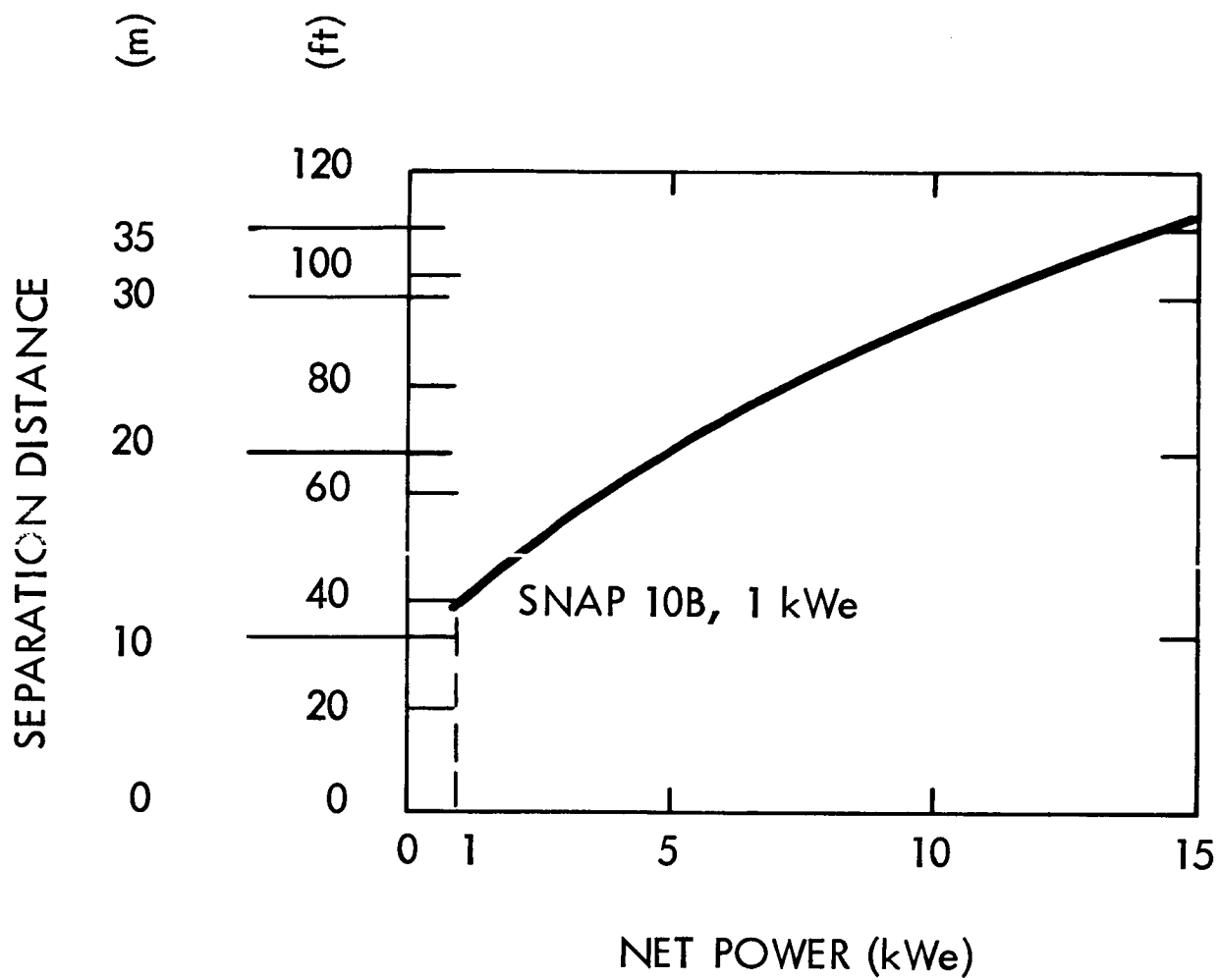
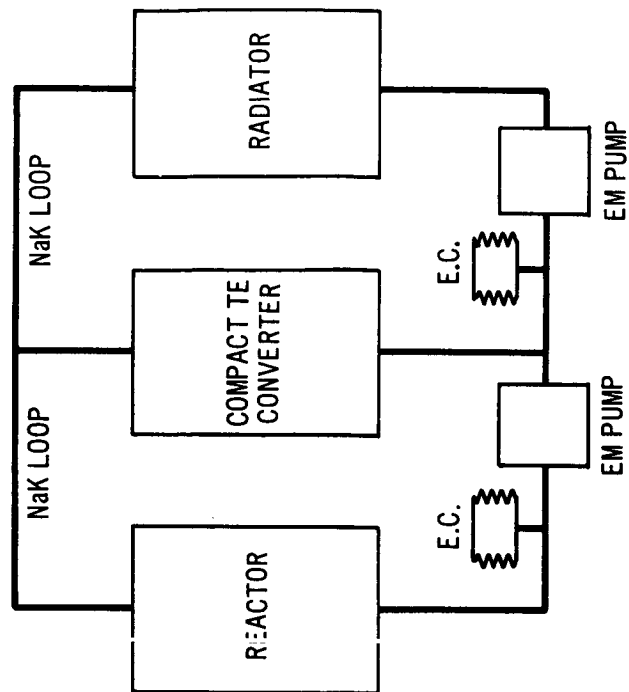
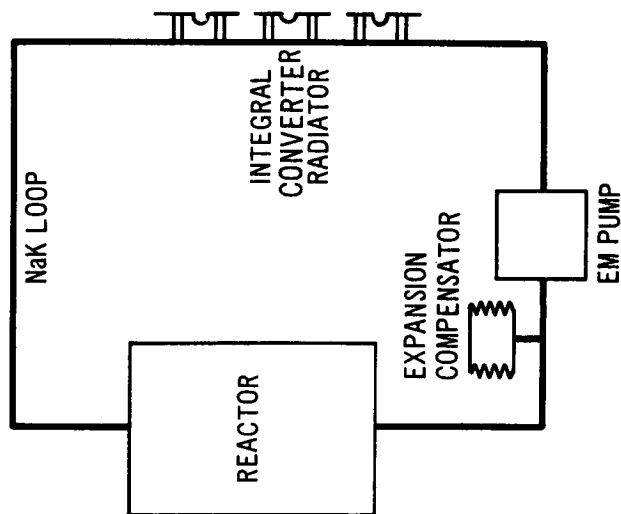


Figure 4.2.1.5-4. Optimum Reactor-Payload Separation Distance vs Power Level



COMPACT CONVERTER
SYSTEM



DIRECT RADIATING
CONVERTER SYSTEM

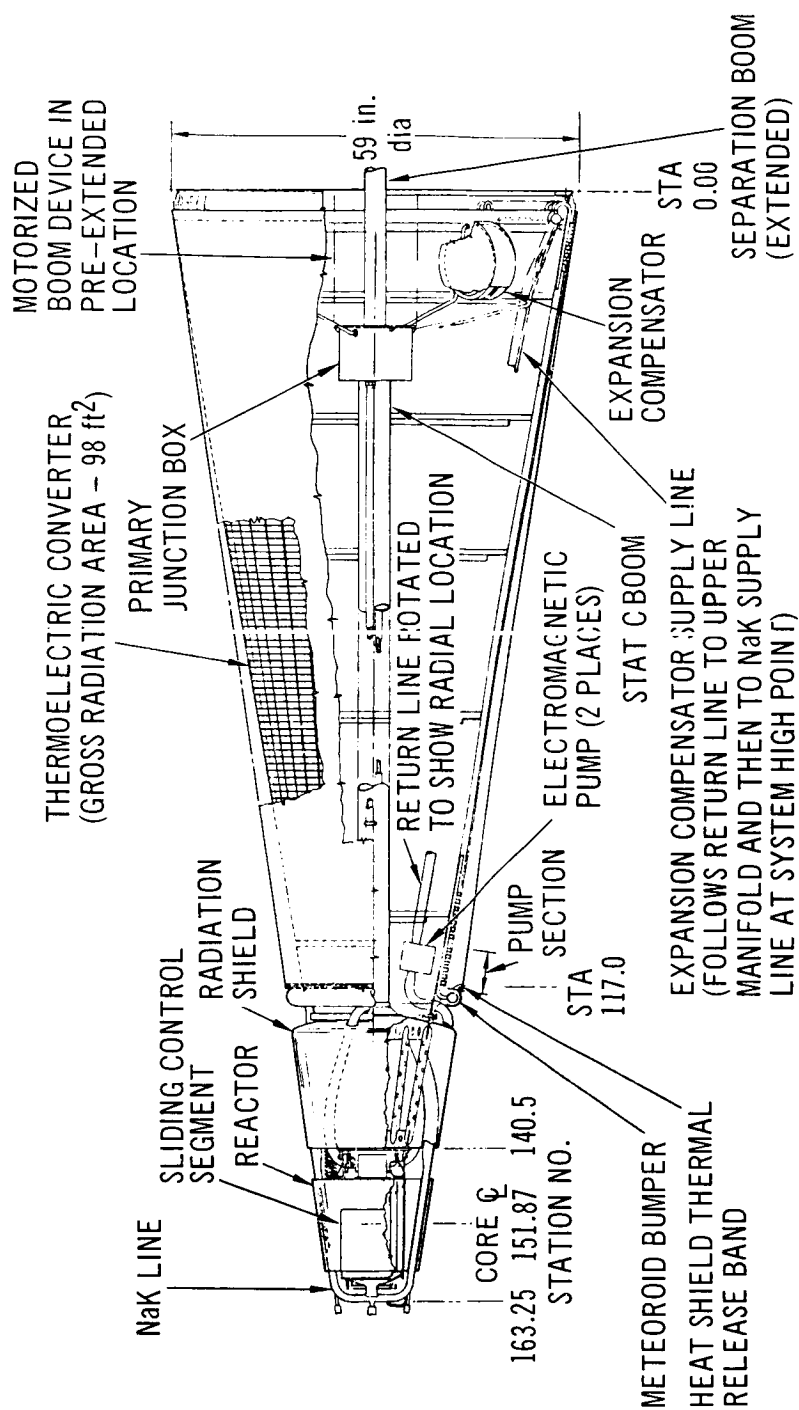


Figure 4.2.1.5-6. Reactor Thermoelectric Power System (2 KWe) *

* Reference: "Nuclear Power Systems for Advanced High-Powered Communications Satellites" J.D. Gylfe, AIAA, Communications Satellite Systems, Washington, D.C., May 2-4, 1966.

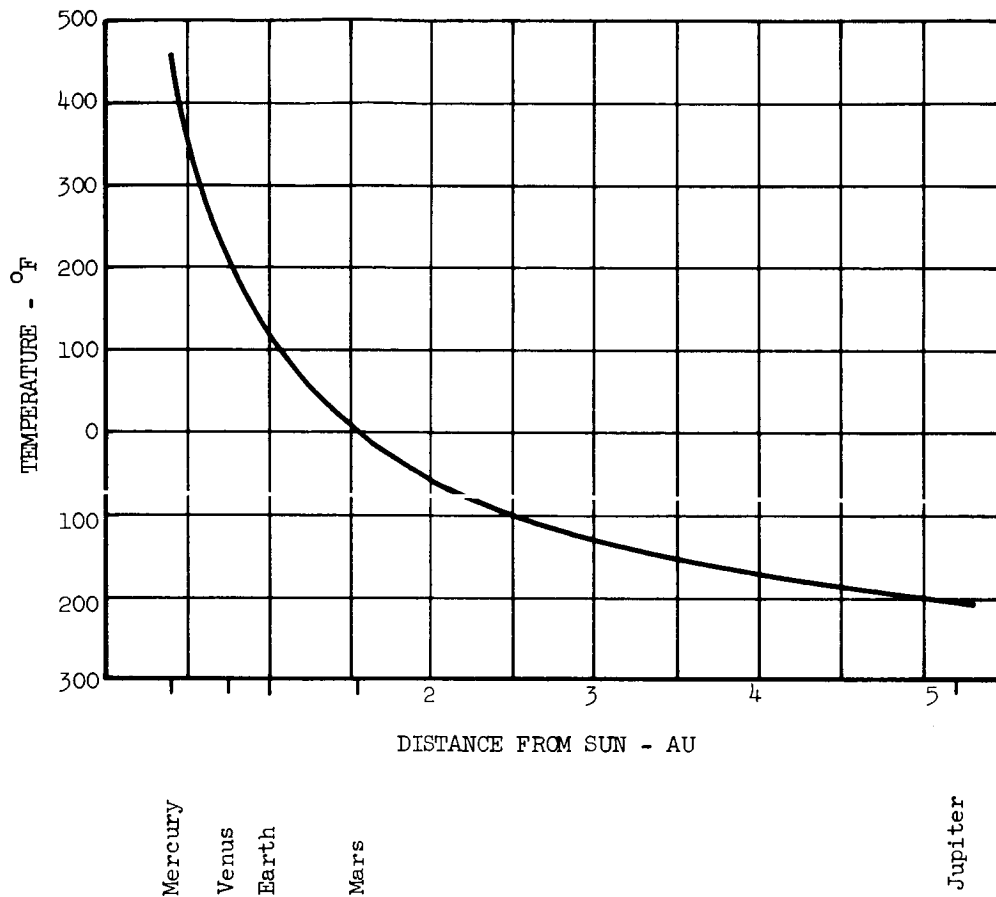


Figure 4.2.2.2.3-1. Temperature of Solar Panels*

* Reference A: Space-General Corporation, Internal Research and Development Report, Space Power, Jan. 1966.

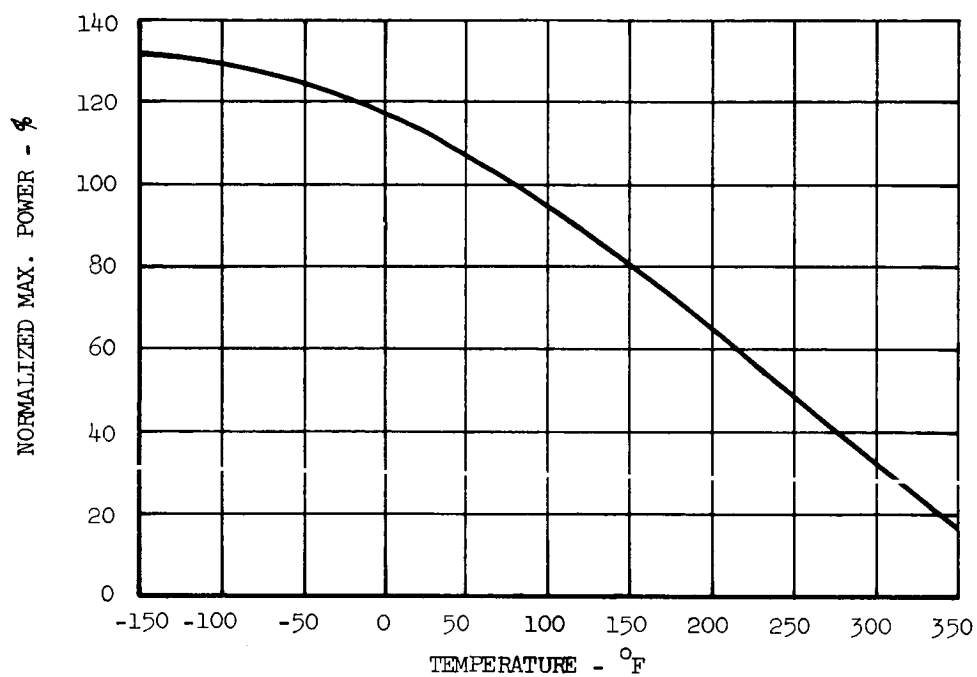
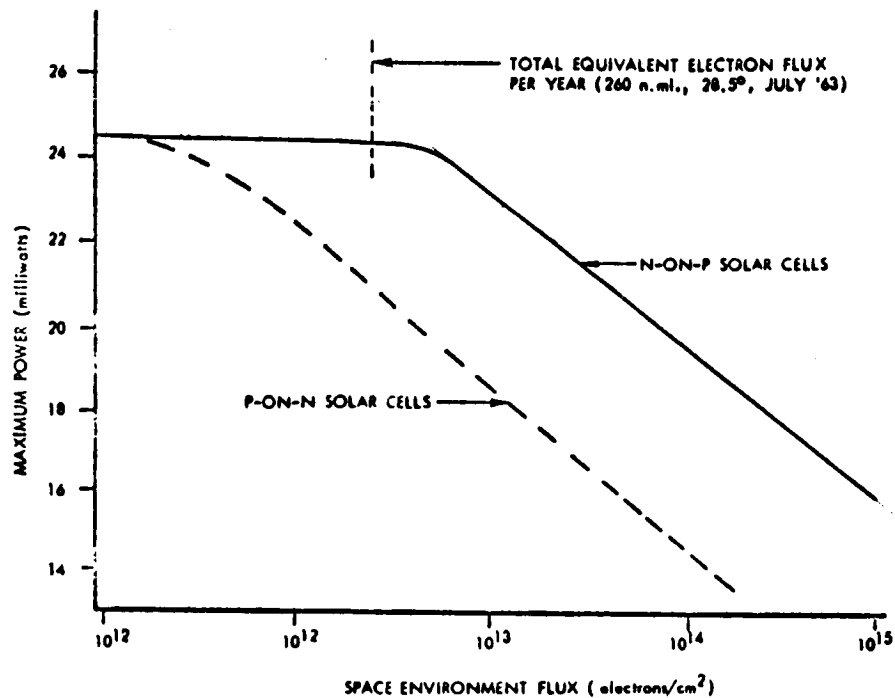
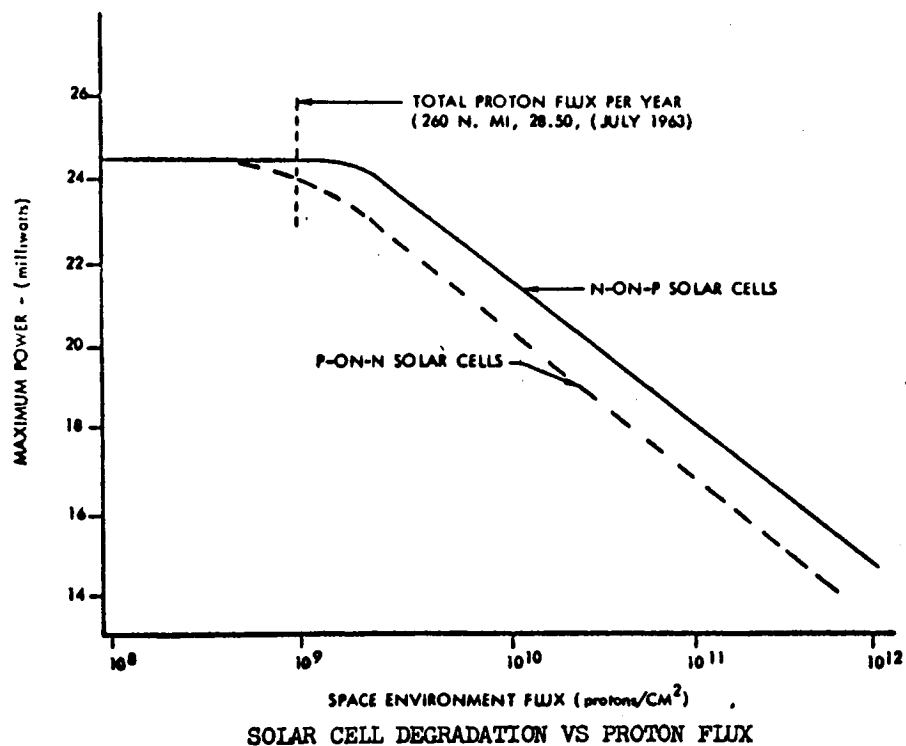


Figure 4.2.2.2.3-2. Temperature Effect on Silicon Solar Cells*

* Reference A: Space-General Corporation, Internal Research and Development Report, Space-Power, Jan. 1966



SOLAR CELL DEGRADATION VS ELECTRON FLUX



SOLAR CELL DEGRADATION VS PROTON FLUX

Figure 4.2.2.2.3-3 Solar Cell Degradation vs Proton Flux

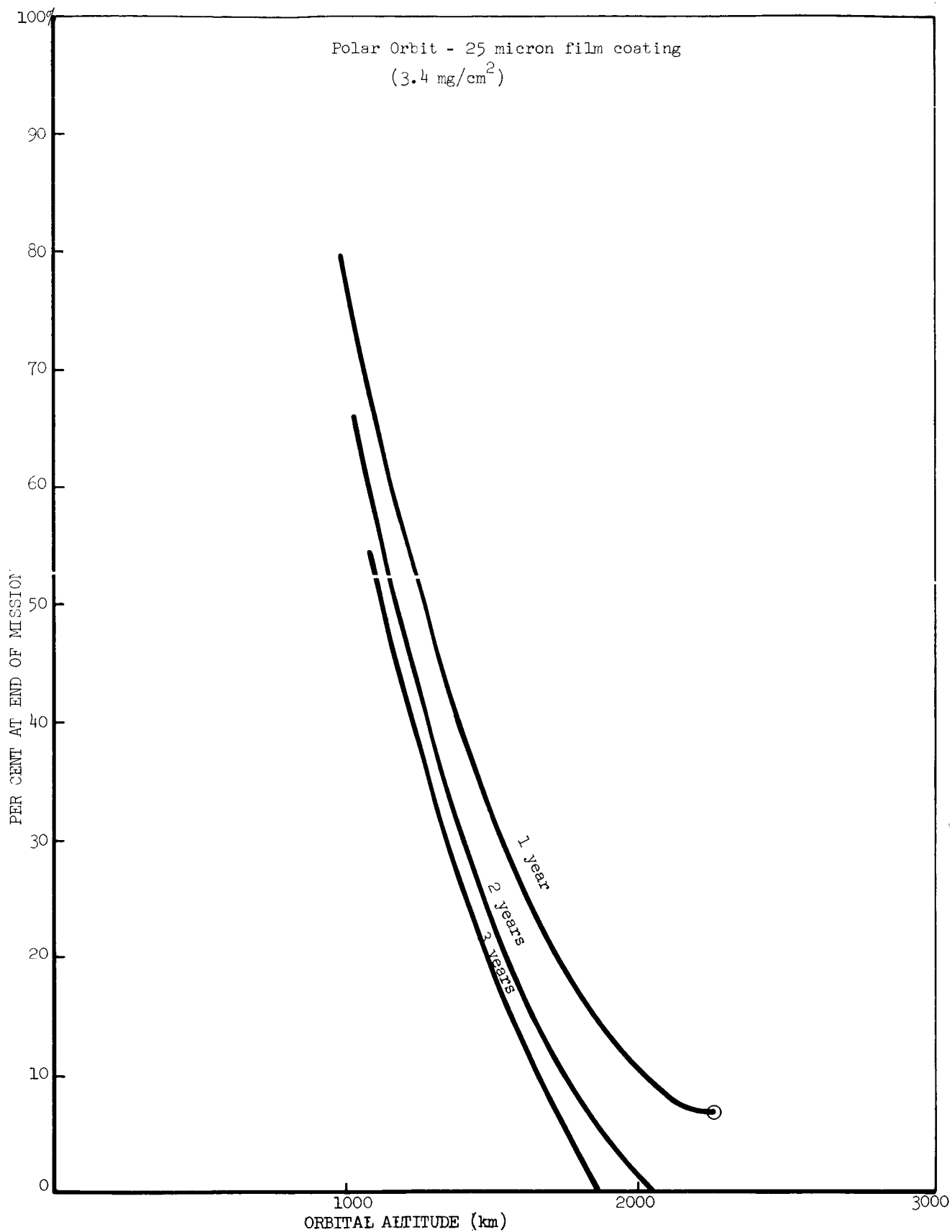


Figure 4.2.2.2.3-4 Solar Cell Endurance

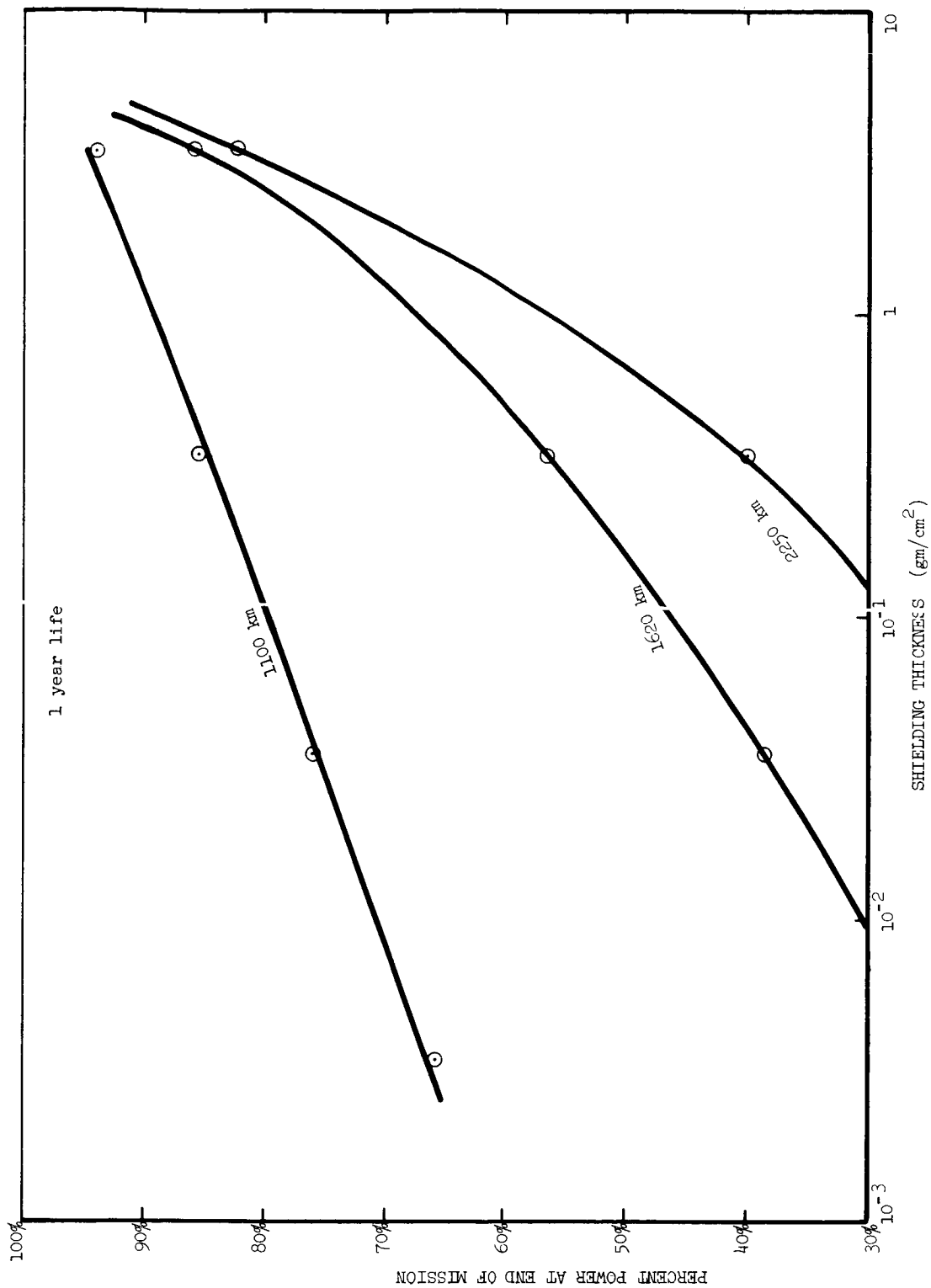


Figure 4.2.2.2.3-5. Effect of Shielding on Solar Cell Endurance*

* Reference A: Space-General Corporation, Internal Research and Development Report, Space Power, January 1966

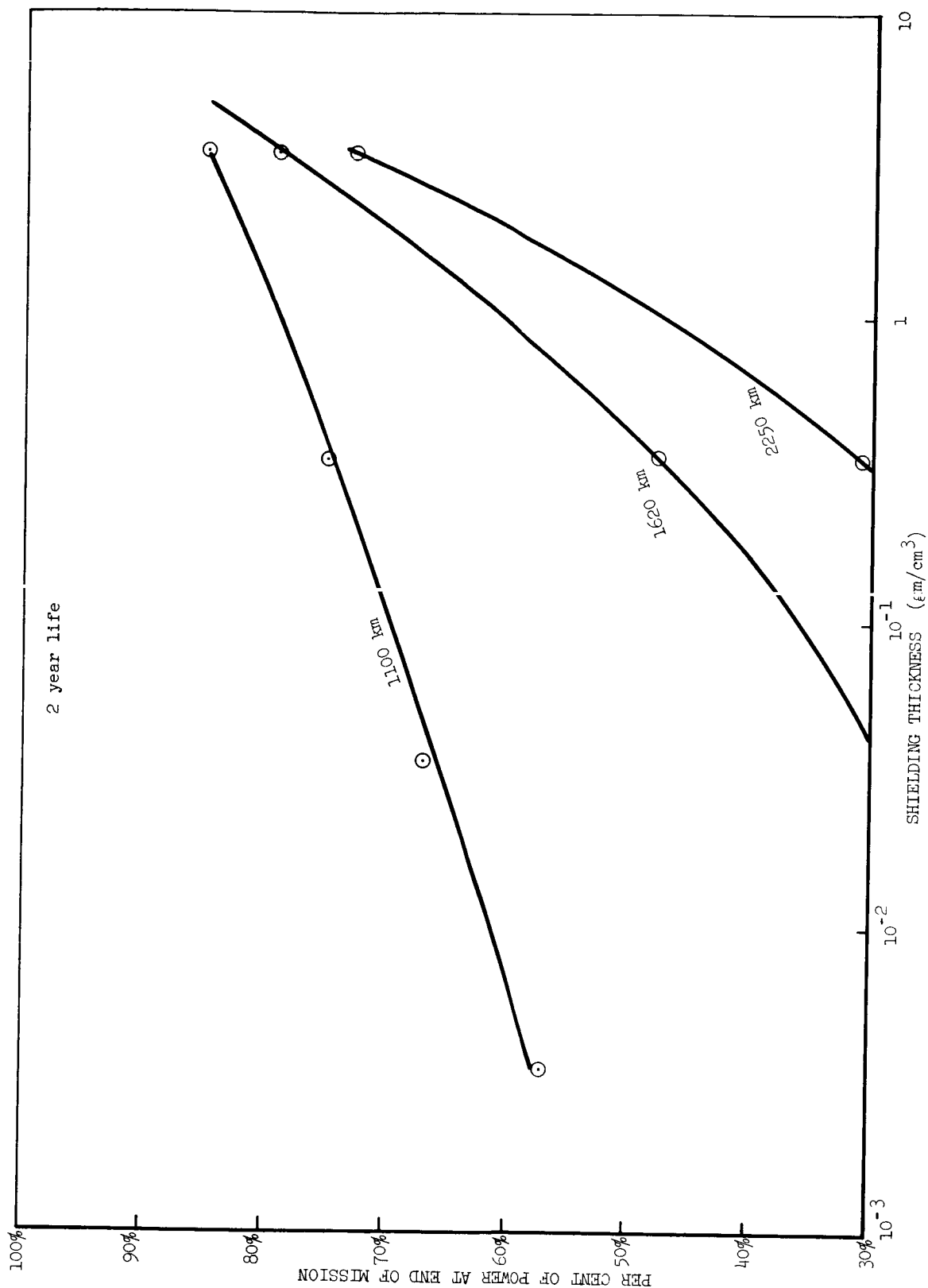


Figure 4.2.2.2.3-6. Effect of Shielding on Solar Cell Endurance *

* Reference A: Space-General Corporation, Internal Research and Development Report, Space Power, January 1966

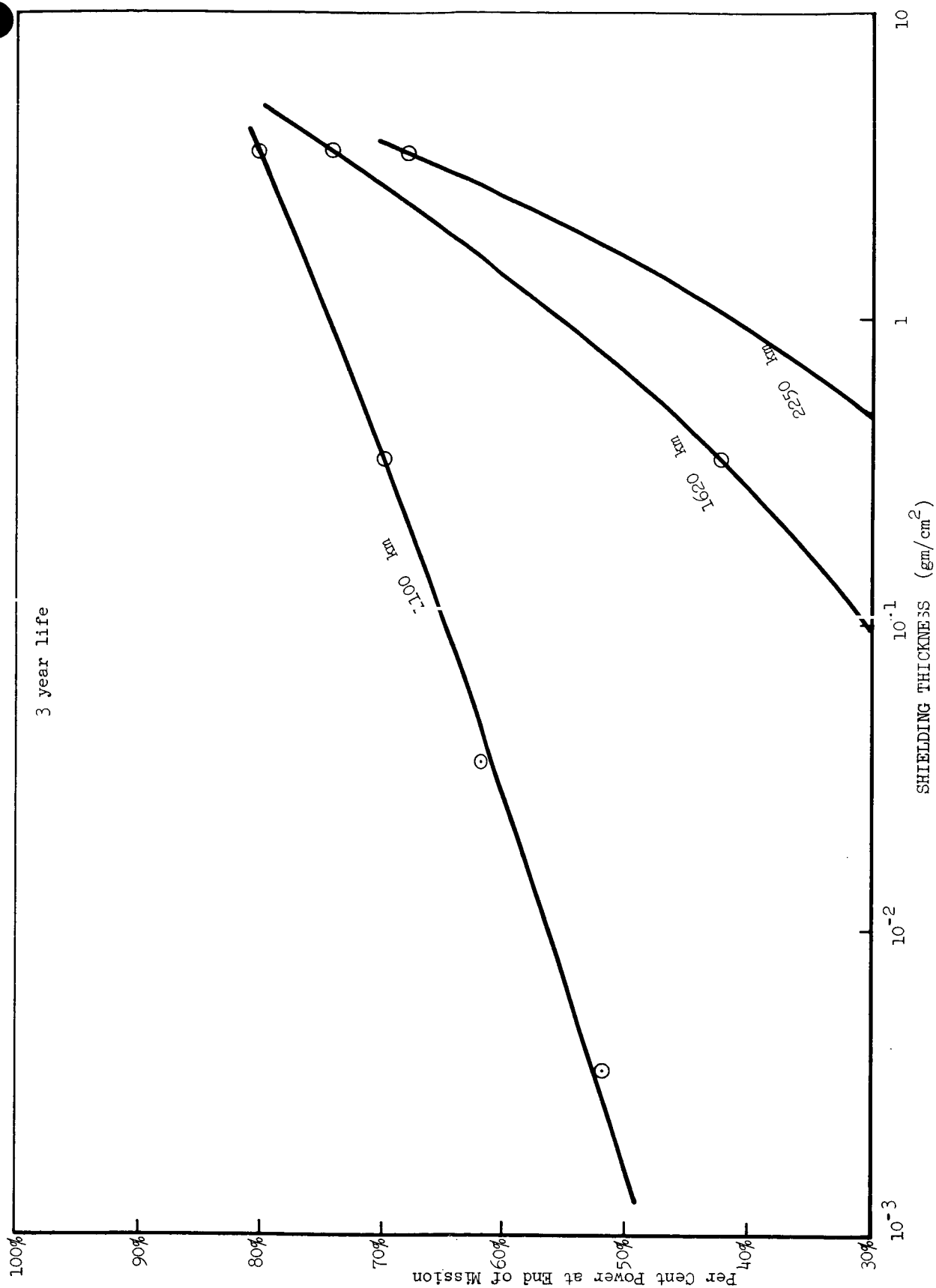


Figure 4.2.2.2.3-7. Effect of Shielding on Solar Cell Endurance *

* Reference A: Space-General Corporation, Internal Research and Development Report, Space Power, January 1966

INTRODUCTION

Attitude control system requirements have been estimated for two DSMCS satellite configurations. The configurations selected are typical of the extremes in geometric size and moment-of-inertia magnitudes. The smaller is a nuclear powered satellite and the larger a solar powered satellite. Physical characteristics of the two configurations are detailed in Section 4.3.2. Mission specifications are defined in Section 4.3.1. These determine functional requirements for attitude control.

4.3.1

MISSION CHARACTERISTICS

In general, the mission of the DSMCS satellite is to continuously monitor a spacecraft operating in deep space. Monitoring is accomplished by pointing a body fixed, high gain, narrow beam antenna along the satellite-to-spacecraft line of sight (LOS) to receive spacecraft transmission. Information received is relayed to a ground based station. In addition, the DSMCS is to communicate angle of the line of sight (ALOS) tracking information to the ground station. Provision for continued tracking and reacquisition in the event of temporary loss of spacecraft transmission is desired. Specifications are as follows.

Orbit

Earth, circular, polar. Longitude of ascending node, any value.
Altitude, 750 km to 1635 km.

Lifetime

One to three years.

Operational era

1975 to 1985

Orientation Requirements

Antenna pointing axis (roll axis) pointing along the LOS to within one-tenth antenna beam width. Angle between the pointing axis and the normal to the orbital plane: 30 degrees maximum maintained for several weeks, 17 degrees average over first year, 14 degrees average over second and third years. Null roll angle inertially fixed.

Initial Acquisition

Remove ± 3 deg/sec tip-off rates and complete initial acquisition of stellar reference frame within 2 hours after separation or after completion of deployment of extendable and erectable equipment, if any.

Calibration Maneuvers

Within one hour after completion of stellar acquisition, orient pointing axis to point normally at ground calibration stations at time of pass over station. The angle, γ , is defined as the angle between the calibration station local vertical and the pointing axis as measured in the plane containing the local vertical and the normal to the orbit. Incrementally sweep γ over the range from plus to minus one antenna beam width at the rate of one-tenth beam width per orbit.

Spacecraft Acquisition

Satisfy orientation requirements within one hour after completion of calibration.

4.3.2 PHYSICAL CHARACTERISTICS

Physical characteristics which influence attitude control system requirements and design have been estimated for two configurations. The Nuclear Powered Profile B Small Dish Configuration, and the Solar Powered Profile B 1600 km Altitude 1 year Small Dish Configuration. For brevity, they will be referred to as the NB and SB configurations in subsequent attitude control discussion.

The two configurations are drawn to the approximate scales indicated in Figures 4.3-1 and 4.3-2. These are deployed configurations corresponding to the normal tracking mode of operation. Orientation of the body fixed

axes are shown with the origins at the centers-of-mass. It is assumed that both configurations have the same basic structure which is the cylinder with diameter, ℓ_r , and length, ℓ_x , shown in Figure 4.3-1. Although the basic structure would probably have a polygonal cross section for purposes of fabrication and for other reasons, the circular cross section should be an adequate representation.

Weight and balance data is given in Table 4.3-1. The antenna hub center-of-mass locations, used later to estimate ACS imparted accelerations of the hub, are measured from the drawings of Figures 4.3-1 and 4.3-2. The hub center of mass (c.m.) location, x_H , is the distance from the satellite center-of-mass or, in other words, the location in body axis coordinates.

Table 4.3-2 shows geometric characteristics which will be used in estimating attitude control system requirements. The projected areas and their centroid locations are needed to approximate aerodynamic, solar, and meteoroid pressure induced torques. As described in the nomenclature, the projected areas are designated by a subscript which corresponds to the body axis normal to the plane of the area; for example, A_x is the maximum area projected on the $Y_B Z_B$ - plane. Numerical values in Table 4.3-2 are estimated from measurements of the drawings of Figures 4.3-1 and 4.3-2.

The NB and SB configurations chosen for evaluation are seen to differ greatly in size; they represent the extremes in weight and balance and geometry over the DSMCS configuration range.

To estimate the effects of disturbance torques of magnetic origin, quantitative descriptions of the satellite magnetic fields are needed. Appendix 1 of Reference (1), "Prediction of Spin Axis Drift", provides a summary discussion of the many difficulties involved in formulating any precise description. There, the problem is simplified by assuming that the magnetic properties of a satellite can be represented by a single dipole moment that remains constant with respect to the body axes. It is noted that although the actual magnetic properties of the spacecraft would not be expected to conform strictly to this assumption, it appears to be true that the strongest magnetic effects are due to the presence of permanent magnetic dipole moments, and that in other studies, this assumption has yielded results reasonably

consistent with observations. This assumption will be used in the DSMCS study. However, assignment of a magnitude and direction to the magnetic moment remains.

Experience in the measurement and control of spacecraft magnetic fields is reported in appreciable detail in Reference (1), "Proceedings of the Magnetism Workshop". In this report, post despin values of magnetic moments derived from tests of a number of spacecraft flight units range from 1.5×10^{-8} weber-meters (12 pole-cm) to 3.0×10^{-6} weber-meters (2350 pole-cm). It is indicated that the residual magnetic moment can be reduced to values in the neighborhood of the 1.5×10^{-8} weber-meter value, dependent upon the extent of magnetic control and testing of the design. Mariner 4 was subjected to a moderate amount of control and testing. A residual magnetic moment of approximately 3.8×10^{-7} weber-meters was obtained. As reported in Reference (2), control of the Mariner magnetic field was accomplished by imposing magnetic field specifications on subsystems as follows.

perm fields	less than 5×10^{-9} weber/m ² at 9 meters
current loop fields (d.c. to 5 Hz)	less than 5×10^{-10} weber/m ² at 9 meters
stability of perm fields	5×10^{-10} weber/m ² at 9 meters

An estimated 30 to 40 percent of the subsystems did not meet these specifications, it is noted.

It will be assumed that the DSMCS satellite will be magnetically "moderately clean" as a result of design control like that on Mariner 4. That is, specifications similar to those above are to be imposed on the DSMCS subsystems. For example, if a maser amplifier subsystem were to contain a superconducting magnet with a 0.5 weber/m^2 (5 kilogauss) flux density in the gap, the field external to this subsystem which would appear to emanate from a magnetic dipole of approximately 1.3×10^{-5} weber-meters (10^4 pole-cm) would be corrected, or nulled, with a compensating magnet associated with this subsystem.

When many subsystems have magnetic moments which are each nulled to within a standard deviation value as specified in the design control specification, the resultant satellite magnetic moment will have a standard deviation value,

$$\sigma_M = N^{\frac{1}{2}} \sigma_{Mi} \quad (1)$$

based on the statistical law of large numbers. In (1),

N = number of subsystems

σ_{Mi} = subsystem magnetic moment standard deviation

Now, a second assumption will be employed. It will be assumed that the number of subsystems or components which contribute to the resultant magnetic moment is proportional to the average (continuous) power. This assumption is thought to be conservative. It would seem to be true that the number of current loops on solar panels for the solar powered systems would increase in proportion to the average power. Otherwise, an increase in average power might reflect an increase in individual subsystem power requirements as opposed to an increase in the number of subsystems with a nominally unchanged demand for each.

Based on the foregoing assumptions, the DSMCS satellite will have a magnetic moment magnitude with a standard deviation,

$$\sigma_M = \left(\frac{P_{AVE}}{P_{AO}} \right)^{\frac{1}{2}} \sigma_{MO} \quad (2)$$

for

P_{AVE} = Average (continuous) DSMCS power

P_{AO} = Average power of a reference spacecraft

σ_{MO} = Magnetic moment standard deviation of the reference spacecraft

The reference spacecraft will be taken to be Mariner 4 with

$$3 \sigma_{MO} = 3.8 \times 10^{-7} \text{ weber-meters}$$

and

$$P_{AO} = 0.2 \text{ kilowatts (References 5 and 6).}$$

Thus,

$$3 \sigma_M = P_{AVE}^{\frac{1}{2}} \left(8.5 \times 10^{-7} \frac{\text{weber-meters}}{\text{kilowatt}^{\frac{1}{2}}} \right) \quad (3)$$

For the DSMCS Power Profile "B",

$$\begin{aligned} P_{AVE} &= 7.5 \text{ kilowatts and} \\ 3 \sigma_M &= 2.3 \times 10^{-6} \text{ weber-meters} \end{aligned} \quad (4)$$

Significance of the magnetic moment of the satellite and, correspondingly, the design control specifications will be discussed further in Section 4.3.3, "Disturbance Torques".

Surface reflectivity characteristics of the satellite are to be assigned in order to assess ACS requirements of aerodynamic and solar pressure origins. Preliminary estimates have indicated that disturbance torques from these sources are small compared to those of gravity gradient and magnetic field origin. For both aerodynamic and solar pressure forces, a variation in reflection coefficients from the minimum value of zero to the maximum of unity will cause a variation in resultant forces and torques which is no more than $\sqrt{5}$ to 1.

Aerodynamic reflection coefficients will be taken to be unity. That is, the surface reflection coefficient for tangential momentum exchange,

$$\sigma_T = 1 \quad (5)$$

and the surface reflection coefficient for normal momentum exchange,

$$\sigma_N = 1. \quad (6)$$

In Section 6 of Reference 4, it is reported that aerodynamic coefficient values of between 0.8 and 1.0 are indicated based on a few measurements made on typical engineering surfaces.

Solar radiation reflectivity will be taken to be zero;

$$\rho_S = 0. \quad (7)$$

The SB satellite solar panels will be designed to have a minimum reflectivity near 0.05 to maximize solar power efficiency.

The above reflection coefficients yield forces which are parallel to the relative direction of incident photons or molecules; thus, subsequent mathematical manipulation becomes relatively tractable.

Offset between the center of pressure and the center of area in each axis is subject to design control to some extent. A value

$$\sigma_{cA} = 0.033 \text{ meters} \quad (8)$$

is selected.

An important physical characteristic of the satellite is structural bending. Structural bending is thought to be the limiting factor on the accuracy with which angular deviations between any two reference lines of the satellite can be determined. It is reported in Reference 7 that development tests on the AOSO experiment compartment, a tube approximately 1.2 meters in diameter and 2.6 meters in length, yielded a thermal distortion of approximately 0.009 millirads for a 1°C average temperature differential across the tube. It is earlier reported in Reference 8 from a JPL study of Ranger that alignment accuracy is likely to be no better than 0.09 millirads as a result of structural bending. This would correspond to an average temperature differential of approximately 10°C across the AOSO experiment compartment. It does not seem unreasonable to expect that the DSMCS satellite, with a basic structure approximately 3.05 meters in diameter and 3.2 meters in length, would suffer a similar temperature differential and corresponding thermal distortion of the structure. Although fine alignments can be achieved under laboratory conditions, it will be assumed that the DSMCS satellite alignment accuracies are limited to 0.09 millirads by thermal distortion of the structure in an orbital environment.

An estimate of structural dynamic properties of the DSMCS satellite is beyond the scope of this study. The first body bending modes would normally be removed from the ACS natural frequencies, sufficiently to avoid cross coupling. It will be assumed that this is the case and minimum beam width for the two configurations is:

$$\beta_N = 0.698 \text{ millirad } (0.04 \text{ deg}) \quad (9)$$

4.3.3 DISTURBANCE TORQUES

Gravity Gradient Torque

With reference to the axis systems and nomenclature described in Figures 4.3-3 and 4.3-4, the origins of the body axes and of the orbit-plane axes are at the center of mass of the satellite. The center of gravity does not coincide with the center of mass because the gravitational potential of the earth varies with altitude. If orientation is such that the line of gravitational force applied at the center of gravity does not pass through the center of mass, a torque tending to rotate the satellite will result. This torque will be experienced by the DSMCS satellite as a disturbance which must be overcome by the attitude control system. An estimate of the magnitudes of the body axis components of gravity gradient torque is developed as follows.

Let \bar{r}_k be the vector location of an increment of mass, m_k , in body axes.

$$\bar{r}_k = x_k \bar{e}_{XB} + y_k \bar{e}_{YB} + z_k \bar{e}_{ZB} \quad (1)$$

The location, $\bar{\rho}_k$, with respect to the center of the gravitational force field, earth, is then

$$\bar{\rho}_k = \bar{R}_O + \bar{r}_k \quad (2)$$

The gravitational force on m_k is given by the inverse square law as

$$\bar{F}_{Gk} = -\mu \frac{\bar{\rho}_k}{\rho_k^3} m_k \quad (3)$$

Gravitational torque about the center of mass contributed by this force is

$$\bar{T}_{Gk} = \bar{r}_k \times \bar{F}_{Gk} \quad (4)$$

Components of \bar{R}_0 in body axes are

$$\bar{R}_{OB} = \begin{pmatrix} R_{OXB} \\ R_{OYB} \\ R_{OZB} \end{pmatrix} = \begin{bmatrix} M_{OB} \end{bmatrix} \begin{pmatrix} 0 \\ R_0 \\ 0 \end{pmatrix} \quad (5a)$$

$$(5b)$$

$$(5c)$$

where

$$\begin{bmatrix} M_{OI} \\ M_{IB} \end{bmatrix} = \begin{bmatrix} M_{OB} \end{bmatrix} \quad (\text{see Figures 4.3-3 and 4.3-4}),$$

or

$$\begin{pmatrix} R_{OXB} \\ R_{OYB} \\ R_{OZB} \end{pmatrix} = \begin{pmatrix} R_0 a_{12} \\ R_0 a_{22} \\ R_0 a_{32} \end{pmatrix} \quad (6a)$$

$$(6b)$$

$$(6c)$$

Combining (1), (2), and (6) yields the components of $\bar{\rho}_k$ in body axes as

$$\bar{\rho}_{kB} = \begin{pmatrix} \rho_{kXB} \\ \rho_{kYB} \\ \rho_{kZB} \end{pmatrix} = \begin{pmatrix} a_{12} R_0 + x_k \\ a_{22} R_0 + y_k \\ a_{32} R_0 + z_k \end{pmatrix} \quad (7a)$$

$$(7b)$$

$$(7c)$$

ρ_k^2 is the sum of the squares of the components given in (7). After noting that the orthogonal matrix, $\begin{bmatrix} M_{OB} \end{bmatrix}$,

$$a_{12}^2 + a_{22}^2 + a_{32}^2 = 1 \quad (8)$$

ρ_k^2 may be written in the form

$$\rho_k^2 = R_0^2 \left[1 + 2 a_{12} \left(\frac{x_k}{R_0} \right) + 2 a_{22} \left(\frac{y_k}{R_0} \right) + 2 a_{32} \left(\frac{z_k}{R_0} \right) + \left(\frac{x_k}{R_0} \right)^2 + \left(\frac{y_k}{R_0} \right)^2 + \left(\frac{z_k}{R_0} \right)^2 \right] \quad (9)$$

Satellite dimensions are very small compared to the orbital radius. In accordance with (8), the direction cosines have magnitudes which are bounded by unity and they cannot vanish simultaneously. Therefore, (9) is very closely the first order approximation

$$\rho_k^2 = R_0^2 \left[1 + 2 a_{12} \left(\frac{x_k}{R_0} \right) + 2 a_{22} \left(\frac{y_k}{R_0} \right) + 2 a_{32} \left(\frac{z_k}{R_0} \right) \right] \quad (10)$$

and

$$\frac{1}{\rho_k^3} = \frac{1}{R_0^3} \left[1 - 3 a_{12} \left(\frac{x_k}{R_0} \right) - 3 a_{22} \left(\frac{y_k}{R_0} \right) - 3 a_{32} \left(\frac{z_k}{R_0} \right) \right] \quad (11)$$

When (3) and (4) are combined,

$$\bar{T}_{Gk} = \mu m_k \frac{1}{\rho_k^3} \bar{J}_k \quad (12)$$

for

$$\bar{J}_k = \bar{\rho}_k \times \bar{r}_k \quad (13)$$

From (2),

$$\bar{J}_k = (\bar{R}_0 + \bar{r}_k) \times \bar{r}_k \quad (13a)$$

$$\bar{J}_k = \bar{R}_0 \times \bar{r}_k ; \quad \bar{J}_{kB} = \bar{R}_{OB} \times \bar{r}_k \quad (13b)$$

In terms of the components in body axes as obtained from (1) and (6),

$$\bar{J}_{kB} = \begin{pmatrix} J_{kXB} \\ J_{kYB} \\ J_{kZB} \end{pmatrix} = R_0 \begin{pmatrix} a_{22} z_k - a_{32} y_k \\ a_{32} x_k - a_{12} z_k \\ a_{12} y_k - a_{22} x_k \end{pmatrix} \quad (14a)$$

$$(14b)$$

$$(14c)$$

ρ_k^{-3} in the form of the right hand member (RHM) of (11) and the components of \bar{J}_k of the RHM of (14) are to be multiplied and substituted into (12) to obtain the components of \bar{T}_{Gk} in body axes. Net torque is then obtained by summing the contributions associated with the increments of mass. That is,

$$\bar{T}_G = \sum_k \bar{T}_{Gk} \quad (15)$$

Because the body axes are defined as principal axes with origin at the center of mass, factors of terms in (15) will be

$$\begin{aligned} \sum_k m_k x_k &= \sum_k m_k y_k = \sum_k m_k z_k = \sum_k m_k x_k y_k = \sum_k m_k x_k z_k \\ &= \sum_k m_k y_k z_k = 0, \end{aligned}$$

and

$$\sum_k m_k x_k^2 = I_X \quad (16a)$$

$$\sum_k m_k y_k^2 = I_Y \quad (16b)$$

$$\sum_k m_k z_k^2 = I_Z \quad (16c)$$

which define I_X , I_Y , and I_Z . Performance of the multiplication and summation with the above relations employed yields

$$\bar{T}_{GB} = \begin{pmatrix} T_{GXB} \\ T_{GYB} \\ T_{GZB} \end{pmatrix} = \frac{3\mu}{R_0^3} \begin{pmatrix} a_{32} a_{22} (I_Y - I_Z) \\ a_{12} a_{32} (I_Z - I_X) \\ a_{12} a_{22} (I_X - I_Y) \end{pmatrix} \quad (17a)$$

$$(17b)$$

$$(17c)$$

Relationships which incorporate the principal moments of inertia, I_{XX} , I_{YY} , and I_{ZZ} are

$$\begin{pmatrix} I_Y - I_Z \\ I_Z - I_X \\ I_X - I_Y \end{pmatrix} = \begin{pmatrix} I_{ZZ} - I_{YY} \\ I_{XX} - I_{ZZ} \\ I_{YY} - I_{XX} \end{pmatrix} \quad (18a)$$

$$(18b)$$

$$(18c)$$

For a circular orbit, the square of the orbit angular velocity is

$$\omega_0^2 = \frac{\mu}{R_0^3} \quad (19)$$

Combining (17), (18) and (19) yields the desired torques in body axes

$$T_{GXB} = 3 \omega_0^2 (I_{ZZ} - I_{YY}) a_{22} a_{32} \quad (20a)$$

$$T_{GYB} = 3 \omega_0^2 (I_{XX} - I_{ZZ}) a_{12} a_{32} \quad (20b)$$

$$T_{GZB} = 3 \omega_0^2 (I_{YY} - I_{XX}) a_{12} a_{22} \quad (20c)$$

From the nomenclature, the direction cosines may be put in the form

$$a_{12} = \cos \psi \sin \theta \sin \lambda - \sin \psi \cos \lambda \quad (21a)$$

$$a_{22} = \cos \psi \cos \lambda + \sin \psi \sin \theta \sin \lambda \quad (21b)$$

$$a_{32} = \cos \theta \cos \lambda \quad (21c)$$

for

$$\lambda = \phi - \eta \quad (22)$$

The off orbit normal pointing angle, α , is such that

$$\cos \alpha = \cos \theta \cos \psi \quad (23)$$

Relations (20) through (23) are used to find the gravity gradient torques for selected orientations, α and ψ , θ , and ϕ . Secular and periodic components of torque can be recognized and calculated more readily when the following forms are used

$$G_X = 3 a_{22} a_{32} \quad (24a)$$

$$G_Y = 3 a_{12} a_{32} \quad (24b)$$

$$G_Z = 3 a_{12} a_{22} \quad (24c)$$

Trigonometric manipulations of (21) yield the forms

$$G_X = G_{XA} + G_{XP} \sin (2\lambda + \Phi_X) \quad (25a)$$

$$G_Y = G_{YA} + G_{YP} \sin (2\lambda + \Phi_Y) \quad (25b)$$

$$G_Z = G_{ZA} + G_{ZP} \sin (2\lambda + \Phi_Z) \quad (25c)$$

which show the periodic components to have twice the orbital frequency. Secular or average values of the torques have the factors

$$|G_{XA}| = \frac{3}{2} \cos \alpha \quad (26a)$$

$$|G_{YA}| = \frac{3}{2} \cos \alpha \tan \psi \quad (26b)$$

$$|G_{ZA}| = \frac{3}{2} \cos^2 \alpha \tan \psi \quad (26c)$$

Magnitudes of the periodic torque components have the factors

$$|G_{XP}| = \frac{3}{2} \left[\cos^2 \alpha (1 - \tan^2 \psi) + \sin^2 \psi \right]^{\frac{1}{2}} \quad (27a)$$

$$|G_{YP}| = \frac{3}{2} \sin \alpha \quad (27b)$$

$$|G_{ZP}| = \frac{3}{2} \sin \alpha (1 - \cos^2 \alpha \tan^2 \psi)^{\frac{1}{2}} \quad (27c)$$

At this point, uncertainties in moments of inertia will be incorporated by defining quantities as follows:

$$\Delta I_X \triangleq (I_{ZZ} - I_{YY}) + \frac{3\sigma_I}{I} \sqrt{I_{ZZ}^2 + I_{YY}^2} \quad (28a)$$

$$\Delta I_Y \triangleq (I_{XX} - I_{ZZ}) + \frac{3\sigma_I}{I} \sqrt{I_{XX}^2 + I_{ZZ}^2} \quad (28b)$$

$$\Delta I_Z \triangleq (I_{YY} - I_{XX}) + \frac{3\sigma_I}{I} \sqrt{I_{YY}^2 + I_{XX}^2} \quad (28c)$$

where $100 \frac{3\sigma_I}{I}$ represents the uncertainty in percent. Combining (20), (24), and (28) yields

$$T_{GXB} = \omega_0^2 G_X \Delta I_X \quad (29a)$$

$$T_{GYB} = \omega_0^2 G_Y \Delta I_Y \quad (29b)$$

$$T_{GZB} = \omega_0^2 G_Z \Delta I_Z \quad (29c)$$

Peak gravity gradient torques are obtained by substituting in (29)

$$G_X = |G_{XA}| + |G_{XP}| \quad (30a)$$

$$G_Y = |G_{YA}| + |G_{YP}| \quad (30b)$$

$$G_Z = |G_{ZA}| + |G_{ZP}| \quad (30c)$$

Peak angular momentum to be stored based on a momentum dump cycle of once per orbit is obtained by integration of (29) or, correspondingly, (25) over one orbital period and allowing the periodic component to be maximum. The resultant angular momentum is

$$H_{GX} = \omega_O \Delta I_X \left(2\pi |G_{XA}| + \frac{|G_{XP}|}{2} \right) \quad (31a)$$

$$H_{GY} = \omega_O \Delta I_Y \left(2\pi |G_{YA}| + \frac{|G_{YP}|}{2} \right) \quad (31b)$$

$$H_{GZ} = \omega_O \Delta I_Z \left(2\pi |G_{ZA}| + \frac{|G_{ZP}|}{2} \right) \quad (31c)$$

For evaluation of peak torques and angular momentums, a worst case orientation is used. Average angular momentums to be dumped per orbit are the first terms of the right hand members of (31) evaluated at the average off normal orientation.

It is interesting that angular momentum per orbit is proportional to the orbital rate and not the square of the orbital rate in (31). The form of (31) is to facilitate comparison of the gravity gradient disturbance with disturbances of other origin. Angular momentum per unit time would retain the squared relationship.

The "G" coefficients obtained as described above are given in Table 4.3-3 based on the values of α given in the Mission Specifications, Section 4.3.1. The corresponding torques and angular momentums shown in normalized form are given in Table 4.3-4.

Torque and momentum requirements of gravity gradient origin are to be determined. A suggested method of alleviating gravity gradient disturbance effects would be to spherically balance the vehicles by use of weights on extendible booms or by addition of solar panels at right angles to those proposed for the SB configuration. An estimate of the radius of gyration and weight requirements to achieve spherical balance is shown in Table 4.3-5 for both configurations. The minimum moment of inertia that can be obtained is found to be greater than the largest without spherical balance; approximately 8% for the NB configuration and 2% for the SB configuration the weight and radii of gyration for the SB configuration assuming a battery for a mass is high. The radius of gyration is a lower bound on boom length; weights indicated are boom weight plus end weight. The assumption that spherical balance can be achieved has been carried into the requirements caused by gravity gradient to compare results with those for the non-balanced configurations. Account is taken of the increased moment-of-inertia and a 5% three sigma uncertainty is assigned to the spherical balance as compared to 2% for the non-balance. These are thought to be conservative moment-of-inertia uncertainties based on Space-General experience with the OV3 satellites which have rigid specifications on control and determination of moments-of-inertia in order to satisfy spin stabilization requirements.

Results are shown in Table 4.3-6 linear momentum or impulse requirements are based on the couple arm lengths available on the basic structure. That is,

$$I_{GX} = \frac{H_{GX}}{l_x} \quad (32a)$$

$$I_{GY} = \frac{H_{GY}}{l_x} \quad (32b)$$

$$I_{GZ} = \frac{H_{GZ}}{l_x} \quad (32c)$$

Total momentum dumping requirements for the first year are calculated from

$$I_{GT} = N_0 (I_{GX} + I_{GY} + I_{GZ}) \quad (33)$$

for N_0 the number of orbits in a year and using first year values. The result of (33) with second year values is added to the first year total to obtain total requirements to the end of the second year and is added again for requirements to the end of the third year.

Interestingly enough, total momentum requirements are greater for the spherically balanced NB configuration than for the non-balanced NB configuration. It is noted that the NB configuration moments of inertia are separated in value by no more than 8%. The combined 5% uncertainty and 8% increase in moment of inertia is less favorable than an 8% imbalance and 2% uncertainty.

The SB configuration with spherical balanced has requirements which are approximately one-fifth, those with non-balance; but, as previously stated, boom weight and length requirements to balance the SB configuration are excessive.

Magnetic Field

The magnitude of disturbance torque caused by interaction of the magnetic moment of the satellite with the magnetic field of the earth is to be determined. The rationalized MKS system of units will be employed.

Based on a magnetic dipole representation of the earth magnetic field, the maximum magnitude of magnetic intensity at orbit radius is given by

$$H_E = \frac{M_E}{2\pi \mu_0 R_0^3} \quad (34)$$

for M_E the earth magnetic dipole strength. Magnetic torque on the satellite is given by

$$\vec{T}_M = \vec{M}_S \times \vec{H}_E \quad (35)$$

for \vec{M}_S the magnetic dipole of the satellite. Thus, the maximum torque is

$$T_M = \frac{M_S M_E}{2\pi \mu_0 R_0^3} \quad (36)$$

The three sigma value of M_S derived in Section 4.3.2 for the "B" power profile is

$$M_S = 2.3 \times 10^{-6} \text{ weber-meters.}$$

Values for M_E and μ_0 are

$$M_E = 4\pi \times 8.1 \times 10^{15} \text{ weber-meters}$$

and

$$\mu_0 = 4\pi \times 10^{-7} \frac{\text{weber}^2}{\text{newton-meter}^2}$$

Thus, for the assigned magnetic moment of the spacecraft,

$$T_M = 2.967 \times 10^{16} \frac{1}{R_0^3} \quad (37)$$

The largest angular momentum, H_M , that could be caused by magnetic effects over one orbit is

$$H_M = T_M P_0$$

for P_0 the orbit period. The following values are obtained at altitude

h (km)	T_M (10^{-3} N-m)	H_M (N-m-sec)
750	0.082	0.491
1635	0.058	0.412

Aerodynamic Pressure

An estimate of the magnitude of aerodynamic disturbance will be made using the areas, area centroid locations, and surface reflection coefficients of Section 4.3.2. For $\sigma = \sigma' = 1$, the aerodynamic pressure on a surface will be

$$P_A = 2 Q \cos \beta \quad (38)$$

and the resultant aerodynamic force will be aligned along the relative velocity vector. In (38), Q is the dynamic pressure and β is the angle between the relative velocity vector and the normal to the surface.

The NB and SB configurations will be treated separately. Consider the NB configuration in Figure 4.3-1 with geometry given in Table 4.3-2. For the relative velocity in the $X_B Z_B$ -plane and β the angle between the X_B -axis and the relative velocity vector, the aerodynamic torque about Y_B that results from use of (38) and from association of appropriate force components with area moment arms is

$$\begin{aligned} \frac{T_{AY}}{Q} = & (-z_{AX} A_X + x_{AZ} A_Z) \\ & + (z_{AX} A_X - x_{AZ} A_Z) \cos 2\beta \\ & + (x_{AX} A_X - z_{AZ} A_Z) \sin 2\beta \\ & + (x_{AX} A_X - z_{AZ} A_Z) \sin 2\beta \end{aligned} \quad (39)$$

when divided by dynamic pressure. In (39), the conservative, but rather gross assumption is that the projected areas are the wetted surfaces. The maximum value of (39) is

$$\begin{aligned} \frac{T_{AY}}{Q} = & (-z_{AX} A_X + x_{AZ} A_Z) \\ & + \left[(x_{AX}^2 + z_{AX}^2) A_X^2 + (x_{AZ}^2 + z_{AZ}^2) A_Z^2 \right. \\ & \left. - 2 (x_{AX} z_{AZ} + z_{AX} x_{AZ}) A_Z A_X \right]^{1/2} \end{aligned} \quad (40)$$

Numerical values of Table 4.3-2 are used to compute the right hand member of (40) except that where zero appears for area centroid location, $3\sigma_{\epsilon A} = 0.1$ meters is substituted.

Numerically,

$$\frac{T_{AY}}{Q} = 56 \text{ meter}^3 \quad (41)$$

A similar procedure for the SB configuration of Figure 4.3-2 yields a maximum torque to dynamic pressure ratio in a worst case orientation of

$$\begin{aligned} \frac{T_{AZ}}{Q} = & (y_{AX} A_X + x_{AY} A_Y) \\ & + \left[(x_{AX}^2 + y_{AX}^2) A_X^2 + (x_{AY}^2 + y_{AY}^2) A_Y^2 \right. \\ & \left. - 2 (x_{AX} y_{AY} + y_{AX} x_{AY}) A_Y A_X \right]^{1/2} \end{aligned} \quad (42)$$

Numerically,

$$\frac{T_{AZ}}{Q} = 1500 \text{ meters}^3 \quad (43)$$

for the SB configurations.

A "worst case" angular momentum requirement over one orbit will be found from the maximum torques by

$$H_A = T_A P_O \quad (44)$$

for P_O the orbit period.

Dynamic pressure varies with solar activity approximately three orders of magnitude during the operational era. The maximum at maximum solar activity occurs circa 1978. Using this maximum dynamic pressure, numerical values for "worst case" aerodynamic disturbances are as follows.

Configuration	Altitude, h (km)	Maximum Torque, T_A (10^{-3} N-m)	Maximum Angular Momentum, H_A (N-m-sec)
NB	750	0.29	1.73
NB	1635	0.0019	0.013
SB	750	8.3	45.0
SB	1635	.05	.4

Solar Pressure

For the coefficient of solar reflectivity, $\rho_S = 0$ as discussed in Section 4.3-2, solar pressure in the vicinity of earth is very closely equal to aerodynamic pressure at 750 km during a period of maximum solar activity. Also, for $\rho_S = 0$, resultant forces are parallel to the direction of incident photons. The effective coefficient of drag that resulted from $\sigma = \sigma' = 1$ for aerodynamic calculations was $C_D = 2$. It can be concluded, then that maximum solar pressure effects will be one-half the aerodynamic effects at 750 km altitude and at maximum solar activity. Solar pressure effects are then as follows for the altitudes considered.

Configuration	Maximum Torque, T_S (10^{-3} N-m)	Maximum Angular Momentum Over One Orbit, H_S (N-m-sec)
NB	0.15	0.863
SB	4.15	22.7

4.3.4 STELLAR SENSORS

Stellar sensors have been developed by a number of industrial firms. Of these, SGC has developed and demonstrated a sensor for use with the Fine Attitude Control System (FACS) of the Aerobee rocket series.

The SGC stellar sensor is designed to provide signals, to the FACS, which are proportional to the Aerobee roll axis angular deviation from a selected star for ± 16 arc minutes, and constant from ± 16 arc minutes to $\pm 4^\circ$. The pointing accuracy of the sensor output (in pitch and yaw) is ± 5 arc seconds with a confidence level of 1σ , and 28 arc seconds at 4σ . When used in conjunction with the Aerobee system, the pointing accuracy is improved because of "inertial filtering".

The figures quoted are true with the condition that the selected star is a G-0 type, and has a visual magnitude of +3.0 at the earth's surface. If brighter stars are selected, the sensor signal accuracy is improved approximately in proportion to the square root of the brightness ratio. Thus, if the selected star were Deneb, a +1.33 magnitude star which is visually 12 times as

bright, as a 3rd magnitude G-0 star, the 4σ accuracy is about ± 9 arc seconds. This neglects photometric wave length response and mechanical noise.

The accuracy of the SGC sensor is, of course, noise limited. The sensor noise is generated mechanically and electrically. The latter is predominant and primarily derived from the light sensing multiplier phototube employed in the system.

Some of the design restrictions imposed upon the present stellar sensor affect its potential accuracy and operational life. These restrictions include the mechanical envelope (.42M long and .13 M diameter), the field of view required for star acquisition (8° optical cone apex angle), and a requirement for a mechanically precise light chopping motor.

While, in theory, SGC sensors could be used with DSMCS, it is doubtful that the present design is suitable; particularly, when consideration is given to the long operational period required. On the other hand, from the experience gained during the development of the present sensor, it can be stated that a suitable sensor system can be developed. For example, if the mechanical envelope is lengthened, mechanical tolerances can be relieved. By reducing the field of view for acquisition to 10 or 20 arc minutes, the requirement for a precision motor is eliminated. (This motor is used to rotate a reticle having a precise and complex pattern. With a reduced acquisition field angle, it is possible to employ fixed reticles and other techniques for modulation in the optical regime.)

Obviously, it is impossible to provide a detailed design for a stellar sensor suited to the DSMCS at this time. However, it is suggested that a single sensor for DSMCS attitude control can be contained in an envelope having approximate dimensions of .61M x .25M x .13M. The largest dimension might be halved by using folding optics.

The operational life of the SGC sensor is probably limited by the chopper motor. This motor includes ring bearings with tolerances held to 1.27×10^{-6} meters. 1×10^{-6} meters is equivalent to one arc second pointing angle, so it can be surmised that, even barring catastrophic failure, it is

probable that the motor driven reticle would go far out of alignment during the desired operational period.

By eliminating the precision motor, the operational life will likely be determined by electronic components and the state of the art.

In conclusion, it is suggested that sun sensors will be employed for the initial orientation of the stellar sensor carrier; and that sun sensor present attainable accuracy is about 6 arc minutes which is well within the stellar sensor acquisition field suggested previously.

4.3.5 ATTITUDE CONTROL SYSTEM

A functional block diagram of a fluid flywheel attitude control system under consideration for the DSMCS is shown in Figure 4.3-5. The fluid flywheel as described in Reference 19 consists, basically, of a dc conduction pump which pumps mercury through a closed loop of stainless steel tubing. It produces a control torque on the spacecraft as long as there is a rate of change of the mercury flow velocity. As indicated in Figure 4.3-5, a power converter is required for the pump. There are no bearings in the system. If an electromagnetic pump were employed instead of the dc conduction pump, there would be no moving mechanical parts. The tubing may be routed about the structure of the vehicle within bend radius limits; thus, the center of the vehicle need not be obstructed.

The flywheel subsystem has a rapid and well damped response without added compensation. It has negligible breakaway torque. Therefore, the accuracy of the system is limited only by the sensor.

GASEOUS N_2 SYSTEM

A conceptual design of a gaseous N_2 ACS and velocity trim system is shown in Figure 4.3-6. This design is to demonstrate feasibility only. The design criteria is:

Total Impulse	-	133. x 10 ³ N-sec (30,000 lb-sec) 67. x 10 ³ N-sec (15,000 lb-sec) each sphere
Minimum Thrust Level	-	.045 newtons (0.01 lbs)
Maximum Thrust Level	-	.45 newtons (0.1 lbs)
Environment	-	space (750 km altitude)
Lifetime	-	1 year

The resulting system has the following component requirements:

- 1) 4300 kg/cm² Gas Bottles - 1 meter dia. spheres with 1.25 cm walls
- 2) Gas Temperature (Time Averaged) - 120°C
- 3) Reaction Nozzles - .23 cm Throat Dia. with a 60:1 expansion ratio ($\epsilon = 60$)
- 4) Line Sizes - 0.5 cm x 0.064 cm Tubing

The weight summary is

Gas Bottles	-	115 kg (empty)
GN ₂ Wt	-	90 kg (each bottle)
Nozzle Wt	-	.023 kg each (includes mounting provisions)
Line Wt	-	0.027 kg/m
Solenoid Valves	-	0.34 kg each
Explosive Valves	-	0.23 kg each
Regulators	-	.45 kg each
Surge Chamber	-	.9 kg each
Filter	-	.23 kg each

Upon initiation of the system, the explosive valve in one bottle outlet is activated open simultaneously with the valve at the inlet of the 143 kg/cm² regulator which gives the 0.45 newtons thrust level capability. When the need for the .45 newtons thrust level has expired, the explosive valve in the

143 kg/cm² regulator outlet is commanded closed and the valve at the inlet of the 1 psia regulator is commanded open. This drops the system thrust capability to .045 newtons. When the first bottle pressure drops to 1430 kg/cm², the second bottle is activated.

The system is fabricated of aluminum with all welded construction to minimize leakage possibilities. The solenoid valves are normally closed, pilot operated valves.

The GN₂ gas supply requirement is based on a specific impulse valve of 75 seconds. This is arrived at by using an effective nozzle thrust coefficient of 1.5 (85% nozzle efficiency) and a gas temperature of 120°C. This high gas temperature is achieved by using a bottle surface finish with a solar absorbtivity to infra-red emissivity of 4 (polished aluminum). The usable required N₂ in each bottle is 90 kg.

4.5.6 RESUME

Angular momentum requirements were computed for all the significant perturbing forces exerted an DSMCS. Torques induced by the satellite magnetic moment acted upon by the earth's field, aerodynamic pressure and solar pressure were found to be small compared to that caused by gravity gradient torques. The angular momentum per orbit necessary to correct for gravity gradient torques was calculated for 2 satellite configurations, a small RTG powered system (B profile) and a solar cell powered system (B profile for 1 year 1600 km). This total momentum was two orders of magnitude higher for the solar cell configuration as for the RTG configuration assuming neither has been balanced. Because the gravity gradient torque is proportional to the differences in the moments of inertia along orthogonal axis, a further reduction by a factor of five was possible for the solar cell powered system by balancing. Balance along the three axis of symmetry was achieved by deploying the power system battery normal to the solar array about 16 meters from the satellite center of mass. RTG powered system balance could be achieved by two small weights 14 kilograms orthogonal to and about 10 meters from the axis of symmetry. The RTG imbalance is so small, six percent, that it could probably be corrected by appropriate location of equipment within the satellite.

The recommended method of stabilizing DSMCS is with a fluid fly-wheel system and N_2 thrusters. The flywheel momentum is dumped once per orbit. The system suggested is completely redundant including an extra 100 percent fuel resource. All the major component masses of the ACS scale with the total momentum above the system described. A 270 kg ACS is required for the RTG configuration and 2700 kg for the solar cell spherically balanced configuration. Fuel consumption or ACS mass is nearly proportional to time for a given DSMCS, since initial maneuvers consume only 5 percent of the first years momentum. The 50 percent spherical and 2 percent non-spherical moment of inertia uncertainty is conservative. With effort the 3 sigma value could be reduced to one percent thus decreasing the larger spherically balanced system mass by a factor of five.

The ACS system design and size was found to be relatively independent of the platform stability accuracy over a 3 to 1 range assuming a relatively noise free error signal. Also, the orientation history for all missions considered are very close to those worked in this section.

Alignment of the tracking antenna to the line of sight in the sense of nulling antenna output error to specifications appears feasible. However, the accuracy of determination of satellite and antenna pointing directions for spacecraft ephemeris data and for antenna calibration appears to be limited to 0.15 millirad with state-of-the-art equipment and is projected to be no better than 0.09 millirad in the operational era. This is considered further in the system tradeoff discussion.

LIST OF REFERENCES

1. "Prediction of Spin Axis Drift", by Leonard Pode, Space-General Report No. 5412-65-25, June 16, 1965.
2. "Proceedings of the Magnetics Workshop", compiled by Joseph G. Bastow, Jet Propulsion Laboratory, Technical Memorandum No. 33-216, September 15, 1965.
3. "Spacecraft Design Specifications, Mariner C", Jet Propulsion Laboratory, July 1965 (Mariner 4).
4. "Space Electrical Power", by W. C. Scott and F. Schulman of NASA Headquarters, Astronautics and Aerospace Engineering, May '63, pp. 48-53.
5. "Flight Performance Handbook for Orbital Operations," Edited by Raymond W. Wolverton, Space Technology Laboratories, John Wiley and Sons, New York, 1963.
6. "Effects of Solar Radiation Pressure Upon Satellite Attitude Control", R. J. McElvain, Paper presented at Guidance, Control and Navigation Conference, August 7-9, 1961 at Stanford University, American Rocket Society Publication.
7. "Development Approach for an Advanced Orbiting Solar Observatory Spacecraft", W. B. Evans, Journal of Spacecraft and Rockets, Vol. 3, No. 1, January 1965.
8. "Attitude Control for Unmanned Spacecraft", James Holahan, Space/Aeronautics, Vol. 39, No. 2, pp 78-86, February 1963.
9. "Research and Investigation on Satellite Attitude Control," Parts I.A, I.B, II and IV, K. C. Nichol et al, General Electric Company, Technical Report No. AFFDL-TR-64-168, June 1965.

Table 4.3-1

WEIGHT AND BALANCE

Configuration Designation	Mass (10^3 kg)	Moments-of-inertia (10^4 kg-m ²)			Hub c.m. Location (m)
		I_{XX}	I_{YY}	I_{ZZ}	
RTG Profile B	m				x_H
NB	6.3	1.96	2.1	2.1	2.7
SB	9.7	22.5	11.6	11.6	2.0

Table 4.3-2

GEOMETRY

Configuration Designation	Worst Case Projected Areas (m ²)			Couple Arms (m)	
	A _X	A _Y	A _Z	l _X	l _r
NB	14.5	13.7	13.7	3.2	3.05
SB	415	415	14.0	3.0	3.05

Worst Case Projected Area Centroid Locations
(m)

	x _{AX}	y _{AX}	z _{AX}	x _{AY}	y _{AY}	z _{AY}	x _{AZ}	y _{AZ}	z _{AZ}
NB	3.68	0	0	1.32	1.5	0	1.32	0	1.5
SB	4.00	0	0	0.67	1.5	0	4.35	0	1.5

Table 4.3-3

COEFFICIENTS FOR GRAVITY GRADIENT DISTURBANCES

	α (deg)	ψ (deg)	$ G_{XA} $	$ G_{YA} $	$ G_{ZA} $	$ G_{XP} $	$ G_{YP} $	$ G_{ZP} $	G_X	G_Y	G_Z
For peak torques and angular momentums	30	30	-	0.75	0.65	-	0.75	0.65	-	1.5	1.3
	0	0	1.5	-	-	1.5	-	-	3.0	-	-
For secular angular momentum, 1st year	17	12	1.43	0.31	0.29						
For secular angular momentum, 2nd and 3rd years	14	10	1.46	0.26	0.25						

Table 4.3-4

NORMALIZED TORQUES AND ANGULAR MOMENTUMS
FOR GRAVITY GRADIENT

	$T_{GXB}/\omega_0^2 \Delta I_X$	$T_{GYB}/\omega_0^2 \Delta I_Y$	$T_{GZB}/\omega_0^2 \Delta I_Z$
Peak torques	3.0	1.5	1.3
	$H_{GX}/\omega_0 \Delta I_X$	$H_{GY}/\omega_0 \Delta I_Y$	$H_{GZ}/\omega_0 \Delta I_Z$
Peak angular momentum to be stored (one orbit)	10.2	5.1	4.4
Secular angular momentum to be dumped per orbit (1st year)	9.0	1.9	1.8
Secular angular momentum to be dumped per orbit (2nd & 3rd years)	9.2	1.6	1.6

Table 4.3-5

ESTIMATE OF REQUIREMENTS
TO ACHIEVE SPHERICAL BALANCE

$$m_x x_b^2 = \frac{1}{2} (I_{00} + I_{XX} - I_{YY} - I_{ZZ})$$

$$m_y y_b^2 = \frac{1}{2} (I_{00} - I_{XX} + I_{YY} - I_{ZZ})$$

$$m_z z_b^2 = \frac{1}{2} (I_{00} - I_{XX} - I_{YY} + I_{ZZ})$$

m_x , m_y , and m_z are the masses to be deployed to radii of gyration x_b , y_b , and z_b , respectively; there is one along each axis X_B , Y_B , and Z_B , respectively. I_{00} is the resultant moment of inertia about each axis.

NB Configuration: $I_{XX} < I_{YY} = I_{ZZ}$

$$\text{Minimum } I_{00} = I_{YY} + I_{ZZ} - I_{XX}$$

$$I_{00} = 2.24 \times 10^4 \text{ Kg-m}^2$$

$$m_x x_b^2 = 0$$

$$m_y y_b^2 = m_z z_b^2 \cong .14 \times 10^4 \text{ kg-m}^2$$

$$14.0 \text{ kg at } 10 \text{ m}$$

This imbalance of 6% could probably be corrected by careful location of equipment inside cylinder volume.

Table 4.3-5 (Continued)

ESTIMATE OF REQUIREMENTS
TO ACHIEVE SPHERICAL BALANCE

SB Configuration: $I_{ZZ} = I_{YY} < I_{XX}$

$$\text{Minimum } I_{00} = I_{XX} + I_{YY} - I_{ZZ}$$

$$I_{00} = 2.3 \times 10^4 \text{ Kg-m}^2$$

$$m_x x_b^2 \cong .56 \times 10^6 \text{ kg-m}^2$$

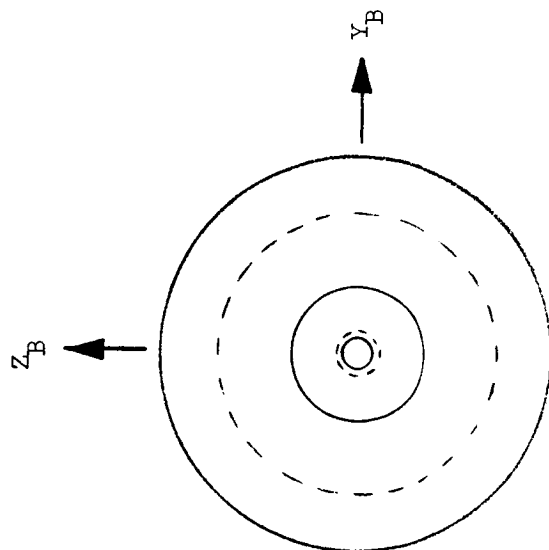
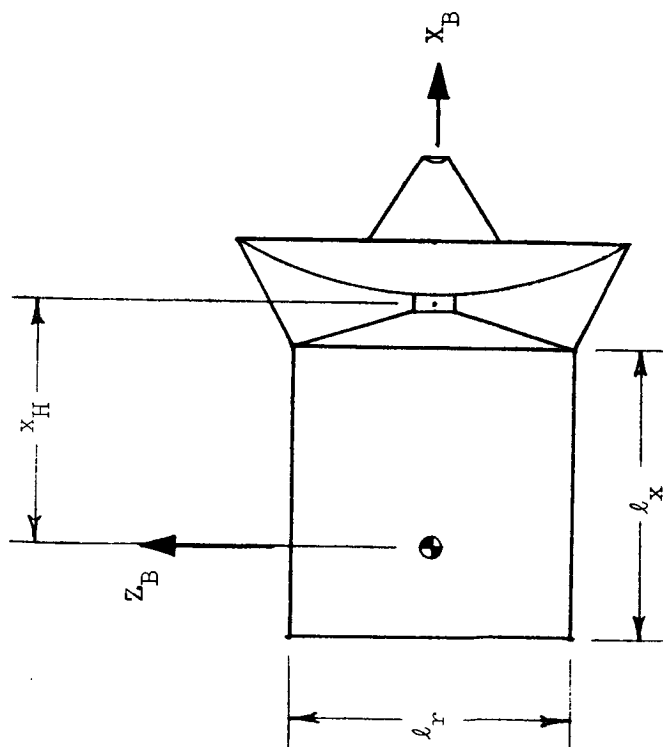
450 kg battery at 16m.

$$m_z z_b^2 = m_y y_b^2 = 0$$

Table 4.3-6
TORQUE AND MOMENTUM REQUIREMENTS OF GRAVITY
GRADIENT ORIGIN

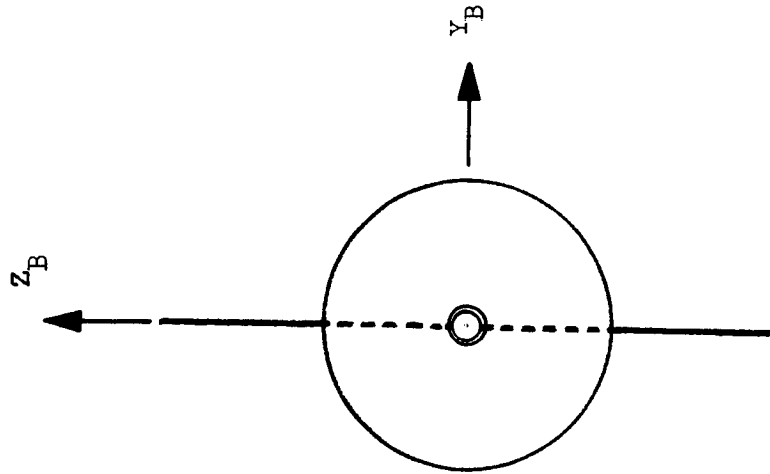
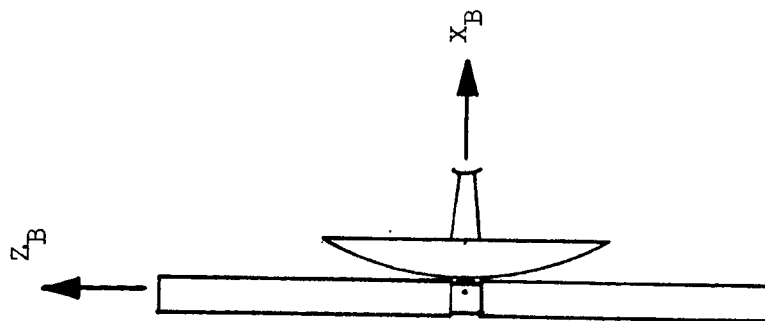
Configura- tion	Altitude (km)	Spherical Balance	$3\sigma_z/I$	Moment of Inertia Differences (10^3 kg-m^2)			Peak Torques (10^{-3} N-m)			Peak Angular Momentum (N-m-sec)			Linear Momentum Dump per Orbit (N-sec)						Total Momentum Dump (10^3 N-sec)		
				ΔI_X	ΔI_Y	ΔI_Z	T_{GXB}	T_{GYB}	T_{GZB}	H_{GX}	H_{GY}	H_{GZ}	I_{GX}	I_{GY}	I_{GZ}	I_{GX}	I_{GY}	I_{GZ}	End 1st yr	End 2nd yr	End 3rd yr
NB	750	No	0.02	.54	1.94	1.94	1.8	3.2	2.8	5.8	10.6	9.1	1.67	1.2	1.14	1.7	1.04	1.01	27.0	52.0	77.0
NB	1635	No	0.02	.54	1.94	1.94	1.26	2.1	1.7	4.9	8.7	7.9	1.4	1.01	.89	1.45	.85	.85	13.0	25.0	37.0
NB	750	Yes	0.05	1.58	1.58	1.58	5.2	2.6	2.25	16.9	8.5	7.3	4.9	.98	.93	5.0	.82	.82	36.0	70.0	106
NB	1635	Yes	0.05	1.58	1.58	1.58	2.15	1.83	1.6	14.3	7.1	6.1	4.1	.82	.79	4.2	.7	.7	25.0	50.0	74.5
SB	750	No	0.02	3.3	114.0	114.0	9.6	440	400	32	1120	1100	3.5	410	400	3.3	420	420	2500	5000	7500
SB	1635	No	0.02	3.3	114.0	114.0	6.9	310.0	300	27	1220	1200	3.3	344	335	2.8	350	350	1720	3900	5300
SB	750	Yes	0.05	16.2	16.2	16.2	60	42	26	19	98	84	56	10.8	10.1	58	10.3	10.3	406	810	1230
SB	1635	Yes	0.05	16.2	16.2	16.2	42	21	18.4	16	82	70	48	10.2	9.6	49	8.6	8.6	300	590	880

GRADIENT ORIGIN



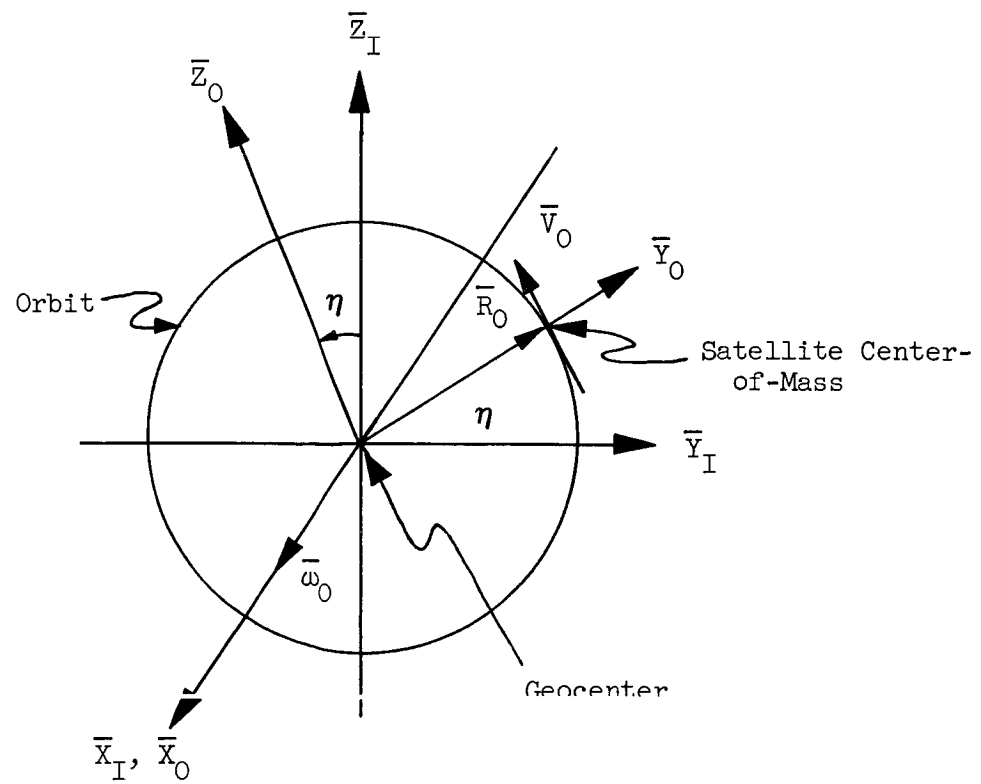
(Scale: two satellite meters per crawling inch)

Figure 4.3-1. NB Geometric Configuration



(Scale: 20 satellite meters per drawing inch)

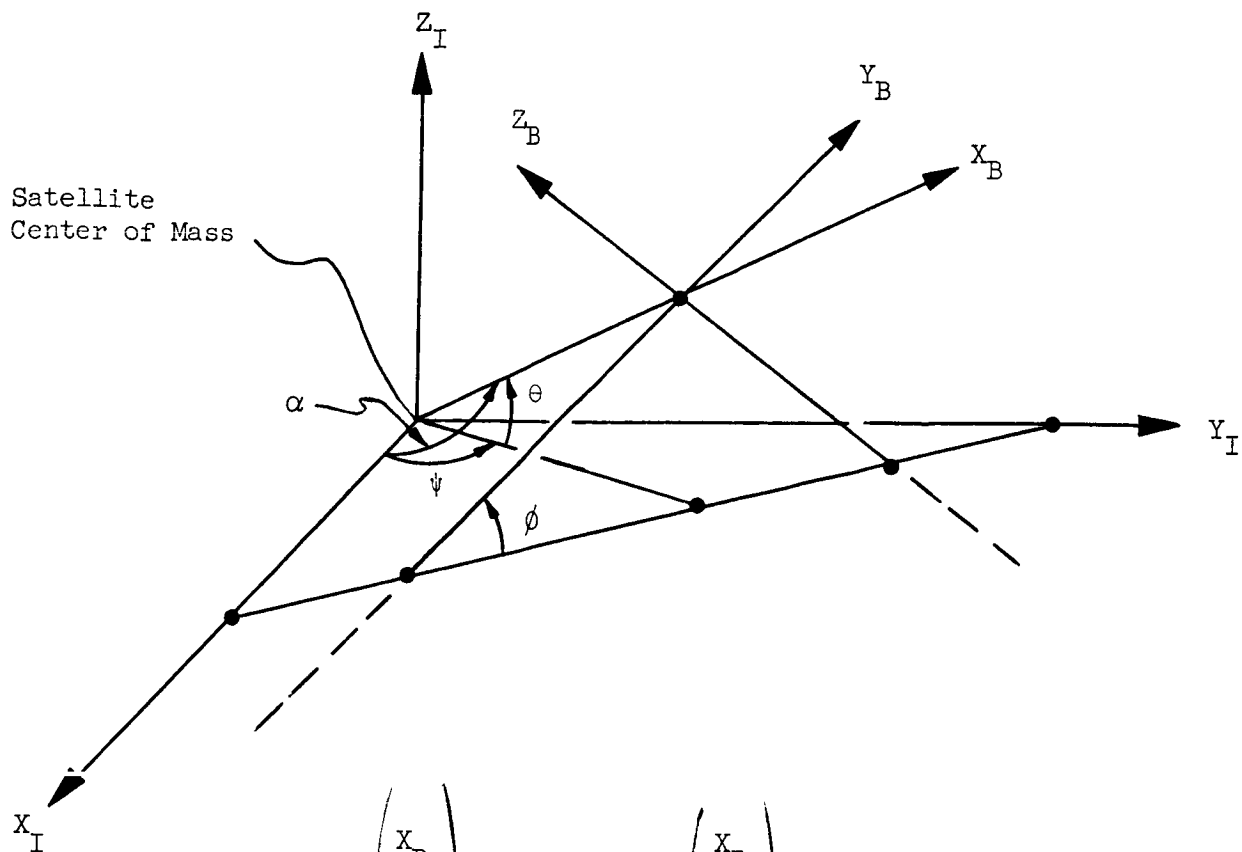
Figure 4.3-2. SB Geometric Configuration



$$\begin{pmatrix} X_I \\ Y_I \\ Z_I \end{pmatrix} = \begin{bmatrix} M_{OI} \end{bmatrix} \begin{pmatrix} X_O \\ Y_O \\ Z_O \end{pmatrix}$$

$$\begin{bmatrix} M_{OI} \end{bmatrix} = \begin{bmatrix} 1 & 0 & 0 \\ 0 & \cos \eta & -\sin \eta \\ 0 & +\sin \eta & \cos \eta \end{bmatrix}$$

Figure 4.3-3. Relationship Between Orbit-Plane Axes and Inertial Axes



$$\begin{pmatrix} X_B \\ Y_B \\ Z_B \end{pmatrix} = \begin{bmatrix} M_{IB} \end{bmatrix} \begin{pmatrix} X_I \\ Y_I \\ Z_I \end{pmatrix}$$

$$\begin{bmatrix} M_{IB} \end{bmatrix} = \begin{bmatrix} \cos \theta \cos \psi & \cos \psi \sin \theta \sin \phi & \cos \psi \sin \theta \cos \phi \\ \cos \theta \sin \psi & -\sin \psi \cos \phi & + \sin \psi \sin \phi \\ -\sin \theta & \cos \psi \cos \phi & \sin \psi \sin \theta \cos \phi \\ & + \sin \psi \sin \theta \sin \phi & -\cos \psi \sin \phi \\ & \cos \theta \sin \phi & \cos \theta \cos \phi \end{bmatrix}$$

For $\phi = 0$,

$$\begin{bmatrix} M_{IB} \end{bmatrix} = \begin{bmatrix} \cos \theta \cos \psi & -\sin \psi & \cos \psi \sin \theta \\ \cos \theta \sin \psi & \cos \psi & \sin \psi \sin \theta \\ -\sin \theta & 0 & \cos \theta \end{bmatrix}$$

$$\cos \alpha = \cos \theta \cos \psi$$

Figure 4.3-4. Relationship Between Body Axes and Inertial Axes

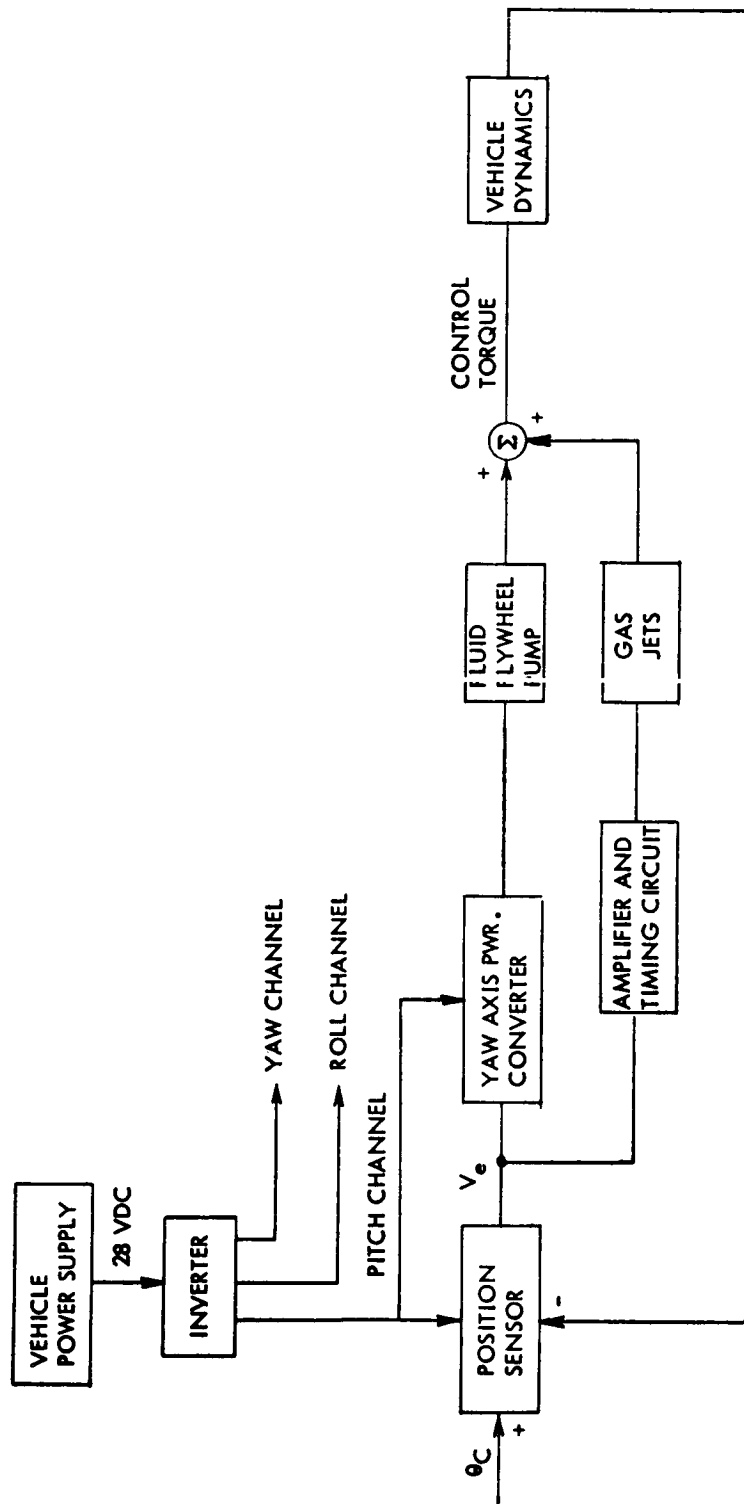


Figure 4.3-5. Functional Block Diagram of Fluid Flywheel Attitude Control System

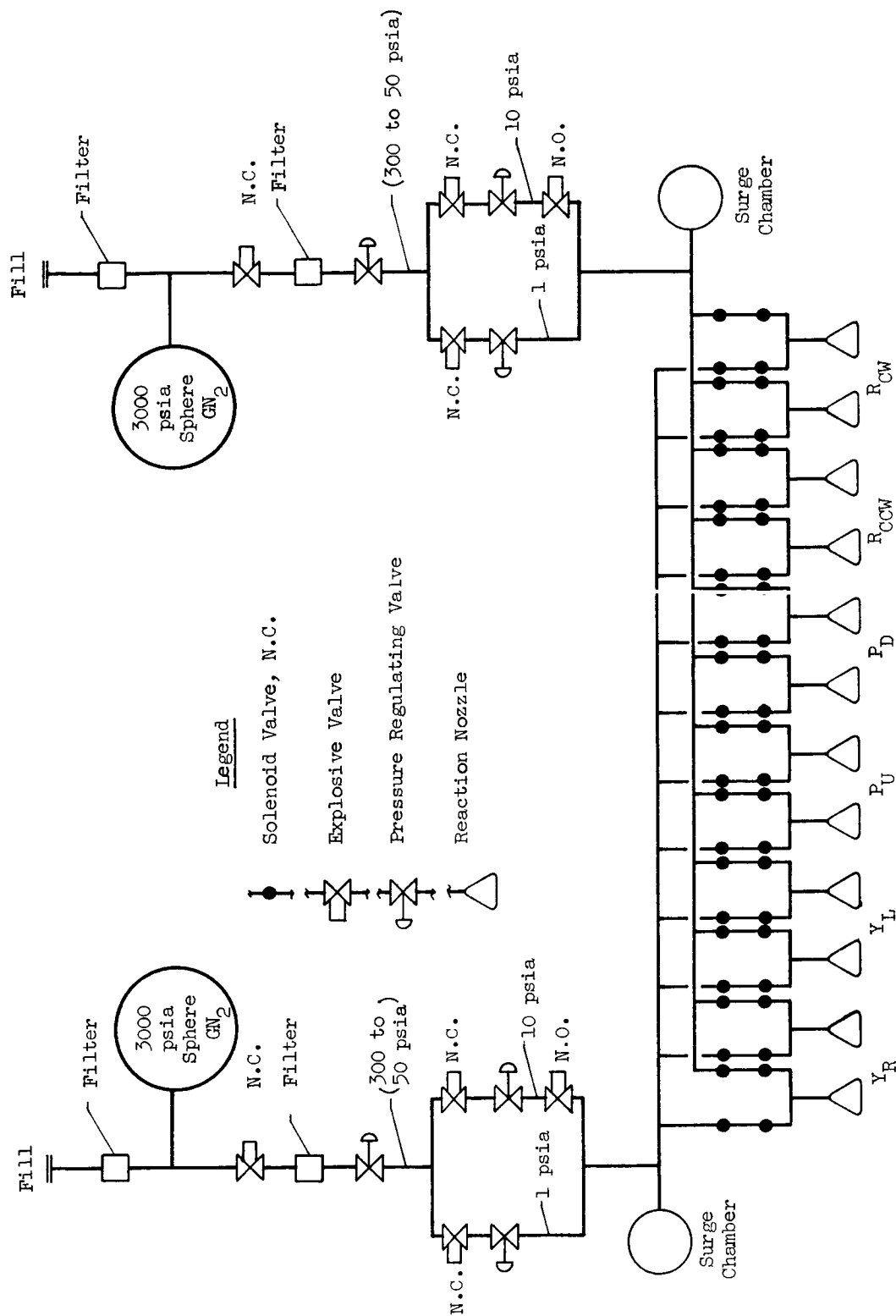


Figure 4.3-6. GN_2 ACS System Schematic

Reference: Space-General Report - Galactic Probe Studies, April 1966

The power output of solar cells varies inversely with their temperature; i.e., increasing temperature results in a decreasing power output. This facet of solar cell technology implies a potential trade-off between temperature control methods and illuminated solar cell area. As an example of this phenomenon, the temperature of a solar cell whose front surface is initially normal to the solar vector will decrease in temperature as the angle between the surface normal and the solar vector is increased from zero. This temperature decrease will result in an increase in the solar cell's power output, however, the decrease in intercepted solar energy will also decrease the electrical power output of the cell. Therefore, there is some angle at which the solar cell power output is a maximum. The value of this angle is highly dependent on the design characteristics of the electrical power system such as low voltage cut-off, solar cell covers, over voltage control method, etc.

To illustrate tradeoffs between competing systems, three hypothetical temperature control systems will be utilized in a simplified approach to find the one which gives the maximum illuminated solar cell surface area under the constraints of fixed gross area and panel temperature. The three subsystems are:

- (1) An active system using a liquid cooling loop and a radiator oriented so as not to see the sun on the two radiating surfaces.
- (2) A passive system which uses surface backed mirrors to reduce the area averaged solar absorptivity to infrared emissivity ratio.
- (3) A passive system which varies the angle between the solar vector and solar cell surface normal to achieve desired temperatures.

In all systems it will be assumed that the back side of the solar cell panel assemblies are radiating to space with an effective emissivity of 0.9 and that steady state conditions prevail.

The thermal energy balance for a unit area of solar cell is:

$$S \alpha_s \cos \theta (1 - \eta_s) (1 - x) + x \alpha_A S \cos \theta - \left[(1 - x) \epsilon_s + x \epsilon_A + \epsilon_B \right] \sigma T_s^4 - Q_L = 0 \quad (1)$$

where

- S = solar constant
- α_s = solar cell solar absorptivity
- θ = angle between solar cell normal and solar vector
- x = decimal fraction of solar cell panel covered by surface backed mirrors
- α_A = surface backed mirror solar absorptivity
- ϵ_s = solar cell I-R emissivity
- ϵ_A = surface backed mirror I-R emissivity
- ϵ_B = rear surface absorptivity
- σ = Stefan-Boltzman constant
- T_s = solar panel temperature (fore and aft)
- Q_L = heat transferred to cooling medium.

The heat transferred to the cooling medium, Q_L , may be written as

$$Q_L = 2 \epsilon_R y_r T_r^4 \sigma \quad (2)$$

where

- ϵ_R = radiator I-R emissivity
- y_r = radiator area relative to solar panel surface
- T_r = radiator temperature ($T_r < T_s$)

The ratio of solar cell illuminated area to gross area for each of the systems may be written as follows:

System (1) - Active using cooling loop

$$\frac{A_s}{A_g} = \frac{1}{1 + y}$$

System (3) - Passive using tilt angle

$$\frac{A_s}{A_g} = \cos \theta$$

System (7) - Passive using surface backed mirrors

$$\frac{A_s}{A_g} = 1 - x$$

The numerical values for each system are shown in Table 4.4.1-1.

Inserting the values in Equation (1) and solving for x , y , or $\cos \theta$ and the illuminated area ratios (A_s/A_g), we find the values in Table 4.4.1-2. In this example, subsystem (3) has the best value of the parameter (A_s/A_g). This would then have to be placed in the satellite systems study to determine the weight penalties required to achieve and maintain this angle.

The effects of temperature are shown in Tables 4.4.1-3 and 4.4.1-4 where the solar cell temperature (T_s) was taken as $+40^\circ\text{C}$ and 0°C , respectively and the radiator temperature (T_R) to $+10^\circ\text{C}$ and -30°C , respectively.

In the three cases considered, subsystem (3) has the best performance. From these results, subsystem (1) is not worthy of further consideration. However, subsystem (2) would probably show significant improvement with small changes in the back-surfaced mirrors absorptivity and emissivity values.

4.4.2 RTG POWER UNITS

RTG units now available or currently under development have certain common thermal limitations imposed on the user:

- (1) The RTG radiation surfaces are normally at temperatures of 600°K or higher.
- (2) The RTG mounting points are partly insulated but still too hot for mounting directly to metal surfaces of electronic components. Therefore additional insulation at the mounting is usually required.
- (3) A 2π steradian field of view for each RTG is desired and little deviation is permissible. Blocking the RTG's field of view would cause non-uniform cold junction temperatures, mismatching the thermal electric units, and reducing output and life. An object blocking the radiation view of an RTG and having the same characteristic dimension should in general be no closer than two or three characteristic dimensions.
- (4) The RTG is designed to accept temperature gradients caused by the sun shining on one side only. This gradient is of the order of 303°K .

With these general thermal characteristics the integration of multiple RTG units into a DSMCS could be accomplished as follows:

- (1) A mounting location such as shown on Figure 4.4.2-1 is desirable to maximize the RTG view of space.
- (2) A three unit group of RTG's offers the best view factors for the units. The use of parabolic reflectors to reflect heat rays to space and not back to the RTG's can be used effectively in this configuration to increase the packing efficiency. The mounting is noted to be a section of a three sided pyramid. This mounting seems to have the following advantages:
 1. Packaging of the RTG is most efficient.
 2. Parabolic reflectors can be used effectively to avoid local heating of the RTG's.
 3. The configuration permits radiation cooling of mounting struts.

The reflectors should be insulated with superinsulation to limit heat flow to the mounting system. Structural fiberglass mounting systems have been analyzed and found to be effective. The RTG mounts are expected to be at approximately 500°K and fiberglass insulating mounts would drop the structural temperatures to 300°K if radiation cooling of the struts is provided. This is

desirable in order that the structural mounts of the RTG system may connect directly to the electronics area and provide a room temperature environment.

In addition to this conventional approach, use of waste RTG thermal energy to heat attitude control system stored gas has been proposed in the past to improve attitude control system efficiency.

4.4.3 MASER AMPLIFIER COOLING

The magnitude of the maser cooling problem at the level of one watt continuous for a year or more is such that the only reasonable solution is a closed cycle heat pump. Over 2200 kg of liquid helium would be required (neglecting boil off) to last one year. This is a volume of approximately 20 cubic meters. A survey of the state-of-the-art on closed cycle refrigeration systems was conducted. Only those refrigerators capable of 4.2°K are of interest for the DSMCS. The best system noted has a specific power of 1000 (watts power input over cooling power at 4.2°K) and a specific weight of 22 (kg weight over watts cooling at 4.2°K). It is difficult to project this state-of-the-art to the mid 70's, however it is expected that an improvement of a factor of two could be accomplished.

A table was prepared listing each manufacturer and his cryogenic cooler in the survey. The following pertinent information was included in Table 4.4.3-1.

- nominal cryo-cooler temperature
- cooling capacity
- thermodynamic cycle employed
- comments on system components
- working fluid
- total power input
- system weight
- typical cool-down time
- design maintenance intervals
- application (ground, airborne, space)
- cost
- status (commercially available or research and development)

The following figures were prepared:

Figure 4.4.3-1 - Specific power (input/capacity) vs temperature for commercially available units and for units under development.

Figure 4.4.3-2 - Specific power (input/capacity) vs specific weight (weight/capacity) for commercially available units and for units under development.

The general requirements for cryogenic coolers for electronic applications (airborne and space) include lightweight construction, small size, low power input, self-containment, easy maintainability, and high reliability.

A number of cryo-coolers of different types are presently commercially available. Because of certain inherent deficiencies in each of the classes or types of closed-cycle coolers, any one commercially available unit falls short in fulfilling the requirements of optimum size, weight, power requirements, cool-down time, reliability, and maintenance-free operating time. Performance specifications for these "production" units are often quoted without sufficient experimental data and must therefore be used with reservation.

Cryogenic closed-cycle coolers are also under development as company sponsored efforts to improve the characteristics of "production" units, or as programs funded by the military. The latter generally involve new concepts for specific applications.

An investigation was made to see if the DSMCS could provide a special environment by which systems integration could provide improvements. The possibility of using LN_2 (whose primary purpose is ACS propellant) to improve the refrigeration cycle was investigated. The one year or more life requirement resulted in an excessive LN_2 requirement. Therefore this solution alone was not suitable. The possibilities of using an oriented space radiator was considered. First the oriented (to cold space away from both sun and earth) radiator is not practical if RTG units are also used. Assuming that an oriented radiator were used with a solar panel system then the effectiveness of the area is given by Figure 4.4.3-3.

Other considerations include the possibility that substantial reduction in cooling requirement at 4.2°K may be accomplished by careful design. A 1-watt load at 4.2°K was assumed for this work. Proper shielding with superinsulation and possibly with LN_2 (ACS) could provide a substantial reduction in cooling requirement especially if RTG units are not present.

4.4.4 TRANSMITTER WAVE GUIDE THERMAL CONSIDERATIONS

The energy loss in the first half meter of a DSMCS transmitter wave guide is estimated at 2 kW. Clearly this amount of energy dissipation in a small volume (about 0.3 cc) will require a cooling system. Figure 4.4.3-3 is the minimum area requirement as a function of temperature of the radiator. Figure 4.4.4-1 is an estimate of the minimum heat radiated and conducted to the maser. Pending a more thorough analysis it appears that a fluid cooling system with a remote radiator is desirable. In addition, the connection between the transmitter wave guide and the maser transmission line will require special consideration. Most probably a disconnect with a radiation shield will be required. A cool-down period after transmitting and reconnection of the maser to the horn would be required.

A major question concerns the relative location of the transmitter and the maser. The transmitter dissipates a total of 20 kW with the wave guide dissipating about 2 kW in the first foot. The maser cavity is to be held at 4.2°K therefore heat transfer from the transmitter and wave guide must be minimized. Using superinsulation, which is highly effective in space vacuum, and laterally conducting shields, the maser holder and the transmitter need be only a few centimeters apart (probably less than 15 cm would be optimum). Mounting and support systems are to be carefully designed. Nichrome electrical wires are recommended wherever practical. Special support systems for the maser cavity are recommended. Tension supports of glass or Nichrome are possible. Impregnated fiberglass support chords have been used successfully on developmental structures.

4.4.5 TRANSMITTER COOLING

The transmitter would occupy a volume of approximately 0.35 m^3 ,

weigh about 100 kg, and dissipate about 20 kW intermittently. Using these assumptions the system temperature rise per minute of operation would be 20°C . If operation were continuous, the temperature level would be excessive (assuming no special cooling system) at a level of about 700°K . Operation at the rate of one minute per hour would result in a mean temperature of about 20°C with a variance of $\pm 10^{\circ}\text{C}$. Operation at the rate of 2 minutes per hour would require radiator area (about 1.4 m^2) in excess of the normal area of the transmitter surface.

The transmitter will have high concentrations of power dissipation within the unit. Probably conduction paths to the sides for radiant dissipation will not be adequate and a circulation fluid will be required. A single phase system (liquid heat transfer fluid) is suggested. The pump for this system would require minimum power, being used to overcome flow friction only. The sides of the transmitter enclosure would provide radiator surface area.

4.4.6 OTHER ENVIRONMENT EFFECTS

In addition to the thermal control considerations discussed in the preceding sections, radiation effects both natural and onboard and other natural environment considerations were investigated. Onboard radiation effects from nuclear power sources are noted under power systems in Section 4.2.1 in this volume. Environment effects on solar panel power systems are presented in Section 4.2.2, Non-Nuclear Power Systems. Other environment considerations are discussed in Section 3.3.2 under Radiation Belts, Solar Plasma and Micrometeoroid Flux.

Table 4.4.1-1

SUBSYSTEM CHARACTERISTICS

Item	Subsystem		
	1	2	3
S	0.140 watts/Sq. Cm.		
α_s^*	0.84		
θ	0°	0°	Unknown
s	0.05		
x	0	Unknown	0
α_A^*	-	0.10	-
ϵ_s	0.82		
ϵ_A	-	0.85	-
ϵ_B	0.90		
σ	$5.67 \times 10^{-12} \text{ watts/cm}^2 - ^\circ\text{K}^4$		
T_s	$20^\circ\text{C} (293^\circ\text{K})$		
y	Unknown	0	0
T_r	$-10^\circ\text{C} (263^\circ\text{K})$	-	-
ϵ_R	0.90	-	-

* Normally a function of θ but will be assumed constant in this illustration.

Table 4.4.1-2

SUBSYSTEM PERFORMANCE
 $(T_s = 20^{\circ}\text{C}; T_R = -10^{\circ}\text{C})$

Item	Subsystem		
	1	2	3
(A_s/A_g)	0.545	0.593	0.644
x	-	0.407	-
y	0.834	-	-
θ	-	-	50°

Table 4.4.1-3

SUBSYSTEM PERFORMANCE
 $(T_s = 40^{\circ}\text{C}; T_R = 10^{\circ}\text{C})$

Item	Subsystem		
	1	2	3
A_s/A_g	0.700	0.719	0.840
x	-	0.281	-
y	0.428	-	-
θ	-	-	33°

Table 4.4.1-4

SUBSYSTEM PERFORMANCE
 $(T_s = 0^{\circ}\text{C}; T_R = -30^{\circ}\text{C})$

Item	Subsystem		
	1	2	3
A_s/A_g	0.380	0.415	0.430
x	-	0.585	-
y	1.63	-	-
θ	-	-	64.5°

Table 4.1.3-1
STATE-OF-THE-ART OF CLOSED-CYCLE
CRYOGENIC COOLERS *

Manufacturer	Nominal Cryo-Cooler Temperature (°K)	Cooling Capacity (watts)	Thermodynamic Cycle	Comments	Working Fluid	Total Power Input (watts)	System Weight (lb)	System Size	Typical Cooldown Time (Minutes)	Main- tenance Interval (hours)	Appli- cation	Cost or Status
1. Air Products and Chemicals	23	0.35 at 25°K	Cascaded Joule- Thompson	2 2-stage dry compr. (air cooled)	Nitrogen	1050	50	10"x13"x12"	28	-		\$17 K (1)
	30	0.35 at 30°K	Cascaded Joule- Thompson	2 2-stage dry compr. (air cooled)	Nitrogen	1050	50	10"x13"x12"	28	300	Space	\$17-20 K (1)
	80 ± 2	2.0 at 80°K	Single Stage Joule-Thompson	1 2-stage dry compr. (air cooled)	Neon	600	18	5"x8"x12"	< 5	500		\$9 (1)
2. Arthur D. Little	15	0 at 15°K	Single Stg. Mod. Taconis Cycle w/ LN ₂ input		Helium	100 to 200		6"dia x 24"lg				R&D
	77 ± 7	2.5 at 77°K	Rotary Stroking Brayton Cycle		Helium	100	22	8"dia x 24"lg		10,000 (30,000)	Space	R&D AF (28 Feb '66)
	160	5.0 at 160°K or 10.0 at 190°K	Single Stage Gifford McMahon		Air		10	6"x6"x10"				R&D
3. Cryogenics Corp.	4.2	1.0 at 4.2°K or 3.0 at 15°K or 10.0 at 80°K	Two Expander Claude Cycle plus J-T	Reciprocating compressor and Expanders	Helium	2500 to 4000	75 to 90	1.25 ft ³	< 5 hrs	500 (5,000)		R&D Completed
	30	3.0-5.0 at 30°K + 10-15 at 80°K	Two Stage Stirling		Helium	1500	20 + Motor	5"x6"x18"	30	2500	Ground	R&D (U.S.Army) Completed
	40	2.5 at 40°K + 3.0 at 70°K	Two Stage Stirling		Helium	750			30	2500		R&D
4. Fairchild Stratos	23	0.2 to 0.3 at 23°K	Cascaded Joule- Thompson	Oil Lubricated Diaphragm Com- pressors	Nitrogen	550 (+ Fan)	35	8"x9"x18"	15	500		
	30	0.4 to 0.5 at 30°K	Cascaded Joule- Thompson	Operating Temp. depends on gas, or gases, used	Nitrogen Neon	550 (+ Fan)	35	8"x9"x18"	10	500	Commer. Available	
	80	2.0 to 10.0 at 80°K	Single Stage Joule-Thompson		Nitrogen	550 (+ Fan)	35	8"x9"x18"	< 5	500		
5. The Garrett Corp.	3.6	1.0 to 2.0 at 3.6°K	Claude Bypass Expansion Cycle plus J-T	1 8-stage turbo- compr. plus 3 turbo-expanders	Helium	9000	88.5	12"dia x 30"lg		10,000 (+)	Space	R&D (AF) Lab Model 30 June '66
	4.2	0.7 at 4.2°K or 0.5 at 12°K or 7.0 at 88°K	Claude Cycle plus J-T	2 4-stage turbo- compr. plus 2 turbo-expanders	Helium	8400	150	11"dia x 30"lg < 8 hr		2,500 (5,000)	Ground	R&D (U.S.Army)
	30	2.0 at 30°K	Reversed Brayton Cycle	1 3-stage turbo- compr. plus 2 turbo-expanders	Neon	550	25			10,000 (30,000)	Space	R&D (AF)
	77 ± 7	2.0 at 77°K	Reversed Brayton Cycle	1 3-stage turbo- compr. plus 1 turbo-expander	Nitrogen	357	17.5	10"dia x 12"lg	2 hr	10,000 (30,000)	Space	R&D (AF) 1 Jan. '66
	77	2.0 at 77°K	Single Stage Joule-Thompson	2-stage Oil Lubr. compr. (air cooled)	Nitrogen	400	23	11"x15"x10-3/4"	5		Aircraft Production	
	77	5.0 at 77°K	Single Stage Dual Expan. J-T	3-stage Oil Lubr. compr. (air cooled)	Nitrogen	480	15.5	7" dia x 15"lg	3-5		Aircraft Production	

*Reference B: Internal Aerojet Material prepared mid 1965

Table 4.4.3-1 (Continued)
STATE-OF-THE-ART OF CLOSED CYCLE
CRYOGENIC COOLERS *

Manufacturer	Nominal Cryo-Cooler Temperature (°K)	Cooling Capacity (watts)	Thermodynamic Cycle	Comments	Working Fluid	Total Power Input (watts)	System Weight (lb)	System Size	Typical Cooldown Time (Minutes)	Main- tenance Interval (hours)	Appli- cation	Cost or Status
6. General Electric	3.6	1.0 to 2.0 at 3.6°K	Modified Claude Cycle plus J-T	3 stage turbo- comp. plus 2 turbo expanders	Helium	3750 watts/w	65	12"dia x 34"lg	10,000 +	10,000 +	Space	Devel. (AP) Lab Model 30 Apr. 66
7. Hughes Aircraft	4.2	5.0 at 4.2°K or 2.0 at 4.2°K + 6.0 at 15°K + 12.0 at 50°K + 60.0 at 150°K	3 Stage Solvay plus J-T	Single Stage Dry Compr. (liquid cooled)	Helium	5000	250 (100)	6"dia. x 30"lg 14"x14"x30" 14"x14"x24"	30	500 (10,000) ult.	R&D Commer. Avail.	R&D Commer. Avail.
	12	0.4 at 12°K	2 Stage Solvay	Single Stage Dry Compr. (liquid cooled)	Helium	575	40 (25)	3"dia x 13"lg 5"x5"x15"	30	300	300	20-30K (8-10) Commer. Avail.
	12	1.0 at 12°K	2 Stage Stirling	Single Stage Dry Compr. (liquid cooled)	Helium	450	12	5"x5"x8"	20	1000	1000	R&D
	20	0 at 20°K or 1.0 at 25°K or 2.0 at 30°K	Single Stage Solvay	Single Stage Dry Compr. (liquid cooled)	Helium	575	40 (25)	3"dia x 13"lg 5"x5"x15"	15	300	300	20-30K (8-10) Commer. Avail.
	25	4.0 at 25°K + 8.0 at 80°K	2 Stage Stirling	Single Stage Dry Compr. (liquid cooled)	Helium	450	12	5"x5"x8.5"	30	1000	1000	R&D
	28	1.0 at 28°K	Single Stage Stirling w/Neon Liq. Trans. Loop	Remote Cooling with Inquifra- tion Loop (Neon)	Helium + Neon	500	18	6.5"x6.5"x12"	< 10	1000	1000	R&D
	45	0 at 45°K or 10 at 60°K or 25 at 80°K	Single Stage Stirling	Air Cooled	Helium	450	10	5"x5"x8.5"	< 5	1000	1000	25-30K (8-10) Commer. Avail.
	77	10.0 at 77°K	Single Stage Stirling plus Leidenfrost Trans. Loop	Remote cooling with Inquifra- tion loop (Air)	Helium + Air	500	15 or 3.5"x5"x8.5"	5.5"dia x 11"lg	< 5	1000	1000	25-30K (8-10) Commer. Avail.
	77	12 at 77°K (N ₂) or 15 at 80°K (Ar)	Single Stage J-T using N ₂ or Ar	Dry Compressor	Nitrogen or Argon	750	65	11"x16"x18"	5	250	250	R&D Commer. Avail.
8. Linde	4.2	1.0 at 4.2°K	Claude Cycle plus J-T	Dry Compressor, 2 Reciprocating Expanders	Helium	2300	75 to 100	18"x24"x36"	5,000 (10,000) ult.	5,000 (10,000) ult.	R&D	R&D
9. Santa Barbara Research (Hughes Aircraft)	79 ± 1	2.0 at 79°K	Single Stg. J-T	Oil Lubr. Comp. (Air cooled)	Nitrogen	326	16	7"dia x 12.5"lg	< 5	500	Airborne	20K (6-8) Commer. Avail.
	80 ± 1	5.0 at 80°K	Single Stage J-T	Oil Lubr. Comp. (Air cooled)	Nitrogen	326	16	7"dia x 12.5"lg	< 5	500	500	500
	82 ± 1	0.5 at 82°K	Single Stage J-T	Oil Lubr. Comp. (Air cooled)	Nitrogen	0	9.5	6"dia x 9.5"lg	< 5	200	Airborne	20K (6-8) Commer. Avail.

* Reference B: Internal Aerojet Material Prepared mid 1965

Table 4.4.3-1 (Continued)
STATE-OF-THE-ART OF CLOSED CYCLE
CRYOGENIC COOLERS *

Manufacturer	Nominal Cryo-Cooler Temperature (°K)	Cooling Capacity (watts)	Thermodynamic Cycle	Comments	Working fluid	Total Power Input (watts)	System Weight (lb)	System Size	Typical Cooldown Time (Minutes)	Main- tenance Interval (hours)	Appli- cation	Cost or Status
10. Malaker Laboratories	5	0.5 at 5°K	3 Stage Stirling Cycle		Helium		45		500			R&D
	10 8°	1.0 at 10-12°K	2 Stage Stirling Cycle		Helium		35		500			R&D
	15	0 at 15°K or 2.5 at 20°K or 20 at 77°K	2 Stage Stirling Cycle		Helium	600	30	5 ft ³	20			R&D Air Force Complete ?
	20	0 at 20°K or 2.0 at 29°K	Single Stage Stirling Cycle	Air Cooled	Helium	375	15	5"dia x 14"lg	10	750	VII-C	\$5 K (1) Commer. Avail.
	32	0 at 32°K or 4.0 at 40°K	Single Stage Stirling Cycle	Air Cooled	Helium	350	15	5"dia x 12.5"lg	5	750	VII-B	\$5 K (1) Commer. Avail.
	32	0 at 32°K or 1.0 at 77°K	Single Stage Stirling Cycle	Air Cooled	Helium	250	15	5"dia x 12" lg	5	750	VII-B	\$5 K (1) 4.3 Commer. Avail.
	67	0 at 67°K or 2.0 at 77°K	Single Stage Stirling Cycle	Extendable Cold Head (3 ft max.)	Helium	250	15	5"dia x 12.5"lg	6	500	VII-H	Avail.
11. North American Philips Co.	15	1.0 at 15°K	2 Stage Stirling Cycle		Helium			0.5 ft ³			Airborne R&D	
	25	0 at 25°K or 1.0 at 50°K or 10.0 at 80°K	Single Stage Stirling Cycle	Liquid Cooled	Helium	450	24	0.32 ft ³	7	250	Airborne	\$7.5 K (1) Commer. Avail.
	77	Produces 120 Gm/hr Liquid N ₂	Single Stage Stirling w Air or N ₂ Leidenfrost Transfer Loop	Remote Cooling with Liquidation Loop	Helium & N Nitrogen	450	25	0.4 ft ³	9	250		R&D
12. Texas Instruments	12.5	0 at 12.5°K or 1.5 at 15°K	2 Stage Cryogenic Gas Balancing Cycle		Helium				25			R&D
	20	0 at 20°K	2 Stage Cryogenic Gas Balancing Cycle		Helium	750			12			R&D
	28	0 at 28°K	Single Stg. Cryo- matic Gas Balance- ing Cycle		Helium							R&D
	50	0 at 50°K	Single Stg. Cryo- matic Gas Balance- ing Cycle		Helium							R&D
13. Westinghouse Electric	77	1.0 at 77°K	Single Stage J-T	Diaphragm Compr.	N Nitrogen			0.12 ft ³	10			R&D

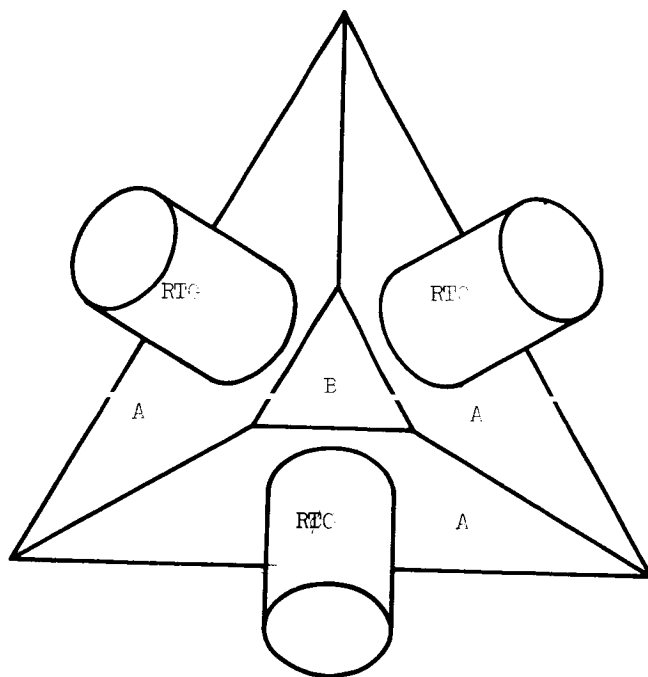
* Reference B: Internal Aerojet Material Prepared mid 1965

Table 4.4.3-1
STATE-OF-THE-ART OF CLOSED-CYCLE CRYOGENIC
COOLERS

DEVELOPED SYSTEMS										SYSTEMS UNDER DEVELOPMENT									
Sponsoring Activity					Air Force					Army					Garrett				
Contract No.					AP33(607)-7888					AP33(615)-1015					DA-36-039 ANG-0725(S)				
Cooling Level, °K					77° ± 1°					77° ± 1°					4.2°				
Capacity (watts)					1-2					1-2					1				
Cool-down Time (minutes)					120					120					360				
Size					8" dia. x 12" L					12" dia. x 34" L					12" dia. x 30"				
Weight					15					30					90				
Service Life					Unspecified					Unspecified					2500				
Input Power, Watts					150					600					5000				
Prototype Test					October, 1964					December, 1965					December, 1965				
Cycle					Reverse Brayton					Reverse Brayton					Claude Bypass				
Working Fluid					Nitrogen					Helium					Helium				
Compressor					2 Stage Centrifugal					2 Stage Centrifugal					8 Stage Centrifugal				
Expansion					Single Stage Turbo-Expander					Single Stage Turbo-Expander					Two Stage Turbo-Expander				
Remarks					2 Stage J-T					2 Stage J-T					2 Stage J-T				

NOTE: Although, at the moment, only two systems have been developed and tested, we will be able to offer, on a fixed price basis, a system to provide 77°K refrigeration in any capacity from 0.5 to 6.0 watts. Only minor modifications would be involved such as changing the bore or stroke of the compressor.

(Frustum of Three Sided Pyramid)
(Base of Pyramid Mounts to Spacecraft)



Surfaces

- A - Highly polished specular reflector surfaces backed by 30 layers of superinsulation.
- B - Heat rejection surface for internal structural members

Figure 4.4.2-1 Suggested Mounting for 3 RTG System

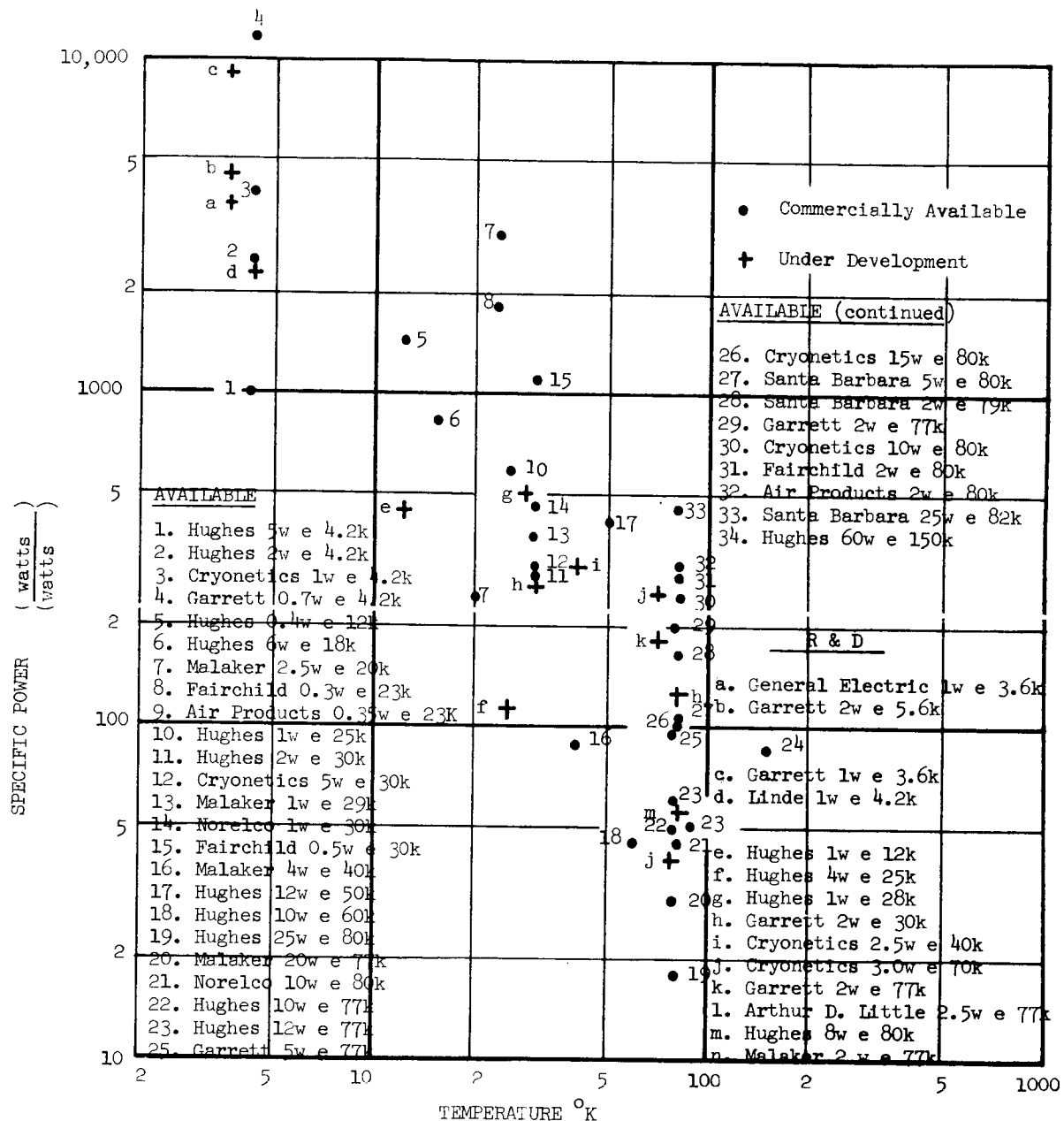


Figure 4.4.3-1. Specific Power vs Temperature for Closed-Cycle Cryogenic Coolers

FOR
CLOSED-CYCLE CRYOGENIC COOLERS

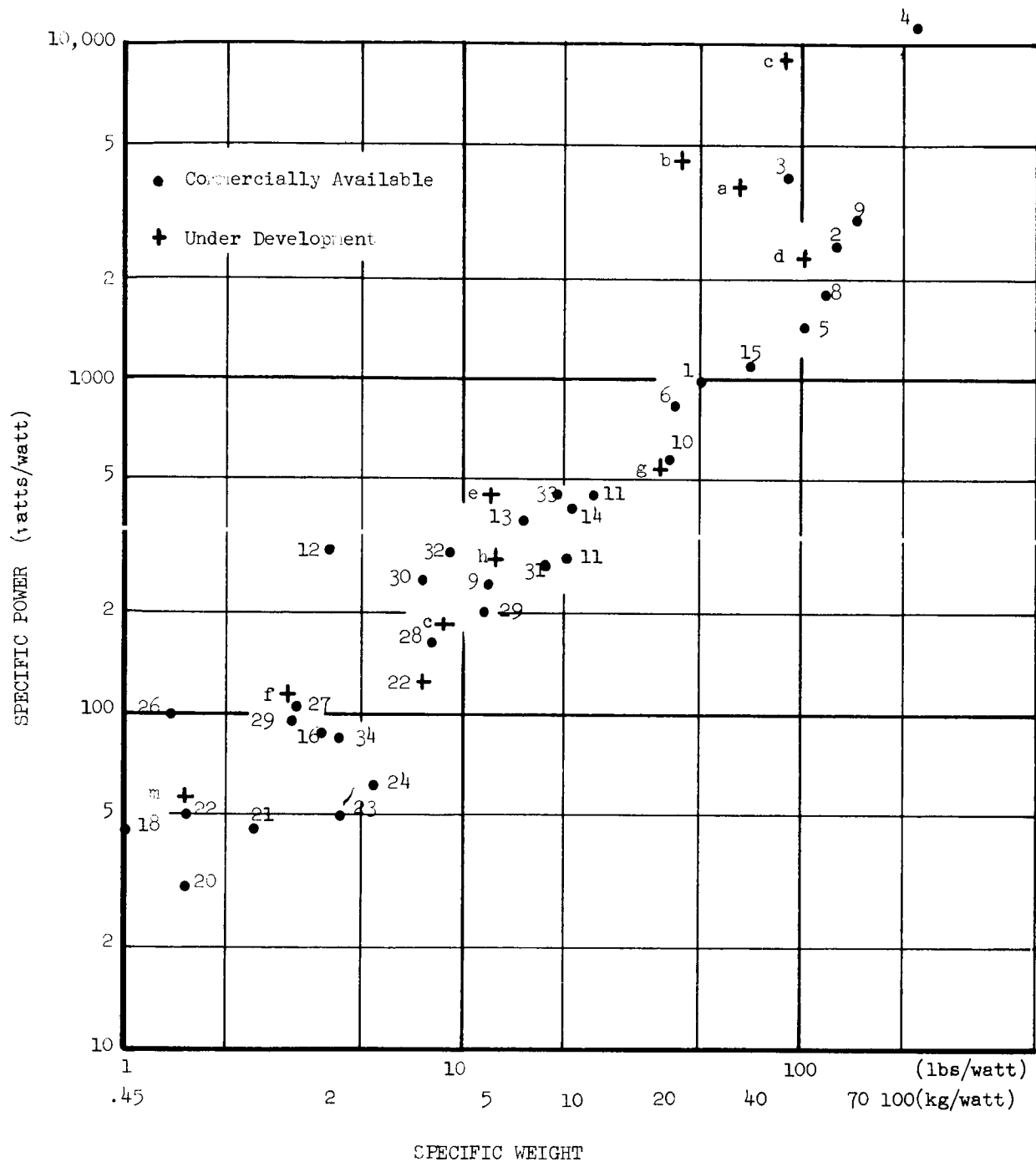


Figure 4.4.3-2 Specific Power vs Specific Weight for Closed-Cycle Cryogenic Coolers

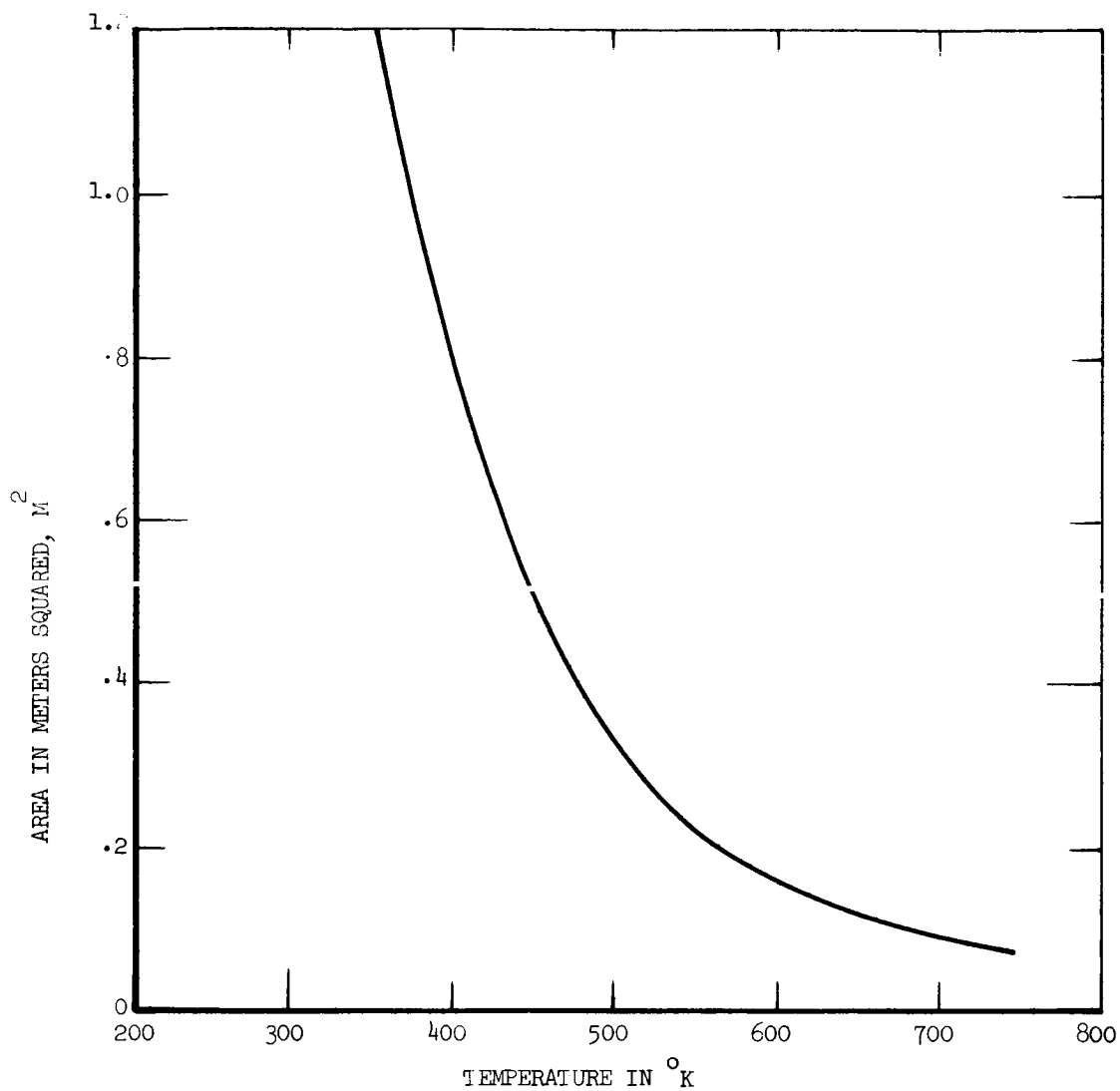


Figure 4.4.3-3 Minimum Area Required to Radiate 1 kw

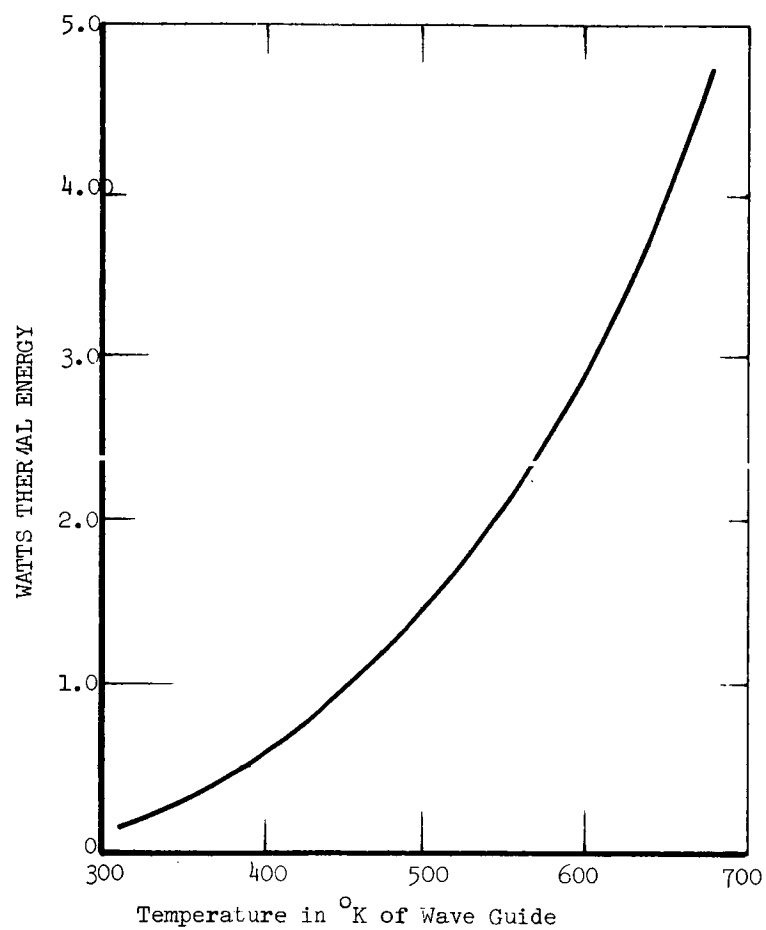


Figure 4.4.4-1 An Estimate of Minimum Heat Flow From Wave Guide to Maser Cavity